Novel characterisation of complex dispersions using acoustic backscatter systems

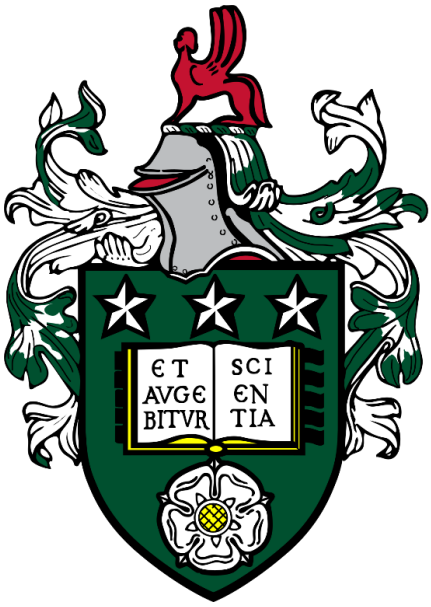

Alastair Simon Tonge

School of Chemical and Process Engineering

University of Leeds

Submitted in accordance with the requirements for the degree of
Doctor of Philosophy

August 2021

The candidate confirms that the work submitted is his/her own, except where work which has formed part of jointly authored publications has been included. The contribution of the candidate and the other authors to this work has been explicitly indicated below. The candidate confirms that appropriate credit has been given within the thesis where reference has been made to the work of others.

Edited portions of Chapter 3 appear in the paper: A. Tonge, J. Bux, D. Cowell, J. Peakall, S. Freear and T. Hunter, "Concentration profiling using a novel acoustic backscatter system with single transducers pulsed at multiple frequencies." In 2017 IEEE International Ultrasonics Symposium (IUS), 2017. https://doi.org/10.1109/ULTSYM.2017.8091603. The candidate was the main author and responsible for the experiments, analysis, figures, calculations, and proof reading. The research was driven by Hunter, Peakall, Freear and Cowell. Provision of the acoustic backscatter system, code used to run the system and experimental support was provided by Cowell. Experimental and analysis support was provided by Bux.

Edited portions of Chapter 3 appear in the paper: A. Tonge, J. Peakall, D. Cowell, S. Freear, M. Barnes and T. Hunter, “Experimental validation of acoustic inversions for high concentration profiling of spherical particles, using broadband technology in the Rayleigh regime.” In Applied Acoustics, Volume 180, 2021. https://doi.org/10.1016/j.apacoust.2021.108100. The candidate was the main author and responsible for the experiments, analysis, figures, calculations, and proof reading. The research was driven by Hunter, Peakall, Freear, Cowell and Barnes. Provision of the acoustic backscatter system, code used to run the system, experimental support and figures detailing the input signal to generate the acoustic signal from the acoustic backscatter system was provided by Cowell.

Data from Chapter 4 appears in the paper: T. Hunter, J. Peakall, D. Egarr, D.M.J. Cowell, S. Freear, A.S. Tonge, L. Horton, H.P. Rice, I. Smith, K. Malone, D. Burt, J. Peakall, G. Randall, S. Biggs, M. Fairweather, “Concentration profiling of a horizontal sedimentation tank utilising a bespoke acoustic backscatter array and CFD simulations.” In Chemical Engineering Science, Volume 218, 2020. https://doi.org/10.1016/j.ces.2020.115560. The candidate provided FBRM data

shown in the paper and experimental support. The research was driven by Hunter, Peakall, Randall, Biggs and Fairweather. CFD analysis was provided by Horton, Burt, and Malone. Experimental support and analysis was provided by Hunter, Cowell, and Smith.

Preliminary data from Chapter 4 appears in the paper: T. Hunter, J. Peakall, A. Tonge, M. Fairweather, H.P. Rice, M. Barnes, “Development of Acoustic Backscatter for In Situ Monitoring of Nuclear Sludge Wastes During Transfer.” In WM2020 Conference Proceedings. WM Symposia, 2020. Scattering cross-section data for Barnon Pond sludge and proof reading was provided from the candidate. Hunter was the primary author with the research driven by Hunter, Peakall, Fairweather and Barnes. Experimental data was also provided by Rice.

Edited portions of Chapter 5 appear in the paper: A. S. Tonge, S. Usher, J. Peakall, S. Freear, D. Cowell, G. Franks, K. Mohanarangam, V. Ravisankar, M. Barnes, and T. Hunter. "Use of In Situ Acoustic Backscatter Systems to Characterise Spent Nuclear Fuel and its Separation in a Thickener." In WM2019 Conference Proceedings. WM Symposia, 2019. The candidate was the main author and responsible for the experiments, analysis, figures, calculations, and proof reading. The research was driven by Hunter, Peakall, Freear, Cowell, Barnes and Franks, experimental support was provided by Usher, Mohanarangam and Ravisankar and all authors provided comments on the paper.

Signed

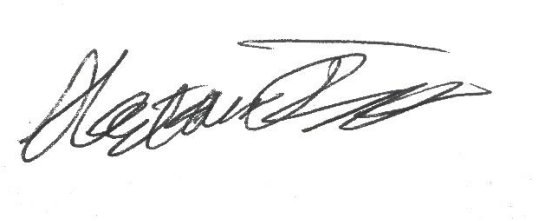

9th August 2021

Acknowledgements

I would foremost like to thank Timothy Hunter, my primary supervisor, for his academic advice, continued motivation and always being receptive to my own ideas. I would similarly like to thank my supervisors Jeff Peakall and Steven Freear. Jeff was readily available to provide insightful input and take a broader perspective on my results. Steve provided both encouragement and a high level of academic guidance, in particular concerning the electronics systems used for which his input is considered invaluable. I would also like to thank David Cowell for his continued technical support and guidance and for the many hours spent developing the UARP II that was used in this study. Martyn Barnes and Geoff Randall, the industrial supervisors for this project, have been of great help in providing industrial context and for their continued support for this project. Particular thanks go to Shane Usher for his extensive experimental assistance and guidance during the thickener experiments at the University of Melbourne and for providing both accommodation and introduction to traditional Australian culture. Krishna Mohanarangam and Vivek Ravisankar kindly provided access to and assistance in commissioning and operation of the experimental setup used to take in-line focussed beam reflectance measurement. Many thanks go to the EPSRC and Sellafield Ltd. for funding this project. This work is also affiliated with the Decommissioning, Immobilisation and Storage Solutions for Nuclear Waste Inventories (DISTINCTIVE) consortium (Grant EP/L014041/1).

I would also like to thank my parents Ian and Jean, my sister Helen and my stepfather David for their support and for being a constant source of inspiration to me. My gratitude also goes out to my friends and colleagues for their camaraderie in times of strife and success. In particular, I would like to thank Alex, Calum Danny, Jaiyana, Mike, Jamie, Jess, Joe, Matt and Toby for all the help they have given me and for making my time in Leeds so memorable.

“The key is to keep company only with people who uplift you, whose presence calls forth your best.” - Epictetus

Abstract

The application of novel measurement techniques to facilitate nuclear waste processing and transport operations is of great interest to Sellafield Ltd. where legacy waste has remained exposed to the environment for many years and formed a complex suspension of both organic and non-organic materials. Ultrasonic techniques may allow for *in situ* measurement of both particle size and concentration and have further applications in a wide array of industries such as mineral and food processing. To this end Acoustic backscatter system (ABS) data collected in laboratory scale calibration was used to explore the limits of the single and dual frequency concentration inversion methods as a function of particle size, sediment type and insonification frequency.

Accurate concentration profiles were able to be obtained up to a limit of 130 g l^{-1} for non-cohesive sediments (three sizes of glass beads) and up to a limit of 35 g l^{-1} for cohesive sediments (calcium carbonate, magnesium hydroxide and pond sludge obtained from Appleby-in-Westmorland) although this limit was lower for certain datasets. Beyond an attenuation limit of ~10 Np m^{-1} inversions became inaccurate that may aid in simple identification of erroneous results during *in situ* measurement. A novel method to correct for erroneous ABS results caused by non-spherical signal spreading close to the transducer is also presented.

The experimental form function, f, and scattering cross section, χ, were determined for all particles studied and cohesive sediment results were density normalised for comparison with model data. It was concluded that, although flocs appear to scatter in a similar manner to solid particles of the same size, a reduction in both the scattering cross-section and form function compared to modelled solid scatterers is seen. The reduction in f and χ is not as significant as the scattering model that incorporates porosity (the Hybrid model) would predict and is instead attributed here to viscous layer overlap causing multiple scattering of the acoustic signal within the floc. By taking acoustic measurements at multiple frequencies a method is given that may allow for determination of the standard deviation of a flocculated particle size distribution by fitting of the porous scattering model to experimental data so long as the mean particle size is known. The heuristic fits used were found to generally

accurate for prediction of χ when viscous attenuation was accounted for however significant variation was found to exist in in the long wavelength regime that may be the result of structural attenuation. Experimental values for *f* were found to deviate significantly, but consistently from model predictions toward the long wavelength limit that provides a path for future model fits.

The ability of ABS to track bed height *in situ* as well as non-intrusively track concentration changes and during pseudo-steady state operation of a laboratory scale thickener was demonstrated via attenuation of the acoustic signal through the settled bed. Bed height measurements were used to model the residence time of the sediment in the bed thickener output concentration that compared favourably with the attenuation and output samples respectively.

Results and methods presented herein could allow for more rigorous application of known methods of analysis of acoustic backscatter results while exploring the limits of these same techniques so they can be applied with confidence in the accuracy of obtained data for the processing of complex dispersions such as spent nuclear fuel. The potential extension of known analysis methods to large-scale industrial systems such as thickeners is also explored that has applications in a number of industries and would aid in the diagnosis and improve the operational efficiency of these systems.

Table of Contents

List of figures

Nomenclature

Roman Symbols

Symbol	Unit	Parameter name
a	m	Particle radius
a_0	m	Number weighted mean particle radius
A	m^2	Cross-sectional area of settling tank
a_t	m	Transducer radius
c	$m\ s^{-1}$	Speed of sound
c_v	–	Scatterer volume fraction
C_f	$kg\ m^{3-m}$	Effective density flocculation constant
d_{comp}	$m^2\ s^{-1}$	Change in settling velocity due to compression
d_{disp}	$m^2\ s^{-1}$	Change in settling velocity due to dispersion
$dh_{compression}$	$m\ s^{-1}$	Combined additional downward bed velocity due to compression, dispersion and hindered settling effects
D_f	–	Fractal dimension
E	$W\ m^{-2}$	OBS radiant intensity
f	-	Form Function
F	MHz	Isonification frequency
G	ln(V m)	G-function
h_{bed}	M	Height of settled bed
I	dB	Acoustic Bascatter Intensity
$I(q)$	m^{-1}	Normalised scattered light intensity (at scattered wave vector, *q)*
Jn	$(kg\ m^{-3})^{Np}$	Normalised acoustic scattering intensity at frequency *n*
k	m^{-1}	Wavenumber
ks	$m\ kg^{-\frac{1}{2}}$	Particle species backscatter constant
kt	$V\ m^{\frac{3}{2}}$	Transducer constant

$k_{f\alpha}$	–	Fluid scattering model scattering cross-section proportionality constant
k_{ff}	–	Fluid scattering model form function proportionality constant
M	kg m^{-3}	Mass concentration
n	# m^{-3}	Number concentration
n_i	–	Refractive index
P_{RMS}	Pa	Backscattered acoustic wave pressure
$\widehat{P_0}$	Pa	Incident acoustic wave pressure
q	m^{-1}	Scattered wave vector
Q_f	kg m^{-3}	Feed concentration
Q_u	kg m^{-3}	Underflow concentration
Q_s	–	OBS particle scattering efficiency
r	m	Distance from transducer
r_n	m	Near field distance
R	–	Transducer receive sensitivity
t	s	Time
t_{res}	s	Residence time
T	℃	Temperature
T_v	V Pa^{-1}	Voltage transfer function
v	m^2 s^{-1}	Kinematic viscosity
v_{hs}	m s^{-1}	Hindered settling velocity
V_{RMS}	m^3	Root-mean-square Voltage
V	m^3	Scattering volume
V_p	m^3	Particle volume
W	–	Packing factor
W_s	m s^{-1}	Settling speed
x	–	Dimensionless product of wavenumber and particle radius
z	–	Ratio of measurement distance to the near field distance
Z	W	Received OBS radiant flux

List of Greek Characters

Symbol	Unit	Parameter name
α	Np m^{-1}	Attenuation constant
β	–	Urick's model coefficient
γ	–	Specific gravity
δ	–	Dirac delta function
ε	–	Fluid heuristic formulation coefficients
ζ	–	Ratio of sound velocity in particle to sound velocity in the fluid
η_{max}	–	Normalised maximum backscattered amplitude
θ	rad	Scattering angle
θ_v	–	Urick's model coefficient
κ	Pa^{-1}	Compressibility
λ	m	Wavelength
$\mu_{1,2}$	–	First and second arithmetic moment for a log-normal distribution
ξ	Np m^2 kg^{-1}	Attenuation coefficient
ρ	kg m^{-3}	Density
σ	–	Standard deviation
τ	–	Urick's model coefficient
ϕ	–	Solids volume fraction
φ	–	Solid sphere scattering formulism coefficient
'χ'	–	Scattering cross-section
'ψ'	–	Near field correction factor
Ω_Σ	Pa	Total backscattered power
Ω_P	Pa	Backscattered power from a single particle
ω	rad s^{-1}	Angular frequency

Subscripts and acronyms

Symbol	Definition
fi	Fluid irregular
s	Sediment
si	Solid irregular
ss	Solid sphere
w	Water
ABS	Acoustic backscatter systems(s)
ABR	Attenuation to backscatter ratio
BAR	Backscatter to attenuation ratio
BPS	Barnon pond sludge
CFD	Computational fluid dynamics
CLD	Chord length distribution
COD	Chemical oxygen demand
COV	Coefficient of variation
ECAH	Epstein, Carhart, Allegra and Hawley
ES	Elastic sphere
FBRM	Focussed beam reflectance measurement
FGMSP	First generation magnox storage pond
FS	Fluid sphere
HLW	High level (radioactive) waste
IEEE	Institute of electrical and electronics engineers
ILW	Intermediate level (radioactive) waste
LISST	Laser *in situ* scattering and transmissiometry
LLW	Low level (radioactive) waste
LSTP	Local sludge treatment plant
NDT	Non-destructive testing
NFCF	Near field correction factor
OBS	Optical backscatter system
PFSP	Pile fuel storage pond
PSD	Particle size distribution
PVM	Particle vision and measurement

RMS	Root-mean-square
SEBP	Semi-empirical backscatter power
SEM	Scanning electron microscopy
SNF	Spent nuclear fuel
TSS	Total suspended solids
UARP	Ultrasound array research platform
UFFC	Ultrasound, ferroelectrics and frequency control (society)

Chapter 1 Introduction

The monitoring of suspended sediment size and concentration is of great importance for both environmental and engineering purposes. For example, in fluvial and coastal environments, physical sampling can become impractical due to natural turbulence and high flow rates limiting the spatiotemporal resolution of the measurements [1]–[4]. Likewise, engineering processes typically have restricted access or large costs associated with sampling due to the hazardous nature of the processes and the materials used such as in nuclear applications [5], [6]. Thus, there is currently a critical need for remote, flexible techniques for monitoring particle concentration in aqueous environments that is also robust to changes in particle size [7]. To this end optical [8]–[11], electrical impedance [12] and, of interest in the work presented here, acoustic [13]–[17] technologies have proved the most promising.

The primary motivation for this project stems from the need arising from the UK nuclear industry to remotely characterise suspended solids in legacy waste sludges and slurries to expedite the transport and storage of these materials [18]. The waste from nuclear operations in the UK can be divided into three categories of low, medium, and high-level waste (LLW, MDW & HLW) with LLW accounting for 90 % of the waste (NDA, 2016). Spent Nuclear Fuel (SNF) from the Windscale Pile Reactor, MAGNOX and Advanced Gas Reactors is stored for reprocessing at Sellafield Ltd (Cumbria) in large cooling ponds whose depth of water provides both a shield from the radiation and a heat sink for the heat generated during radioactive decay during storage. In order to reprocess the fuel, it must undergo a number of transport processes through varying geometries of equipment such as pipes, ponds and silos during which the composition and material properties are likely to change [19]. As the initial drive to deal with these wastes was low during Sellafield's early years during the 50's, 60's, and because of an overhaul in reprocessing during the 70's causing a backlog of SNF, much of the waste in the Pile Fuel Storage Pond (PFSP) began corroding and formed a complex radioactive system made up of stored solids, sludge from corroded materials and pond water containing a multitude of organic constituents as the pond was exposed to the outside environment for over 65 years [18], [20]. The characterisation, transport and even storage of legacy materials such

as the wastes encountered in the PFSP is therefore challenging and of high importance as the ponds and other containments built to store the waste are reaching the end of their operational lifetime and must therefore be decommissioned soon [18], [20]. As a result, flocculated systems are of particular interest with regards to the legacy wastes at Sellafield Ltd. as the exposed nature of the PFSP has caused development of significant algal growth containing leading to particle structures containing large amounts of interstitial water. This algal and bacterial growth acts effectively as a flocculating agent in the form of a bio-polymer [21] thereby resulting in a particle structure that is more closely related to a flocculated particle system with natural bio-polymers acting as a flocculating agent for the decaying radioactive waste that consists mostly of heavier, inorganic minerals, metals and metal-oxides [22]. The development of novel techniques to characterise this waste in such a hazardous environment is therefore imperative to allow for efficient and safe processing of these various wasteforms.

Another critical aspect of legacy waste processing at Sellafield, is an understanding of potential volume consolidation upon transfer to interim storage. Indeed, the dewatering of cohesive sediment suspensions is of great interest more generally to minerals, wastewater processing and nuclear industries, where storage and packaging costs are high and so minimisation of waste volume is crucial. The ability to model these systems as a function of parameters such as rake speed, aggregate size and, of concern in this paper, bed density, has therefore been studied extensively through both semi-empirical settling models and CFD modelling of flocculation, aggregation and settling dynamics within thickener operations [23]–[28]. The application of various sludge blanket and particle concentration measurement techniques [29] such as X-ray and gamma-ray absorption [30] and conductivity and light based measurements [31] have thus been studied in previous reported literature. However, many of these are limited, either by their cost, the scale of the process they may be applied to or by the solids fraction range that is able to be monitored [32].

Acoustic backscatter systems (ABS) are used routinely to study sediment transport in coastal and estuarine environments as well as for measuring the flow of currents [33]. Sediment transport is calculated from the suspended sediment concentration which can be estimated from the intensity of the backscattered signal at each distance point

from the transducer [34], [35]. This method of concentration measurement, however, relies on taking many samples in order to determine an empirical relationship between concentration and the backscattered signal intensity. Taking enough samples to establish such a relationship would prove to be both difficult and costly in applications where chemical or radiological hazards make access to process fluid dangerous or completely impossible such as in the Pile Fuel Storage Pond or Local Sludge Treatment Plant (PFSP, LSTP) at Sellafield Ltd. This method of ABS calibration also fails to describe the level of flocculation present within the system which can be very important information for transport/pumping operations such as when the sludge from the storage ponds will be pumped into containers for long term storage or transported throughout the Sellafield site unit operations. This information would also be important for sedimentological and for industrial applications such mineral settling and water treatment operations where settling rates are critical in the design and operation of process equipment [26], [27], [35]. It would also be of great benefit to be able to perform continuous in situ monitoring of particle concentration using acoustics in other areas of Sellafield such as in other LSTP operations as the data collected would present significant cost savings as the tanks could be emptied in a shorter time period as the acoustic backscatter system would allow operators to know whether the tanks had a settled bed, the bed depth and the concentration profile throughout the tank therefore reducing labour and operating costs.

The focus of this project will be to further characterise the acoustic backscatter response for flocculated systems so that an Ultrasonic Array Research Platform [36], [37] can be developed for use an *in situ* instrument to take measurements rapidly and remotely for up to sixteen probes to determine either the bulk density profiles or bed depth via the bed surface echo [38]. Flocculated systems are the focus of this research as the structure of the materials flocculated through bacteria and other biological processes, which will be the likely cause of aggregation in the legacy wastes at Sellafield Ltd., have been shown previously to produce flocs with a similar structure to those produced using bridging flocculation [39], [40]. Bridging flocculation can also be induced using man-made, high molecular weight, medium charge density polymers. The use of these man-made polymers in combination with common nuclear simulants such as calcite and magnesium hydroxide may therefore allow for relatively accurate simulation of legacy waste particle structure. Further applications may also

lie in other areas within Sellafield and other sites such as Savannah River and Hanford in the USA that regularly handle material that has been flocculated either naturally or as part of a processing step [19], [41] as well as multiple other industries such as mining [42], paper production [43], water treatment [44] and food production [45]. It can therefore be seen that there exists a large scope for further acoustic characterisation of flocculated materials as greater understanding would allow for more efficient processing of material in a number of industries where other measurement techniques have proved ineffective due to issues such as cost, the inability to gather light-based data due to opaqueness of the material to be classified or hazards and inaccuracies associated with physical sampling or other instrumentation.

1.1 Thesis outline

In this section a brief summary of each chapter is given for the reader's reference.

Chapter 2 gives a review of the available literature concerning flocculation, due to the expected aggregated state of legacy wastes at Sellafield Ltd. A review of optical methods for flocculated particle characterisation is also provided as these instruments are often used in conjunction with acoustic backscatter systems. Finally, a review of ABS studies on both cohesive and non-cohesive sediments with a particular focus on concentration inversion of the backscattered profiles

Chapter 3 investigates the concentration inversion of spherical glass particles at multiple particle sizes and concentrations in a laboratory scale calibration tank. Acoustic constants are determined using the extended *G-function* method [15], [17] (see Section 2.3.4) and compared to heuristic model predictions. The single (Section 0) and dual frequency (Section 2.3.6) concentration inversion methods limits are explored as a function of particle size, frequency, and concentration. A novel method for determining the near-field correction factor that corrects ABS measurements taken close to the probe is demonstrated and applied to inversion results. A semi-empirical backscatter power model [46] (see Section 2.3.8) for point concentration measurement is also investigated as method for measuring significantly attenuating dispersions.

Chapter 4 investigates the single and dual frequency concentration inversion of a range of synthetic and naturally occurring flocculated sediments that were also studied in their unflocculated state (where available) in the same calibration tank as in Chapter 3. Acoustic constants are determined using the extended *G-function* method [15], [17] (see Section 2.3.4) and compared heuristic model predictions from the Hybrid model [47] (see Section 2.3.10) and the irregular Solid Scattering model [48] (see Section 2.3.2). Experimental and modelling results are normalised by the specific gravity of the experimental and modelled floc density respectively to enable comparison between datasets as per the method of Bux *et al.* [17]. A novel method to determine flocculated particle size distribution and specific acoustic impedance by fitting the Hybrid model to experimental data is provided so long as the mean

flocculated particle size can be determined independently of acoustic measurements and ABS measurements at multiple frequencies are available.

Chapter 5 investigates the ability of ABS to detect concentration changes non-intrusively in a laboratory scale settling column by taking horizontal measurements of acoustic attenuation through a settled bed of flocculated sediment. Pseudo-steady state operation of the thickener allowed for simulation of all operations states of the thickener (start-up, steady state operation at a constant bed height and bed depletion) with additional measurements taken intrusively with a vertically facing probe that utilised the bed reflection echo to track the bed height during thickener operation. A transitive volume balance model is presented that is based on the measured bed height at each time step. The proposed model allows for calculation of the residence time as a function of bed height and experiment time. The output concentration of the thickener is also able to be calculated using the model using an assumed concentration for the top sediment layer in the bed. Modelled output concentrations are compared to underflow samples collected during the experiment to determine the validity of the model. Horizontal attenuation results are compared to the bed height and the modelled residence time at the height of the horizontal probe. Horizontal attenuation measurements taken in a second experiment at multiple depths additionally allowed for comparison of the attenuation as a function of bed depth.

Chapter 6 provides a summary of all results and findings for this project and highlights potential areas for novel innovations that might stem from the work performed here.

Chapter 2 Literature review

The first section of this literature review covers flocculation mechanisms and the various particle structures and characteristics that are produced under different conditions and with different flocculating agents as the waste contained within the storage ponds at both Sellafield and other nuclear reprocessing sites such as Hanford and Savannah River will have been flocculated either by natural processes or deliberately during processing on-site. Section 2.2 covers some common light-based imaging techniques as these are to be used in conjunction with the acoustics during calibration of test materials to provide additional information about particle size and structure as well as to verify results from the ABS and to establish the limitations of such methods. Finally, Section 2.3 covers general theory regarding ABS systems and the current methods used by other authors to determine the acoustic backscatter parameters and otherwise calibrate the device as well as the issues and complications surrounding the acoustic measurement of flocculated systems.

2.1 Flocculation

While many of the wastes encountered at Sellafield Ltd. are coagulated colloidal mixtures a large portion of legacy waste has been allowed to decay for decades with exposure to the outside environments. The wastes contained within the ponds are therefore highly variable mobile low-density organic sludge, inorganic material such as debris from fuel and metal corrosion and organic debris such as plant matter and bird guano [49], [50]. The plethora of organic material coupled with the low radioactivity in these ponds allows for further growth of bacteria and algae that secrete natural bio-flocculants such as polysaccharides and proteins [21]. These bio-flocculants tend to have a somewhat similar bridging flocculation mechanism to that of synthetic anionic polymers such as polyacrylamide. The kinetics and particle structures produced during flocculation are therefore of interest so that particle structures, and hence acoustic properties of legacy wastes at Sellafield, might be accurately simulated in this study.

Wastewater produced from various industries often contains very fine suspended solids that must be removed or settled out of solution. Their small size and possible presence of a surface charge means that settling rates are slow and filtration of these fine particles is challenging [51]–[53]. Coagulation and flocculation are two of the most widely used techniques for solid-liquid separation that facilitate the removal of suspended and dissolved solids, colloids, and organic matter from industrial wastewater. Coagulation and flocculation are used in processes such as palm oil mill effluent, sanitary landfill leachates, textile, pulp mill and oily wastewater as well as many others [54]–[59]. By addition of a coagulant/flocculant fine particles are aggregated together to form large particles (flocs) which will therefore settle faster according to Stokes law. Increased dewatering properties may also be observed in flocculated suspensions [23], [27], [42] that further reduce processing time and allows a greater volume reduction in waste sludges obtained during settling processes.

Coagulation is normally induced by inorganic metal salts such as aluminium sulphate and ferric chloride and in some cases it may also be used without the assistance of flocculants [59], [60]. Coagulation occurs as a result of charge interactions between neighbouring particles and can be explained using DLVO theory [61]. The theory encompasses both the Van der Waals attraction between the particles as well as the electrostatic forces exerted by the particle on surrounding ions in solution. For a charged particle counter-ions in the surrounding fluid will be drawn to the particle surface and form a rigid, strongly bound layer known as the Stern layer beyond which the diffuse layer of mobile counter-ions exists. These layers together form the electric double layer that results in screening of the particle charge beyond the limit of this layer (the slipping plane) defined as the Debye length at which the zeta potential (the electrostatic potential exerted by the particle at this distance) is defined. This screening effect initially allows for close approach of oppositely charged particles; however, as two charged particles approach each other the diffuse layers will overlap and the local counterion concentration will be increased and the surrounding fluid will move in as a result of the increased concentration gradient and force the particles apart that results in a stable colloidal dispersion. Coagulation therefore attempts to reduce or eliminate the double layer surrounding the particles in solution either by addition of more counterions to allow for greater screening and therefore closer approach of neighbouring particles or by adjustment of the pH to reduce the magnitude of the

particle zeta potential [62], [63]. As particles are only bound by weak electrostatic and Van der Waals forces, however, coagulation is typically used a pre-treatment step or combined with flocculation by using flocculants of varying charge densities [64] to counteract particle surface charge during the flocculation process.

In most cases polymeric flocculants are preferable to coagulants due to greater solids removal efficiency at smaller dosages, natural inertness to pH changes and ease of handling [65]. In order to determine the flocculation efficiency the main process variables used are the settling rate of flocs, sediment volume (sludge volume index, SVI), percent solids settled turbidity or clarity of the supernatant, percentage of pollutants removal or water recovery depending on the industrial application [66]. All of these variables, however, are ultimately determined by the floc size distribution and the shape and structure of flocs produced during the flocculation. Larger, stronger flocs are preferable for sedimentation, ease of filtration and high clarification and it is typically the goal of flocculation studies to determine an optimum floc dose to produce this ideal floc structure [67]. As a large number of parameters such as the pH, temperature, salinity, particle zeta potential and the flocculant charge and molecular weight can affect the flocculation kinetics [58], [68]–[71] the different flocculation mechanisms and resulting particle structures induced by adjusting these parameters is discussed in Sections 2.1.1-2.1.3.

In general flocculants can be classified in to three main categories: Chemical coagulants/flocculants, natural bio-flocculants, and grafted flocculants. Chemical flocculants are typically applied in wastewater treatment and are derived from chemical/petroleum-based materials. Natural bio-flocculants have been extensively explored for the last few years due to their biodegradability compared to chemical-based flocculants. Finally, grafted flocculants have been investigated recently by combining the properties of natural and chemically derived flocculants [67]. The classifications of various flocculants used in wastewater treatment are shown in Figure 2.1 as a summary.

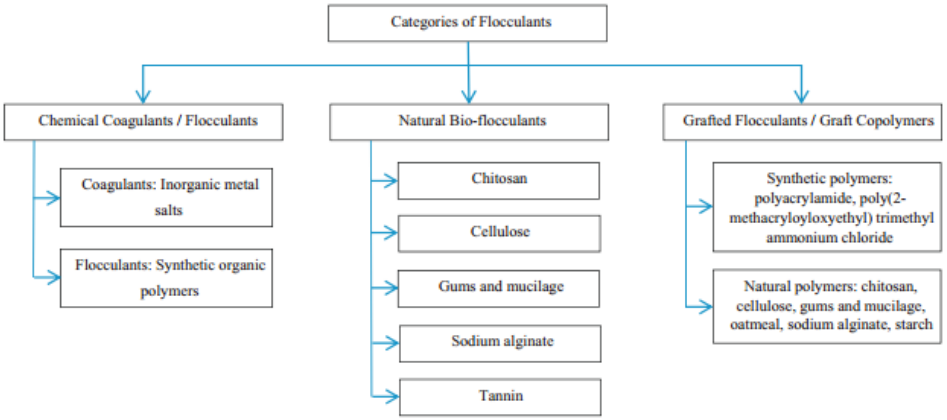

Figure 2.1 Classification of Flocculants [67]

2.1.1 Flocculation methods

Coagulation-flocculation is the conventional treatment method where cationic inorganic metal salts are commonly used as coagulants and long chain, non-ionic or anionic polymers are used as flocculants [72]. This is due to fact that suspended particles in wastewater are typically negatively charged and so addition of the metal salt causes the salt to hydrolyse at the isoelectric point (at which the zeta potential is zero) and form cations in solution. These cations cause a reduction in the Debye length as the charge density in the surrounding fluid is increased subsequently allowing for the formation of micro-flocs [73]. Anionic and non-ionic polymeric flocculants are therefore used to bring together and agglomerate the microflocs to form larger, faster-settling flocs with better dewatering properties [74]. The use of flocculants can also reduce the consumption of coagulants and increases the reliability of treatment operations and throughput capacity of treatment equipment [75]. It was found by Amuda and Amoo [76] that combined use of a coagulant (ferric chloride) and polymer (non-ionic polyacrylamide) gave a 60 % reduction in the amount of sludge produced compared to using just coagulant for the process for industrial beverage wastewater. This process is not perfect, however, as low temperatures will cause smaller flocs to be produced and flocs that are formed may be fragile and break when subjected to shear force [67].

In direct flocculation, medium charge density, high molecular weight cationic polymers are used most frequently (although anionic polymers may also be used depending on the charge of the sediment to be flocculated). These have two functions, firstly, to neutralise any charge the suspended particles may have and, secondly, to

bridge the aggregated particles to form flocs [72]. The polymers used for direct flocculation have been shown to be workable in a large pH range from acidic environments (pH 5.1) [77] to basic environments (pH 11.2) [58] This is in contrast to coagulation flocculation where the metal hydroxide precipitates are only obtained after adjusting the solution to the desired pH [67]. Direct flocculation also generates less volume of sludge because the flocs formed with the bridging mechanism are densely packed and, as the flocs are organic in nature, they are non-hazardous and make therefore make for ease of disposal [67]. It was found by Chong [72], after preliminary cost analysis, that the cost of conventional treatment (coagulation-flocculation) was 3.6 times higher than when direct flocculation was used due to the larger volume of sludge produced. It has been shown by a number of authors that high flocculation efficiency could be achieved where more than 90 % removal of turbidity, total suspended solids, chemical oxygen demand and colour was desired in wastewater [57]–[59], [63], [78]–[81].

Direct flocculation is mostly limited to organic-based wastewater with a high concentration of suspended and colloidal solids and so coagulation-flocculation is more widely applied despite direct flocculation having the advantage of using less chemicals, being a simpler process, producing less sludge and a lower treatment cost [72]. As the wastes expected to be encountered at Sellafield Ltd. likely to fit the criteria for direct flocculation this method is of great interest due to the advantages listed above. Table 2.1 below summarises the comparisons between the two processes. As the intended application for the acoustics is in environments containing significant amounts of algal growth and flocculation caused by bacteria, which produce slime films typically consisting of polysaccharides and other polymers with a similar appearance to the organic matter found in flocs, the structure of the particles in the legacy waste ponds can be assumed to be of a similar to structure to flocs produced using direct flocculation [39]. There will be differences in the size and strength of the flocs produced, however, as the legacy waste has been left to stagnate for a significantly long time (~50 years) before undergoing shear prior to deposition in to the settling tank [38] and so the initial flocs produced will have been larger and of a different strength than would typically be found in wastewater. These flocs will then have been broken down by shear during pumping/suspension operation and so the final structure and characteristics of these particles in suspension is largely

unknown but may be assumed to most closely resemble particle structures produced using natural bio-flocculants that produce flocs via the bridging mechanism that is discussed further in the following section.

Table 2.1 Comparison between coagulation-flocculation and direct flocculation [67]

Comparison Criteria	Coagulation-flocculation	Direct flocculation
Application	Inorganic and organic-based wastewater	Organic based wastewater
Treatment ability	Suspended and dissolved particles	Suspended and collloidal particles
Types of chemicals to be used	Coagulant(s) (e.g. inorganic metal salts) followed by polymeric flocculant(s) (usually anionic)	Cationic or anionic polymeric flocculants (usually cationic)
Treatment process	More complicated, requires pH adjustment	Simpler, without pH adjustment
Sludge generated	More sludge is produced, may contain metals and monomer residue	Less sludge is produced, may contain monomer residue
Overall treatment cost	More expensive due to chemicals cost (coagulant and flocculant) and large sludge treatment cost	Less expensive because only one chemical is used and less sludge treatment cost
Flocculating mechanism	Charge neutralisation (coagulation) followed by bridging (flocculation)	Charge neutralisation and bridging occur concurrently

2.1.2 Flocculation mechanisms

The development of a floc occurs in several sequential stages:

1. **Dispersion of the flocculant into the solution**
2. **Diffusion of the flocculant towards the solid-liquid interface**
3. **Adsorption of the flocculant onto the surface of the particles**
4. **Collision of particles with adsorbed flocculant**
5. **Adsorption of the flocculant onto other particles in order to form microflocs**
6. **Growth of the microflocs to larger and stronger flocs by further collision and adsorption**

Several mechanisms such as polymer bridging, polymer adsorption and charge neutralisation (including electrostatic patch effects), depletion flocculation, displacement flocculation etc. have been proposed to explain the growth of flocs and the mechanisms of floc formation [82], [83]. The main mechanisms which are often cited are charge neutralisation, bridge formation and electrostatic patch and are explained below.

In cases where the flocculant and adsorption site are of opposite charge, such as in wastewater where the typically negative charge of the colloidal particles means that cationic polyelectrolytes are used, then charge neutralisation is generally the proposed mechanism. This mechanism indicates that flocculation occurs as a result of reduced surface charge/zeta potential of the particles in suspension causing the electrical repulsion force to decrease allowing van der Waals forces to cause aggregation to form microflocs [64], [84]. It has been found by a multitude of authors that the optimum flocculant dose is around that needed to neutralise the particle charge or give

a zeta potential close to zero. This is called the isoelectric point at which the particles will agglomerate under the influence of van der Waal forces causing the suspension to become destabilised [85]. The use of too much polymer can cause charge reversal, however, due to the polyelectrolyte covering the particles and providing a layer of positive charge thus resulting in the formation of a double layer of negatively charged ions. Often, as they are held together by van der Waals forces, the flocs formed with charge neutralisation are fragile and loosely packed with a low settling rate and so a HMW polymer is often used to induce bridging flocculation for better water recovery [67].

Normally associated with direct flocculation, polymer bridging occurs when long chain polymers, with molecular weights up to several million, and a low charge density [86] are adsorbed on to a particle surface with long loops and tails that extend past the electrical double-layer allowing for interaction with particles and possible ‘bridging’ of particles by these polymer chains [74], [87], [88]. The high molecular weight of these polymers is part of the reason they are able to form bridges as the elongated structure means that they extend further in to solution than their lower molecular weight counterparts [63]. As the polymer also requires a binding site on both particles to be effective too much polymer can result in restabilisation of the particles when the particle surface becomes saturated with polymer and all the binding sites become occupied [89] and is demonstrated in Figure 2.2. There is therefore an optimum dosage for bridging flocculation as too much will result in restabilisation while too little will result in too few bridging contacts being formed [82]. It is well established that bridging flocculation can give much larger and stronger (shear-resistant) flocs than those formed in other ways [67].

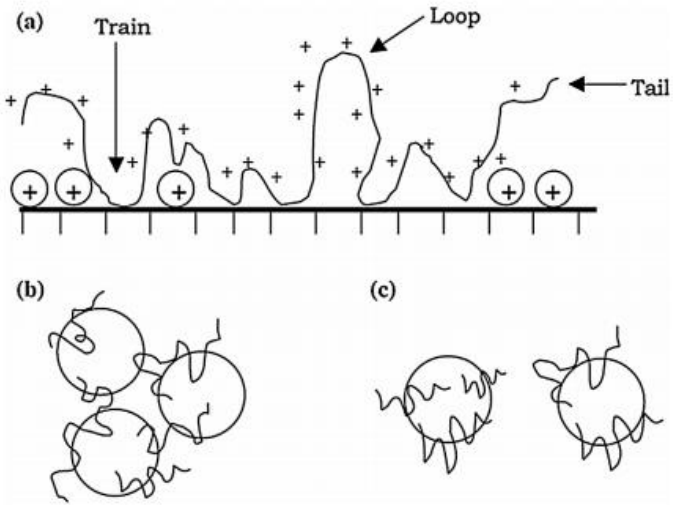

Figure 2.2 (a) Adsorption of polymer and formation of loops available for binding. (b) Polymer bridging between particles to form flocs. (c) Restabilisation of colloidal particles [90]

When the density of charged sites available on a particle is low and the charge density of the polymer is high then bridging capability is reduced and another mechanism arises called the 'electrostatic patch' mechanism. The principle is that when the polymer adsorbs on to a weakly charged surface to fully neutralise its charge then it is not possible for each surface charged site to be neutralised by a cationic polymer segment [88]. This causes formation of cationic 'patches' or 'islands' between regions of uncoated, negatively charged surfaces. These patches of opposite charge are attracted to one another as they approach leading to particle attachment and hence flocculation [82]. Flocs produced via patching are not as strong as those formed with bridges but stronger than those produced from charge neutralisation or metal salts. The polymer charge density must be high for patch flocculation to occur: as the charge density is reduced the likelihood of bridging flocculation increases [91].

Naturally occurring flocculants and their corresponding flocculation mechanism are of particular interest in this work as the large amount of bacterial and algal growth in the legacy waste ponds at Sellafield Ltd. will mean that the flocs formed there are likely to resemble those produced using natural bio-flocculants such as polysaccharides, proteins, lipids and possibly glycoproteins, liposaccharides, and lipoproteins. These are products of microbial secretions and can comprise as much as 50-90 % of the organic matter content of microbial aggregates [21]. Most of these possess a neutral pH and a net negative charge due to the presence of anionic functional groups such as carboxyl, hydroxyl and phosphoryl groups outweighing the

positive charge from the less populous amino acids. As such, they have a somewhat similar bridging flocculation mechanism to that of synthetic anionic polymers such as polyacrylamide. This mechanism is called divalent cation bridging where positive cations such as calcium and magnesium are bridged by the bacteria and polymer. Additionally, the negative charge of the bacteria and polymer helps reduce the electrostatic repulsion of positive cations in the water by reducing the electron double layer according to DVLO theory [92], [93]. In an extensive microscope based study by Liss *et al.* [40] they observed that, while some evidence of electrochemical aggregation was present, polymeric fibrils that served to bridge the particles (a mix of cellular, organic and inorganic constituents) predominantly provided structural support for the floc for both the natural and synthetic flocs studied. It was thought also that the dense bridging networks may promote fluid flow resistance within the floc as they will lead to increased absorption of surrounding contaminants and limit pore water flow ability. The absorption of surrounding contaminants that may not otherwise flocculate and settle easily would be advantageous for settling processes of sludges and mineral slurries as settling times could be reduced even for particles that cannot be flocculated directly.

2.1.3 Effect of particle species and flocculant concentration

It has been shown, although the mechanism is not well understood, that an increase in particle species concentration leads to a reduction in aggregate size when patching flocculation is the primary mechanism [94]–[96]. It was found by Heath *et al.* [94] that as the solid fraction was increased the viscosity of the suspension increased while the shear rate decreased that was determined by measuring the pressure drop along the length of the pipe. As the shear rate is typically defined as the square-root of the ratio between the energy dissipation per unit mass and the kinematic viscosity an increase in viscosity would cause a corresponding decrease in the shear rate. Although the energy dissipation rate increases in proportion to the measured pressure drop the viscosity is proportional to the pressure drop raised to the power 4 thereby giving an overall reduction in shear rate with an increasing pressure drop for a given system. Results published by Heath *et al.* [94] are shown in Figure 2.3. The reduction in aggregate size at higher solid fractions was therefore attributed to a reduced particle collision rate at lower shear and an increase in breakage due to the increased viscosity causing greater energy dissipation.

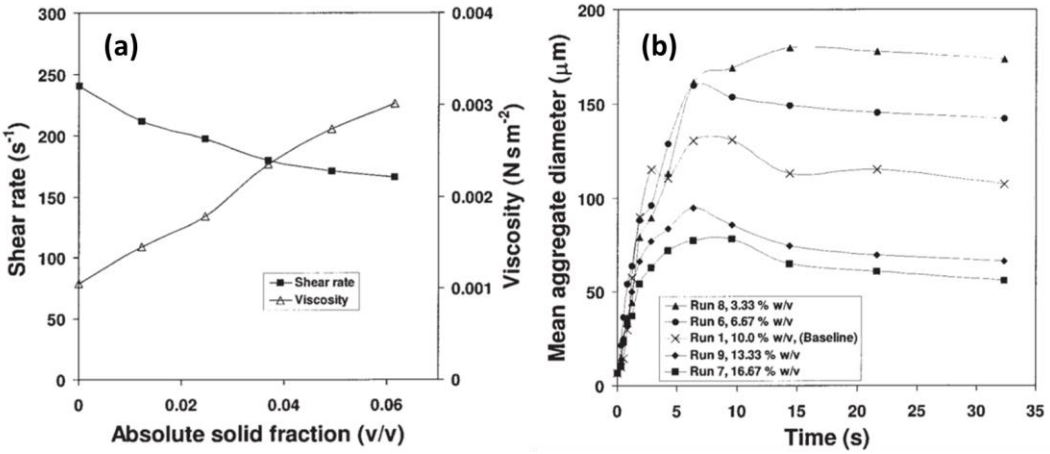

Figure 2.3 Showing a) the effect of feed suspension solid fraction on the shear rate and viscosity of the fluid b) the effect of feed suspension solid fraction on the volume-weighted mean aggregate size [94]

Collisional breakage is sometimes proposed to account for the reduction in size with solid fraction due to increased collision rate at higher solid concentration [97], [98]. It was shown by Zhou and Franks [71], using equations from Elimelech [99], that at higher concentration the characteristic collision and adsorption times (that is the average time before a particle encounters another and the time taken to adsorb a given fraction of the polymer from solution) both decreased with increasing particle concentration. This result means that the time available for a polymer to adopt a flat conformation on the particle surface before encountering another particle will decrease and so the aggregation rate would be increased. This extended polymer conformation will greatly facilitate flocculation via bridging, but it can cause destabilisation of particles that undergo patching flocculation as the flat patches of polymer required will not be formed.

It can be predicted, therefore, that for polymers with a high charge density an increase in the initial particle concentration may decrease aggregate size. This is in contrast to low charge density polymers that will produce larger aggregates as particle species concentration is increased [71]. It was also proposed by Wågberg and Åssel [69], however, that as higher charged polymers will find it most energetically favourable to lie flat on the particle surface they will always adopt this conformation regardless of particle concentration in which case the aggregate size would not be affected. For lower charge polymers the reconformation rate would be low and, if the corresponding timescale for reconformation is greater than that for adsorption and collision, then a

more extended conformation will be adopted thereby increasing the efficiency of the bridging flocculation process and producing larger flocs [70], [100]. At very low solid fractions other studies have suggested that the aggregate size may be reduced which could possibly be attributed to a decrease in collision rate compared to the rate of aggregate breakage [96], [97], [101], [102].

As stated earlier, for charge neutralisation flocculation, the optimum dose is that at which the isoelectric point is reached above which charge reversal and hence restabilisation of the colloidal particles occurs [71]. For bridging flocculation, restabilisation can occur when all the bridging sites on the particles in solution are occupied and therefore no additional bridges can be formed. There is therefore an optimum dosage for maximising the size of aggregates formed from bridging flocculation as too much flocculant will result in steric restabilisation occurring before particles have a chance to bridge to one another resulting in smaller particles being formed. This phenomenon has also been used by Blanco *et al.* [103] to explain the lower strength of flocs at a large excess of flocculant. Too little flocculant, however, will result in too few bridging contacts being formed, again resulting in a smaller particle. It should be noted, however, that for a lower flocculant concentration, the same polymer chain has the opportunity to become bound to more particle sites and so the polymer will be much more strongly attached to the particle for lower concentrations which would therefore lead to greater floc stability.

It was found by Rasteiro *et al.* [104] that the breakup percentage was highest at the largest floc size (i.e. the optimum floc dosage) as might be expected as larger flocs will undergo greater shear forces and therefore be more susceptible to breakage. It has also been found by Blanco *et al.* [103] that a moderate excess of polymer, above the optimal dosage, can improve floc strength; however, at the floc level where the zeta-potential became positive the flocs lost the ability to reform after breakup. At high polymer concentrations patching flocculation was not deemed to be possible as polymer flattening would be limited due to the high coverage grade and, following deflocculation due to shear, these particles will adsorb more polymer and further increase repulsive forces until the coverage grade is 100 %. Because of this plethora of concentration-dependent effects it can therefore be seen that if the flocculant is not mixed into solution homogeneously there could be zones of both high and low

concentration of flocculant and hence will cause variation in the produced floc structure. In order to produce a consistent floc size and structure, therefore, it should be ensured that adequate dispersion of the flocculant takes place on addition to a system.

2.2 Optical methods for characterising flocculated suspensions

As particle size must first be known to obtain the concentration or *vice versa* from ABS measurements, light-based measurements are often used in conjunction with acoustic measurements to allow acoustic backscatter inversions to be performed and to compare measured particle size and concentration. The following section presents a background for both *in situ* and *ex situ* light-based techniques for characterising flocculated dispersions some of which were performed for results shown in Chapters 3 and 4.

2.2.1 Optical backscatter systems

Optical backscatter systems (OBS) are typically used for relative measurement of suspended solids in a number of scientific and engineering applications and are based on the Mie scattering theory [9] that states that the intensity of the received radiant flux (Z), for an emitted irradiance intensity (E), is a function of particle radius (a), mass concentration (M), scattering efficiency (Q_s) and scattering volume (V) as shown in the equation below [105], [106]. The scattering volume is defined as the volume intersected by the source light beam and the field-of-view of the detector, both of which are conical and are therefore a function of the source and detector angle and displacement [107].

$$Z = \frac{3}{4}\frac{VMEQ_s}{\rho a} \qquad \textbf{2.1}$$

Calibration of these sensors is necessary because particle shape, surface roughness, degree of flocculation and the refractive index all impact on the OBS response as the operating principle relies on using a light source to achieve reflection off the suspension at a specific angle where the intensity is detected using a photodetector [8], [108]. The intensity of the returned signal is mainly affected by the illuminated surface area of the particles and as this is proportional to the particle volume the volume concentration of particles can be deduced. This means, however, that

unknown time variation in particle size, aggregation/flocculation and fouling (chemical or biological) can result in inaccurate OBS data [9]. The concentration range of OBS sensors is relatively large, however, and can measure particle concentration up to 100 g l^{-1} (see Figure 2.9) and, when properly calibrated and maintained, can detect changes in concentration as low as 100 μg l^{-1} [9]. For flocculated or cohesive sediments, however, it has been reported that operational ranges are limited to as high as 0.5 g l^{-1} for kaolinite as opposed to the 20 g l^{-1} limit normally encountered for sand [109]. As they are only technically capable of providing a measure of the volume concentration they will also be limited in applications where large density variations that might be expected for flocculated sediments.

2.2.2 Focussed beam reflectance measurement (FBRM)

The FBRM probe operating principle relies on using a solid-state laser of monochromatic light that is projected through a set of rotating optics and a sapphire window into the particle suspension to be measured. The beam's focal point is made to follow a circular path at a distance close to the probe face where light is scattered back by any particle, droplet, or bubble from the focal point back towards the probe. As the rotation or scan speed of the laser is fixed and known, the length of time that a backscattered signal is detected for can be translated to a chord length for a particle that has been intersected by the laser as shown in Figure 2.4.

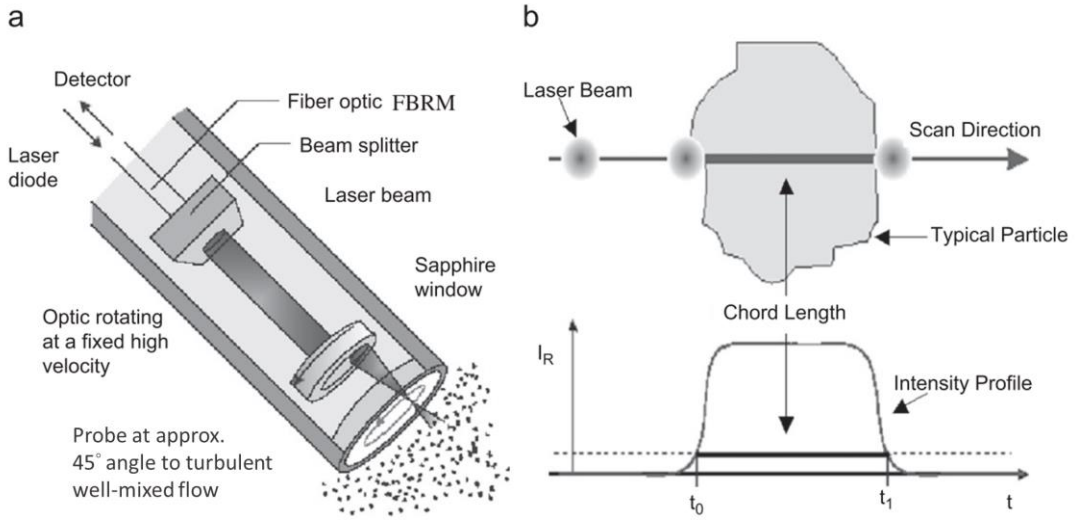

Figure 2.4 Showing a) the working principle of a FBRM device b) a representation of the measurement of a chord length [110]

The use of FBRM to study flocculation kinetics has been utilised successfully by authors such as Blanco *et al.* [88] and Heath *et al.* [94] (see Figure 2.3 (b)) although it is typically used as an indicator of aggregation as opposed to an absolute measure of particle size [111] as, in order to transform the raw chord length distribution to a particle size distribution, information about the floc shape and how it changes with size must be known. As the laser in the FBRM device will typically measure a chord length that is less than the actual particle diameter the resultant data must be transformed from a chord length distribution to a particle size distribution. This conversion is not trivial, however, due to lack of a theoretical framework for non-spherical particles [112]. For transparent particle systems Vay *et al.* [113] and Li and Patchigolla [114] found that transparent particles gave FBRM number count results that were too low for a valid measurement as there is both not sufficient pulse strength and the rise time of the electronic pulse is not sufficiently short [115], [116].

A numerical method, that has been validated both in simulations [112] and in experimental work [117], is outlined by Li and Wilkinson and has been applied successfully to a number of solid particle systems. The application of FBRM with other imaging techniques such as X-ray tomography has been utilised by recent authors to estimate bubble size distributions in water saturated sediment beds [118]. FBRM devices have also been combined with in-situ microscope measurements by Agimelen *et al.* [119] to capture further deviations from sphericity in three particle systems and construct a method to more accurately determine the aspect ratio and hence the correct PSD for the system. Li and Patchigolla [114] also found that when comparing image-analysed PSDs to FBRM CLDs the PSD estimated by the FBRM was consistently lower than that seen by the micrograph (~10 %), for the zinc dust particles used in their study.

2.2.3 Static light scattering

Small angle static light scattering is a laser diffraction technique that measures particles within the Mie and Fraunhofer regimes used by instruments such as the Malvern Mastersizer (Malvern Panalytical Ltd.) and the LISST (Sequoia Scientific Inc.). Such devices can be placed in-situ but will be unable to operate in opaque environments. It was found by Vincent and MacDonald [120] that data from a

forward-scattering light device (a LISST-100) gave particle sizes three times smaller than that of a camera for flocculated particles (shown in Figure 2.5).

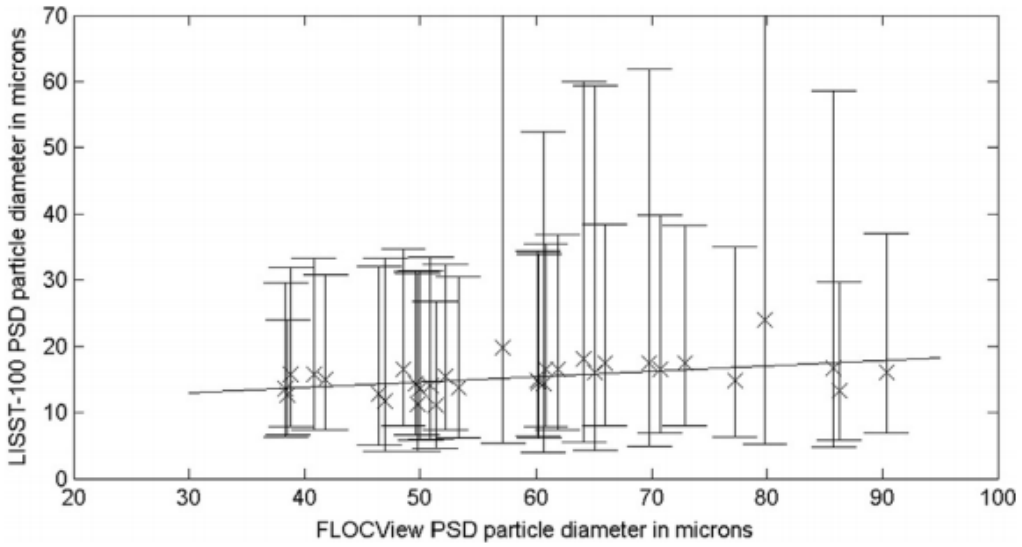

Figure 2.5 The mean particle diameter of the peak in the LISST-100 PSD against mean particle diameter from the FLOCView camera system (R^2=0.2) [120]

It can be seen from Figure 2.5 that, although a qualitative relationship can be drawn between the LISST-100 and the FLOCView camera data, the corresponding error is large and very little change is seen in the LISST signal compared to the camera system. Mikkelsen *et al.* [121] found that the LISST gave floc size estimates typically 3 times lower than that of the camera system for flocs from five field location. It was also found by Hill *et al.* [122] that an upper size limit caused discrepancy between the LISST and digital floc camera results in muddy flocs in Willapa Bay. Graham *et al.* [10] suggested that the tail of fines in the PSD from the LISST that was not seen by the camera system was due to the laser diffraction responding to multiple length scales in the bound flocs although they were unable to deconvolute the resulting PSD without independent size verification of the system. The reliability of the LISST-100 and other in situ light scattering devices for measuring the exact size of flocculated systems is therefore questionable but raises the possibility that the acoustic signal may also respond to these sub-structures (discussed further in Section 2.3.9).

Light scattering instruments may also provide further structural information about flocculated sediments as it is known that aggregates/flocs formed from random aggregation processes have a fractal mass structure such that the structure is self-similar at multiple length scales [44], [123]–[126]. For such structures the mass,

and therefore the density, is proportional to the radius, *a*, raised to the power of the fractal dimension, D_f. The density of the floc, ρ_f, is therefore given by

$$\rho_f = \rho_s\left(\frac{a}{a_{primary}}\right)^{D_f-3} \quad \textbf{2.2}$$

where, ρ_s, is the density of the sediment/ primary particles and $a_{primary}$ is the primary particle size. The fractal dimension is not limited to integer values but should be between 1 and 3 for 3-D objects. A completely void free object would be represented by a fractal dimension of 3 while lower fractal dimensions would indicate an increasingly open structure with an increase in size [71]. In terms of light scattering, the fractal dimension can be measured experimentally as, for a mass fractal object constructed of monodisperse primary particles that lies within the Rayleigh-Gans-Debye regime, the following relationship between the scattered intensity *I(q)* at the scattering wave vector *q* can be used.

$$I(q) \propto q^{-D_f} \quad \textbf{2.3}$$

where

$$q = \frac{\pi R_i \sin\left(\frac{\theta}{2}\right)}{\lambda} \quad \textbf{2.4}$$

For which R_i is the refractive index of the fluid, λ is the wavelength of light used and θ is the scattering angle. This relationship holds so long as the length scale (*1/q*) is much larger than the primary particle radius and much smaller than the aggregate or floc radius. A plot of *log(I(q))* vs *log(q)* will therefore have slope $-D_f$. Results from Zhou and Franks [71] for silica flocculation using three cationic polymers indicated that they were successful in being able to characterise different flocculation regimes by analysing fractal dimension data collected using a Malvern Mastersizer S (Malvern Panalytical Ltd., UK) shown in Figure 2.6 below.

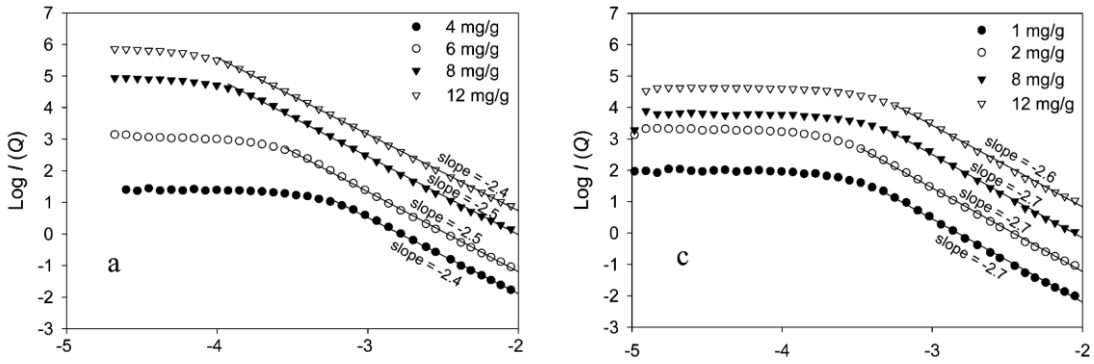

Figure 2.6 Typical scattering pattern of silica flocculated with (a) 10 % charge polymer and (b) 100 % charge polymers at various polymer dosages [71]

The fractal dimension therefore provides a description of how compact the aggregate structure is and ranges from 1, for a very open structure, and 3, for a solid particle with no voids. Typical values for flocs produced during forced (i.e. non-Brownian) aggregation are between 2 and 3 [125]–[129]. As size changes during aggregation/flocculation can often be of one or two orders of magnitude, however, the fractal dimension can have a drastic effect on final floc densities with upper or lower limits normally placed very close to the density of water for modelling depending on whether the particulate density is less than or greater than the density of water respectively [47]. Determination of the fractal dimension is therefore crucial to modelling floc density as a function of size. Static light scattering has proven to be successful in accurately determining the fractal dimension of various aggregate types [125], [128] as well as being able to characterise the shear history [104] and flocculation mechanism [71], [126] flocculation process. Light scattering devices have also been used by previous authors to determine the floc fractal dimension *in situ* [129] and as such it represents a useful measurement tool for studying flocculated sediment systems.

2.2.4 Disadvantages of light based measurement techniques

As is discussed in the previous sections optical techniques are able to obtain information about flocculated particle size, structure, and concentration. Inherent disadvantages are present in the optical techniques presented here, however. The foremost limitation is the low concentrations that are accessible using both *in situ* LISST devices particularly for small particle sizes (typically ~100 $\mu g\ l^{-1}$ for 10 μm particle sizes [130]) and for *ex situ* devices such as the Mastersizer. Similarly there are limits on the measurable concentration using OBS that is dependent on particle size and optical properties of the sediment [9]. The optical properties of the sediments must also be known *a priori* or obtained through calibration that may be either costly or impossible in hard-to-access or hazardous process environments.

Although FBRM technology is still able to operate at high concentrations the size data obtained is limited in that only a chord length distribution is obtained and must be converted to a PSD [131]. FBRM measurements may also be adversely affected by the pores that would be present in a flocculated particles as it may perceive individual

clusters within the floc to be independent particles or otherwise not measure the smaller particles depending on the measurement mode selected [132]. All optical methods are also inherently limited to translucent environments meaning the majority of measurements must be taken intrusively and may be adversely affected by fouling during extended deployment scenarios. The legacy waste inventories at Sellafield Ltd. may be expected to comprise various size fractions of both cohesive and non-cohesive materials at relatively high concentrations [18]. The optical properties and density of the inorganic and organic waste components may vary significantly in a given storage vessel and optical based measurements may therefore be limited in the target process.

2.3 Acoustics

There is currently a large drive for the clean-up of nuclear waste as policy dictates that the legacy waste that has built up in the UK must be dealt with in a timely manner [133]. Waste left over from the Pile Fuel Reactors in the 60s has been left to degrade for over 50 years in the Pile Fuel Storage Ponds (PFSPs) at Sellafield Ltd. with exposure to the outside environment and so has formed a complex system containing both radiological and toxic hazards as well as a variety of waste in different forms [18], [20]. Knowledge of the settling and transport dynamics of these wasteforms would allow for optimisation of thickening and pumping operations that are necessary to package the waste for long-term storage [134]. The development of novel techniques to characterise the particle size and concentration of this waste in such a hazardous environment is therefore imperative to allow for efficient and safe processing operations. Acoustic devices represent a promising technique as they are used extensively to measure sediment transport in estuarine environments [33] and, by appropriate adjustment of the measurement frequency, particle size and concentration can be measured non-destructively and non-intrusively [135]. The measurement of particle concentration will be the focus here as this would allow for direct determination of settling front heights, bed formation dynamics and waste volume reduction.

Acoustic devices for measuring particle concentration are generally used in either a forward transmission or a backscatter setup. In transmission, an acoustic signal is generated by one transducer and the signal is “caught” by another receiving

transducer. A backscatter setup requires only a single transducer that both generates the pulse and subsequently listens for the reflected echo from the insonified particle known as “pulse-echo” mode. Acoustic transmission techniques for process monitoring have been studied by a number of groups as a method for particle concentration measurement from the signal attenuation for many aqueous suspensions, such as glass beads [136], kaolin [5], [137], dolomite [138] and silica [139], [140]. A transmission setup can also provide particle size measurement by measuring the frequency dependency of the backscatter strength, attenuation and the “peak-frequency”, at which the backscattered power is greatest [141]. Research into the development of theoretical equations governing these relationships and their experimental validation has been undertaken by a number of authors to include factors such as morphological irregularities, temperature and material properties (bulk modulus, elasticity, density and compressional and shear wave speed as a function of porosity.) [142]–[151].

In particular, much work has gone into determining the effect of the scattering angle [152]–[156] as this allows for additional data to be collected by taking the measurement of the acoustic signal across a plane or in pulse-echo mode using multiple receivers. Practically, this allows more complex or access-restricted geometries to be measured and a greater volume of data to be collected. Fleckenstein *et al.* [157] performed acoustic measurements on glass bead suspensions at receiver angles of 0^0, 90^0 and 180^0 with respect to the pulsing transducer. Their experimental investigation showed a linear relationship between particle concentration and forward attenuation (i.e. at a receiver angle of 180^0) up to 5 g l^{-1} for 20 μm diameter glass particles for frequencies of 2 and 4 MHz however an obvious linearity was not seen for the 105 μm particles at the same frequencies indicating both a concentration and size limit to the linear relationship between attenuation and particle concentration [157]. Despite their high signal-to-noise ratio, transmission setups are limited in their applicability, with issues around the measurement of highly concentrated or attenuating dispersions as the gap between the pulsing and receiving transducer must be reduced accordingly increasing the likelihood of blockages by coarse particles or highly viscous media during measurements [46].

By operating in pulse-echo mode (i.e. a receiver angle of 0^0) acoustic reflections from particles at multiple distance points in front of the transducer can be collected and a distance profile of backscattered signal strength can be produced. These are referred to commonly as acoustic backscatter systems (ABS). The work of many authors over a number of years [3], [15], [24]–[26], [16]–[23] has led to the development of an equation to relate the backscattered voltage to the particle concentration so long as the electronic system gain and two key parameters that describe the scattering characteristics of the suspended particles are known. That is, the ensemble backscatter form function (f) and the scattering cross-section (χ). As f increases more energy is scattered back to the sensor and so the voltage from the receiver increases. Physically, the form function is the ratio of the backscattered pressure to incident pressure (i.e. the relative scattering strength) for a three-dimensional scatterer as a function of distance from the transducer and the characteristic dimension of the scatterer that depends on the scatterer shape [165]. Conversely, as χ increases the backscattered pressure decreases as more energy is scattered away from the sensor as it quantifies scattering from a particle over all angles relative to its cross-sectional area [13] . While these terms have been defined as a function of particle size and insonifcation frequency for spherical glass beads and irregularly shaped sand particles [48], [159] they have not been determined exactly for cohesive/flocculated fine sediment systems and so modelling efforts have been limited [35], [47], [120], [166].

A quantitative model that relates the backscattered acoustic signal received by an active piezoelectric transducer [33], [167] to the concentration of particles in suspension has been employed and further developed by a number of previous authors [2], [153], [158], [160], [164], [168], [169]. Summarily, if the backscatter and attenuation parameters of a suspension are known or can be estimated as function of distance from the transducer then a particle concentration profile can be produced using either a single frequency [33] or dual-frequency inversion method [14]. The advantage of multi-frequency methods are that they eliminate numerical instabilities in the far-field, normally associated with other inversion methods [2], [153], [164]. These models and the methods used to determine the acoustic constants that were used as inputs by various authors are discussed in detail in Section 2.3.1-2.3.11.

2.3.1 Acoustic backscatter theory

In this section the basic theory of an Acoustic Backscatter System will be described as well as the reliability and limitations of various models, inversions and experimental data that can be obtained from an ABS. The following model (Equation 2.5) as presented by Thorne and Hanes [33], gives the variation of backscattered root-mean-square voltage, *V*, with distance from the transducer face, *r*, for a given mass concentration, *M*, of particles suspended in water for single particle scattering where k_s is the particle species backscatter constant (that is directly proportional to the measured scatterer form function and inversely proportional to square root of the particle size), α_s is the attenuation constant for the sediment (that is directly proportional to the particle scattering cross-section, mass concentration and inversely proportional to the particle size), α_w is the attenuation due to water, ψ is the near field correction factor (NFCF) and k_t is the transducer constant, which captures the inherent gain of the system and probe characteristics.

$$V(r) = \frac{k_t k_s M^{\frac{1}{2}}}{r\psi} e^{-2r(\alpha_w+\alpha_s)} \quad \textbf{2.5}$$

The first set of terms in the equation ($\frac{k_t k_s M^{\frac{1}{2}}}{r\psi}$) describes the decrease in backscattered acoustic wave pressure with increasing distance from the transducer and the increase in backscattered wave pressure with increasing particle concentration (through *M)* and individual particle scattering strength (through k_s). As the acoustic transducer is piezoelectric, the backscattered pressure induces a voltage that is proportional to the incident pressure wave and the transducer receive sensitivity. The voltage produced may then also be amplified by the acoustic backscatter system hardware that defines the voltage transfer function of the system. The product of the transducer receive sensitivity and voltage transfer function gives the proportionality constant between the backscattered pressure and the measured voltage from the transducer that are captured in the k_t term.

ψ is a correction factor that accounts for non-spherical spreading of the acoustic signal in the near field of the transducer. The second term in Equation 2.5, ($e^{-2r(\alpha_w+\alpha_s)}$) represents the inclusion of attenuation due to both the particles and fluid in suspension. As the distance, *r*, from the transducer increases a greater proportion of the incident wave is either scattered at angles away from the transducer or

dissipated through viscous absorption of the acoustic signal [33], [170]. Functionally, this term provides the fraction of the acoustic signal that is received by the transducer when attenuation is accounted for over a given distance.

The near field correction factor (ψ, NFCF) tending to unity in the far-field, when the measurement distance is much greater than the near-field distance, $r \gg r_n$) is given by Downing *et al.* in Equations 2.6-2.8 as [163];

$$\psi = \frac{1 + 1.35z + (2.5z)^{3.2}}{1.35z + (2.5z)^{3.2}} \quad \textbf{2.6}$$

$$z = \frac{r}{r_n} \quad \textbf{2.7}$$

$$r_n = \frac{\pi a_t^2}{\lambda} \quad \textbf{2.8}$$

where z (Equation 2.7) is the ratio of the measurement distance of a scatterer to the calculated near field distance, r_n (Equation 2.8.), that physically describes the extent to which near-field, non-spherical spreading effects will influence the backscattered signal, r_n (Equation 2.8.) is the distance from the transducer beyond which near-field, non-spherical spreading effects become insignificant and physically represents the ratio between the radiating aperture (the transducer face area) and the wavelength of the ultrasonic signal, a_t is the transducer radius and λ is the wavelength of the ultrasonic signal. The model was arrived at by Downing *et al.* [163] by plotting results from a number of particle size distributions and concentrations, insonified at 1-5 MHz, in terms of normalised source level Pr_n/P_0r_0 and the normalised range dependence z Here, P_0 is a far-field pressure at r_0 and P is the measured acoustic pressure.

By fitting this data, the backscattered signal dependence on frequency and transducer radius and allowed the results in the near-field to fall onto a single non-dimensional curve. Using numerical techniques, a rational equation in terms of z could then be found as shown in Equation 2.6 where r_n is the near field distance, a_t is the transducer radius and λ is the wavelength of the ultrasonic signal. The near-field distance therefore increases with increasing frequency (i.e. decreasing wavelength) and transducer radius.

k_s is the particle species backscatter constant and can be found using:

$$k_s = \frac{\langle f \rangle}{\sqrt{a\rho_s}} \quad \textbf{2.9}$$

Where a is the particle radius in metres, ρ_s is the particle density and f (Equation 2.20) is the form function for which angled brackets indicate a number average over the particle size distribution given in Equation 2.13. The attenuation due to water at zero salinity, α_w in Np m^{-1}, is defined by Rice *et al.* [15] (derived from equations by Ainslie and McColm [170]) and is shown in Equation 2.10.

$$\alpha_w = 0.05641\, F^2 \exp\left(-\frac{T}{27}\right) \quad \textbf{2.10}$$

where F is the insonification frequency in MHz and T is the temperature in ^{0}C (valid for $6^0\text{C} < T < 35^0\text{C}$) [15]. The sediment attenuation constant, α_s is given by Thorne and Hanes [33] as

$$\alpha_s = \frac{1}{r}\int_0^r \xi(r')M(r')dr \quad \textbf{2.11}$$

where ξ in m^2 kg^{-1} is known as the sediment attenuation coefficient and can be expressed as

$$\xi = \frac{3\langle \chi \rangle}{4\langle a \rangle \rho_s} \quad \textbf{2.12}$$

where χ is the normalised total scattering cross-section and (Rice, et al., 2014)

$$\langle f \rangle = \left(\frac{\langle a \rangle \langle a^2 f^2 \rangle}{\langle a^3 \rangle}\right)^{\frac{1}{2}} \quad \textbf{2.13}$$

$$\langle \chi \rangle = \frac{\langle a \rangle \langle a^2 \chi \rangle}{\langle a^3 \rangle} \quad \textbf{2.14}$$

where angled brackets indicate a number average over the particle size distribution (Equation 2.14) by number. From this it can be seen that k_s and ξ both depend on the particle size distribution and shape and therefore distance from the transducer, as do M and α_s.

In terms of predicting the scattering and attenuation parameters based on the particle size and insonification frequency the Elastic Sphere (ES) [171] (Equations 2.16 and 2.17) and Fluid Sphere (FS) [172] (Equations 2.18 and 2.19) models allow for the prediction of the values of χ and k_s for spheres if the sphere radius is known by providing expressions for $f(x)$ and $\chi(x)$ as follows

$$x = ka \quad \textbf{2.15}$$

$$f^{ES}(x) = \frac{2}{ix}\sum_{q=0}^{\infty}(-1)^q(2q+1)b_q \quad \textbf{2.16}$$

$$\chi^{ES}(x) = \frac{2}{x^2}\sum_{q=0}^{\infty}(2q+1)\left|b_q\right| \quad \textbf{2.17}$$

$$f^{FS}(x) = \left|\frac{2}{x}\sum_{q=0}^{\infty}\frac{(-1)^q(2q+1)}{1+ic_q}\right| \quad \textbf{2.18}$$

$$\chi^{FS}(x) = \frac{2}{x^2}\sum_{q=0}^{\infty}\frac{(-1)^q(2q+1)}{1+c_q^2} \quad \textbf{2.19}$$

where k is the wave number of sound in water, a is the particle radius, $i = \sqrt{-1}$, b_q [171] and c_q [172] are complex functions involving Bessel and Hankel functions and their derivatives. The elastic sphere model applies to solid elastic particles that are able to support both compressional and shear waves. For a fluid sphere, such as an oil droplet suspended in water the shear wave speed is assumed to be zero [166] although viscous dissipation of the acoustic wave will cause conversion to shear waves in the surrounding fluid [173]. To resolve these models therefore the compressional and shear wave speed in the medium and the particle must be known. As Equations 2.16 and 2.19 are restricted to spheres and fairly computationally complex, heuristic expressions for f and χ have been determined previously for both glass beads and irregular sandy sediment and have been presented by Betteridge *et al.* [159] (Equations 2.20 and 2.22) and Thorne and Meral [48] (Section 2.3.2, Equations 2.24 and 2.25) respectively in terms of the acoustic wavenumber, k, of the ultrasound and the particle size, a. This set of equations assumes that no multiple scattering occurs such that the signal reflected from each particle is not affected by the neighbouring particles.

It was observed by Betteridge et al. [159], that the form function for glass beads was variable above $ka = 5$ with sharp dips associated with spherical resonances of the spheres in suspension when modelling a monosized particle distribution. By

introducing even a small size range (size range of the sieves used = +/- 0.09a) the dips in the form function were significantly reduced making for a simpler model (shown in Figure 2.7). The introduction of a size range had little impact on the scattering cross-section χ and allowed the scattering characteristics to be represented by the following equations. The form function, as modelled heuristically as a function of ka for glass beads by Betteridge et al. [159] is given in Equation 2.20 in terms of x, the product of the acoustic wavenumber, k, and the particle radius, a, and ς (Equation 2.21), a function of x (Equation 2.15).

$$f_{ss} = \frac{\varsigma x^2}{1.17 + 0.95x^2} \quad \textbf{2.20}$$

$$\varsigma = \left(1 - 0.5e^{-\left(\frac{x-1.5}{0.5}\right)^2}\right)\left(1 + 0.4e^{-\left(\frac{x-1.5}{3.0}\right)^2}\right)\left(1 - 0.5e^{-\left(\frac{x-5.9}{0.7}\right)^2}\right) \quad \textbf{2.21}$$

The scattering cross section, χ_{ss}, where "ss" indicates this model applies to solid spheres, as modelled by Betteridge *et al.* [159], is given in Equation 2.22 in terms of *x* and φ (Equation 2.23), a function of *x*.

$$\chi_{ss} = \frac{0.24\varphi x^4}{0.7 + 0.3x + 2.1x^2 - 0.7x^3 + 0.3x^4} \quad \textbf{2.22}$$

$$\varphi = 1 - 0.4e^{-\left(\frac{x-5.5}{2.5}\right)^2} \quad \textbf{2.23}$$

As *f* and χ are approximately proportional to $(ka)^2$ and $(ka)^4$ then ξ and k_s are therefore proportional to $(ka)^{1.5}$ and $(ka)^3$. Figure 2.7 shows the model values of f and χ (solid lines) plotted with experimental data from Thorne and Buckingham [174] and Schaafsma and Hay [175] against *x* where $x = ka$.

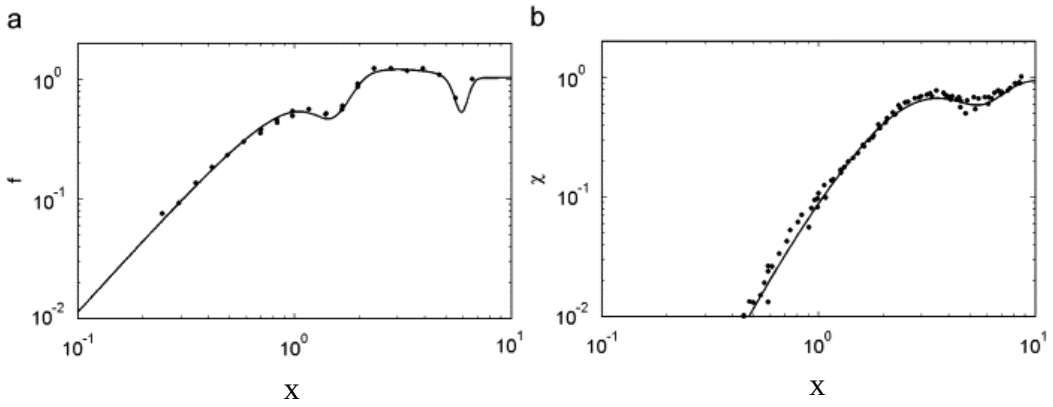

Figure 2.7 Graphs of *f* and χ vs *x* (= *ka*) from the Betteridge *et al* model compared with measured values (●) [159]

It can be seen that for the system studied the scattering model proposed by Betteridge *et al.* [159] fitted the data very closely with the deviations in the scattering cross-section being the largest. If suspensions other than those sieved to a size range of $a \pm 0.09a$ were used Equations 2.20-2.23 may have to be modified.

2.3.2 Irregular solid scattering model

For irregular solid scatterers, such as non-cohesive sediment encountered in fluvial environments, Thorne and Meral [48] similarly used experimental data from a number of authors to fit heuristic expressions for the form function, *f*, [156], [174], [176], [177] and the scattering cross section, χ [156], [174], [175], [178]–[180] as a function of *x*. The subscript "si" indicates values for an irregular solid scatterer and expressions for the form function and scattering cross section are shown in Equations 2.24 and 2.25.

$$f_{si} = \frac{k_{sf}x^2(1 - 0.25e^{-\left(\frac{x-1.5}{0.5}\right)^2})(1 + 0.35e\text{^} - \left(\frac{x-2}{2}\right)\text{^}2}{1.13 + 0.8k_{sf}x^2} \qquad \textbf{2.24}$$

$$\chi_{si} = \frac{k_{s\alpha}\, x^4}{1 + x^2 + 0.9k_{s\alpha}x^4} \qquad \textbf{2.25}$$

k_{sf} and $k_{s\alpha}$ are given by Morse and Ingard [181] and are shown in Equations 2.26 and 2.27.

$$k_{sf} = \frac{2}{3}\left|\frac{(\kappa_s - \kappa_w)}{\kappa_w} - \frac{3(\rho_s - \rho_w)}{(2\rho_s + \rho_w)}\right| \qquad \textbf{2.26}$$

$$k_{s\alpha} = \frac{4}{3}\left(\frac{\left(\frac{(\kappa_s - \kappa_w)}{\kappa_w}\right)^2 + \frac{\left(\frac{3(\rho_s - \rho_w)}{(2\rho_s + \rho_w)}\right)^2}{3}}{6}\right) \quad \textbf{2.27}$$

The lower *ka* limit for the data used to fit the models was ~0.1 and the upper limit was ~5 and so the applicability of this model to measurements in the Rayleigh regime (*ka* << *1*) is of interest for marine sedimentology [47], [120] and for engineering applications where acoustic measurement in this regime may be necessary for measurement of concentration and particle size where instrument access is restricted [5], [6], [15], [38].

2.3.3 Urick's Model for Viscous Absorption

If viscous losses are to be accounted for when *ka* << *1*, then Urick's model [143] (shown to be valid for kaolin up to 200 g l^{-1}) can be used to calculate an additional attenuation term, χ_{sv}, caused by visco-inertial interactions between the particles and surrounding fluid. The additional viscous cross-section term to be added on to the scattering cross section is shown in Equation 2.28 in terms of the density ratio between the spheres and the surrounding fluid (γ) and $\beta = \sqrt{\omega/2\nu}$ where ω is the acoustic angular frequency and *v* is the kinematic viscosity of water.

$$\chi_{sv} = \frac{2}{3}x(\gamma - 1)^2 \frac{\tau}{\tau^2 + (\gamma + \theta_v)^2} \quad \textbf{2.28}$$

$$\tau = \frac{9}{4\beta a}\left(1 + \frac{1}{\beta a}\right) \quad \textbf{2.29}$$

$$\theta_v = \frac{1}{2}\left(1 + \frac{9}{2\beta a}\right) \quad \textbf{2.30}$$

$$\chi = \chi_{ss} + \chi_{sv} \quad \textbf{2.31}$$

By using heuristically or experimentally determined values of *f* and χ, and accounting for viscous losses if necessary, Equations 2.9, 2.10 and 2.12 can be substituted into Equation 2.5 leaving only the transducer constant, k_t, as an unknown. Acoustic measurements on homogeneous suspensions of particles at fixed low concentrations

with known scattering properties can then be used to find k_t, for the combined probe and electronics system using Equation 2.32 as detailed by Betteridge *et al.* [159].

$$\frac{r\psi V(r)}{k_s\sqrt{M}}e^{2r(\alpha_w+\alpha_s)} = k_t \quad \textbf{2.32}$$

2.3.4 *G-function* modelling

In order to be able to determine the attenuation coefficient in arbitrary suspensions, previous authors [1], [15], [166], [174] have linearised Equation 2.5 with respect to distance by taking the natural logarithm of the product of the measured RMS voltage, V_{rms}, and the distance from the transducer, *r*, to produce the *G-function* shown in Equation 2.33

$$G = \ln(\psi r V_{rms}) = \ln(k_s k_t) + \frac{1}{2}lnM - 2r(\alpha_w + \alpha_s) \quad \textbf{2.33}$$

Where α_w and α_s are the attenuation due to the water and sediment respectively and k_s and k_t are the backscatter and transducer constants. If the particle concentration, *M*, does not change with distance from the transducer, *r*, the derivative with respect to *r* gives

$$\frac{\partial G}{\partial r} = -2(\alpha_w + \alpha_s) \quad \textbf{2.34}$$

with the requirement that such a relationship only holds for a homogenously mixed system i.e. the concentration and scattering constant are not functions of distance. Applying this same condition to Equation 2.11 gives

$$\alpha_s = \xi M \quad \textbf{2.35}$$

where ξ is the attenuation coefficient. Substituting equation 2.35 into 2.36 and differentiating with respect to the mass concentration, *M*, produces

$$\xi = -\frac{1}{2}\frac{\partial^2 G}{\partial M \partial r} \quad \textbf{2.36}$$

thus, by taking the gradient of *G* plotted against distance, $\frac{\partial G}{\partial r}$ can be determined at multiple concentrations for a given particle system. $\frac{\partial G}{\partial r}$ can then be plotted against concentration and the gradient of a linear fit to that plot used to find ξ via Equation 2.36.

A calibration following the *G-function* method is also given by Bux *et al.* [17] for finding the transducer constant, k_t, and the scattering constant, k_s. Once the attenuation

coefficient , ξ (and its dimensionless equivalent, χ, through Equation 2.12) is known, k_t can be estimated from data collected at known low and intermediate concentrations using Equation 2.32 by substituting in values of the sediment backscatter constant, k_s, estimated using a heuristic expression such as that provided by Betteridge *et al.* [159] (Equation 2.20). The backscattering constant can then be estimated experimentally at higher concentrations using the same equation used to find k_t (Equation 2.32, a rearrangement of Equation 2.5) by substituting in the calculated value of k_t to find k_s for any given particle system. This will be referred to hereafter as the extended *G-function* method.

2.3.5 Single frequency inversion methods

If the system has been calibrated such that k_t is known then k_s and α_s must be determined which requires knowledge of how $\langle a \rangle$ and M vary with distance from the transducer to evaluate Equation 2.37 below [33].

$$M = \left\{ \frac{V_{rms} \psi r}{k_s k_t} \right\}^2 e^{4r\alpha} \qquad \textbf{2.37}$$

Where α is the sum of the attenuation due to water and the sediment that includes both scattering and viscous dissipation terms. How $\langle a \rangle$ and M vary with distance from the transducer is exactly the information we are trying to obtain, however, and so there are several ways in which to approach the problem which are detailed below. If only one frequency is available an estimate must be made for $\langle a \rangle$ to allow k_s and ξ to be calculated. If $M\xi \ll 1$ then α_s can be assumed to be zero yielding the relationship shown in Equation 2.38 [33]

$$M_0 = \left\{ \frac{V_{rms} \psi r}{k_s k_t} \right\}^2 e^{4r\alpha_w} \qquad \textbf{2.38}$$

Knowing all terms on the right side of the equation an initial estimate of the concentration profile with distance ($M_0(r)$) can therefore be produced. If it cannot be assumed that $\alpha_s \approx 0$ then an iterative approach is used. The calculation is performed assuming $\alpha_s \approx 0$ for the first range bin with the assumption that the attenuation very close to the transducer will be insignificant and Equation 2.38 will provide an accurate measure of the concentration. The resulting concentration is then used to estimate the sediment attenuation through the first range bin using Equation 2.11 the result of which is fed into Equation 2.39 to revaluate the concentration at the first range bin. The iteration is then repeated until both the concentration and sediment attenuation

are convergent. The same process is then repeated stepwise for each proceeding range bin using Equation 2.11 to estimate the sediment attenuation at each range bin.

$$M_1 = M_0 e^{4r\alpha_s} \quad \textbf{2.39}$$

This approach has been used previously but caution must be used as the iterative feedback between M and α_s is positive (on overestimate or underestimate of M will result in an overestimate or underestimate of α_s respectively through Equation 2.11). As the values of M and α_s at preceding range bins are used to estimate the sediment attenuation at a given range bin (Equation 2.11) errors in their estimation may therefore cause the solution to diverge to zero or infinity as the distance from the transducer increases [33].

Developed by Lee and Hanes [164] the implicit inversion method relies on taking the analytical solution of Equation 2.5. Having taken the natural logarithm and operating a change of variable the derivative with range r can then be integrated to produce Equation 2.32

$$M = \frac{J_l}{1 - 4\xi_S \int_{r_1}^{r_l} J(r)dr} \quad \textbf{2.40}$$

where J_l is the normalised intensity at each range bin *l*. This method relies on the assumption that the sediment attenuation between the first range bin of the profile and the transducer is negligible such that $M_1 = J_1$. The integral of the normalised intensity $J(r)$ must also be approximated by a discrete numerical scheme such as rectangular discretisation scheme. The instabilities associated with this method arise from terms in the denominator of Equation 2.40 as the value of 1 used is only valid assuming that $M_1 = J_1$. If this is not valid then the concentrations will either be over or underestimated. The second error is caused by the integral approximation in the second denominator term as, if the term becomes close to unity, the calculated concentration will approach infinity. Before this singularity is induced the concentration will be overestimated. After the singularity it will become negative before asymptotically approaching zero. Furthermore, in the same way as is described for the iterative method, the errors in $J(r)$ are positively propagated with increasing distance from the transducer and so an error at any distance interval will affect the subsequent concentration estimate.

If multiple frequencies are available, then the concentration and particle size can be obtained acoustically. Typically three frequencies are used in the range of 1-5 MHz. By rearranging Equation 2.5 we can write [182].

$$\frac{\langle f_i \rangle}{\langle f_j \rangle} = \frac{\frac{\psi_i V_{rmsi}}{k_{ti}}}{\frac{\psi_j V_{rmsj}}{k_{tj}}} e^{2r(\alpha_i - \alpha_j)} \quad \textbf{2.41}$$

$$M_i = \left\{\frac{V_{rmsi}}{k_{si} k_{ti}}\right\}^2 \psi_i^2 r^2 e^{4r\alpha_i} \quad \textbf{2.42}$$

Where $i \neq j$ and i and j refer to any two of the frequencies used. The mean particle size, $\langle a \rangle$, can be extracted from the form function ratios at different frequencies so long as sediment attenuation can be neglected. As there will likely be a size distribution of sediment particles $\langle f \rangle$ is obtained from f using an estimated probability distribution for a which acts as a smoothing function on f. It was found by Thorne and Hardcastle [2] that estimating $\langle a \rangle$ from $\frac{\langle f_i \rangle}{\langle f_j \rangle}$ resulted in multiple values of $\langle a_s \rangle$ which can be resolved by using the three ratios of $\frac{\langle f_i \rangle}{\langle f_j \rangle}$ with a three-frequency system after which particle size and concentration profiles can then be produced the results of which are shown in Figure 2.8. The range of $\frac{\langle f_i \rangle}{\langle f_j \rangle}$ over which the particle size can be determined is limited as if $k\langle a \rangle \ll 1$ then $\frac{\langle f_i \rangle}{\langle f_j \rangle} = \frac{{k_i}^2}{{k_j}^2}$, provided that viscous dissipation is not significant, and when $k\langle a \rangle \gg 1$ then $\frac{\langle f_i \rangle}{\langle f_j \rangle} = 1$ both of which mean no size information about the system can be extracted [33]. It was additionally found Thorne and Hardcastle [2] that the 5 MHz signal at the highest measured concentrations gave differences in the calculated near-bed concentration of 3000% when incorporating attenuation effects due to accumulating errors with range. The errors introduced by the large amount of attenuation therefore also resulted in invalid size and concentration estimates when attempting to couple data across multiple frequencies that are indicated by the discontinuities and plateaus seen most prominently in the 5/1 particle size inversion (Figure 2.8 (a)).

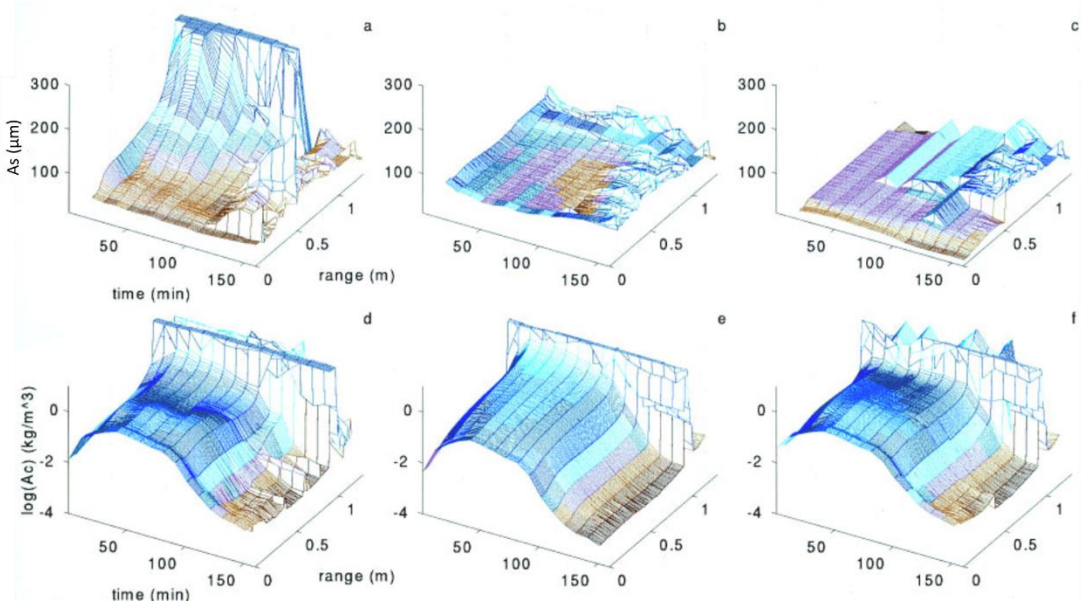

Figure 2.8 a) – c) measurements of the suspended particle radius, obtained using the 5/1, 2.5/1, and 5/2.5 MHz backscattered pressure ratios, and the concentration, d) – f) obtained using the 1.0, 2.5, and 5.0-MHz backscattered pressures. The bed echo was at approximately 0.98 m from the transceivers. [2]

If sediment attenuation is significant then the implicit iterative approach can be used. This does still have the issues associated with positive error propagation with increasing distance from the transducer, however, and still has the limitations for $\frac{\langle f_i \rangle}{\langle f_j \rangle}$ described previously. Furthermore, the approach is particularly unstable when the concentration approaches 1 kg/m^3, the acoustic frequency is about 2 MHz or higher and the mean sediment radius above 100 μm [14]. While this approach does have its drawbacks careful choice of frequencies and proper data analysis and processing can allow for accurate determination of profiles for particles size and concentration [33].

2.3.6 Dual-frequency inversion method

In this section the dual-frequency inversion method originally proposed by Bricault [161] and further developed by Hurther *et al.* [14] and Rice *et al.* [15] is divulged as it represents a promising technique to produce concentration profiles *in situ*.

If two frequencies are available then a dual-frequency approach can be adopted to eliminate the cumulative error in the far-field associated with the single-frequency approach [33]. The model, as described by Rice *et al.* [15], is shown in Equations 2.43-2.48. Equation 2.43 essentially shows the squared form of Equation 2.5 simplified to two terms, *J(r)* and $\Phi^2(r)$. The *J(r)* term (Equation 2.45)

contains the sediment attenuation coefficient, ξ, and mass concentration, M, while $\Phi^2(r)$ (Equation 2.44), contains the sediment backscatter and system gain constants, k_s and k_t, the attenuation due to water, α_w, and the near-field correction factor ψ.

$$V^2(r) = \Phi^2(r)J(r) \quad \textbf{2.43}$$

$$\Phi^2(r) = \left(\frac{k_s k_t}{\psi r}\right)^2 e^{-4r\alpha_w} \quad \textbf{2.44}$$

$$J(r) = Me^{-4\int_0^r \xi(r')M(r')dr'} = \frac{V^2(r)}{\Phi^2(r)} \quad \textbf{2.45}$$

If the particle size, and therefore ξ and k_s, do not change with distance from the probe, as would be the case for a homogeneously mixed suspension, then the attenuation term can be moved outside of the integral and Equation 2.45 can be written as follows

$$J_i(r) = Me^{-4\xi_i\int_0^r M(r')dr'} \quad \textbf{2.46}$$

where i = 1, 2 for probes/frequencies 1 and 2 (2 and 2.5 MHz in this study). Dividing equation 2.46 by M, taking the natural logarithm and dividing by ξ_i yields

$$\left(\frac{J_1}{M}\right)^{\xi_2} = \left(\frac{J_2}{M}\right)^{\xi_1} \quad \textbf{2.47}$$

rearranging for M gives

$$M = J_1^{\left(1-\frac{\xi_1}{\xi_2}\right)^{-1}} J_2^{\left(1-\frac{\xi_2}{\xi_1}\right)^{-1}} \quad \textbf{2.48}$$

For this method to function the attenuation ratio $\xi_1/\ \xi_2$ must be sufficiently different from unity to prevent mathematical instabilities and subsequent errors in Equation 2.48. A single narrowband transducer could therefore possibly be used for quasi-simultaneous measurement in co-located sample volumes so long as the attenuation coefficient can be measured at each frequency to ascertain the accuracy of the subsequent inversion and warrants further investigation [14].

An equation for calculating the relative (mean-normalised) error in the dual-frequency inverted concentration, $\frac{\delta M}{M}$, in terms of the attenuation ratio and relative error in the measured scattering constant at a single frequency, $\frac{\delta K_1}{K_1}$, has been derived previously by Rice *et al.* [15] (Appendix A.3 Equations A.6-A.19) where K is the product of the sediment scattering constant, k_s, and the transducer constant, k_t, and is extended here

to include the relative error at the second frequency $\frac{\delta K_2}{K_2}$. The result is shown in Equation 2.49

$$\frac{\delta M}{M} = \sqrt{\left(-2\left(1-\frac{\xi_1}{\xi_2}\right)^{-1}\left|\frac{\delta K_1}{K_1}\right|\right)^2 + \left(-2\left(1-\frac{\xi_2}{\xi_1}\right)^{-1}\left|\frac{\delta K_2}{K_2}\right|\right)^2} \quad \textbf{2.49}$$

As the ratio $\xi_1/\ \xi_2$ approaches unity then the terms inside the bracket will approach infinity causing mathematical instabilities in the concentration inversion.

Although other implicit and explicit methods for concentration inversion exist, they tend to accumulate errors with increasing distance from the transducer leading to numerical instability in the far-field as well as having limitations regarding the concentration and frequencies selected [33]. The dual-frequency method, however, has been shown to agree with local Optical Backscatter measurements of sand up to 60 kg/m^3 by Hurther *et al.* [14] and for particle concentration measurement in pipe flow for glass and plastic particles between 41-691 μm by Rice *et al.* [15]. The divergence in results obtained by Hurther *et al.* using the single frequency iterative and explicit inversions from those obtained using OBS and dual frequency inversion is shown in Figure 2.9 and demonstrates the increase towards infinitely high values for the single frequency inversions due to cumulative errors in the monotonically increasing concentration profile. Meanwhile the dual-frequency inversion method is seen to obtain an accurate profile free of error propagation with errors comparable to the point measurements of the OBS despite the fact that the sand suspension is highly attenuating.

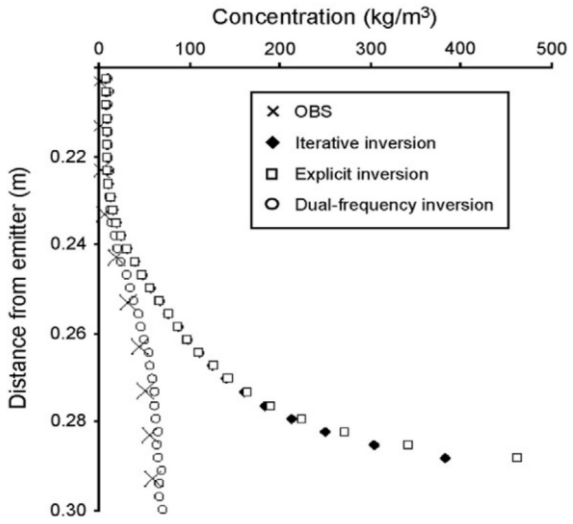

Figure 2.9 Sand concentration profiles obtained with the three acoustic inversion methods and Optical Backscatter System (OBS) data (for which measurement uncertainty is below 20 %) [14]

The advantages of this method are that no assumption needs to be made for the sediment attenuation at any given distance point and by eliminating the attenuation integrals in Equation 2.45 that are present during the single frequency inversion through Equation 2.11 the propagation of errors along the profile generated is avoided. In order for this method to work, however, the smallest of the two frequencies used must lie within the Rayleigh scattering regime (equivalent to Mie scattering for electromagnetic waves) which occurs when the value of $k\langle a\rangle$ is less than 1. This condition can be satisfied for acoustic frequencies between 1 and 5 MHz for fine and coarse sand up to 500 μm mean radius. Furthermore, when $k\langle a\rangle$ is less than 1 then $\xi_S \approx (k\langle a\rangle)^4$. Therefore, so as long as the difference between the frequencies is in the range of 100 KHz, ξ_{Si}/ξ_{Sk} will give ratios sufficiently different from unity. As a result, a single narrowband transducer may be used instead of two separate probes to allow for co-located measurements at different frequencies to be compared [14], [15].

2.3.7 Qualitative correlations to measure particle concentration in aqueous suspensions

It was found by Hunter *et al.* [160] that the concentration predicted by quantitative scattering theory for Vaquashene 0-44 size grade (average size = 44 μm) glass powder (ρ= 2500 kg m^{-3}) correlated closely with the known values of concentration up to 2.5 g l^{-1} (see Figure 2.10). Above this value theoretical predictions overestimate the

concentration by multiple orders of magnitude in some cases with greater deviation seen at higher frequencies. This result would be expected in a system undergoing significant inter-particle scattering as this would attenuate the signal more than would be predicted theoretically and would become more pronounced at higher frequencies and concentrations [11], [183].

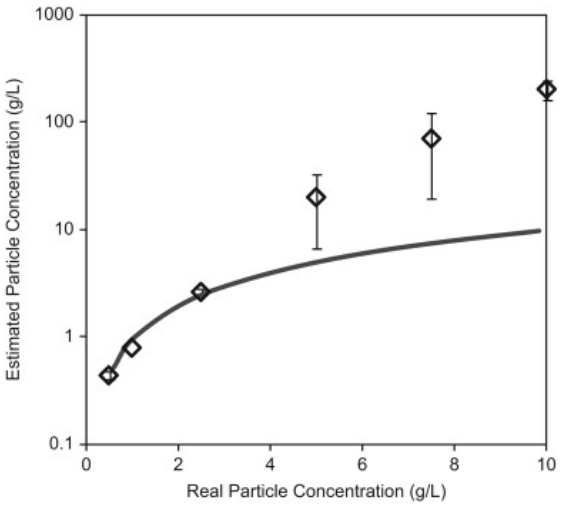

Figure 2.10 Comparison between average particle concentrations estimated from acoustic echo responses using scattering theory, to the known real values, within a small 0.05–0.15 m depth range. Theoretical estimations are also averaged between the 2, 4 and 5 MHz transducer responses. The 100 % correlation is shown by the solid line [160].

Although there is an upper concentration limit to quantitative theoretical predictions, the backscatter response will still be dictated by both a backscatter and attenuation component. Therefore, as multiple-scattering effects increase, and the attenuation is enhanced, a correlation using the rate of signal decay with distance, rather than the raw backscatter strength, would allow for estimation of particle concentrations above this limit. This has been attributed by Hunter *et al.* [160] to the fact that when attenuation is enhanced the backscatter component will become negligible and the resultant profile will exhibit a linear decay on a decibel scale with distance and has also been found in previous work by other authors [139], [140], [184], [185]. The linear relationship between attenuation and particle concentration predicted by Equation 2.36 therefore provides a simple method to observe concentration changes by correlating the change in the approximated linear attenuation slope with concentration.

Moore *et al*. [155] demonstrated the ability to obtain depth profiles using of up to 10 metres in dilute (<1 g l^{-1}) suspensions using this qualitative method by using

empirical expressions from Thorne and Meral [48] to estimate the expected attenuation at each concentration and frequency. However, as both particle size and concentration affect the backscattered signal, the ABS was unable differentiate between changes in the two parameters as the optical backscatter system (OBS) used to obtain concentration data was found to contain significant errors above 50 mg l^{-1}. Error in such measurements may be reduced if independent information about the particle size distribution is known [186]. It was also seen, however, that the attenuation slope only became linear with distance for the 4 & 5 MHz probes used and not for the 1 or 2 MHz. This would be expected if there were a greater influence of inter-particle scattering effects at higher frequencies as was evidenced in the small-scale tests performed by Hunter *et al.* [160] demonstrated in Figure 2.11.

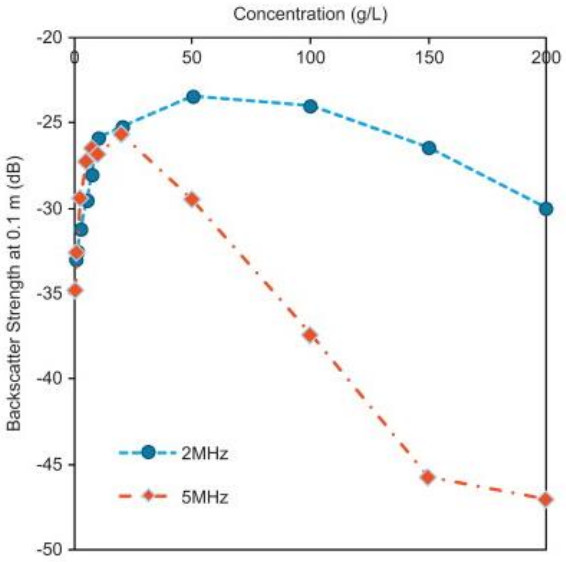

Figure 2.11 Strength of raw backscattered signal at a depth of 0.1m from 2 and 5 MHz transducers for spherical glass dispersion concentrations of 0.2 to 200 g l^{-1} [160]

It can be seen in Figure 2.11 that initially the signal strength increases with concentration due to larger surface area of scatterers in solution until the point at which the signal begins to attenuate due to absorption of the signal due to both scattering and attenuation components of the ultrasound as would be generally predicted by modelling [187], [188]. As the 5 MHz signal will have a shorter wavelength the attenuation of the signal is greater than that seen in the 2 MHz probe [11]. Furthermore, inter-particle scattering effects will decrease the signal further at higher concentrations as the signal will scatter between particle surfaces before echoing back to the receiver leading to greater attenuation. These attenuation effects will also be more pronounced at higher frequencies [11], [185]. It should also be noted

that a linear correlation between returned signal voltage and particle concentration can be produced at low concentrations (<1-2 g l^{-1}) but this would be unsuitable to most engineering applications where particle concentration will be higher [160]. Despite the non-linear decay of the 1 and 2 MHz probes with respect to distance it was still possible to obtain a frequency correlation for the probes by taking the differential of the decay slope at various distances and plotting these as a function of concentration as shown in Figure 2.12.

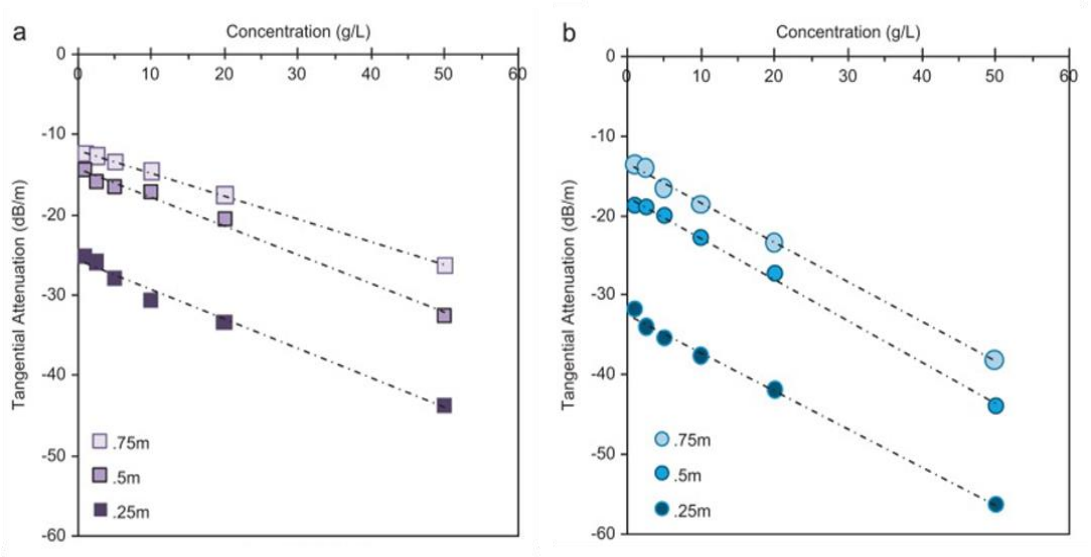

Figure 2.12 Change in tangential attenuation estimated from interpolated differential of the a) 1 MHz and b) 2 MHz ABS response at 0.25, 0.5 and 0.75 m depths through spherical g lass dispersions between 1 and 50 g l^{-1} with dashed lines showing the linear correlations produced [160].

It should be noted that, while the absolute value of tangential attenuation (the slope of the backscatter strength (dB) vs distance profiles) was different at each depth point, the gradient of the tangential attenuation-concentration correlation slope is independent of depth and so, at a given transducer frequency, the variation in particle concentration at any depth point can be found by measuring the absolute change in attenuation at any other depth point even though the actual attenuation value itself will depend on the measurement depth [160]. Another advantage of using attenuation as a measure of concentration is that it will produce a much lower noise floor than using the raw backscatter strength as at high particle concentrations the return signal will be weak but if the rate of signal decay is used the strength of the echoed signal will not influence the accuracy of the readings so significantly so long as the echo is above the instrument threshold. The final advantage of this method is that the technique can be applied to systems that are heterogeneous in concentration so long as correlation fits are made in well mixed homogeneous systems by measuring the differential of the

backscatter return at multiple depth points [160]. These qualitative relationships coupled with ABS measurements would allow operators of mixing and settling operations to gauge the performance of a system both spatially and temporally without the need for physical sampling [160].

In terms of the measurement of consolidated sludge systems, such as those that might be encountered during waste consolidation at Sellafield Ltd., studies are limited. Nevertheless, concentration inversion models exist for both low (up to ~150 g l^{-1}) [14], [15], [33] and high concentration (up to ~30 %v/v) [46] suspensions, provided certain acoustic parameters such as the velocity of sound in the solid and particle characteristics such as size are known or can be estimated. Limitations in these models exist, however, due to either error propagation with increased measurement depth [33] or the need to model particle acoustic properties where sampling is limited and particle acoustic properties cannot be assumed *a priori* [46]. ABS attenuation measurements for determining bed density have been demonstrated previously by Hunter *et al.* [189] in the same laboratory-scale thickener used in this study. It was found that, although attenuation measurements were not depth-independent vertically through the bed, response at fixed depths for the same bed height could be qualitatively correlated to changes in concentration over time [189]. It was therefore proposed that by taking horizontal measurements through the bed attenuation determined while keeping the measurement zone fixed at a single height, rather than across a range of heights, bed depth influence can be eliminated when determining the attenuation value in the consolidated sludge bed.

If sediment concentration through the hindered settling zone and in the compressed bed can be determined on-line, then detailed aggregation models such as those employed by Usher *et al.* [24], [26] can be used to optimise solid-liquid separation by increasing the underflow concentration or the solids flux through the thickener by altering operational parameters such as the rake speed and underflow flowrate to control the bed height and solids residence time [190]. Coupling this system with in-line particle size data, collected on devices such as a Focussed Beam Reflectance Monitor (FBRM) [126], [127], [191], would allow for CFD models, such as that proposed by Heath and Koh [28], to be compared simultaneously with *in situ*

measurements [24]–[27] to allow for real-time monitoring and optimisation of waste transport processes at Sellafield.

2.3.8 Semi-Empirical Backscatter Power Model

More recently, measurements performed on glass beads in a water suspension by Weser *et al.* [46], showed agreement with their semi-empirical scattering theory for glass beads up to 30 vol. % for values of the wavenumber such that $0.1 < ka \leq 1$. A packing factor that reduces the modelled backscatter strength at high concentrations was calculated using the hard sphere model which is valid in the case of absence of far-reaching (in terms of the interparticle distance) non-viscous interactions. It also assumes the presence of spherical particles and, while a small degree of deviation in shape (such as that caused by surface roughness or concavity) is acceptable, a significant shape difference, such as rods or disks, have a different concentration dependency for their packing factor which are given by Mo and Cobbold [192] and Percus and Yevick [193]. The introduction of this concentration dependent packing factor allows for the extension of single particle scattering theory, normally valid only at low concentration, to concentrations up to 30 % by volume for spherical glass particles as is incorporated as follows. Starting with the single scattering equation, the backscattering amplitude of a number concentration of *n* particles ($\Omega_{\sum}$) can be written as [46]

$$\Omega_{\sum} = \Omega_p . n = \Omega_p \frac{c_v}{V_p} \qquad \textbf{2.50}$$

Where V_p is the volume of a single particle, c_v is the volume concentration of scatterers dispersed in the medium and Ω_p is the backscattering amplitude of a single particle. The model assumes that the signal amplitude backscattered from a collection of particles is equal to sum of the theoretical backscattered amplitude of each particle in the insonified volume that is described by the $\Omega_p . n$ term. The number concentration, *n*, is then expressed in terms of the volume concentration of particles, c_v, and the volume of the particle V_p. This is only valid for low particle concentration, however, until the following packing factor for hard spheres shown in Equation 2.51, used previously by Mo and Cobbold [192], is introduced.

$$W(c_v) = \frac{(1 - c_v)^4}{(1 + 2.c_v)^2} \quad \textbf{2.51}$$

This is then incorporated into Equation 2.50 to produce Equation 2.52

$$\Omega_\Sigma = \Omega_P.n.W(c_v) = \Omega_P.\frac{c_v}{V_P}.W(c_v) \quad \textbf{2.52}$$

The packing factor accounts for the overlap between the surface of the particles that will decrease as the volume concentration of particles is increased. In general terms, the packing factor (W) in the Weser *et al.* model can be defined from the "excluded volume" (v_e, the volume around a particle that the centre of another particle cannot occupy), the average number of observed scatterers ($\bar{N}$), its variance (σ_N) and the average number concentration of scatterers ($\bar{n}$) by [192] as shown in Equation 2.54 below.

$$W = [(1 - v_e.\bar{n}.\left(1 + \frac{\sigma_N^2}{\bar{N}^2}\right)] \quad \textbf{2.53}$$

A broadening of the particle size distribution would therefore both increase the particle number variance and the excluded volume leading to a decrease in the packing factor and the backscattered amplitude.

The results obtained by Weser *et al.* [46] are displayed in Figure 2.13. Ignoring the results which lay outside of the Rayleigh scattering regime, this combination of theory for single particle scattering and the concentration dependent packing factor show good agreement with experimental data. Although this method has not yet been applied to flocculated systems it does allow for higher concentrations of non-cohesive particle systems to be evaluated without having to use a qualitative method to determine the acoustic parameters. Additionally, as the measurement is taken close to the transducer, even highly attenuating suspensions can be measured however only a single point measurement of concentration is obtained and therefore represents a technique that may likely only be applied where the single or dual-frequency methods fail. Despite the disadvantages of the model, it is relatively simple to implement and represents a method that can easily be used in conjunction with other inversion methods to allow for initial estimates of the concentration to be used in the single frequency inversion method (Section 2.3.5, Equation 2.39) to better ground results and produce an accurate concentration profile.

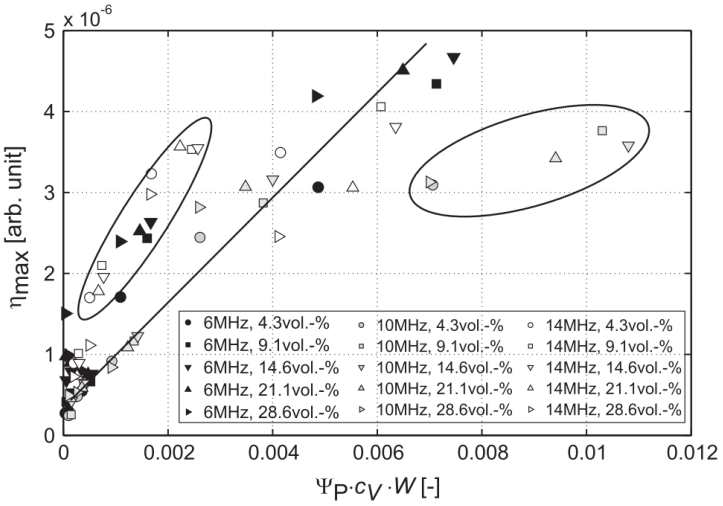

Figure 2.13 Measured backscatter amplitude plotted against theoretical values predicted by Faran's model [194], [195] in conjunction with packing factor ($\widetilde{\Psi_p}.\, n.\, W(c_v)$) where $\widetilde{\Psi_p} = \Omega_p$. Calculated using Equation 2.52. Data points within ellipses indicate measurement values for which *ka*>1 *and ka*<0.1.

2.3.9 Flocculated systems

McClements [196] presents some of the first attempts to investigate the ultrasonic properties of flocculated systems by taking measurements of oil droplets from 1 – 4 MHz at 25 %w/w using a short range (25 ml sample volume) pulse-echo setup. Depletion flocculation was induced by adding anionic surfactant up to 12 %w/w and it was found that the size of the individual droplets making up the floc influenced the degree of overlap in thermal layers that surround the particle as a result of acoustic attenuation. These results were validated by modelling by McClements *et al.* [197] using an adapted form of the Epstein, Carhart, Allegra and Hawley (ECAH) model [144], [146] that accounts for overlap of thermal layers between the individual droplets. As the thermal layers overlap less energy is dispersed by the particle and the overall acoustic attenuation is reduced. While the model accounts for individual droplet size, floc size, droplet packing within the floc and degree of flocculation it fails to take account of polydispersity in floc and droplet sizes, non-sphericity, and the effect all of these parameters may then have on viscous losses within the floc.

A transmission setup has also been utilised by Austin and Challis [198] to study the flocculation of kaolin suspensions (nominally platelets of 1 μm diameter and 50 nm thickness) by varying the pH to produce floc sizes from ~0.25 – 2.5 μm at up to 8 %v/v. Acoustic measurements were taken at frequencies of 2 – 12 MHz. They observed that attenuation increased on deflocculation at low (< 5 %v/v) volume

fractions and increased on flocculation at higher volume fractions. It was also found that, when the mean particle radius was kept constant, an increase in the particle size distribution width would lead to a decrease in the attenuation. It was therefore postulated that, at low volume fractions, flocculation causes a significant widening of the size distribution and a corresponding reduction in the attenuation despite an increase in the mean particle size that would normally increase attenuation. For the high volume fraction dispersion, for which the opposite was true, it was proposed that due to the fractal structure of the flocs there will be a floc radius at which the effective density of the floc is equal to that of the bulk fluid. Beyond this floc radius it was proposed that an increase in particle concentration will decrease the floc radius and thereby decrease the PSD width and subsequently increase the attenuation.

Austin and Challis [198] additionally found that results from the Harker and Temple [199] model gave accurate results for the attenuation when measured particle size and the experimentally derived effective viscosity were incorporated into the model. For this model to be applied, however, fairly detailed information such as the volume of attached liquid around each particle due to non-sphericity and, for concentrated colloids, an empirical factor that depends on the interface between particles that may be difficult to determine for arbitrary particle suspensions. Moreover, Harker and Temple [199] themselves suggest that a frequency range covering two orders of magnitude would be required to accurately measure both mean particle size and concentration although such a technique would prove useful for on-line monitoring of particle size and concentration in processing streams for suspensions.

In order to produce expressions for the backscattering cross-section and form function for flocculated particles it must first be determined what type of waves propagate through the floc structure. An elastic solid will support both shear and compressional waves while a fluid will only allow for sustained propagation of compressional waves where viscosity is sufficiently large [166]. It may be expected, therefore, that as a floc grows larger and incorporates more water into its structure the acoustic properties may gradually come to resemble that of a fluid sphere. In order to investigate this assumption MacDonald *et al.* [166] performed measurements on kaolin primary particles and flocs at a number of concentrations of both floc and sediment (up to 3.2 g l^{-1} kaolin) in a 0.6 metre high settling column using ABS at 3, 4

and 5 MHz using an *ex situ* camera system to measure floc size and settling rate. Attempting to fit experimental values of the particle species backscatter coefficient (k_s) for a flocculated system to those predicted by the Elastic Sphere and Fluid Sphere models it was found by MacDonald *et al.* [166] that, although the ES and FS models bounded their data, the ES model was found to be more accurate than the FS model as the particle grew larger [166]. This was counter to the expectation that the flocs would resemble fluid spheres as more water was incorporated into their structure with growth. Even applying a distributed mass model to account for floc density change gave results that suggested the flocs are more accurately represented by the ES model as the flocs grew larger and therefore an alternative model is required [166]. Figure 2.14, taken from MacDonald *et al.* [166] shows the ratio of viscous absorption, calculated using Urick's Model [143] (Section 2.3.3, Equations 2.28-2.30) to water absorption in order to determine the relative importance of each parameter at different particle sizes (a) for three commonly used isonification frequencies.

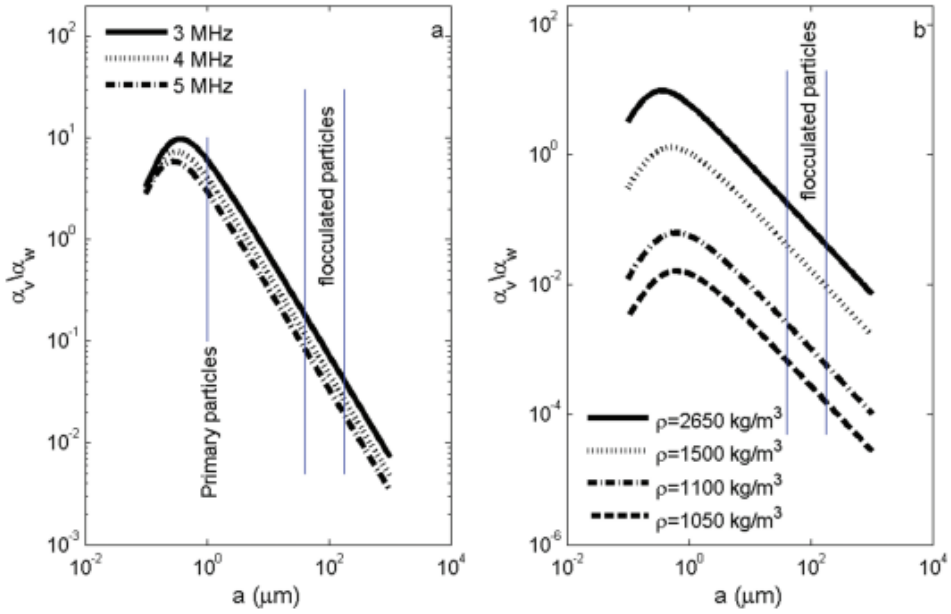

Figure 2.14 a) Ratio of viscous absorption to water absorption (αv/αw) as a function of particle radius at 3, 4 and 5 MHz for Kaolin. (b) αv/αw for particles with densities of 2650, 1500, 1100 and 1050 kg/m3 for the 3 MHz transducer and a mass concentration of 3.2 g l^{-1}

It can be seen from Figure 2.14 that in the primary particle range α_v is significantly larger than α_w while for flocculated particles α_w is larger than α_v. The upper limit of this ratio, however, is around 0.2 (i.e.α_v is $ca.\,20$ % of α_w) at which α_v is too large to be ignored. It has also been found by MacDonald *et al.* [166], however, that the floc density decreases with increasing floc size as more of the ambient fluid is incorporated into their structure and so the density of flocs approaches that of the surrounding fluid.

An example conversion of a size distribution to an effective density distribution by MacDonald *et al.* [166] is shown in Figure 2.15 below to give an idea of how significant this density change is with particle size and how the viscous attenuation is affected. The particle density is obtained from the measured settling speed and particle size using Stokes law.

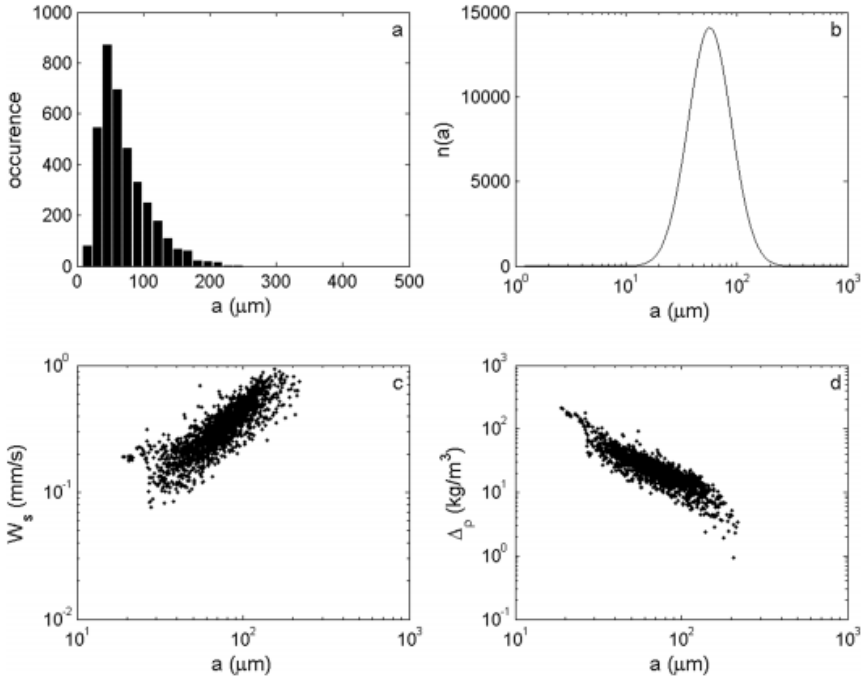

Figure 2.15 FLOCView camera system results for run 1, 3.2 g l^{-1}, FL1. (a) Particle size distribution. (b) Particle size probability density function. (c) Settling speed (W_s) distribution. (d) Effective density distribution (Macdonald, et al., 2013)

Because of the fractal geometry of flocs a power law relationship between a and $\Delta\rho$ is frequently applied (Section 2.2.3, Equation 2.2) [200] that indicates that they will decrease in density with increasing size. It can be seen from Figure 2.15 (d) that, given the typical size range for flocculated particles in Figure 2.15 **(**b), the typical density of the flocs will be considerably less than 2650 kg/m^3 (the density of kaolin). Observing the viscous attenuation curves for densities lower than that of kaolin it can be seen that the ratio of α_v/α_w will be much less than 0.2 at the measured floc size. MacDonald *et al.* [166] therefore concluded that viscous absorption could be neglected for flocs.

Using the same experimental dataset as MacDonald et al. [166], Thorne et al. [47] then produced a Hybrid model that incorporated the effect of increasing porosity of the floc with size predicted using the correlations given by Manning et al. [201] that

assume a fractal structure of the floc (see Section 2.2.3). This change in porosity is then correlated with changes in the sound speed and density of floc using a correlation from Wood [202]. Wood's equation, in combination with Urick's [143] model for viscous absorption and a modified empirical expression for a fluid sphere [203] (made to resemble the irregular scattering model from Throne and Meral [48] for the primary particles), allowed for modelling of the floc form function and scattering cross-section as a function of floc size and frequency shown in Figure 2.16. The model was found to fit the experimental data relatively well however the model was shown to be sensitive to input parameters such as the fractal dimension, density of the sediment, sound speed, flocculation kinetics and particle size distribution with the resulting variation due to these uncertainties indicated by the grey area in Figure 2.16.

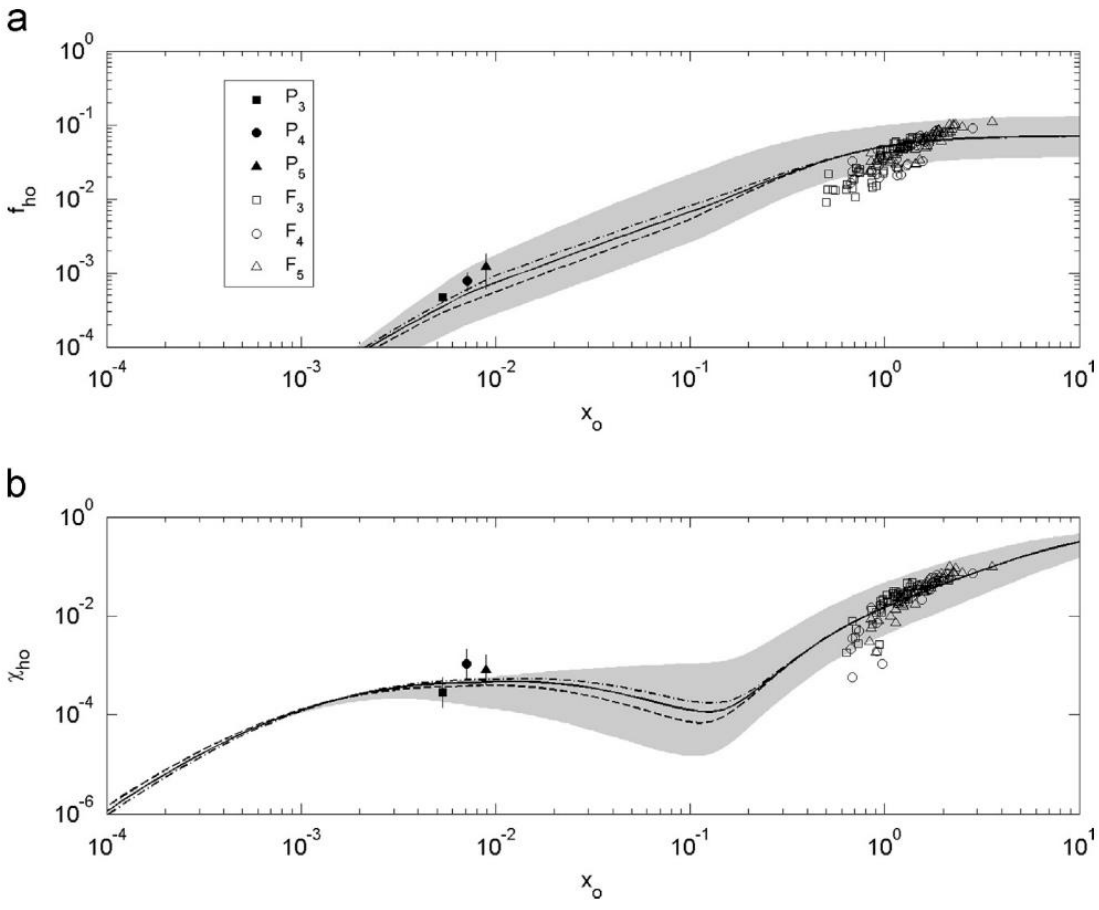

Figure 2.16 Comparison of the model output with the measurements taken from Thorne *et al* [47]. In the legend for the measurements P refers to primary particles, F to flocs and the subscript is the acoustic frequency in megahertz. The three lines are the modelled scattering characteristics at 3.0 MHz (– –), 4.0 MHz (-–) and 5.0 MHz (– • –)

2.3.10Hybrid scattering model

In order to model flocculated particle acoustic parameters from unflocculated primary particles to large, low-density flocs Thorne *et al.* [47] first expressed the density and

compressional wave speed of the scatterers as a function of the particle size. The density of the floc, $\rho(a)$, at a given particle size, a, is given in Equation 2.54.

$$\rho(a) = \frac{C_f}{a^m} \quad \textbf{2.54}$$

C_f (kg m$^{(m-3)}$) and m vary depending on the process of flocculation [201]. C_f is found by empirically fitting combined size and settling data [47], [200]. C_f is empirically fitted to the combined size and settling data [47], [200] and comparing to Equation 2.2 (Section 2.2.3). It can be seen that C_f captures the density of the sediment and the primary particle size while m is a measure of the fractal dimension. Once the floc density is known the density ratio between the particle and fluid, γ, and the porosity of the floc, ϕ, can be found. Following this the ratio of the sound velocity in the scatterers to that in the fluid, $\zeta(a)$, can be defined using Wood's [202] equation by assuming the solid and water components contribute to the bulk compressibility in proportion to the porosity of the particle, ϕ [47], [143], [204], [205], shown in Equation 2.55.

$$\zeta(a) = \frac{1}{c_{\mathrm{w}}}([\phi\kappa_w + (1-\phi)\kappa_s][\phi\rho_w + (1-\phi)\rho_s])^{-\frac{1}{2}} \quad \textbf{2.55}$$

Where κ_s, κ_w, ρ_s and ρ_w are the compressibility and density of the sediment and water and c_{w} is the speed of sound in water. For both the sediment and water it is assumed that the compressibility is given by $\kappa = 1/\rho c^2$. While this assumption is not technically correct for the solid primary particles it causes $\zeta(a)$ to approach the correct value as the porosity approaches zero and results in similar predictions between the Hybrid model and the solid particle scattering model for primary particulates. When performing model calculations, the maximum density is set to be that of the solid primary particulates and the minimum density set at 1020 kg m^{-3} (as defined by Thorne *et al*. [47]).

Having defined the sound speed ratio and density in the particle as a function of floc size then the scattering cross section, χ (Equation 2.58), and form function, f (Equation 2.59), are calculated firstly by using expressions from Medwin and Clay [206] (originally given by Johnson [203]) to find the corresponding constants, $k_{f\alpha}$ and k_{ff} (Equations 2.56 and 2.57) that represent the change in floc acoustic scattering and attenuation parameters with sediment density, compressibility, porosity and compressive wave speed under the assumption that the flocs act as fluid scatterers. These constants are subsequently used in heuristic expressions for χ and f, that are

otherwise a function of *x* (the product of the acoustic wavenumber, *k*, and the particle radius, *a*). The subscript "fi" indicates an irregular fluid sphere

$$k_{ff} = 2\left(\frac{\gamma\zeta^2 - 1}{3\gamma\zeta^2} + \frac{\gamma - 1}{2\gamma + 1}\right) \quad \textbf{2.56}$$

$$k_{f\alpha} = 2\left(\left(\frac{\gamma\zeta^2 - 1}{3\gamma\zeta^2}\right)^2 + \frac{1}{3}\left(\frac{\gamma - 1}{2\gamma + 1}\right)^2\right) \quad \textbf{2.57}$$

$$f_{fi} = \frac{k_{ff}x^2}{1 + \varepsilon_1 x^2} \quad \textbf{2.58}$$

$$\chi_{fi} = \frac{k_{f\alpha}x^4}{1 - \varepsilon_2 x + \varepsilon_3 x^2 + k_{f\alpha}x^4} \quad \textbf{2.59}$$

The values used for the coefficients ε_1, ε_2 and ε_3 used in the study by Thorne *et al.* [47] were 1.2, 1.0 and 1.5 respectively but it was stated that these values may depend on floc structure and their variability is still to be determined. Values used for the coefficients ε_1, ε_2 and ε_3 were determined by Thorne *et al.* [47] by fitting the produced heuristic form function and scattering cross-section to the fluid sphere model from Anderson [172] between $x = 0.2$ and $x = 2$. The form of the heuristic expressions used are similar to the form of those described by Thorne and Meral [48] (Equations 2.24 and 2.25) for irregular elastic scatterers (i.e. non-cohesive sediment) that is hereafter referred to as the Solid Scattering Model. It should be noted that this is not the same model used from Betteridge *et al.* [159] as that model was developed for spherical glass spheres. The Hybrid model therefore represents both the solid particle scattering characteristics for small particle sizes and transitions toward modelling a fluid sphere as the particle size increases and more water is incorporated into the structure of the modelled floc particle. With increased water content the sound speed ratio in the floc and hence the acoustic attenuation decreases. As viscous absorption also becomes significant for small particles, such as the unconsolidated sediment, Urick's [143] model can be used to calculate an additional viscous cross section term to be summed with the scattering attenuation term to correctly estimate the total attenuation at all particle sizes and porosities.

2.3.11 Flocculi Model

Utilising the same data as MacDonald et al. [166], however, Vincent and MacDonald [120] proposed their "flocculi" model when they found that data from the forward-scattering light device (LISST-100) gave particle sizes three times smaller than that of a camera for flocculated particles and inversion of the ABS data gave particle sizes similar to those seen by the LISST (see Figure 2.5). This phenomenon had been seen previously by Graham [10] with a high resolution holographic camera and by other authors [121], [122]. Hence it was proposed by Vincent and MacDonald [120] that both the light and ultrasound were interacting, not with the whole structure of the floc, but with flocculi that are the small, tightly-bound aggregate structures that comprise the floc macrostructure.

If the flocculi theory is correct however, viscous absorption will be relevant as these aggregates were shown by Vincent and MacDonald [120] to be most accurately modelled when it was assumed that they have acoustic properties and density close to that of the bulk sediment. Indeed, it was found that the attenuation of sound with range through their laboratory suspensions was consistent with the values predicted by Urick [143] for particles of the size and density of the flocculi/aggregates and so should be considered in future work if it is confirmed that the acoustic scattering is due to these aggregates. Although the correlation coefficient was typically only 0.44-0.49 when correlating the ABS size data with the LISST-100, if the model proposed by Vincent and MacDonald is correct then the structure of the larger macro flocs would not need to be preserved during sampling as the aggregate structure would still remain intact due to its robust nature [120].

If viscous interactions were to prove significant for primary particles that make up the floc then the reduction in attenuation typically seen on flocculation may be explained by the overlap of viscous layers with floc causing a reduction in the attenuation [207]. This phenomenon, that has been modelled by Forrester and Pinfield [207], would possibly explain the results seen by MacDonald *et al.* [166] where flocs attenuated less than solid particles of the same size but tended toward similar values at large floc sizes. The reason being, that beyond a given floc size the spacing within the floc will be equal to the spacing between floc interfaces [198] and could therefore be expected to attenuate in a similar manner to a deflocculated suspension of the same mean size

of the individual floc constituents (termed flocculi by Vincent and MacDonald [120]). For denser aggregates that are typical of bridging flocculation, common in both natural [21], [208] and industrial [63], [126] processes, this will not be true and remains a subject for further investigation.

2.3.12 Laboratory Based Studies for Non-Cohesive Sediments

The use of ABS to study non-cohesive sediment has been greatly expanded over the past 20-30 years. Presented here, therefore, is a brief review of the laboratory-based studies and techniques used by previous authors to quantify the scattering and attenuation parameters of non-cohesive sediments and the relevance of their results to those that will be gathered in Chapter 3. According to the single-scattering model derived by Thorne and Hanes [33], if particle scattering properties remain constant with distance, the decay of the acoustic signal caused by the sediment should vary linearly with concentration and the sediment attenuation coefficient, ξ, an intrinsic particle property, so long as multiple scattering effects are not significant. The limit of this predicted linear relationship between the particle concentration and acoustic attenuation has been a subject of study for many groups [6], [134], [137], [141], [148], [149], [156], [160], [209]. Due to non-spherical spreading of the acoustic beam in the near-field, Downing *et al.* [163] developed a dimensionless correction factor based on the transducer radius and isonification frequency to be integrated into a model by Thorne and Campbell [210], originally based on work by Sheng and Hay [148]. Further studies on the near-field correction are mostly limited to weapons detection systems [211] however its accuracy is important for pipe flow [15], bedform [3] and in-line mixing [212] studies where taking measurements close to the transducer is unavoidable due to access restrictions or unpredictable sediment fluxes.

At high concentrations relevant to engineering systems, inter-particle distance decreases and multiple scattering effects therefore increase, causing deviation in the linearity of attenuation with concentration that is predicted by single-particle scattering models such as the Faran [194] or ECAH [144], [146] models. Ma *et al.* [213] modelled the effect of multiple scattering by extending Twersky's multiple scattering formalism [214] to elastic scatterers in water and found that the predicted attenuation increased up to 17 %v/v (for $a = 2\text{-}4\ \mu m$, $ka = 0.1$, where k is the acoustic wavenumber) before reaching a maximum and decreasing thereafter.

Similar trends that see the attenuation term increase linearly and reach a peak at a certain concentration before decreasing have been observed by a number of other authors [136], [139], [141], [215] and it is normally attributed to an increase in either multiple scattering or inter-particle effects, in cases where overlap of thermal or viscous layers (termed inter-particle effects here) around the particle cause model deviations or multiple scattering becomes significant [17], [138], [216]. It should be noted that for the larger particle systems (> ~30 μm) in these studies a decrease in attenuation is not seen until much higher concentrations. The non-linearity between attenuation and concentration was observed by Hipp *et al.* [139] to become more pronounced at low *ka* values. Thus indicating that, as *ka* increases and scattering attenuation becomes dominant over viscous attenuation [166], these inter-particle effects are less pronounced extending the linear concentration limit.

For scattering attenuation, which is the increasingly dominant mode of attenuation as *ka* increases toward unity [217], it was found by Masao [218] that multiple scattering effects became prevalent for $ka > 0.5$ in a glass bead system at high solids volume fraction (~0.6) when calculating the attenuation using their modified Biot model [219]. It was also found by Shukla *et al.* [136] that for glass beads in oil and water the attenuation was linear up to higher concentrations for lower values of *ka*. While this would appear to contradict the result found by Hipp *et al.* [139], where a greater linear region was observed at higher *ka* values, the results from Hipp *et al.* were attributed to overlap of thermal and viscous layers between particles as a result of the small particle sizes used (0.1 – 1.2 μm) (termed "particle-particle interaction" by Hipp *et al.* [220]) while the results from Shukla *et al.* [136] were taken for larger particles (43 – 114 μm) that lay within the scattering regime. For particles in the scattering regime Duhkin and Goetz [221] have shown that particle-particle interaction effects are minimal up to 40% v/v and so Shukla *et al.* [136] concluded their results to be caused by a shift in the frequency peak of the received signal due to attenuation of higher frequency components of the transmitted signal. Multiple scattering also causes spreading of the acoustic signal over the time-domain [222] and it was found by Page *et al.* [223] that for transmission measurement through packed beds of glass beads the received pulse was spread over a much larger time domain indicating the long path lengths travelled by the multiple scattered wave and that such an effect was well predicted using a diffusion model. An extensive review of the literature and

models concerning multiple scattering and inter-particle effects is given by Challis *et al.* [11] and modelling results for a number of models [216] and experimental validation by Hipp *et al.* [139].

Weser *et al.* [46] have found success in modelling multiple scattering using a simple semi-empirical approach based on the work of Mo and Cobbold [192], to relate the maximum backscattered amplitude to particle concentration. Using a packing factor based on pair-correlation theory [193] the effective volume of the particles is calculated from a hard sphere packing assumption and corrects the linear relationship with particle concentration predicted by Faran's [194] single particle scattering model. The predicted backscatter amplitude increases rapidly up to 10 vol. %, reaches a maximum value at ~13 vol. % followed by a decrease at higher concentrations as opposed to the linear increase with particle concentration predicted by single particle scattering models as has been observed by Hunter *et al.* [160] in dispersions of spherical glass beads. The model assumes no far-reaching non-viscous interactions such as those caused by an electric double-layer and spherical particles that do no inter-penetrate. Measurements performed by Weser *et al.* [46] on glass beads in water showed good agreement with theory up to 30 %v/v for $0.1 < ka \leq 1$ using a single broadband transducer pulsed at 6, 10 and 14 MHz. As the model requires the attenuation to be negligible, however, only the peak backscatter amplitude can be used, and so only a single point measurement close to the transducer is possible.

As the backscattered signal is affected by both particle concentration and particle size, one must either be measured independently or assumed to determine the other. A number of possible inversion techniques are discussed by Thorne and Hanes [33] for both single [2], [153] and dual frequency cases [182], based on previous work [2], [148], [153], [162], [182], [210] provided measurements are taken when the acoustic scattering regime is Rayleigh (the product of the wave number of the ultrasound, k, and the particle radius, a, must be less than 1). In order to invert a received voltage to a concentration profile, the system gain constant, particle backscattering and attenuation coefficients must be known, as they are all contained in the expression given by Thorne and Hanes [33] for the received backscatter voltage as a function of distance and concentration [48]. A calibration method for determining the constant that captures the inherent gain of the electronic system, k_t, is provided by

Betteridge *et al.* [159]. Heuristic expressions for form function and scattering-cross section coefficient of glass beads are provided as a function of particle size and isonification frequency (Section 2.3.1, Equations 2.20 and 2.22) which allow for calculation of k_t by taking calibration measurements at known, low concentrations where the single particle scattering model is accurate. A number of alternate empirical formulations exist for natural sediments to account for variability in particle composition, shape and size distribution [48], [148], [174], [175], [224]. If viscous losses are to be accounted for (when $ka << 1$) then Urick's model [143] for viscous absorption may be used to calculate an additional viscous attenuation term which is added on to the sediment attenuation predicted using the heuristic models.

Rice *et al.* [15] provided an experimental calibration method for determining the attenuation coefficient of arbitrary sediments by taking acoustic measurements at just a few fixed concentrations in homogeneously mixed suspensions referred to hereafter as the "Extended *G-function* method". Similar methods that involve taking the slope and intercept of the logarithm of the product of the backscatter voltage and receive distance have also been used by other authors to estimate the attenuation and scattering parameters of the system [1], [166]. Such methods therefore eliminate the need to estimate the sediment attenuation coefficient based on particle size using heuristic expressions [17]. The Extended *G-function* method, however, has the additional advantage of allowing measurements at multiple concentrations to be corroborated and allows for more accurate determination of the attenuation coefficient. The Extended *G-function* method has been applied previously by Bux *et al.* [6], [17] to aid in measurement of the jet impingement, suspension and settling dynamics of barytes in a 2.5 m high and 2.6 m wide tank and for a range of organic and inorganic particles of various sizes in a smaller (0.3 m wide 0.8 m high) calibration tank. Bux *et al.* [17] also present a novel calibration process in which the attenuation coefficient is found using the Extended *G-function* method and a heuristic expression used to find the backscattering constant from which their dimensionless equivalents the scattering cross-section, χ, and the form function, f, can be calculated. These values are then used with the experimental voltage profiles to find the transducer constant for the system. The effect of density normalisation when comparing experimentally determined backscatter constants and attenuation coefficients to the heuristic values predicted by Betteridge *et al.* [159] and Thorne and

Meral [48] was subsequently investigated by Bux *et al.* [17]. The form function results were found to align well, however scattering cross-section data at low particle sizes and frequencies was less consistent and variation was attributed to increasing viscous attenuation effects not accounted for in the heuristic expressions [17]. Nevertheless, acoustic properties for a range of particle types for which $0.01 < ka < 1$ were obtained with relatively few calibration measurements and evidence of both viscous and thermoacoustic attenuation regimes were able to be identified for the relevant particle systems.

If sediment backscatter and attenuation parameters are known then the dual-frequency method proposed by Bricault [161] can be utilised. The dual-frequency method eliminates the cumulative error in the far-field caused by the attenuation error feedback with distance along the profile associated with the single-frequency approach [33]. The dual frequency method has been applied by Rice *et al.* [15] for 41 and 71 μm diameter spherical glass particles up to a concentration of 250 kg m^{-3} and for 468 and 691 μm diameter irregular plastic particles up to 150 kg m^{-3} in pipe flow and by Hurther *et al.* [13] in tank measurements of 126 μm diameter sand particles up to 60 kg m^{-3} using a single probe pulsed at multiple frequencies. For the method to be applicable, the smallest of the two frequencies used must lie within the Rayleigh regime, where the attenuation coefficient varies strongly with frequency, as additional error is introduced into the calculations as the ratio of the attenuation coefficients at the two frequencies used approaches unity [15]. An acceptable attenuation ratio has been shown to be obtained readily for frequencies of 1 to 5 MHz and for fine to coarse sand up to a mean diameter of 250 μm [15].

An alternate, multi-frequency method has also been proposed recently by Wilson and Hay [225], referred to as a statistical method, that involves calculating a time-averaged background state for the measured system with acoustic constants and received echo-voltage modelled using empirically modified forms of the equations given by Moate and Thorne [224]. To define the time-averaged background state values the particle size and concentration are assumed as unknowns and the particle size assumed to be constant with distance. The value for the background state particle size is estimated by minimising the sum of the error between the observed and predicted voltage ratio (i.e. a cost function) for all possible frequency pairs. The

background state concentration value is then found by minimising the cost function for the observed and modelled voltage in the same way for each individual frequency. This is an adaption of the "ratio method" originally proposed by Hay and Sheng [182]. Once the time-averaged background state is calculated a tangent-linear model is used to define the change in the observed echo-voltage for a given change in concentration and particle size using Jacobian matrices. The cost function containing the difference between the observed and time-averaged echo-voltage, particle size and concentration can then be defined and minimised to find the time-dependent values for concentration and particle size. Constraints containing expected deviation from the time-averaged background state are used for the voltage, concentration, and particle size to dampen the effect of non-physical errors and account for inherent variability due to instrument noise, smoothness of the spatial profile and time-dependent variation in the observed particle size. Although the statistical model is highly computationally efficient and robust with respect to errors in the input constraints, calibration of the heuristic scattering model was required, and significant variation was seen in the inverted particle size results. The statistical method was also able to overcome the instability seen in single-frequency inversion methods for measurement of a sediment laden jet at high concentrations where the large attenuation component contributes to errors in the single-frequency method.

2.3.13 Experimental Field Studies for Cohesive Sediments

In terms of field studies on naturally occurring flocs, of interest here due to their likely similarity to the flocs encountered in legacy nuclear wastes, many authors have investigated ABS systems, typically in combination with OBS or *in situ* light scattering, to measure floc particle size and concentration in marine environments. Fugate and Frederichs [35] provide one of the first studies that utilised both LISST, to obtain *in situ* concentration and particle size optically, coupled with ABS measurements of flocs in Chesapeake Bay (Maryland, Virginia, USA). Their results suggested that, as the ABS was largely insensitive to floc size, the constituent grains dominate the acoustic signal as opposed to the overall floc as the acoustic signal penetrates the pores of the flocs. A study by Gartner [226] showed the ability to successfully produce concentrations profiles up to 0.3 g l^{-1} for flocs in the San Francisco Bay, USA at 1200 and 2400 kHz. A field study by Guerrero *et al.* [16] using LISST and ABS at 1200 kHz. In their results they found that the negative BAR values

(the backscattering strength derivative minus the sound attenuation rate) may indicate the presence of flocs in field studies. Ha *et al.* [227] performed measurements in both the laboratory and in Mobile Bay, Alabama, USA using a 1500 and 600 kHz ABS device respectively. Their findings indicated that flocs behave more like bound particles corresponding to the size of the floc as the floc density increases and that inconsistencies in particle size inversion may be resolved by using multiple measurement frequencies. Sahin *et al.* [228] applied numerical modelling techniques and OBS devices stationed at multiple heights to correlate LISST and ABS results at 1500 kHz in Atchafalaya Bay, Louisiana, USA up to 1.5 g l^{-1}. They found that modelling the scatterers as flocs showed a better agreement with measurement results when a minor correction due to the primary particle viscous effects. In a more recent study, Sahin *et al.* [31] took measurements in the Seine Estuary using an ABS and LISST for concentrations up to 3 g l^{-1}. Results taken were found to be in good agreement with the Hybrid model proposed by Thorne *et al.* [47]. Size ranges for flocs in the above studies are highly variable. As a reference, however, typical size values given range from around 50 – 400 μm for the flocs and 1 – 10 μm for the aggregates that are typical of natural marine sediments [227], [229].

2.4 Research outlook

In this section the motivation and experiments undertaken for each chapter are briefly summarised for the reader. The single and dual frequency method for high concentration (4 %v/v for glass particles of density 2500 kg m^{-3}) have currently only been explored in pipe flow [15] and for only a single particle size and frequency pairing [14] up to 60 g l^{-1}. The results in Chapter 3 therefore investigate the concentration inversion results using both the single and dual frequency method for three sizes of glass beads that are typically used in acoustics studies due to their high acoustic contrast and predictable scattering characteristics. Narrowband transducers used during the experiments pulsed at the central (2.25 MHz) and at +/- 15 % of the central frequency so that the dual frequency method could be applied over multiple frequency pairings. Measurements were taken over a 0.3 m range to determine to ability of the ABS to produce concentration profiles over distances that might be encountered for *in situ* unit processes at Sellafield Ltd. and in mineral sludge settling systems. Sediment acoustic scattering and attenuation parameters were determined

using the method provided by Bux *et al.* [17] so that results could be compared to predictions from heuristic fits that have been derived previously for glass beads to evaluate the accuracy of the fit as a function of particle size, frequency and concentration. A novel method for revaluating the near-field correction factor that accounts for non-spherical spreading of the acoustic signal close to the transducers is demonstrated by correcting near-field results to lie on the linear slope of *G-function* vs measurement depth that is predicted by single scatter theory (Section 2.3.4, Equation 2.34) The proposed method allows for accurate correction of the acoustic signal that may account for probe surface defects caused by either damage to the probe, manufacture error or build-up of particulate or organic matter on the probe surface. As there is significant organic growth present in the legacy waste storage ponds at Sellafield Ltd. then the accumulation of organic matter on the probe may be expected for long term deployment regimes to which the proposed method provides and adequate solution even when particle acoustic properties are unknown.

There are currently no laboratory studies that have investigated the single and dual frequency inversion method for flocculated particles, that are thought to represent the legacy wastes at Sellafield Ltd. Chapter 4 therefore shows results from ABS studies on two synthetic floc systems (calcium carbonate and magnesium hydroxide flocculated with high molecular weight anionic flocculant) and one set of naturally occurring mud flocs (obtained from a pond located near a dairy farm in Appleby-in-Westmorland, UK) for solids concentrations up to 40 g l^{-1}. The optimum flocculant dose for calcite was found using focussed beam reflectance measurement to determine the dose at which floc size was largest and showed the least size change with time as this would allow for flocs to remain the same size throughout the course of the acoustic measurements with the same dose used for magnesium hydroxide due to their similar charge density. Floc and particulate acoustic scattering and attenuation parameters were estimated using the same method as in Chapter 3. The measured acoustic parameters were compared to heuristic models that independently assumed a solid particle [48] and a porous particle [47] with voidage determined by the particle size and fractal dimension that was measured using static light scattering. A wider range of frequencies were investigated than in Chapter 3 by using three probes with different central frequencies (1, 2 and 5 MHz) also pulsed at ~+/- 15 % of the central frequency. A novel method was proposed where flocculated particle size distribution

coefficient of variation (COV) and fractal dimension might be estimated by fitting the porous particle ("Hybrid") model [47] to the measured acoustic parameters across a range of frequencies so long as the mean particle size could be determined independently of ABS measurements or assumed. The scattering cross-section and form function, that determine the attenuation and scattering characteristics of the sediment respectively, collected for all particle sets in this study were also compared to evaluate the necessity and practicality of revaluating the heuristic fits used to predict these values to the data collected here.

Finally, in order to develop the ABS further as a measurement technique in hazardous or geometrically restricted environments where probe deployment *in situ* is not possible Chapter 5 investigates the ability of ABS to detect concentration changes non-invasively was of great interest. It has also been shown previously [189] that particle concentration can be qualitatively measured by corresponding changes in the decay (attenuation) of the acoustic signal with distance where the attenuation is too great to allow direct concentration inversion. Extending this method to non-invasive measurements would therefore allow for the settling dynamics in industrial processes to be evaluated without the need for invasive measurements that may disrupt the process itself. For this reason, initial ABS measurements at 1 MHz were taken horizontally from the outside of a laboratory scale thickening column (~0.8 m height, 0.3 m diameter) and at 2 MHz using a probe suspended vertically from the top of the column. A 4 %w/w calcite solution was pumped in-line with anionic flocculant into the column to produce large, fast settling flocs. The underflow was manipulated to allow a bed to form and maintained at steady state for ~2 hours. The attenuation of the ABS signal from the horizontal 1 MHz was measured and compared to the bed height and the calculated residence time at the height of the probe. Bed heights were estimated at 1 second time intervals using the bed reflection from the vertically facing 2 MHz probe and allowed for relatively accurate prediction of the output concentration from the thickening column. Additional measurements were taken in the same system for a bed that was allowed to deplete from an initially large height over the course of the experiment so that all operational cases (start-up, steady-state and emptying) could be evaluated. In this case however, both probes were placed horizontally to determine if independent ABS attenuation measurements at multiple

bed heights could be used to measure the increase in concentration that is expected at increased bed depths.

Chapter 3 Glass particle studies

3.1 Introduction

In this study, the calibration method proposed by Rice *et al.* [15] with the subsequent modification by Bux *et al.* [17] was used in order to find the backscatter cross-section, χ, and form function, f, as the method is straightforward and requires only a few measurements at known, homogeneous concentrations. It also provides a means by which to study the change in acoustic attenuation with sediment concentration so that results can be compared with literature [141], [150]. Values for f and χ were determined for three sizes of glass spheres at three frequencies by additionally pulsing the transducers at +/- 10 % of the central frequency in order to demonstrate the ability of a narrowband transducer to accurately observe changes in acoustic constants over its available bandwidth. The form function and scattering cross-section were then compared to values determined using the heuristic model from Betteridge *et al.* [159] in conjunction with Urick's model for viscous absorption [143]. The backscatter voltage responses were inverted to produce concentration profiles using the single frequency method given by Thorne and Hanes [33] and the dual frequency method originally proposed by Bricault [161] that has been utilised previously by Hurther *et al.* [14] and Rice *et al.* [15]. A novel method for determining the near-field correction factor that corrects ABS measurements taken close to the probe is demonstrated and applied to inversion results. Finally the semi-empirical backscatter power model proposed by Weser *et al.* [46] was investigated as a method for point concentration measurement at high solids content. Such studies will allow for a greater understanding of the limitations of both prediction of the acoustic constants and subsequent concentration inversion for non-cohesive sediment system using ABS so potential techniques can be identified for application to flocculated systems that might be encountered in legacy wastes at Sellafield Ltd [49].

3.2 Materials and methods

3.2.1 Materials characterisation

Three sizes of spherical glass beads (Honite 22, Honite 16 and Honite 12) purchased from Guyson International Ltd., UK [230] were used in this study as test material, as

they are ideal acoustic scatterers and both heuristic expressions [159] and experimental methods [15], [17] exist to determine their acoustic scattering and attenuation properties. Particle size was measured using a Mastersizer 2000T (Malvern Panalytical Ltd., UK) and the resulting size distributions are shown in Figure 3.1 with dashed lines highlighting the corresponding median distribution, D_{50}, values of 40, 78 and 212 µm. The distributions indicate a log-normal distribution typical of sieved sediments. The size distributions are relatively monodisperse and the coefficient of variation, (*COV*, the standard deviation divided by the mean) for each size is small. Values are shown in Table 4.1 with the largest COV (0.31) seen for the smallest particle size, Honite 22, and the smallest COV (0.27) seen for the largest particle size. Measurements were repeated three times for each particle size before taking an average of the measured distribution.

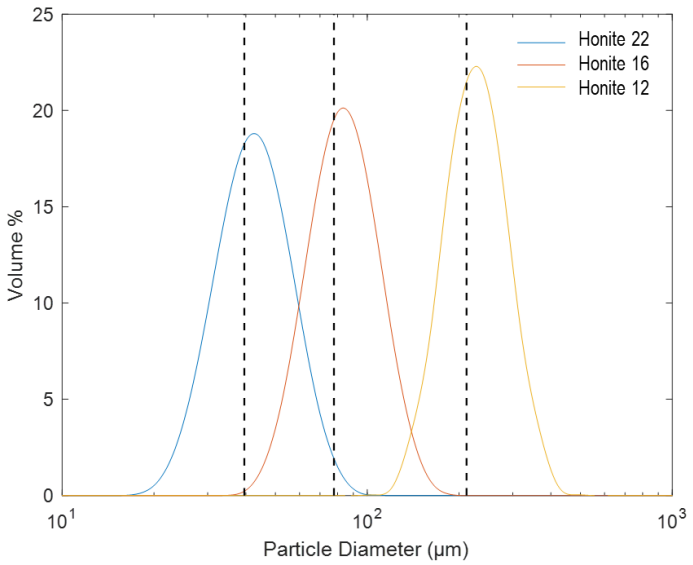

Figure 3.1 Particle size distributions for the three glass particle species used in this study

Table 3.1 Particle size data and statistics for the materials used in this study

Material Name	Particle d_{50} (µm)	Coefficient of Variation, *COV*
Honite 22	39.5	0.31
Honite 16	77.8	0.29
Honite 12	211.6	0.27

To confirm the sphericity of the Glass species SEM images were taken using a TM3030 Plus desktop SEM (Hitachi High-Technologies Corporation, Europe) and are shown in Figure 3.2. Although small surface defects and shape deviation are seen

the glass particles are highly spherical. Figure 3.2 also demonstrates the fairly significant fraction of particles smaller than the median values and the resulting coefficient of variation values for each particle set shown in Table 3.1, from the Mastersizer data (Figure 3.1).

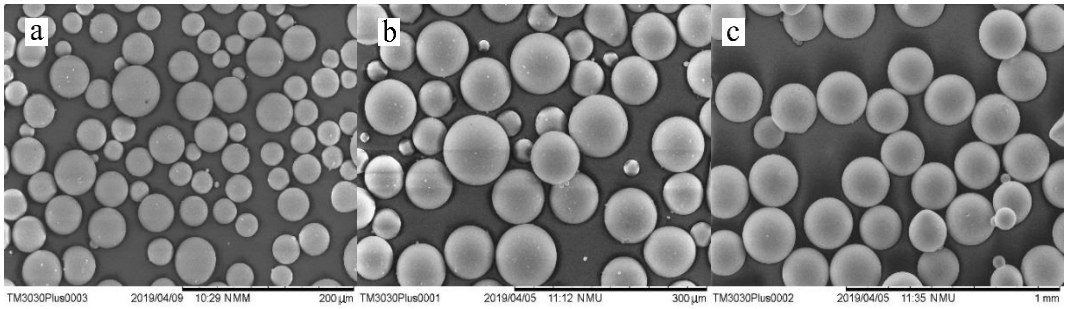

Figure 3.2 Scanning Electron Microscope image of the glass particles used in this study, a) Honite 22, b) Honite 12 and c) Honite 12

3.2.2 Experimental apparatus

The acoustic backscatter system used was a bespoke device developed at the University of Leeds; the Ultrasound Array Research Platform (UARPII-16), featuring 16 individual transducer connections [36]. A high measurement speed is necessary to achieve real-time measurement to reduce the time averaging effects inherent in taking the root mean square of multiple measurements. The data path within the instrument is pipelined such that, while a measurement is in progress, received data is stored in local memory in real-time while prior measurements can be downloaded from the instrument for analysis [231].

The UARP modules are built around an Altera Stratix V field-programmable gate array (FGPA) and feature commercial off-the-shelf transmit and receive front end integrated circuits [232]. The transmit signal used was a switched mode waveform, with five discrete voltages of -96V, -48V, 0V, 48V and 96V. Through the use of Harmonic Reduction Pulse Width Modulation (HRPWM) an excitation waveform with reduced harmonic content and time-varying frequency and amplitude can be made [37], [233].

The receive path is based around integrated analogue front-end circuits, combining multi-stage amplification, filtering, and analogue to digital conversion. High speed serial digital data is received by the FGPA and stored in local memory [232]. The UARP is controlled using a custom MATLAB (Mathworks, USA) interface. All raw

data was processed in real-time for operator feedback and archived for further offline processing [234].

Eight identical immersion transducers with a 2.25 MHz central frequency and 0.25 in. (63.5 mm) diameter elements were tested (Olympus NDT V323-SM). As an example of the system scattering regime, the corresponding *ka* values for each glass particle size studied, when insonified at the central 2.2.5 MHz frequency, are 0.19, 0.37 and 1.01, for the 40, 78 and 112 µm particles respectively. A Harmonic Reduction Pulse Width Modulation (HRPWM) algorithm was used to create three separate transmit waveforms in turn, with local central frequencies of 2.00, 2.25 and 2.50 MHz, each with Hann windowing and a 5 µs duration. The received echo voltage was recorded using 31172 points spaced over the 0.3 m range with 10,000 repeat measurements made over a 5-minute period, resulting in a ~85 dB noise floor after signal processing. An example of the excitation signal for the central 2.25 MHz frequency, as well as an example of the time-domain received signal (for the case of 78 µm particles at a nominal concentration of 2.5 g/l) are shown in Figure 3.3 below.

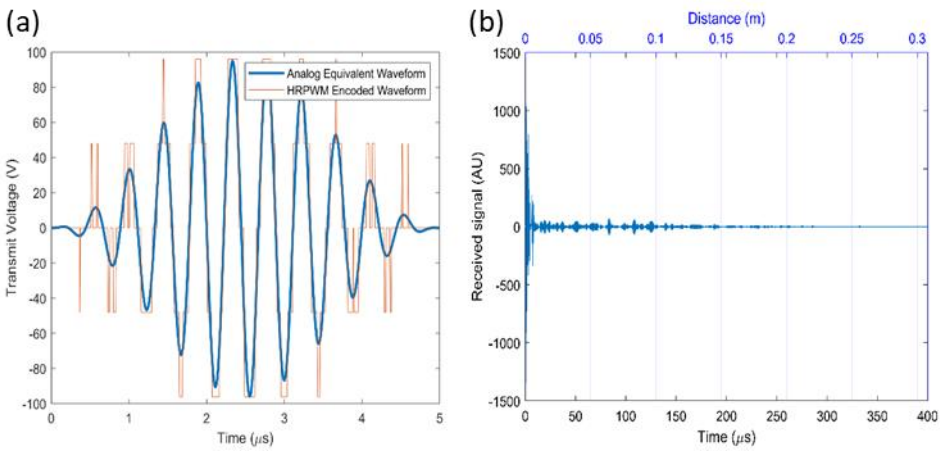

Figure 3.3 a) Excitation signal generated by the UARP at the central probe frequency of 2.25 MHz, and b) example of the time-domain receive signal from the 78 µm glass particles at a nominal concentration of 2.5 g/l (also using the central 2.25 MHz frequency).

Measurements were taken in an impeller-agitated, 0.8 m tall, 0.3 m diameter calibration tank over a 0.3 m range using eight Olympus transducers (Olympus NDT V323-SM, 0.25-inch active diameter, -90 dB noise floor) arranged in a circle, facing perpendicular to the tank base. Transducers were excited at frequencies of 2, 2.25 and 2.5 MHz for eight nominal particle concentrations ranging from 2.5 to 133.7 g l^{-1}. A schematic of the experimental setup is shown in Figure 3.4. A recirculation pump was used to redistribute suspension from the conical base of the tank to the manifold

arranged at the top of the tank to prevent particles from settling out and to ensure homogeneity. Suspension samples were taken at three depths simultaneously using a multi-headed pump, and particle concentrations determined gravimetrically (shown in Figure 3.5). It was found that in all cases, the sampled particle concentration was slightly lower than the nominal weighed concentration, likely caused by small amounts of settling in the recirculation system. Samples taken before and after each measurement did not however indicate that the particle concentration changed with time, and so the measured values were used when performing all calculations presented. No significant concentration gradient is seen with height in the column for any of the particle sizes or concentrations investigated and so it is assumed that the dispersions were homogeneous in all cases.

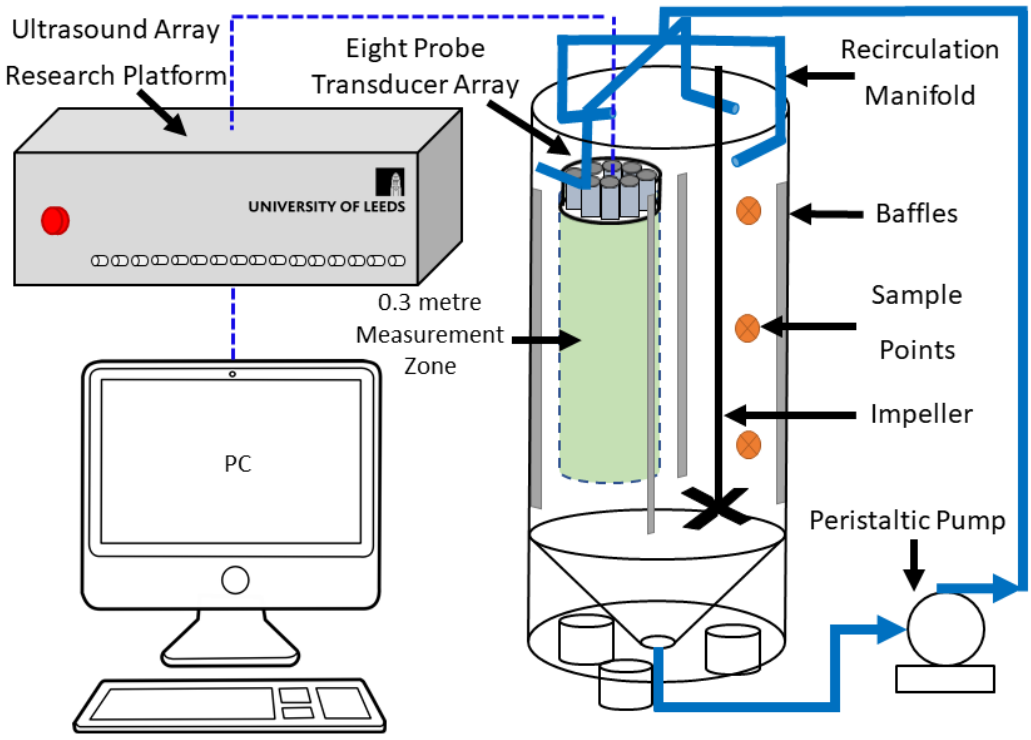

Figure 3.4 Schematic of the experimental setup used for acoustic backscatter measurements

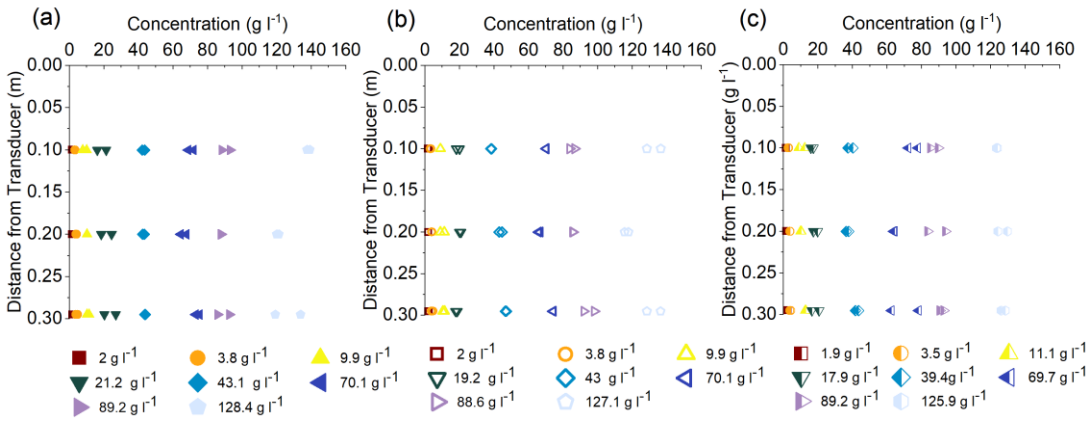

Figure 3.5 Sample values taken for a) Honite 22, b) Honite 16 and c) Honite 12 as a function of distance from the transducer. Legend values indicate the mean concentration in the tank calculated from the sample data

3.2.3 Acoustic analysis

In order to determine the acoustic attenuation constant, ξ, and subsequently the scattering cross section, χ (Section 2.3.1, Equation 2.12) for each size of glass particle the Extended *G-function* method [15] (Section 2.3.4, Equations 2.33-2.36) was used in this study as it has been applied with success previously by other authors [6], [17]. Following this, the novel process derived by Bux *et al.* [17] (Described at the end of Section 2.3.4) was used with the heuristic expression for f provided by Betteridge *et al.* [159] (Equation 2.20) to find k_t (Equation 2.32) and subsequently experimental values of k_s and the form function, f (Equation 2.9) for each experimental profile. An average value for f and χ at each frequency and particle size was then taken across the concentrations measured, so that experimentally determined values of f and χ could be compared to those predicted by the heuristic Betteridge *et al.* model [159]. This analysis method is summarised in the flowchart in Figure 3.6.

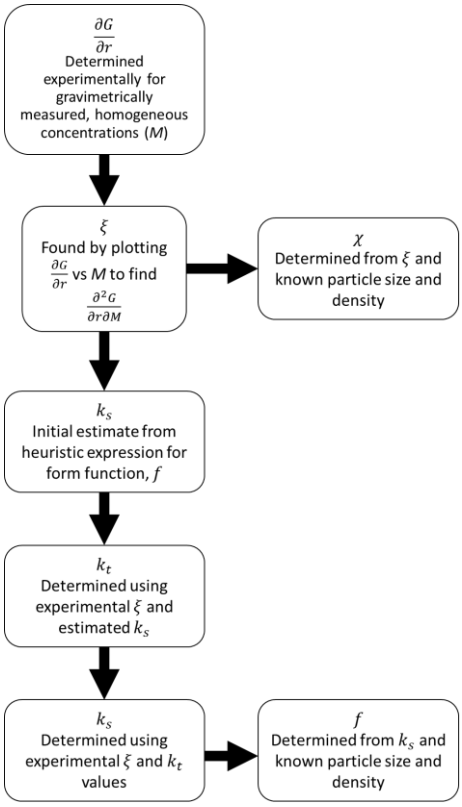

Figure 3.6 Flowchart demonstrating acoustic analysis method used in this study to find acoustic scattering and attenuation parameters for the sediments

To improve results in the near field (taken here as 14 – 57 mm from the probe face) for both the Extended *G-function* method and concentration profiling, an alternative correction factor, ψ_G, to that proposed by Downing *et al.* [163] was modelled. Due to excessive noise in the signal at distances closer to the probe measurements could not be used at distances below 14 mm and the upper distance limit of 57 mm was selected as Equation 2.8 indicated that the greatest near field distance would be 54 mm when operating the transducers at the highest frequency (2.5 MHz). ψ_G was calculated on the basis that the resultant *G-function* profile (given by Equation 2.33) would maintain the linear relationship predicted by the *dG/dr* fits when the newly modelled ψ_G was used in place of ψ. The same form of the equation proposed by Downing *et al.* [163] in terms of the ratio of the measurement distance to the near field distance, *z*, was used to fit the model parameters (a_n)) to minimise the objective function, *Z*, shown in Equation 3.1, using MATLAB with a non-linear least squares fit with a lower and upper bound of 0.1 and 10 for the model parameters. Starting points for each variable were identical to those in the original model (Equation 2.6) Subscripts *i* and *j* indicate each concentration and insonification frequency and *c* is the y-axis intercept for the *dG/dr* fits.

$$\sum_{i,j}^{n}\left[exp\left(\frac{dG_{ij}}{dr}r + c_{ij}\right) - V_{ij}r - \frac{a_1 + a_2z + (a_3z)^{a_4}}{a_2z + (a_3z)^{a_4}}\right] = Z \qquad \textbf{3.1}$$

Following the minimisation, the experimentally fitted near field correction factor is then defined as in Equation 3.2 below.

$$\psi_G = \frac{a_1 + a_2z + (a_3z)^{a_4}}{a_2z + (a_3z)^{a_4}} \qquad \textbf{3.2}$$

Single frequency concentration-distance profiles were inverted from experimental data using the iterative method described by Thorne and Hanes [33] (Section 2.3.5, Equations 2.38 and 2.39) using only a single iteration with the initial guess for the concentration set to be equal to the nominal particle concentration (confirmed from sample data). This process allows assessment of the applicability of the single-frequency inversion method for high particle concentration measurement at a range of *ka* values for each size of glass particle using a narrowband transducer pulsed at +/- 10 % in addition to its central frequency.

Similarly, the application of dual frequency method originally proposed by Bricault [161] (Equations 2.43-2.48) was also investigated as it is stated in literature to avoid cumulative errors with distance that are associated with the single frequency method [14], [15]. The dual frequency method also provides an opportunity to generate additional results by comparing signals at different frequencies as well as across co-located probes that could be used to more effectively constrain results from statistical methods [225]. To this end, the error sensitivity in the inverted concentrations using the dual frequency method was investigated as a function of the attenuation coefficient ratio based on equations derived from work by Rice *et al.* [15] (Appendix A.3, Equations A.6-A.19) so that future statistical modelling results might be made more accurate.

In order to account for multiple scattering effects at high concentration, the SEBP model taken from Weser *et al.* [46] (Equations 2.51 and 2.52) was used. As the model estimate for particle backscatter is given in terms of a relative backscatter amplitude the measured backscattered pressure (P_{RMS}) must be scaled in proportion with the

pressure of the incident acoustic wave ($\widehat{P_0}$) as well as the transducer receiver sensitivity (R) and voltage transfer function (T_v) defined by Thorne *et al.* [33] in Equation 3.3.

$$V_{rms} = R.T_v.P_{rms} \quad \textbf{3.3}$$

The incident wave pressure, transducer receiver sensitivity and voltage transfer function will be constant for the same gain, frequency and probe [33]. Equation 3.3 can then be combined with Equation 3.4 from Weser *et al.* [46] to produce Equation 3.5.

$$\Omega_\Sigma = \frac{P_{rms}}{\widehat{P_0}} \quad \textbf{3.4}$$

$$\frac{P_{RMS}}{\widehat{P_0}} = \frac{V_{rms}}{\widehat{P_0}.R.T_v} = \Omega_\Sigma \quad \textbf{3.5}$$

Therefore, by taking a least-squares, linear fit of the experimental backscatter amplitude (V_{rms}) to the relative amplitude predicted by the SEBP model (Ω_Σ, from Equations 2.50, 2.51 and 2.52) across all concentrations and frequencies an overall scale factor can be found that represents an estimate for the product of the incident wave pressure, transducer receive sensitivity and the voltage transfer function. By dividing experimental results by the newly found scale factor they can then be compared directly to modelling results and the previous results found by Weser *et al.* [46]. The relative trend between the experimental results as compared to modelled values can then subsequently be determined. As backscatter data at distances below 14 mm was found to contain significant scatter the maximum amplitude was selected between a range of 14 – 58 mm from the face of the probe after applying the near-field correction factor determined using the original equation from Downing *et al.* [163].

An estimation of the single particle scattering power, Ψ_P, is also necessary in order to model the system. For this study the scattering model chosen to compute Ψ_P was the Faran model [194] as it has been found by Fleckenstein *et al.* [157] that the Epstein, Carhart, Allegra and Hawley (ECAH) model [144], [146], Hay and Mercer model [147] (a simplified version of the ECAH model that neglects thermal effects) and Faran model all overlap for the calculation of backscatter values for glass beads in a similar *ka* range to that studied here. Furthermore, the Faran model is easy to implement, computationally efficient, numerically stable and only requires knowledge of the particle elastic properties and the sound velocity in the disperse

phase [157] and would allow direct comparison of results to those obtained by Weser *et al.* [209] in their study on a similar glass particle system.

Faran modelling was performed in MATLAB using code published by IEEE-UFFC authored by Anderson [195] in order to model the backscatter strength as a function of distance for a glass particle at an angle of 180˚ to the incident ultrasound for each particle size and frequency combination. Experimental backscatter amplitudes used for modelling with Equation 2.50 were averaged over 9.6 – 13.5 mm from the probe face due to excessive noise and model deviation at points closer to the transducer.

3.3 Results and discussion

3.3.1 Determination of acoustic constants and near field correction factor modelling

Examples of typical decibel profiles for a single probe collected with the UARP, are shown in Figure 3.7 (a)-(c) for all three particle sizes at three concentrations; measured using the central frequency of the transducer (2.25 MHz). Once outside of the near field (~0.05 m from the transducer) a logarithmic decay of the signal with distance, typical of moderately attenuating suspensions, is observed. This relationship is governed by both scattering and attenuation parameters (Equation 2.5). On a decibel scale ($amplitude\ /dB = 20\ log_{10}\ (V_{RMS}/V)$) the negative linear slope with distance is determined by the attenuation parameters and the linear decay by the scattering parameters [160]. It can be seen in Figure 3.7 (a)-(c) that the initial backscattered amplitude close to the transducer increases with particle size. In terms of Equation 2.5 (Section 2.3.1) this is due to an increase in the sediment backscatter constant, k_s, (Section 2.3.1, Equation 2.9) via an increase in the form function, f (Section 2.3.1, Equation 2.20). The attenuation also becomes larger with increasing particle size, however, and so at greater distances, where the attenuation is felt strongly, the relative backscatter amplitude is lower for larger, more attenuating particle sizes. A similar effect is seen with increasing concentration, M, as it causes both the scattering term and the exponent of the attenuation term to increase in Equation 2.5 (Section 2.3.1) leading to larger backscattered power close to the transducer and smaller backscattered power at greater distances.

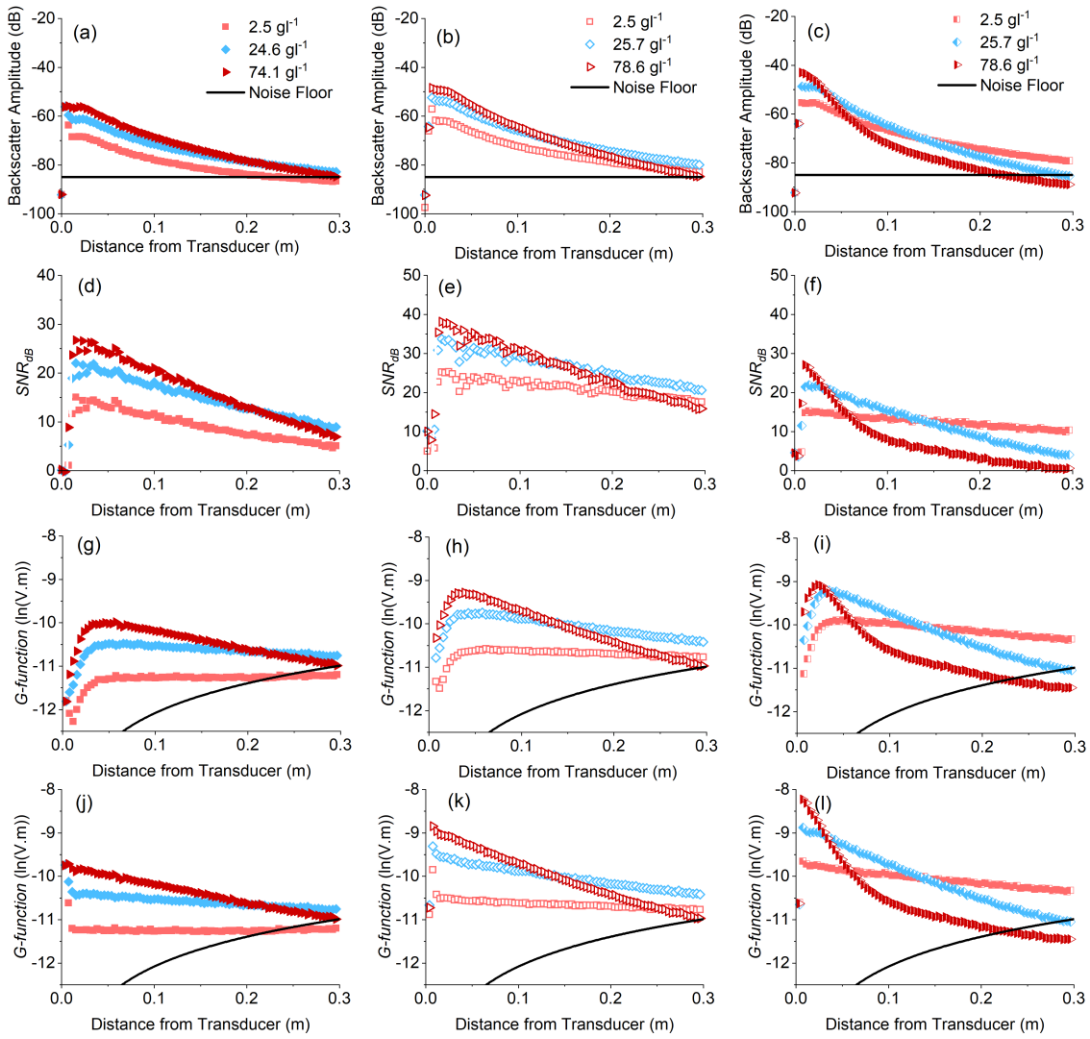

Figure 3.7 a) – c) showing decibel profiles, d) – f) signal-to-noise ratio on a decibel scale (SNR_{dB}), g) – i) showing uncorrected ($\psi = 1$) *G-function* profiles, j)-l) showing *G-function* profiles adjusted using experimentally fitted NFC (ψ_G, Equation 3.2) for Honite 22, Honite 16 and Honite 12 at 2.25 MHz

Using measurements taken at 0 g l^{-1} of sediment signal-to-noise ratio profiles were calculated and are shown in Figure 3.7 (d)-(f). In general data from Honite 16 shows the highest SNR values at a given particle concentration of the three sizes of glass particles. At low concentrations (~25.7 g l^{-1}) Honite 12 gives a similar SNR to that seen for Honite 22. For Honite 12, as the concentration and attenuation increase the SNR is seen to decrease more dramatically with distance compared to Honite 22 and Honite 16. Despite the decay of SNR with distance as concentration increases the SNR close to the transducer increases with concentration and this effect is seen across all glass particle sizes studied here for the same reasons as described for the decibel profiles in Figure 3.7 (a)-(c). Using Equation 2.33, the backscattered signals were converted to *G-function* values and are shown in Figure 3.7 (j)-(l). The expected linear relationship between the *G-function* and distance is seen outside of the near field,

confirming the homogeneity of the system [15]. Within the near-field ($r < 0.05\ m$) there is the expected reduction in the *G-function* at distances close to the transducer when no near field correction factor (i.e. $\psi = 1$) is applied due to non-spherical spreading of the acoustic signal in the near field causing backscattered power to be reduced [163]. Very small positive *G-function* slopes are also seen for the lowest concentration of Honite 22, likely due to a low signal to noise ratio caused by the decreasing backscattering constant, k_s, as particle size is decreased [33].

For Honite 12, above ~70 g l^{-1}, there is notable change in the slope of the *G-function* with distance at ~0.09 m. It would appear from results presented here that below a *G-function* value of around -11 non-linearity of the backscattered signal with distance occurs. Below this value it is possible that, as a logarithmic decay of the decibel profile is required to produce linear *G-function* profiles, the approach of the noise floor limits this decay and causes the non-linearity observed in the *G-function*. Indeed, a decrease in the signal-to-noise ratio with increasing concentration (and hence attenuation) has been observed previously by other authors [188], [235] and is attributed to the fact that the attenuated signal will be sensed by the transducer as an incoherent signal (i.e. additional noise). This may also explain the non-linearity observed for Honite 22 at low concentrations despite the attenuation being relatively small as the low scatter strength of Honite 22 will also negatively impact the signal-to-noise ratio.

It may also be possible that because of the high concentration the inter-particle distance is smaller and significant multiple scattering of the compressional wave between particles begins to occur [214]. The coherent multiple scattered signals detected by the transducer will have a longer path length than the single-scattered signal. This coherent signal may effectively be sensed as an echo from a greater distance for a backscatter setup as the received signal is transformed from the time domain to the distance domain by assuming a constant speed of sound (1454 m s^{-1}) and a direct path away from and back to the transducer (i.e. $measurement\ distance = \frac{c\Delta t}{2}$ where c is the speed of sound and Δt is the time delay between transmit and receive of the acoustic pulse). leading to the observed decrease in attenuation at greater distances. As the primary mode of attenuation for large particles, where *ka* approaches 1, is scattering attenuation (as opposed to primarily viscous attenuation as *ka* approaches zero) then this result may be expected. For the

larger particles the multiple-scattered signal would be larger due to the higher particle scattering coefficient and will not be limited to the viscous boundary layer width [149] and therefore allowed to propagate through the solution and back to the transducer. Spreading of the received acoustic signal over a greater time domain (equivalent to distance in this experimental setup) has been observed over very short distances (~10 mm) in transmission setups by other authors [222], [223] for larger glass beads at higher concentrations. In a larger scale backscatter setup, however, Tourin *et al.* [236] have also shown that in multiple scattering media (over a measurement distance of 8 cm) a coherent scattered wave that was most prominent in the backscattered direction was observed at multiple record times for steel rods suspended in water insonified at 3.2 MHz. It may even be possible that viscous attenuation effects are contributing to a decreased attenuation with distance in a similar fashion. The effect of incorporating second order multiple scattering, in which shear waves are partially converted to compressional waves, has been shown by Pinfield and Forrester [237] to cause a reduction in attenuation that is further enhanced at high concentrations that may also explain the decreased attenuation at higher concentrations seen in Figure 3.7 (l).

To improve *G-function* fits in the near field, an alternative correction factor, ψ_G, to that proposed by Downing *et al.* [163] was modelled as detailed in Section 3.2.3 using Equation 3.1. The newly modelled near field correction factor Ψ_G (shown in Figure 3.8) was used to improve the *G-function* fits in the near field region and the corrected *G-function* profiles, as shown in Figure 3.7 (j)-(l). The fitted correction factor noticeably improves the fit in the near-field region and would therefore allow for more accurate determination of the *G-function* in applications where dispersion attenuation or physical geometry limits the available measurement range. It should be noted that the original model proposed by Downing *et al.* [163] was also effective in improving the fits, and only a small difference in seen in the corrected profiles (profiles corrected with the Downing *et al.* [163] correction factor are shown in Appendix A.2, Figure A.2).

Figure 3.8 (a)-(c) shows the fitted data used to produce Ψ_G. Data for certain probes/ concentrations were omitted when the data lay outside twice the root-mean square error of the initial model fit. Data above concentrations of ~70 g l^{-1} was excluded

manually for the fit as it was found to predict significantly lower values for ψ_G compared to other particle sizes and concentrations. Comparison to the NFCF model proposed by Downing *et al.* [163] (Section 2.3.1, Equation 2.6) is shown in Figure 3.9. A good general agreement is shown with both the original model and the form of the equation taken from Downing *et al.* [163] (Section 2.3.1, Equation 2.6) and confirms the necessary normalisation of the measurement range, r, to the near-field range, r_n (Section 2.3.1, Equations 2.8). From Figure 3.9, it can be observed that ψ_G is consistently above the value predicted by the original NFCF equation. The cause of the deviation is likely due to small imperfections in the transducer shape and surface affecting the near-field spreading characteristics of the acoustic signal. As expected, ψ_G is not seen to vary with particle size [163], and an overall model, fitted to data from all three particle sizes, was used to correct the *G-function* values shown in Figure 3.7 (g)-(i). As fitting of the model was not computationally intensive and was easily implemented using the MATLAB curve fitting package it is recommended that the NFCF fit method presented here is incorporated whenever a *G-function* calibration is performed for a given set of probes if measurements in the near-field are to be used for further analysis. This would account for determination of the form of the NFCF for probes, where the transducer face dimensions are not known or deviate from the circular face used for determination of the original NFCF by Downing *et al.* [163]. This procedure would subsequently improve measurements in zones close to the transducer such as in pipe flow applications [15], [138] and when taking backscatter measurements in highly attenuating or concentrated dispersions [160], [189].

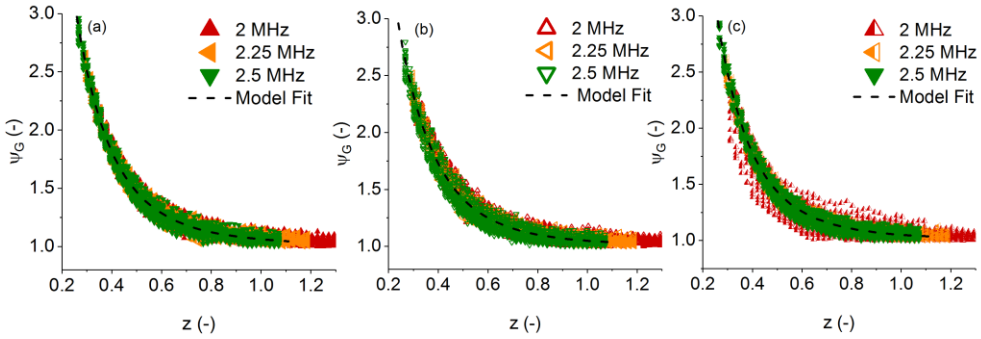

Figure 3.8 Fitted Near Field correction factor model for a) Honite 22, b) Honite 16 and c) Honite 12

Table 3.2 Coefficient values for Ψ_G fits compared to the original model from Downing *et al.* [163]

	a1	a2	a3	a4
Honite 22	1.18	1.53	2.37	3.31
Honite 16	1.05	1.74	2.30	3.55
Honite 12	1.13	1.50	2.39	3.49
Downing *et al.* Model	1.00	1.35	2.50	3.20

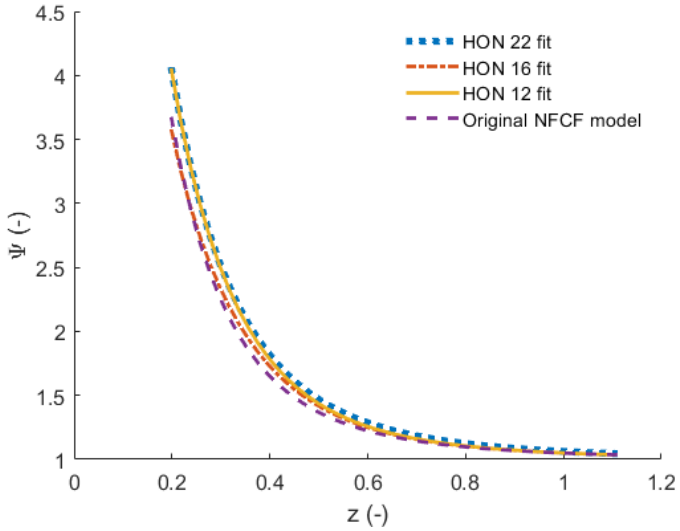

Figure 3.9 Comparison of fitted NFCF against Downing, Thorne and Vincent model for Honite 22, Honite 16 and Honite 12 [163]

dG/dr values are shown in Figure 3.10 , with dashed linear interpolations indicating the fits taken to find the attenuation coefficient (Equation 2.34). Due to non-linearity between *dG/dr* and concentration in data obtained for the Honite 12 system the highest three concentrations were excluded when determining the attenuation coefficient. *dG/dr* values were determined by assessing the gradient of the *G-function* profiles (Figure 3.7) between 0.05 – 0.24 m from the transducer. The fit distance was adjusted to obtain the most negative value for the gradient while maintaining a minimum fit range of 0.05 metres and ensuring that data below the noise floor (set as -85 dB to provide a 5 dB safety margin) were excluded. The most negative value of the gradient was sought for two reasons. Firstly, to attempt to minimise the occurrence of positive values for *dG/dr*, seen for Honite 22 at the lowest concentration, as these are not physically real but a result of a low signal to noise ratio. Secondly, to minimise the effect of multiple scattering on the attenuation at greater distances, seen for Honite 12 at high concentrations. Although the correlation coefficients for *dG/dr* fits were low

when the attenuation was small (as the relative change in the signal must be large compared to the noise) the R^2 value was commonly above 0.99 for intermediate and high concentrations.

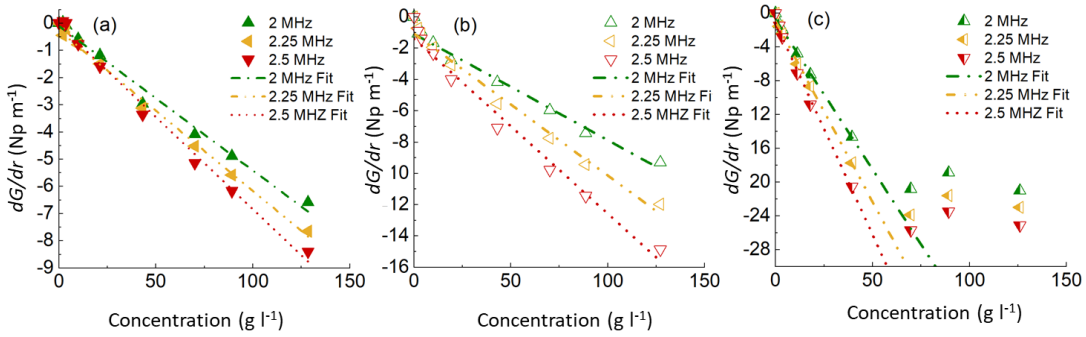

Figure 3.10 *dG/dr* vs concentration plots to allow determination of attenuation coefficient of a) Honite 22, b) Honite 16 and c) Honite 12 (last three points of Honite 12 data not used for fit)

The expected linear slope is seen over all concentrations for Honite 22 and Honite 16 and linear fits generally had R^2 values of ~0.99 while Honite 12 had values ~0.92. With respect to the Honite 12 results (Figure 3.10 (c)), there is a clear concentration limit at which the measured attenuation is no longer proportional to concentration. A similar concentration limit in transmission measurements has been observed by both Stolojanu and Prakash [141] and Atkinson and Kytomaa [150] for glass particles in water, as well as other authors for differing particle systems [11], [136], [139], [151] and is widely attributed to an increase in multiple scattering effects [138]. It is also noted that both authors [23], [32], observed an increase in this non-monotonic behaviour as *ka* increases towards unity, an effect also observed in the experimental results in Figure 3.10. As discussed previously, there is also a change in the gradient of *G-function* with distance (Figure 3.7 (l)) that may also be an indication of strong multiple scattering effects.

For the multiple scattered signals to contribute a significant amount to the recorded signal, the attenuated portion of the signal (some fraction of which is subsequently multiple scattered) must be large when compared to the portion that is backscattered. When the attenuation due to water is small, the exponential term in Equation 2.5 (Section 2.3.1) effectively gives the fraction of the backscattered signal that is not scatter-attenuated and is received by the transducer, while the remaining portion is scattered into the surrounding medium. Therefore, when the value of the exponential

term approaches 0 (i.e. when the attenuation term is very large) multiple scattering effects would be expected to occur and would increase with concentration, distance, and sediment attenuation, as can be observed in Figure 3.10. It is proposed here that the decreasing linearity of attenuation with concentration at high solids loading is caused by incoherent multiple scattering leading to a decrease in the signal-to-noise ratio at greater distances from the transducer, thereby causing the non-linearity of the signal and the observed reduction in attenuation at greater distances.

Having found the attenuation coefficient from the straight-line fits in Figure 3.10, the Extended *G-function* method (described in Section 2.3.4) was then applied. Equation 2.32 was therefore used to obtain distance profiles of the transducer constant, k_t, for the lowest two particle concentrations (2.5 and 5 g l^{-1}). Theoretically, the transducer constant will not vary with distance and is only plotted as a function of distance here so that the validity of Equation 2.5 to model the system can be checked and to determine an appropriate range of distance and concentration values to average for an overall estimate of the transducer constant for each probe and frequency. Measured sample concentrations for the experiments were used in conjunction with the measured attenuation coefficient and a heuristically estimated scattering constant from the Betteridge *et al.* [159] correlations. The k_t profiles were concentration and distance averaged 0.1-0.3 m from the transducer to avoid any potential near-field effects. Having found k_t, Equation 2.32 was rearranged so that k_s profiles could be recalculated using the nominal concentration and attenuation coefficient. As k_t and k_s are calculated through the same equations and set of experimental values they inversely proportional and will follow the same trend with distance when one of them is assumed to be constant. Example profiles are provided in Appendix A (Figure A.1) for completeness, shown over the range for which k_t was calculated.

Figure 3.11 shows the calculated k_s as a function of distance for each particle size at the central frequency for a single probe as an example calculated using the Extended *G-function* method (See Section 2.3.4). Although it should be constant with range according to Equation 2.5, k_s is seen to increase exponentially with distance at higher concentrations for the 212 μm glass particles and a less drastic but similar trend is seen for both 40 μm and 78 μm glass particles. A likely factor contributing to this effect is the overall decreased contribution of the scattering term to the backscattered

signal as attenuation effects begin to dominate. Small errors or deviations in the estimation of the attenuation coefficient can therefore cause large deviations in the calculation of k_s at high concentrations, as any deviation in the attenuation coefficient, ξ, will be multiplied through by the concentration value (having substituted Equation 2.35 into Equation 2.5). The increase of k_s with distance therefore suggests that either the attenuation term has been overestimated at these distances or that an un-modelled effect is causing the scattering signal to increase with distance and concentration in an unexpected fashion. As proposed earlier, multiple scattering may be pronounced for highly scatter-mode attenuating particles causing the observed attenuation (assumed to be constant for calculation of k_s) to decrease with distance, seen in the *G-function* results for Honite 12 in Figure 3.7 (f). This would subsequently cause the overestimation of the attenuation at greater distances causing the non-linearity in k_s to become more pronounced at higher concentrations.

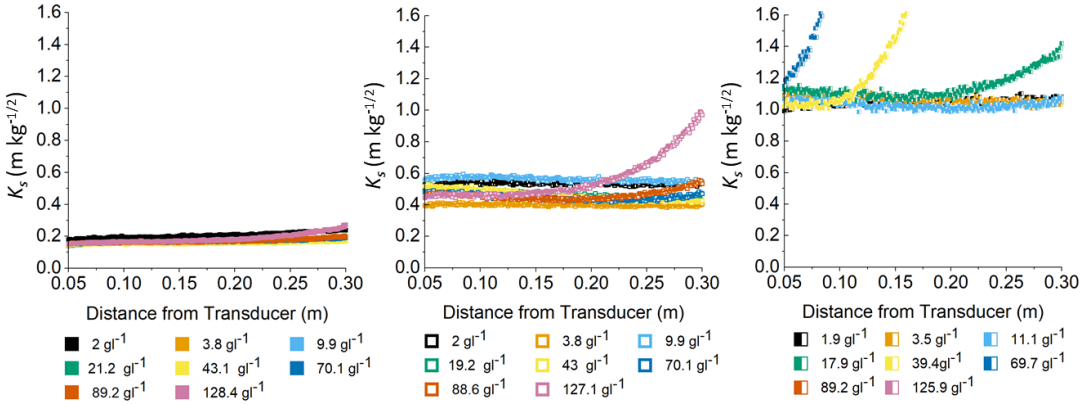

Figure 3.11 k_s vs distance for a) Honite 22, b) Honite 16 and c) Honite 12 at 2.25 MHz

3.3.2 Comparison of experimentally determined acoustic parameters to model values

Figure 4.10 shows a comparison of the experimental values for the scattering cross-section, χ, (obtained using Equations 2.12, 2.34 and 2.36 as part of the Extended *G-function* method, Section 2.3.4) compared with predictions by the heuristic Betteridge *et al.* [238] model. Values for k_s were averaged between 0.1 and 0.2 m from the transducer for Honite 22 and Honite 16 and over 0.05-0.1 m for Honite 12 due to limitations caused by the higher attenuation. ξ, and k_s were averaged over the concentrations indicated by the fits shown in Section 3.3.1, Figure 3.10. It is seen that viscous absorption has very little effect on the overall scattering cross section for Honite 12 particles, where ka ~1 and only a minor effect for Honite 16. For Honite

22, however, there is notable improvement in the prediction of the scattering cross-section when viscous losses are accounted for indicating that viscous losses are significant at ka < ~0.6 and must be accounted for to accurately model the acoustic properties of these particles. Experimental results from Thorne and Meral [48] followed a similar trend when introducing a size distribution for calculation of the scattering cross-section. Deviation from the overall predicted value can be seen despite the correction for viscous losses and the greatest deviation is seen for the Honite 12 data at 2.5 MHz for which the model result was 28% above the experimentally measured value for the scattering cross-section. This may not be unexpected however as Thorne and Meral observed that χ was larger than would be predicted for a uniform size distribution for $ka < 1$ and lower than predicted for $ka > 1$. Although the size distribution for Honite 12 is fairly narrow it may be having an effect on the measured value. With careful treatment of the data, however, relatively accurate (mean error of 13% across all results shown) values for the sediment backscatter cross-section were able to be found.

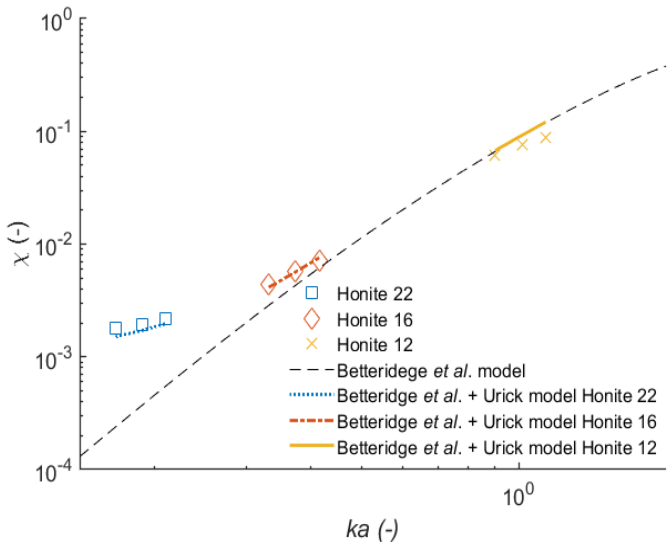

Figure 3.12 Normalised experimental total scattering cross-section (χ) as a function of particle size (*a*) and wavenumber (*k*) using the Betteridge *et al.* model [159] in conjunction with Urick's model [143]

Using Equation 2.9 the form function, *f*, was calculated based on the distance-averaged mean value of k_s for the experimental data (shown as points in Figure 3.13) and modelled using Equations 2.20 and 2.21 and are shown as a function of *ka* for each particle size. A good fit to the Betteridge *et al.* [159] model when including the Urick model [143] for viscous dispersion is seen indicating that the *G-function* calibration procedure is valid for calculating the particle backscatter

coefficient, k_s. While overall the experimental values for the form function and align well with the Betteridge *et al.* [159] model (mean error of 7% across all results shown) an increasing error was seen at lower *ka* values with the greatest deviation (12%) observed for Honite 22 at 2 MHz. As the Honite 12 data lie on the edge of the Rayleigh regime (*ka* = 0.9 – 1.13), the Thorne model [13], and by extension the Extended *G-function* method [15], [17], becomes increasingly invalid and larger attenuation leads to a lower signal-to-noise ratio which subsequently affects the calculation of k_s and *f*. Similarly, as Honite 22 lies outside of the *ka* range used to produce the Betteridge *et al.* [159] model (minimum *ka* ~= 0.25) model deviations may also be expected and will be further affected by the low signal-to-noise ratio that is a product of scattering strength decreasing with decreasing particle size which is readily observed in Figure 3.7 (d).

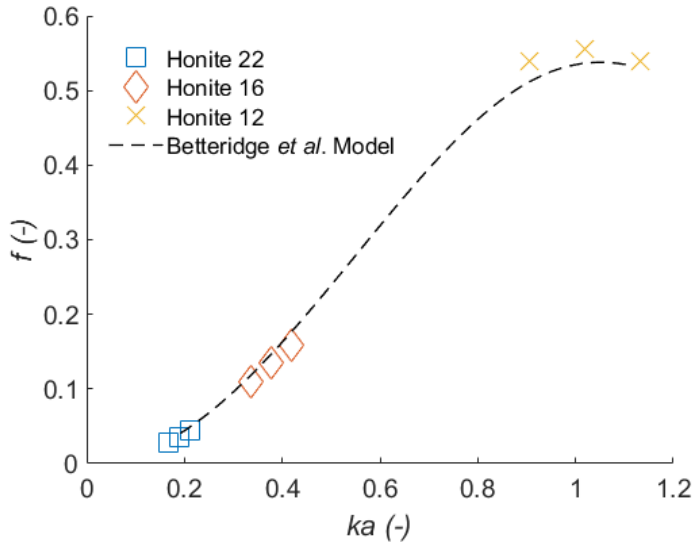

Figure 3.13 Form function (*f*) as a function of particle size (a) and wavenumber (k) calculated from experimental data and using the Betteridge *et al.* model [159]

3.3.3 Single and dual frequency concentration inversion

In order to determine the limits of the single frequency method (Section 2.3.5, Equations 2.38 and 2.39) and dual frequency method (Section 2.3.6, Equations 2.43-2.48) values for the backscattering constant, k_s, and attenuation coefficient, ξ, were first estimated using the extended *G-function* method [15], [17] (Section 2.3.4). Values for k_s were averaged between 0.1 and 0.2 m from the transducer for Honite 22 and Honite 16 and over 0.05-0.1 m for Honite 12 due to limitations caused by the higher attenuation. ξ was averaged over the concentrations indicated by the fits shown in Section 3.3.1, Figure 3.10 however individual values of

k_s for each concentration were used to account for the apparent variation of k_s with distance at high concentrations (shown in Figure 3.11). The same values were used for both the single and dual frequency inversion as the calibration tank was homogeneously mixed and so the particle size, and hence the scattering properties, would not be expected to change with distance [13]. Errors in the concentration profiles would therefore be expected to occur when the calculated k_s profile (Figure 3.11) deviates significantly from the constant value used in the inversion. It is important to note that, as k_s is calculated using experimentally determined values of ξ (using Equation 2.36) any errors in the measured attenuation are reflected in the k_s profiles, i.e. if attenuation is overestimated at a particular range then k_s will also be overestimated and indicates that the received signal is larger than that predicted by the model.

Figure 3.14 and Figure 3.15 show the concentration profiles produced using Equations 2.38 and 2.39 without and with the ψ_G correction factor. The inversion is effective up to ~40 g l^{-1} for Honite 22 and Honite 16 and ~20 g l^{-1} for Honite 12, highlighting the effectiveness of the Extended *G-function* method in determining the acoustic parameters necessary for the inversion. Above these values, however, the predicted concentration deviates increasingly with distance and concentration. Similar results can be found in previous literature [14], [160] and are attributed to the fact that, as feedback is positive between the estimated concentration and sediment attenuation term, errors accumulate along the profile causing a solution that diverges to zero or infinity [33]. In contrast, for the data presented here the gravimetrically measured concentration was used for the inversion calculation at all distances and so this positive feedback is avoided. As either the concentration or distance from the transducer increases, however, errors in the predicted attenuation coefficient, derived from the straight line fits in Figure 3.10, will be magnified by the concentration (Equation 2.35, Section 2.3.4 subsequently feeding into Equation 2.39, Section 2.3.5).

As the straight line fits to estimate the attenuation coefficient (Figure 3.10) are seen to be accurate up to the highest measured concentrations for Honite 22 and Honite 16, it is unlikely that a poor fit for estimating attenuation coefficient is the cause of the errors in the inversions at high concentrations for the smaller two particle sizes. The

more probable cause is the previously discussed multiple scattering effects leading to a lower signal-to-noise ratio and causing a smaller decrease of G with increasing r at greater distances (i.e. smaller apparent attenuation) from the transducer when the particle concentration is high (e.g. Figure 3.7 (l) and Figure 3.8 (c)). Such a result is not thought to indicate that the intrinsic particle attenuation decreases with distance at high concentrations but that multiple scattering/low SNR presents a concentration limit at which the theory used here [15], [33] to calculate the scattering and attenuation parameters becomes invalid. It would also appear that, even when the straight-line fits used to estimate the attenuation are relatively accurate, the concentration inversion will be dramatically affected by multiple scattering effects. This is supported by the accurate inversions obtained for Honite 16 up to the highest concentration for distances less than ~0.15 m from the transducer beyond which the attenuation term is large enough that multiple scattering begins to dominate the signal leading to significant system noise and thus causing the appearance of decreased attenuation. It might be expected, therefore, that the best inversion results would be obtained for Honite 22, the smallest and therefore least scatter-mode attenuating [150] of the three particle sizes. Honite 22 also therefore has the lowest backscattering strength, however, as is seen in Figure 3.7 (a) and so the low signal-to-noise ratio causes small additional errors in the inversion seen in Figure 3.14 (a). An improvement in the inversion in the near field is seen when the experimentally determined NFCF, ψ_G, is applied (Figure 3.15) compared to using no correction factor (Figure 3.14) however the original Downing, Thorne and Vincent [163] model was also seen to improve the fits to a similar degree and was still largely accurate.

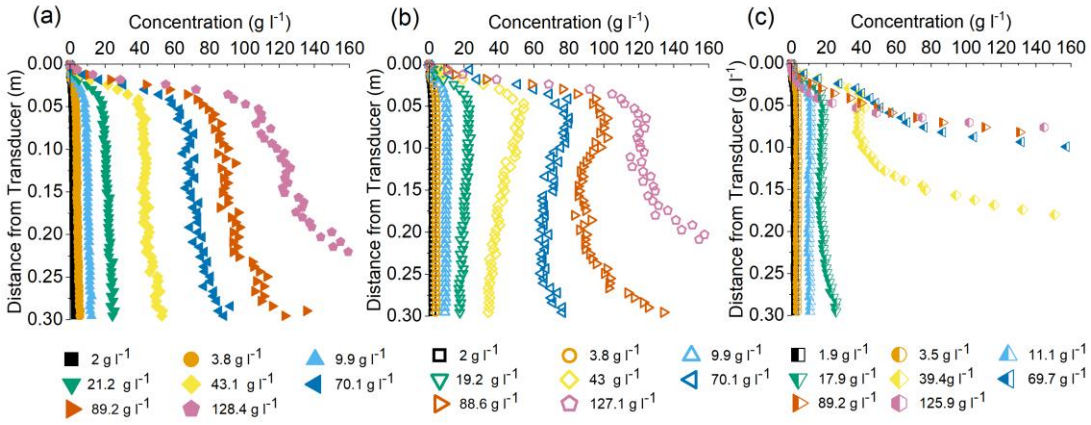

Figure 3.14 Single Frequency inversion profiles for a) Honite 22, b) Honite 16 and c) Honite 12 at 2.25 MHz (without correction factor)

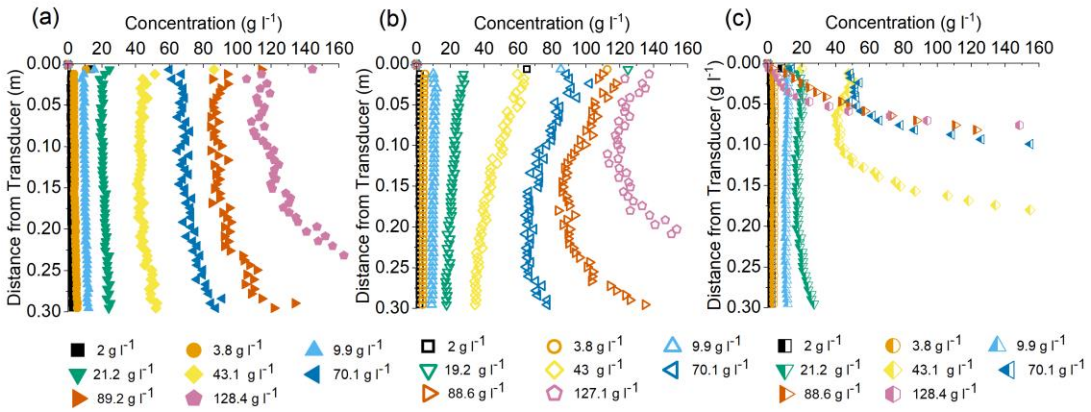

Figure 3.15 Single Frequency inversion profiles for a) Honite 22, b) Honite 16 and c) Honite 12 at 2.25 MHz (with *G-function* based correction factor)

In order to eliminate the propagation of errors along the profile seen in the single frequency inversion due to the attenuation term, the dual frequency method described in Section 2.3.6 (Equations 2.43-2.48) [14], [15], [161] was applied to the data using the experimentally determined values for k_s and ξ. Figure 3.16 shows the dual-frequency concentration profiles obtained for each particle size at a frequency pairing of 2 and 2.5 MHz. The widest frequency spacing was chosen, as this offered the attenuation ratio most different from unity and therefore, it was assumed, the smallest relative error in the concentration inversion according to the relationship derived by Rice *et al.* [15] (Section 2.3.6, Equation 2.49). It is seen that the inversion obtains accurate concentration profiles up to ~20 g l^{-1} after which the inversion converges towards zero with increasing distance from the transducer. This is likely a result of multiple scattering effects and low signal-to-noise ratio (discussed previously in Section 3.3.1) causing the linear relationship between the attenuation and concentration, a necessary assumption for the dual-frequency method, to be invalid. The second phenomenon seen is that above ~20 g l^{-1} there is significant scatter that worsens with particle concentration. This random deviation can be predicted using the equation derived by Rice *et al.* [15] (Section 2.3.6, Equation 2.49) and is seen to increase as the attenuation coefficient ratio $\frac{\xi_1}{\xi_2}$ approaches unity. The additional error introduced by the dual-frequency method as compared to the single frequency inversions is therefore likely caused here by insufficient differences in the attenuation coefficients at each frequency. It is also noted that the deviation is much more pronounced for Honite 22 compared to the other two particle sizes and may perhaps be related to a smaller change in the attenuation coefficient with frequency and hence an overall increase in the attenuation coefficient ratio.

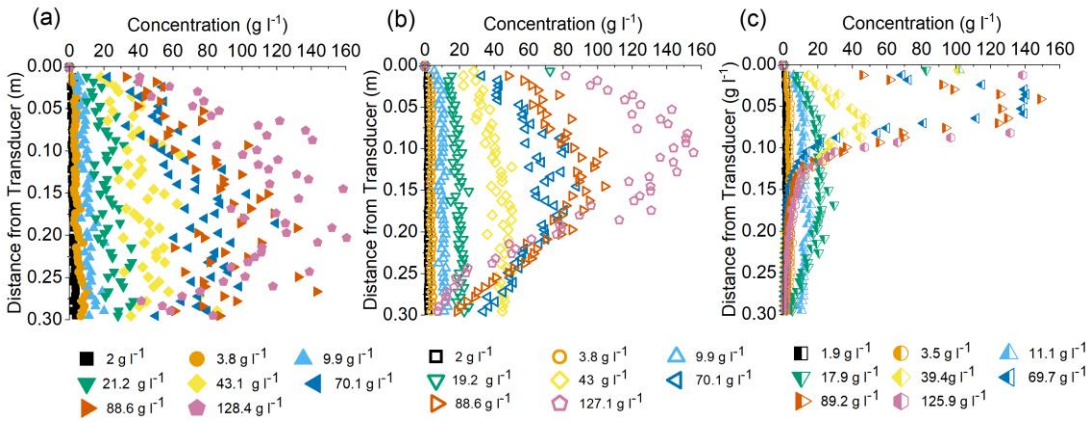

Figure 3.16 Dual Frequency inversion profiles for a) Honite 22, b) Honite 16 and c) Honite 12 with a frequency pairing of 2 and 2.5 MHz (with *G-function* based correction factor)

In order to fully investigate the accuracy limits of the concentration profiles obtained using the single and dual frequency inversion methods, mean concentration values are compared to sample values in Figure 3.17 (a) and (b) that were averaged over the same distance ranges used to calculate k_t and k_s to avoid both near-field and multiple scattering effects. Comparing Figure 3.17 (a) and (b) it can be seen that despite taking an average over the aforementioned distance range, that could be expected to overcome the random scatter about the mean value observed in the dual frequency inversion profiles (Figure 3.16), there is still significant deviation from the gravimetrically measured concentration for the dual frequency method as compared to the single frequency inversion results. The discrepancy between single and dual frequency results is thought here to be a result of an insufficient difference in the attenuation coefficients at the frequency pairs used (explored further in the discussion of Figure 3.19).

As the intended aim of the ABS is to accurately determine full concentration versus distance profiles, the coefficient of variation (COV), used here as a measure of the scatter of the results with distance, for the ABS-measured concentration was calculated over the same range used to calculate the mean concentration values for each particle size and frequency/ frequency pairing for the single and dual frequency inversion methods and values are shown as a function of the measured sample concentrations in Figure 3.18. For the single frequency inversion, shown in Figure 3.18 (a), a rapid increase in the coefficient of variation is seen for the Honite 12 above 40 g l^{-1} while Honite 22 and Honite 16 data remain relatively accurate (COV < 0.24) up to 127 g l^{-1}. Furthermore, for the single frequency inversion, Honite 16

obtains a lower COV than Honite 22 up to 5 g l^{-1} at 2.5 MHz and up to 10 g l^{-1} at 2 and 2.25 MHz that is likely a result of the higher signal strength seen for Honite 16 in Figure 3.7 (b) as compared to Honite 22 in Figure 3.7 (a) for which the signal is close to the estimated noise floor. In addition, for Honite 16 and Honite 12 there is a consistent increase in the COV with increasing frequency at concentration greater than 10 g l^{-1} that is thought here to be the point at which multiple scattering effects begin to significantly contribute to errors in the inverted concentration profiles. Comparing the COV observed in the dual frequency results to the single frequency data an overall increase in the COV across all particle sizes is seen except where the mean ABS-measured value is significantly over-estimated (thus also significantly decreasing the calculated COV value), as would be expected from the observed scatter in the concentration profiles in Figure 3.16. Of note, however, is that Honite 16 consistently show the lowest COV values of all three particle sizes for the dual frequency inversion and also obtains the most accurate concentration values that is thought to be a result of the greater difference in attenuation values between the frequencies used and is explored further below.

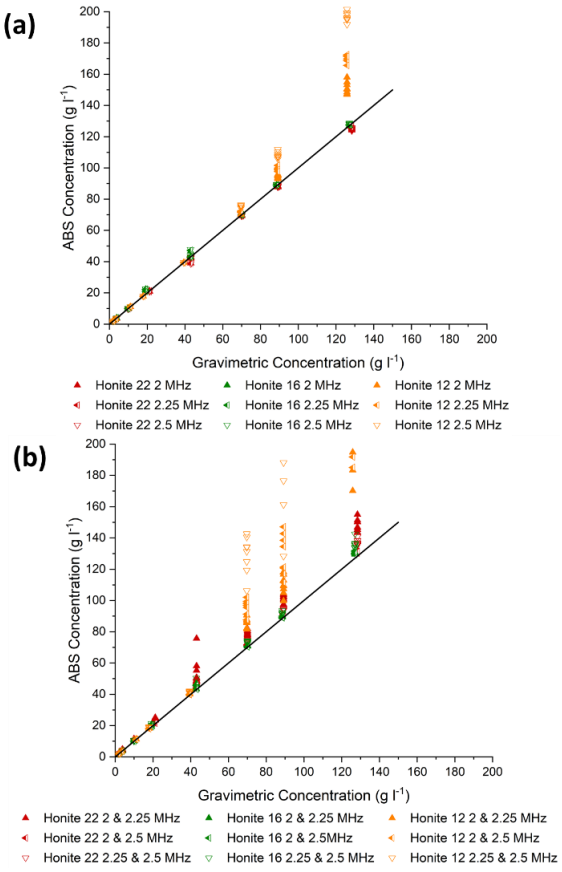

Figure 3.17 Showing concentration measured by the ABS plotted against gravimetrically determined concentration for the a) single frequency inversion and b) dual frequency inversion

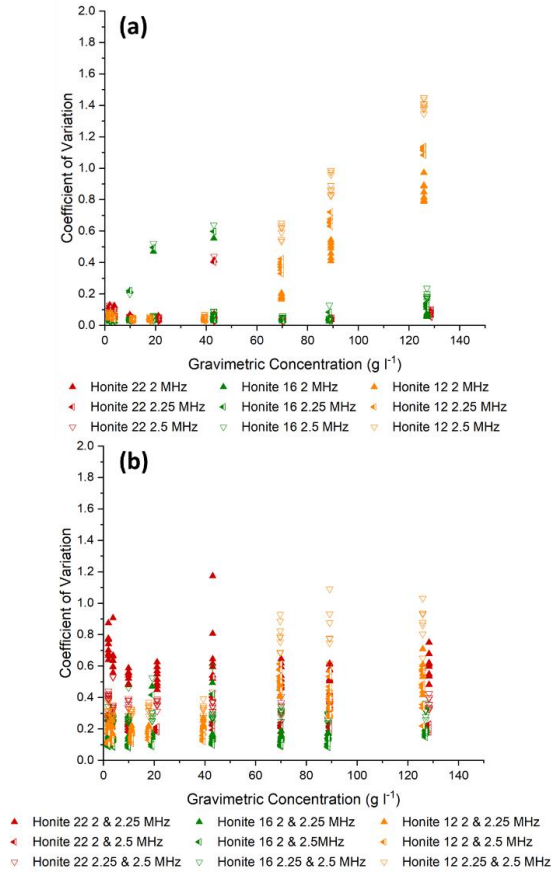

Figure 3.18 Showing coefficient of variation in concentration measured by the ABS plotted against gravimetrically determined concentration for the a) single frequency inversion and b) dual frequency inversion

To investigate the predictability of the scatter seen in the dual frequency inversion, the equation given by Rice *et al.* [15] (Section 2.3.6, Equation 2.49) was used to compare the measured error in experimental concentration profiles to the error estimated with Equation 2.49 from calculated k_s profiles. Figure 3.19 shows the error in the measured concentration values, $\frac{\delta M}{M}$, as a function of the attenuation coefficient ratio, $\frac{\xi_1}{\xi_2}$, where solid markers indicate the actual experimental errors for the dual frequency method and the hollow markers correspond to the estimate for the error calculated using Equation 2.49. For each profile, the relative error in the scattering constants at each frequency, $\left|\frac{\delta K_1}{K_1}\right|$ and $\left|\frac{\delta K_2}{K_2}\right|$, and relative error in the concentration, $\frac{\delta M}{M}$ were determined by taking the mean absolute deviation for the calculated k_s and M profiles and scaling it to the mean value for the profile. The same distance range as that used to determine k_t was chosen to determine the mean value and relative error of the k_s and M profiles as this represented a range where the error was largely random and would cause the random scatter seen in Figure 3.16, as opposed to the consistent

deviation toward zero caused by the error in the apparent attenuation. In order to avoid additional errors from a poor estimate of the attenuation value seen at high concentrations (Figure 3.10 (c)) $\frac{\delta M}{M}$ was only calculated up to 25 g l^{-1} and averaged to produce the mean error for each probe at each $\frac{\xi_1}{\xi_2}$ ratio (plotted as the empty markers in Figure 3.19). It is noted that the attenuation ratios associated with the widest frequency bandgap (2 – 2.5 MHz) were not solely used in error analysis, but those with the other frequency pairs (2 – 2.25 MHz, 2.2.5 – 2.5 MHz) were also used giving three ratio values for each particle size. The estimated error is greater than the observed error in all cases but does follow a similar trend with the attenuation coefficient ratio, increasing as $\frac{\xi_1}{\xi_2}$ approaches unity. As k_s was calculated by assuming all the other terms in Equation 2.32 (Section 2.3.1) as constant, the error in estimating all these terms is absorbed in to the calculated ks values and hence $\left|\frac{\delta K_1}{K_1}\right|$ and $\left|\frac{\delta K_2}{K_2}\right|$. These errors may not scale in the same way with the attenuation coefficient ratio as $\left|\frac{\delta K_1}{K_1}\right|$ and would therefore cause Equation 2.49 to predict values that are offset from the real measured values of $\frac{\delta M}{M}$ as seen in Figure 3.19.

Additionally, as the experimental error results for Honite 16 match closely with predicted values, this suggests that the majority of the error was actually due to small random variation in k_s for Honite 16, likely a result of turbulence in the tank and the small size distribution in the glass spheres used for the experiments. This would therefore imply that the other parameters used to calculate k_s (Section 2.3.1, Equation 2.32) i.e. the experimentally estimated attenuation coefficients are not contributing significantly to errors in the inverted concentration profiles. Development of similar error estimates for other variables that account for further experimental variations could therefore allow for estimation of the relative error of each variable to produce more accurate constraints in statistical methods [225]. Furthermore, using transducers pulsed at multiple frequencies combined with the dual frequency method allows greater amounts of data to be collected from a given probe array. This, coupled with a rigorous understanding of how errors propagate through the inversion, could be used to improve the calculation of constraints and optimization parameters in statistical methods such as that proposed by Wilson and Hay [225]. Here, the dual-frequency method was applied on a probe-by-probe basis i.e. signals

were not compared from different probes using the dual-frequency method. From eight probes and three possible frequency pairings 24 profiles were therefore able to be produced. Comparing across probes would allow for an additional 84 profiles to be obtained, significantly enhancing the potential for data mining in scenarios where only modest variation (here +/- 10 %) around the probe central frequency is available.

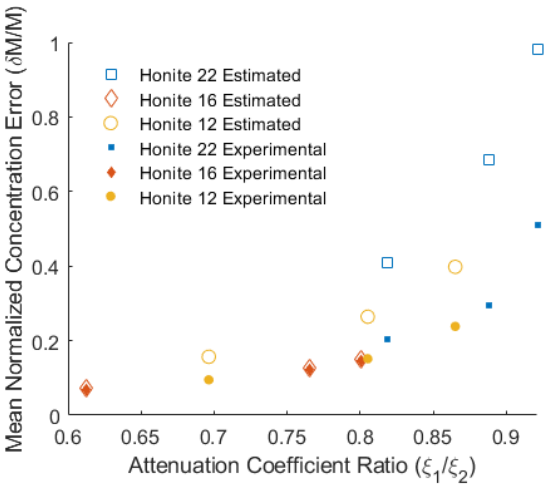

Figure 3.19 Calculated and experimental mean normalised error in the dual frequency inversion profiles ($\frac{\delta M}{M}$) for all particle sizes and frequency pairings plotted as a function of the attenuation coefficient ratio ($\frac{\xi_1}{\xi_2}$).

Despite the difference seen between the measured and predicted error, it is clear that the level of scatter seen in the dual-frequency inversion results is generally within expected values and indicates that, so long as the frequency range is wide such that the resulting attenuation coefficient ratio is < ~0.6 a single narrowband transducer is able to obtain an accurate dual-frequency concentration profile. The dual frequency profile is advantageous compared to the single-frequency method where concentration must be estimated or calculated iteratively causing errors to accumulate in the inversion with distance [14]. Even if the scatter from the dual-frequency profile is large, it may still provide good initial estimates for the concentration to be inputted into the single frequency inversion. The dual frequency method can also be applied when the attenuation coefficient is not known as by taking *dG/dr* values when the attenuation due to water is known (Equation 2.34, Section 2.3.4) the sediment attenuation term, α_s, can be found at each frequency and used in Equation 2.48 in place of the attenuation coefficient. Replacement of the attenuation coefficient with the directly measured attenuation is possible because, for co-located transducers, and assuming the concentration, *M*, is identical, $\frac{\xi_1}{\xi_2}$ will be equivalent to $\frac{\alpha_{s1}}{\alpha_{s2}}$ and so the value can be substituted into Equation 2.48 (Section 2.3.6) and the dual frequency inversion can be performed.

3.3.4 Semi-empirical backscatter power model results

In order to account for the observed multiple scattering effects at high concentrations, the Semi-empirical backscatter power (SEBP) model taken from Weser *et al.* [46] (Equations 2.51 and 2.52) was investigated. By taking a measurement of the maximum backscattered amplitude close to the transducer (that was corrected for near-field spreading effects using the Downing *et al.* [163] model, Equation 2.6) and estimating single particle scattering characteristics, a hard sphere pair-correlation model [192], [193] can be applied to determine the concentration that corrects for multiple scattering effects. Although only a single value for the concentration is obtained close to the transducer, Weser *et al.* [46] found good agreement with the theory for measurements of glass beads in water up to 30 %v/v. This semi-empirical method is therefore of interest for investigating high concentration dispersions where single-scatter theory fails to produce accurate concentration measurements. As the model calculates the relative backscatter measured amplitudes, it must be scaled in proportion with the pressure of the incident acoustic wave as well as constants that capture the transfer function of the probe and instrument electronics. The method used in this study for estimating these constants is given in Section 3.2.3 with supporting equations and the method proposed by Weser *et al.* [46] provided in Appendix A.1 (Equations A.1-A.4).

Having estimated the scale factor for each probe and frequency, experimental backscattered amplitudes, shown on the y-axis in Figure 3.20 (a), could be compared to the values predicted by the SEBP model on the x-axis. For a given particle size, an increase in frequency or concentration will move the value further along the x-axis, while an increase in particle size will increase both the particle volume term, *Vp,* and the single particle scattering strength, Ω_p. While an acceptable fit was seen for Honite 16 (R^2=0.963) and Honite 22 (R^2=0.971) the fit for Honite 12 was found to be poor (R^2=0.851). As Honite 12 lies on the edge of the Rayleigh regime the scattering model may not be as accurate and similar results were found by Weser *et al.* [46] when $ka < 0.1$ or $ka > 1$. For Honite 16 and Honite 22 the strongest deviations from the predicted values were for the low concentrations where the predicted value is much lower than that measured. Although the signal-to-noise ratio will be lower for the lower concentrations, this is not likely to be an issue so close to the transducer.

Another possibility is that the fits used to obtain the scale factor ($\widehat{P_0}RT_v$, Equation 3.5) are being underestimated due to the non-linearity in the SEBP model observed at higher concentrations shown in Figure 3.20. Oddly, the Weser model appears to predict a lower received backscatter signal as particle size is increased, a relationship not seen in Figure 3.7 (a) – (c). This is likely a result of the Faran model underestimating the sensitivity of the backscattering strength to concentration at large particle sizes that lie on edge of the Rayleigh regime (ka = 0.9 – 1.13). It may be beneficial to use a single particle scattering model that more accurately reflects this relationship, such as the Betteridge *et al.* [159] heuristic fits in conjunction with the Thorne model [13], and apply the packing factor in the same way. Figure 3.20 (b) shows the concentration that would be predicted by the SEBP model, obtained by determining the particle concentration that would give the abscissa values for the experimental data points in Figure 3.20 (a), plotted as a function of the gravimetrically measured sample concentration. Significant errors exist for the low concentration data with the lowest frequency measurements showing the highest accuracy. Regardless, there is significant error in the model, but values obtained may aid in obtaining an initial estimate of the particle concentration so that more rigorous methods can be employed.

The SEBP model could therefore be used to obtain a single value for particle concentration or size in systems where direct inversion is not possible due to the upper concentration and *ka* limits found for Equation 2.5. The SEBP model may also be of use in estimating the concentration so that the *G-function* calibration can be performed in systems where *in situ* concentration cannot be found. Even if a good linear fit for the calibration cannot be obtained over the measured range of concentrations to find the attenuation coefficient or if just a single measured concentration is known it would be possible to use fitted values of *dG/dr* to replace the $-2(\alpha_w+\alpha_s)$ term in Equation 2.5 and calculate k_s for the measured sediment and use the measured concentration value to calculate the attenuation coefficient . The single frequency concentration inversion can then subsequently be performed without prior knowledge or without a full calibration to find the attenuation coefficient. Further to this, the dual frequency inversion could also be performed so long as α_w is known, as α_s could then be experimentally determined via Equation 2.34. As the value of M would be equal the

ratio of $\alpha_{s1}/\ \alpha_{s2}$ would be equal to $\frac{\xi_1}{\xi_2}$, effectively eliminating the need for a full calibration *in-situ* to find ξ_1 and ξ_2.

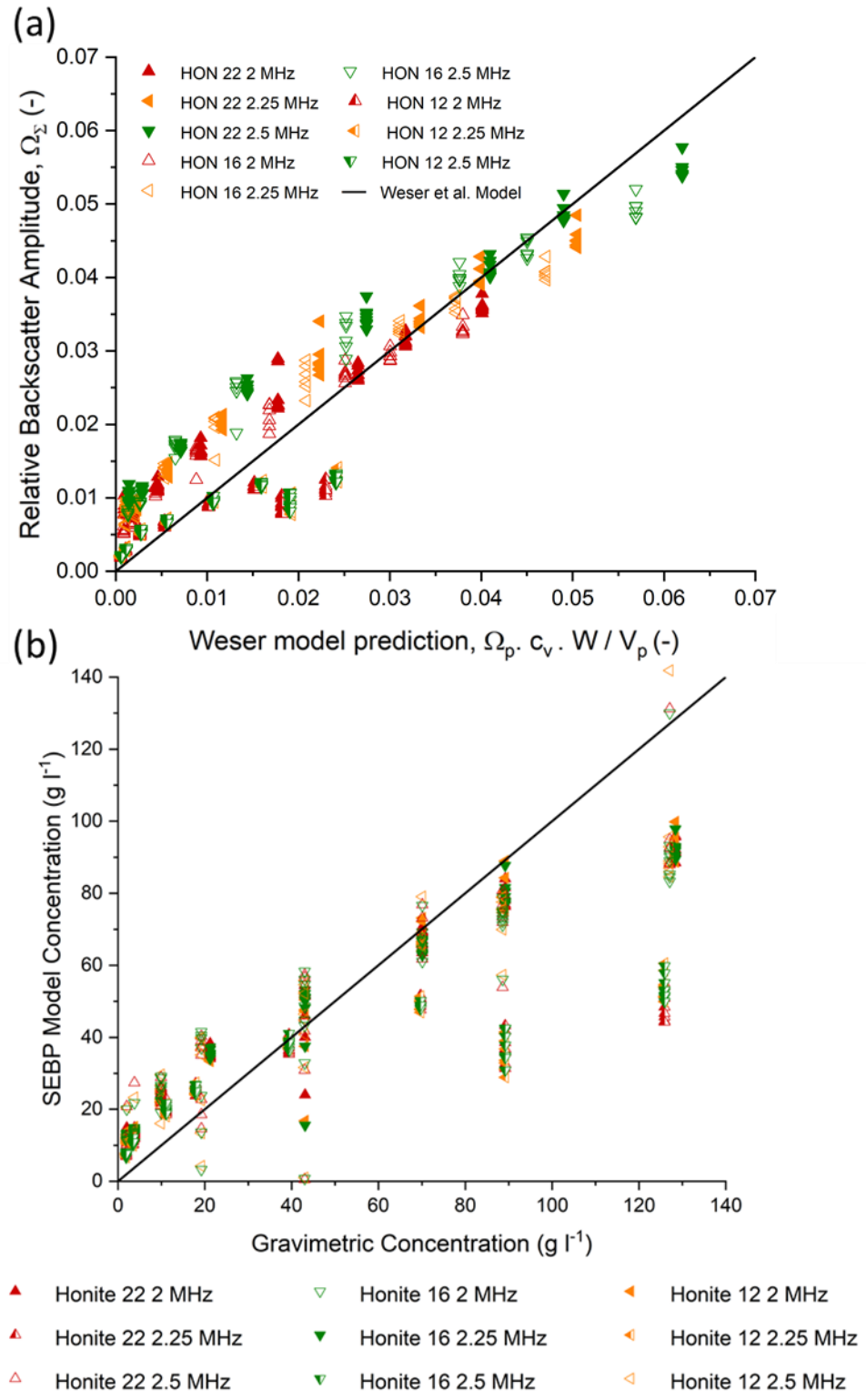

Figure 3.20 a) Experimentally determined backscatter amplitudes plotted as a function of theoretical backscatter amplitude calculated using the SEBP model [46] and b) comparison of concentration calculated using SEBP model and the sample gravimetric concentration from experiments

3.4 Conclusions

The concentration and *ka* limits of the *G-function* calibration method [15], [17], have been explored for three sizes of glass spheres insonified at 2, 2.25 and 2.5 MHz. The subsequently calculated attenuation (Figure 3.10) showed a linear relationship with concentration up to ~125 g l^{-1} for the two smallest particle systems (Honite 22 (*ka* ~0.2) and Honite 16 (*ka* ~0.4) and up to ~40 g l^{-1} for Honite 12 (*ka* ~1.0). Beyond ~40 g l^{-1} the expected linear relationship between attenuation and concentration is not seen and the observed attenuation appears to reach a plateau. The trend of a linear increase in attenuation before reaching a plateau has been observed in literature for glass spheres at similar *ka* values using transmission measurements [141], [150] and it is similarly observed by Shukla *et al.* [136] that the linear region is extended to higher concentrations for lower *ka* values as found in this study.

For the largest particle size, the observed attenuation also appears to decrease with distance (Figure 3.7 (i)). It is thought that this decreasing attenuation is caused by the multiple scattered signal, a result of high attenuation, enhancing the received signal at greater distances or limitations in the instrument as multiple scattering due to high attenuation may also be decreasing the signal to noise ratio in the system [235]. As the multiple scattered signal takes a longer path through the medium [222], [223] it may therefore be detected by the transducer as an additional coherent signal component for the single-scattered echo at a greater distance thus enhancing the measured signal. Alternatively, if the multiple scattered signals are simply sensed as incoherent noise the effective noise floor for the instrument will be increased leading to the non-linearity observed for the highly attenuating suspensions in the results presented here. Despite these limitations, the backscatter cross section and form function were also able to be determined as part of the Extended *G-function* method from experimental data. The expected trend of increasing attenuation with increasing particle size and frequency (Figure 3.10) was observed using only a modest (+/- 10 %) variation in the pulsed frequency around the central frequency of the transducers (2.25 MHz). Results compared well overall with the heuristic model from Betteridge *et al.* [159] coupled with Urick's model [143] for viscous absorption. The

greatest deviation was seen for Honite 12 due to its high *ka* value (~1) and the Rayleigh regime limitations of the *G-function* calibration method [15], [17].

An alternate method for modelling the near field correction factor ψ_G (shown in Figure 3.8) using *dG/dr* fits taken as part of the Extended *G-function* method [15], [17] was presented to improve the *G-function* fits in the near field. Variation from the original model proposed by Downing *et al.* [163] was small but fits lay consistently above that predicted by the literature model. This could be attributed to small variations in the probe face from manufacture leading to a different effective transducer radius than stated or damage to the probes during transport and use and so it is recommended to incorporate this procedure when the *G-function* calibration method is performed as it is computationally simple and requires only the active transducer radius as an additional input. This would allow for a more accurate calibration of acoustic probes before they enter deployment in scenarios such as pipe flow [15], [138], [215] and when taking backscatter measurements in highly attenuating or concentrated dispersions [160], [189].

Single frequency profiles (Figure 3.14) obtained using the method outlined in Section 3.2.3 with a single iteration at the nominal concentration of the calibration tank were found to be accurate (mean error across all probes and frequencies < 10%) up to ~130 g l^{-1} for 78 μm and 40 μm glass particles and for the 212 μm glass particles up to ~40 g l^{-1} so long as the measurement range was truncated to match the range used to estimate the transducer constant and scattering coefficient (Figure 3.17 (a), with ranges of 0.1 – 0.2 m from the transducer for Honite 22 and Honite 16 and 0.05-0.1 m from the transducer for Honite 12). As has been found by other authors [14], [160], the estimated concentration diverges to infinity at greater distances from the transducer as errors accumulate along the profile through the attenuation term [33]. At high concentrations and distances errors in the attenuation term of Equation 2.39 will become magnified (through Equation 2.35 and Equation 2.5). Therefore, the error induced in the attenuation term by both the experimental estimation of the attenuation coefficient and multiple scattering cause the inversion to become unstable with this limit becoming more prominent as scattering-attenuation, and subsequently multiple scattering effects, are increased.

The ability of the dual frequency method to be applied to a single narrowband transducer pulsed at multiple frequencies has been successfully demonstrated and the dual frequency concentration profiles (Figure 3.16) produced here using the method proposed by Bricault [161] were accurate (mean error across all probes and frequencies < 8%) up to ~20 g l^{-1} (Figure 3.17 (b),). Above ~20 g l^{-1} the concentration profiles were significantly scattered when compared with the single frequency inversion. Although the mean value for the concentration profiles obtained for Honite 22 and Honite 16 were still relatively accurate above 20 g l^{-1} (mean error across all probes and frequencies < 13%) Honite 12 showed a mean error of 56% at 70 g l^{-1} that further increased with increasing concentration. The scatter about the mean value was seen to increase with concentration due to increasing error in the calculated value of k_s with distance. The qualitative scatter in the profiles was also seen to increase further as the attenuation ratio ξ_1/ξ_2 became closer to unity due to mathematical instabilities in Equation 2.48 (See Appendix A.3, Equations A.6-A.19). Results presented here indicate that a $\xi_1/\xi_2 < \sim 0.5$ be used if the dual frequency inversion is to be accurate.

Experimental errors were quantitatively compared with those estimated using an equation derived from Rice et al. [15] (Equation 2.49) and it was found that the estimated error experienced a similar increase to the experimental error as ξ_1/ξ_2 approached unity. The difference between the predicted and experimental error may provide a measure for determining the uncertainty or statistical variation in the experimental parameters used for the inversion. The dual frequency method also represents a significant opportunity to enhance the total volume of data collected for a given ABS. Coupling an understanding of error propagation in the inversion with the large amount of data collected would allow for statistical methods [225] to be more accurately constrained and optimised.

The SEBP [46] model (Figure 3.20) was seen to fit the data somewhat well for which $0.1 < ka < 1$, similar to results found by Weser *et al.* [46] however significant errors existed at high and low concentrations. Despite the inaccuracies in the model it represents a method to obtain at least a single point value for the concentration where the *G-function* calibration (Section 2.3.4) and the single or dual frequency inversion (Sections 2.3.5 and 2.3.6) are not possible due to the concentration or size limits explored in this paper. It could also be used to obtain measurements of concentration

so that the *G-function* calibration can be performed when the particle size is known but concentration is not as Ω_P can be estimated with a single particle scattering model (e.g. Faran's model [195]) and Equation 2.52. By performing the *G-function* analysis *dG/dr* values in conjunction with known values for α_w can be used to find α_s and the dual frequency method can then be utilised.

It has therefore been demonstrated that using narrowband transducers pulsed at multiple frequencies, coupled with the aforementioned calibration and inversion techniques, allows the intrinsic acoustic properties of the sediment, the backscatter cross-section and form function, to be determined as a function of frequency [15], [17], [159]. Even for a modest variation in the frequency the expected trends predicted by heuristic models [159] are seen. Inverted profiles using both the single and dual frequency method are accurate up to modest (~40 g l^{-1}) concentrations and the semi-empirical backscatter power model is seen to fit the data well for moderate concentrations. The limit of the linear relationship between concentration and attenuation was also explored in Figure 3.10 and the limiting concentration at which the linear relationship broke down was found to decrease with increasing size as *ka* approaches unity for the glass spheres used as has been found by other authors [141], [150].

In terms of future work, the effect of particle size distribution width on the packing factor also represents an area of interest as it has been shown by Weser *et al.* [46] to be sensitive to the particle size as this is implied by the hard-sphere correlation model (Appendix A.1, Equation A.5). The semi-empirical backscatter power model could therefore be used to estimate the PSD width if average particle size and concentration are known such as in a clarifier where settling rate, and hence the average particle size, could be determined from under and overflow concentration measurements. However further study is needed to extend this to flocculated particle systems as an accurate prediction for the single particle scattering strength based on floc properties is needed. The ability to do so would allow for the potential measurement PSD changes during flocculation and aggregation processes where particle concentration is constant or known but the PSD is changing. Further development of statistical methods is also of interest as using the predictive error equations explored in this paper may lead to better identification of erroneous concentration inversions. The

proceeding chapter will focus on expanding the modelling presented here to cohesive, flocculated particle systems where viscous losses will become more apparent [47] and other models for the estimation of the backscatter cross-section, χ, will be investigated such as the Hybrid scattering model presented by Thorne *et al.* [47] which incorporates a particle density function to calculate particle porosity as a function of floc size so that the acoustic properties can be estimated at all stages of floc growth.

Chapter 4 Flocculated particle studies

4.1 Introduction

As discussed in Chapter 1, there is currently a need to develop *in situ* ABS to monitor solids concentration *in situ* to optimise waste transport and sedimentation processes throughout Sellafield Ltd. [5], [6], [15], [38]. Due to open air storage methods being utilised much of the legacy wastes at Sellafield have become polluted with organic matter and detritus over the 70 years for which they have been stored with over 1000 varying wasteforms identified in the Pile Fuel Storage Pond [49], [50]. It is therefore thought that the structure of the particles in these wastes will resemble flocculated structures encountered in both natural marine [9], [10], [122], [200] and engineering [71], [86], [191], [239] systems. As such, it is imperative that the accuracy of current models for estimating the scattering and attenuation parameters for flocculated sediments be evaluated so that concentration inversion models developed over a number of years by a number of authors [3], [15], [24]–[26], [16]–[23] can be employed successfully.

Controlled laboratory experiments were therefore undertaken on flocculated particle systems, using multiple probes pulsed across a range of insonification frequencies, as suggested by Ha *et al.* [227]. Measurements were taken for two synthetic floc systems before and after inducing flocculation and one naturally occurring floc system across a range of concentrations. The synthetic flocs were produced using a high molecular weight anionic polymer to induce bridging flocculation as it was thought these floc structures would most closely resemble those found at Sellafield Ltd. [21], [40], [49], [240]. All the necessary parameters to accurately model flocculated particles (particle size distribution, fractal dimension, concentration, system calibration constants and sediment acoustic properties) were determined experimentally where possible using a combination of *in situ* ABS techniques to determine sediment acoustic properties, such as the previously discussed extended *G-function* method (Section 2.3.4), and *ex situ* light scattering to determine particle size distribution and fractal dimension. ABS results were then compared to the most recent modelling efforts used for flocculated

systems [47], [120] in order to clarify the nature of the ensemble backscattered system from a distribution of flocs and primary particles. Following this, the effect of changes in the modelled particle size, fractal dimension and PSD were investigated so that the sensitivity of the Hybrid [47] (Section 2.3.10) and irregular Solid Scattering models [48] (Section 2.3.2) to these parameters could be found. Understanding these effects will subsequently further the use of ABS as an *in situ* particle size measurement device for flocculated systems. Of particular interest is the variation in model values seen at low *ka* where data used to produce the models discussed above [47], [48] is sparse. Following this, single [33] and dual frequency [161] concentration inversion methods were investigated to determine the accuracy and measurement limits of flocculated particle concentration inversion. Such data will allow ABS to be developed further as an *in situ* measurement device for concentration measurement in hazardous engineering environments where particle structures may change due to process conditions such as shear [103], [127], [241], chemical or biological aggregation [23], [30], [87], [97], [122], [242], pH, temperature and salinity [42], [55], [56], [59], [63], [71], [76], [109], [125], [243].

4.2 Materials and method

4.2.1 Materials selection

Three simulants were used in this study. Firstly, Omyacarb 2 calcite (d_{50} approximately 2 μm) from Omya was chosen as a simulant material in this study as it has been used previously for ABS studies in both the same laboratory scale thickener [189] and in large scale settling trials [38]. Its polymer flocculation and settling dynamics have also been studied extensively [127], [240], [244], 29] and are of great interest for mining and waste processing operations involving limestone or marble. Versamag magnesium hydroxide obtained from Martin Marietta was also used as magnesium hydroxide sludges are commonly encountered at Sellafield due to decommissioning of spent Magnox fuel cladding. There is approximately 6300 m^3 of Magnox cladding and miscellaneous solid waste, as reported in the 2016 NDA waste inventory [245] ~38 % of which is comprised of Magnox sludge by weight. Further inventories are also reported that will likely result in additional magnesium hydroxide sludge production as processing continues. Additionally, the flocculation mechanisms of magnesium hydroxide have been well studied [246] as it has been shown to be

effective in dye removal processes [62] and, as the settling of the hydroxide form is a necessary step in the production of magnesia, flocculation studies to increase this settling rate have been performed by previous authors [68]. Finally, due to exposed nature and long waste storage period (~70 years) of the PFSP [49], [50], that would be an ideal target site for an acoustics array installation, natural sediment obtained from the base of a dairy farm pond (Apple by-in-Westmorland, UK obtained from Barnon Ltd, UK) was selected to be studied as it was thought that it would give a representation of the naturally occurring flocs that may now be present in the PFSP.

The flocculant chosen for this study was AN934SH (SNF Ltd., UK) an anionic high molecular weight, medium charge density polymer. A medium charge density and high molecular weight were chosen as this will be likely to induce bridging flocculation [67], [71] that produces flocs that are both large, due to the long polymer chains, and strongly bonded due to the covalent bridges formed between aggregates by the polymer [87], [93]. The negative charge of the polymer allows it to both adhere to the positive cations (Ca^{2+} and Mg^{2+}) to form the connection for the bridge while also reducing the electric double layer surrounding the particle thereby encouraging aggregation [92], [93], [240]. Furthermore, aggregates formed from natural bio-flocculants, such as those that are likely to have been produced in the exposed legacy waste ponds at Sellafield [50], typically also form flocs via a bridging mechanism [21], [40], [247]. It is therefore thought that synthetic flocs produced via a bridging mechanism will most closely resemble the particle structures likely to be encountered on-site at Sellafield.

Data from all three sediment sets would also be relevant for the extensive studies that have taken place in coastal and fluvial environments [14], [120], [129], [200] as controlled lab studies on flocs are limited with particle characterisation methods complicated by floc breakup and reformation during transport and storage prior to characterisation.

4.2.2 Floc production and materials characterisation methodology

As multiple concentrations were to be used for the acoustic measurements and changing the initial particle concentration would affect the floc structure, and hence the acoustic signal, the initial floc solution was produced in the tank at 4 %w/w of the

sediment with a flocculant concentration of 40 ppm. This was subsequently diluted multiple times for lower concentration measurements by pumping off half of the tank contents to effectively remove half the mass of sediment from the system. The tank was then refilled with water with additional flocculant added in-line to maintain the flocculant concentration of 40 ppm to prevent disassociation of flocculant from the flocs in solution that could be caused by a lower flocculant bulk density. No floc was used in the BPS experiments, however, as the natural flocculants present were unknown. Doing so will also inform us if the floc acoustic properties of the types of wastes likely to be encountered at Sellafield Ltd. [49], [50] will change significantly upon dilution. The impeller was set at 450 RPM during flocculation and ABS measurements and turned down to 150 RPM when emptying the tank to avoid excessively shearing the flocs when the tank volume was reduced. The total time taken over the course of each experiment was just over an hour with around 5 minutes taken to take the ABS measurements and 15 minutes taken to empty and refill half the tank to dilute the flocs as described earlier.

Flocculated particle samples were obtained during acoustic measurements from the calibration tank (schematic shown in Section 3.2.2, Figure 3.4) by teeing off the recirculation lines that used a peristaltic pump and ¾ inch diameter tubing to collect floc samples in a 200 ml flask. Samples were then carefully transported to the Mastersizer and measured in an aqueous environment at the same flocculant concentration used in the experiment. Shear in the Mastersizer was controlled by minimizing the mixing rate on the attached dispersion unit (Hydro 2000SM) while still maintaining a valid measurement signal (typically ~1500 RPM). Scanning electron microscope (SEM) images of the unflocculated sediment (particulates) were taken using a TM3030+ SEM (Hitachi High-Technologies Corporation, Europe) and are shown in Figure 4.1. SEM stubs were prepared by preparing solutions at 1 %w/w of the sediment and allowing them to mix for 15 minutes. The SEM stubs were then loaded with two drops of solution and allowed to dry prior to measurement. A summary of the particle characterisation data collected is shown in Table 4.1.

Additionally, *in situ* measurements of the flocs was achieved using a focussed beam reflectance measurement device (FBRM, model N^0 D600S, originally from Lasentec now manufactured by Mettler-Toledo, Section 2.2.2) in the calibration tank described

in Section 3.2.2 (Figure 3.4) so that the optimum flocculant dose and floc stability over the length of the ABS experiments was known. It should be noted that these experiments were performed separately to the ABS experiments to avoid reflection from the FBRM casing influencing the acoustic measurements. These experiments are detailed further in Section 4.2.5.

4.2.3 Materials characterisation

It was crucial to determine accurate size distributions for the sediments to be studied as these data were subsequently used to produce results that were to be fed into acoustic modelling through Equations 2.12-2.14. A summary of the data collected is presented in Table 4.1. Offline particle size was measured using static light scattering performed in a Mastersizer 2000 (Malvern Panalytical Ltd., UK). Raw intensity-angle data collected in the Mastersizer also allowed for measurement of the fractal dimension using the same method employed by Zhou and Franks [71]. Fractal dimension fits were taken over 20 angles with a search algorithm employed using Matlab 2019b to find the range over which the correlation coefficient was greatest.

From the SEM images shown for calcite and magnesium hydroxide in Figure 4.1 (a) the aggregation behaviour of calcite on drying can be clearly seen as large clusters form that are comprised of smaller particulates of ~3-4 μm, thought here to represent the typical size of the calcite in solution. Similar clusters are seen for the magnesium hydroxide particulates in Figure 4.1 (b) with typical sizes seen of ~4 μm. Both particle sets exhibit significant irregularity in shape that is typical of aggregated mineral systems [65], [134], [248]–[251]. Additionally, both calcite and magnesium hydroxide are typically stated to form roughly spherical aggregates from primary crystalline structures stated to consist of hexagonal nanoplatelets for Magnesium Hydroxide [134] and roughly spherical nanoagglomerates for milled calcite [249]. Although these particles are therefore technically aggregates, they will be referred to as particulates for clarity with respect to flocculated particles (flocs).

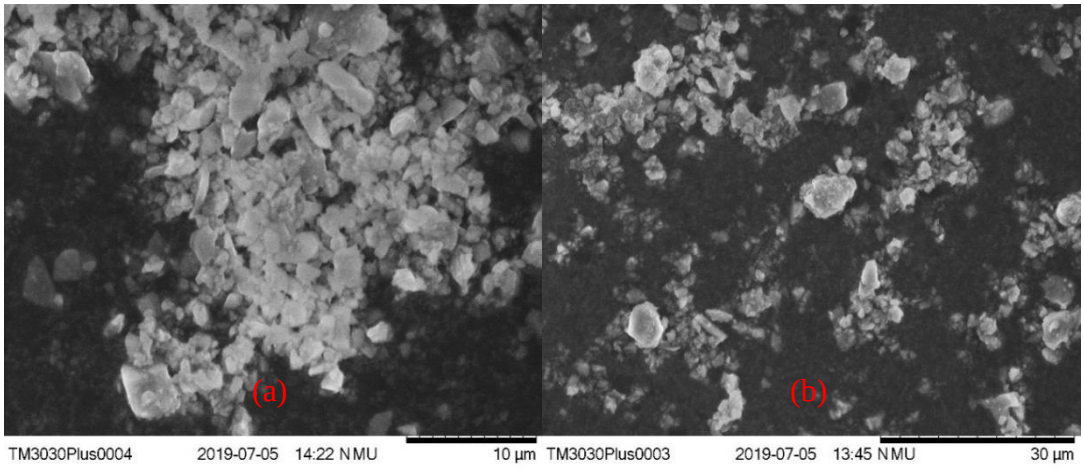

Figure 4.1 SEM images of particulate a) calcite and b) magnesium hydroxide

Particle size distributions are shown for calcite, magnesium hydroxide and Barnon pond sludge (BPS) in Figure 4.2, Figure 4.3 and Figure 4.4 respectively. From the PSD shown in Figure 4.2 it can be seen that the non-flocculated calcite (particulates) has a fairly broad particle size distribution (coefficient of variation, COV = 0.7) with a small degree of aggregation present indicated by the much smaller peak at 100 µm. It is unlikely these larger aggregates would significantly affect the acoustic signal measured during experiments as the extended mixing time in the calibration tank would allow these particles to break up and their volume count is very low. After undergoing flocculation, a size increase is seen accompanied by a small increase in the COV to 0.75. This small increase in the COV is likely caused by some degree of floc breakup indicated by the small shoulder at ~5 µm seen in the flocculated particle results.

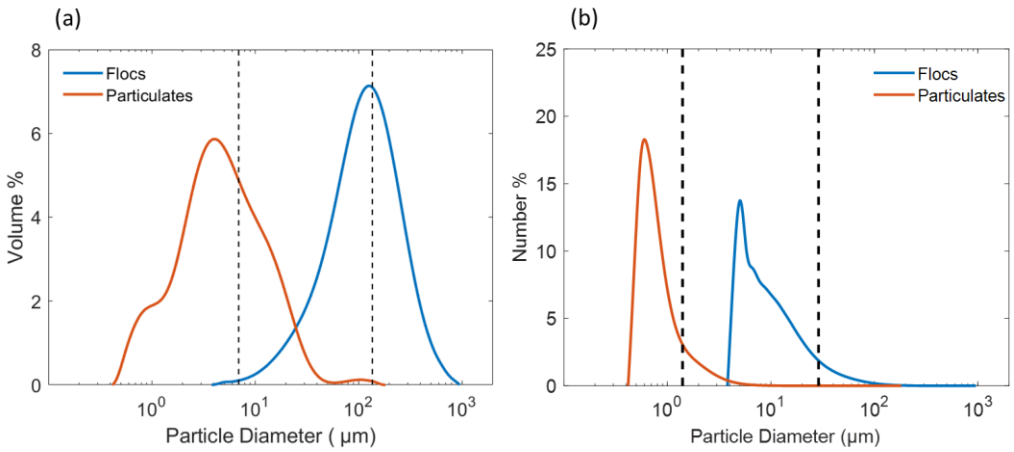

Figure 4.2 Particle Size Distribution for calcite shown as a) a volume distribution with a dotted line indicating the D[4,3] and b) a number distribution with a dotted line indicating the d0 value

Particulate data for magnesium hydroxide, shown in Figure 4.3, indicates some degree of aggregation when compared to the calcite particulate data, with a peak at ~5 µm and a shoulder at ~0.8 µm. It is possible that this shoulder is simply caused by aggregate fracture during measurement; however, such particles are still visible in the SEM images taken (Figure 4.1) and so it is assumed that there is a natural bimodality in the particulate data for calcite and magnesium hydroxide as they are both recognized to be aggregates themselves [134], [249] (although much more densely bound than the flocs). Similar to results presented for calcite (Figure 4.2) a clear size increase is seen during flocculation and the COV was seen to increase from 0.51 to 0.87 and is again attributed to a small amount of floc breakup indicated by the shoulder at ~50 µm. It should be noted, however, that flocs produced using magnesium hydroxide were roughly twice the size of those using calcite and it is therefore expected that they will have differing acoustic properties and therefore allow for investigation of a range of particle structures in the acoustic measurements described in Section 4.2.4.

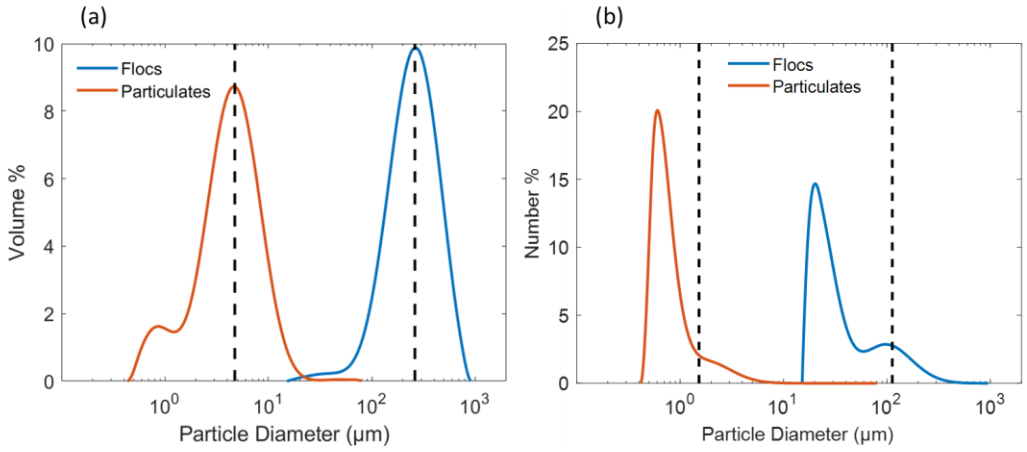

Figure 4.3 Particle Size Distribution for magnesium hydroxide shown as a) a volume distribution with a dotted line indicating the D[4,3] and b) a number distribution with a dotted line indicating the d0 value

Figure 4.4 shows the Mastersizer data obtained for BPS. As the sediment is naturally occurring a much wider size distribution is observed. The largest peak at ~20 µm is assumed here to indicate the typical floc size (based on volume) which would likely be composed of the smaller aggregates indicated by the smallest peak at ~0.6 µm. The secondary peak at 700 µm, although fairly small, would become acoustically significant if it is comprised of dense sediment. Typically, however, particles in this size range and above are suggested to be organic matter that is either fresh or resistant to degradation such as plant material or organic remnants such as charcoal [252] that

would not contribute significantly to the acoustic signal due to their low density. Additionally, on conversion to a number count that is used in the acoustic modelling, these large particles do not represent a significant portion of the distribution as evidenced by the reasonable COV value obtained for the sediment. On a number count, the BPS actually exhibited the smallest floc size studied here (~1.8 μm diameter). Although biopolymers are often known to flocculated particles via the bridging mechanism that typically produces large, strong flocs that are shear resistant this does not appear to be the case for the BPS. As the BPS was obtained from a dairy farm pond the organics content may be expected to be high; it may therefore be the case that excessive bacterial and plant growth has caused the sediment surface to become saturated with these polymers and hence caused some degree of stabilisation that limits further aggregation.

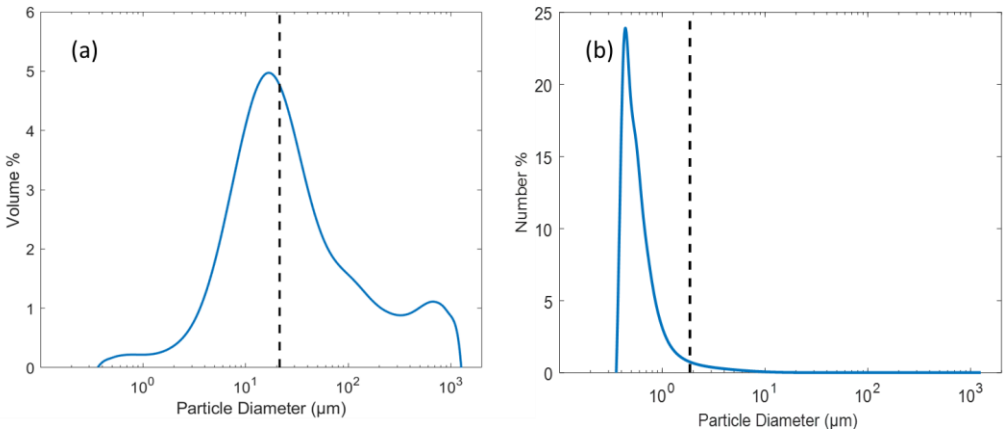

Figure 4.4 Particle Size Distribution for Barnon pond sludge shown as a) a volume distribution with a dotted line indicating the d_{50} and b) a number distribution with a dotted line indicating the d0 value

Figure 4.5 shows the light scattering data from calcite, magnesium hydroxide and BPS that was used to determine the fractal dimension. A good linear fit is seen for all three data sets (all $R^2 > 0.995$) and fractal dimension values correspond to those typically found for flocculated sediments (D_f = 2 – 2.7) [71], [166] indicating an open, porous structure as opposed to that of a solid sphere (D_f = 3). The highest fractal dimension was seen for the magnesium hydroxide flocs with the lowest fractal dimension corresponding to the BPS. Such a result is expected as the flocs in the BPS would have been formed in a comparatively quiescent flocculation environment when compared with the commercial sediments that were flocculated in the impeller mixed calibration tank. Due to the quiescent environment particle collision rates would be correspondingly low allowing time for the natural bio-polymers present to reconform

onto the surface of the particle leading to patching flocculation and a correspondingly lower fractal dimension [71]. Additionally, as the naturally occurring flocculants present in the pond would likely have a lower charge density than AN934SH these fractal dimension results align well with the findings of Zhou and Franks [71] that low charge density polymers tend toward producing flocs via the patching mechanism and also correspond well with fractal dimensions typically found for flocs in coastal and fluvial environments [47], [120], [166].

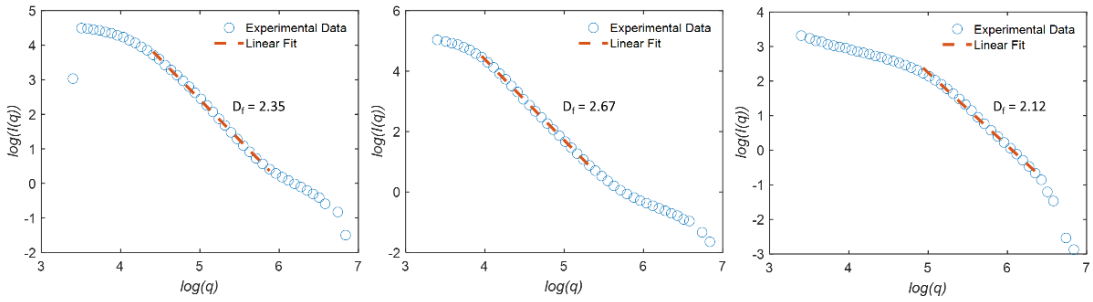

Figure 4.5 Light scattering data for a) flocculated calcite, b) flocculated magnesium hydroxide and c) BPS used to find the fractal dimension

Table 4.1 shows a summary of the particle characterisation data. Floc density was estimated using Equation 2.2 using the fractal dimension values for the flocs determined in Figure 4.5. While the density for magnesium hydroxide and calcite were known BPS sludge particulate density was assumed to be the same as that of kaolinite, used by Thorne *et al.* [47] as a simulant for naturally occurring marine flocs that was thought to therefore be appropriate here. Additionally, it has been found by other authors that the soil primary particle density is typically in a narrow range of 2600-2700 kg m^{-3} with a typical value of 2650 suggested for general mineral soils [253]. A high organic matter content in the BPS may however lead to reduced density compared to more mineral rich soils. This is not thought to be significant here, however as, although addition of dairy manure has been demonstrated to increase organic carbon production in soils [254], particle densities for farmyard manure deposits (2-5 %w/w organic carbon) have been shown to only be as low as 2440–2590 kg m^{-3} [255]. In terms of the repeatability of the floc sizes shown here, it cannot be confirmed how easily these same systems may be reproduced. Considering the system is well-mixed, as evidenced by the sample data shown in Figure 4.6 and Figure 4.7 and the polymer was mixed in-line to ensure an even distribution throughout the tank it is thought that the particle size and structure obtained would be similar if the experiments were to be repeated.

Table 4.1 Particle characterisation data for the calcium carbonate (calcite), magnesium hydroxide ($Mg(OH)_2$) and Barnon pond sludge (BPS)

Material Name	Particle a_0 (µm)	Particle d_{50} (µm)	Coefficient of Variation, COV	Fractal Dimension	Particulate Density (kg m^{-3})	Floc Density
Calcite particulates	0.7	4.3	0.70	-	2710	-
$Mg(OH)_2$ particulates	0.75	4.0	0.51	-	2340	-
Calcite flocs	14.5	107.6	0.75	2.35	2710	1238
$Mg(OH)_2$ flocs	56.3	235.1	0.87	2.67	2340	1288
BPS	0.92	21.4	0.78	2.12	2650	1525

4.2.4 Experimental apparatus and acoustics experimental methodology

Measurements were taken in an impeller agitated calibration tank that is previously described in Section 3.2.2 (Figure 3.4) over a range of 0.3 metres using 3 transducers (PIM501, PIM5025 and PIM3750 from Sonatest Ltd., UK) arranged in an equilateral triangle, facing perpendicular to the tank base in the same configuration as those in Chapter 3. The transducers had central frequencies of 1, 2.25 and 5 MHz and were additionally pulsed at approximately +/- 15 % of the central frequency. These transducers were selected over those used in the previous study (Section 3.2.2) as they allowed for exploration of wider array of frequencies. The NFCF recalculation method (Section 3.2.3, Equation 3.1) was not performed during the k_t calibration as the signal-to-noise ratio for the lowest frequency probe (1 MHz) limited the accuracy of the calibration. In order to avoid introducing error from a poorly fit NFCF for particular probes, and as the previous data (Section 3.3.1, Figure 3.9) had shown fairly good agreement with the Downing *et al.* [163] model, it was decided to use the standard formulation for the NFCF (Section 2.3.1, Equation 2.6) for consistency when processing the data.

For the cohesive sediment studies, 5 nominal particle concentrations (4 for BPS) ranging from 2.5 to 40 g l^{-1} were investigated for both particulate and flocculated sediments. A schematic and full description of the experimental setup and sampling methodology are given in Section 3.2.2, Figure 3.4. The sample data is shown in Figure 4.6 and Figure 4.7 and in Table 4.2 for the particulate and floc data

respectively for calcite, magnesium hydroxide and BPS. It was found that in almost all cases, the sampled particle concentration was lower than the nominal weighed concentration for the floc data likely caused by settling on the top of pipework and the probe bracket used to secure the ABS probes. For the Barnon sludge, however, the measured concentration is slightly higher in most cases and is likely a result of the inherent inhomogeneity of the sludge itself leading to variation between the initial bulk density and the diluted sludge concentrations shown here. Samples taken before and after each measurement do not indicate that the particle concentration is changing with time however although a small degree of change is seen for the very highest concentration for calcite and magnesium hydroxide (highlighted with red arrows). Additionally, no significant scatter is seen in the resulting decibel profiles and so it is assumed that this effect is not significantly affecting the results. Furthermore, no concentration gradient is seen with distance from the transducer in the results and so it is assumed that the dispersions were homogeneous in all cases.

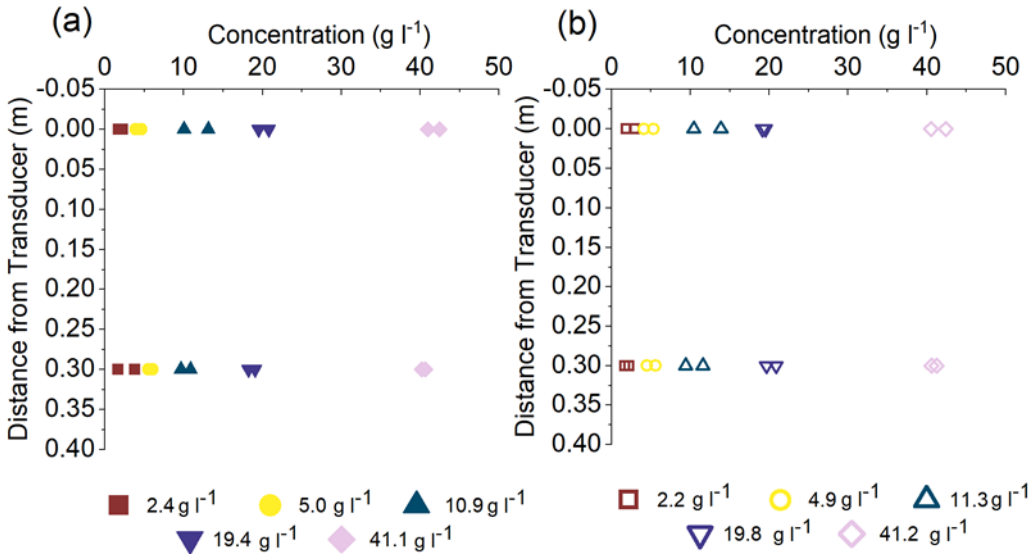

Figure 4.6 Gravimetric sample data for particulate sediments a) calcite and b) magnesium hydroxide

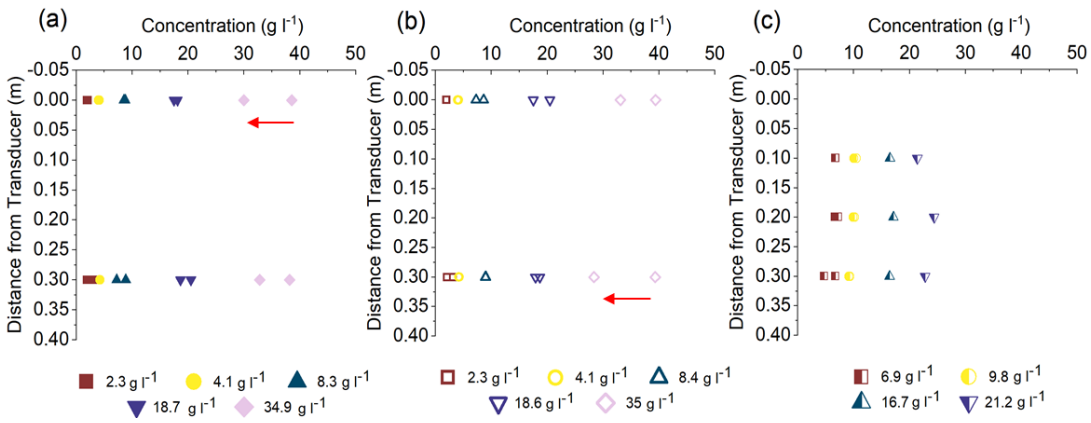

Figure 4.7 Gravimetric sample data for flocculated sediments a) calcite, b) magnesium hydroxide and c) BPS. Red arrows indicate where a notable change in concentration was observed in samples before and after acoustic measurement.

Table 4.2 Nominal weighed and measured concentrations for all cohesive sediment systems studied (all concentrations are in g l^{-1})

	Calcite Particulates	Calcite Flocs	Magnesium Hydroxide Particulates	Magnesium Hydroxide Flocs	Barnon Pond Sludge	
Nominal	Measured	Measured	Measured	Measured	Nominal	Measured
2.5	2.4	2.3	2.2	2.3	5.0	6.9
5.0	5.0	4.1	4.9	4.1	10.0	9.8
10.0	10.9	8.3	11.3	8.4	15.0	16.7
20.0	19.4	18.7	19.8	18.6	20.0	22.9
40.0	41.1	34.9	41.2	35.0	-	

4.2.5 Flocculating polymer dose and stability studies

In order to ascertain that floc size would be stable over the course of acoustic measurement and to obtain the optimum polymer dose to produce these stable flocs a focussed beam reflectance measurement device (FBRM, model N^0 D600S, originally from Lasentec now manufactured by Mettler-Toledo, Section 2.2.2) was used to take *in situ* measurements during flocculation in the calibration tank described in Section 3.2.2 (Figure 3.4). The FBRM probe was mounted facing downward into the tank at a 45-degree angle with the window placed at the manifold outlet to maximise particle counts for a more accurate measurement of the system. Flocculant was added at ~5 ml/s using a small peristaltic pump with the outlet placed 0.1 metres above the

impeller to ensure the flocculant was well-mixed into solution so that flocs of a consistent structure were produced.

In order to mimic the conditions that were to be used in the ABS experiments the calcite was flocculated from primary particles at a concentration of 4 %w/w, the same concentration at which the flocs are initially produced for the acoustic studies, for each floc concentration shown in Figure 4.8. The observed particle size increased for experiments with a greater flocculant concentration up until the observed optimum dose of 40 ppm that was subsequently used for all ABS studies. This result is expected and attributed to the fact that a greater flocculant concentration will increase the amount of bridges able to be formed by particles and thus larger, more stable flocs will be formed during flocculation [67]. In contrast, higher floc concentrations will lead to steric stabilisation and only weaker Van der Waals forces between particles and correspondingly low fractal dimensions [71]. Of particular relevance to the ABS experiments, all floc doses were seen to achieve a stable size after ~30 minutes that did not change with time thereafter with the 40 ppm dose showing particularly good stability that is typical of bridging flocculation [71].This therefore indicates that these flocs will retain their size, and hence acoustic properties [33], as well as mimic the structure of legacy wastes at Sellafield Ltd. [40], [49], [50].

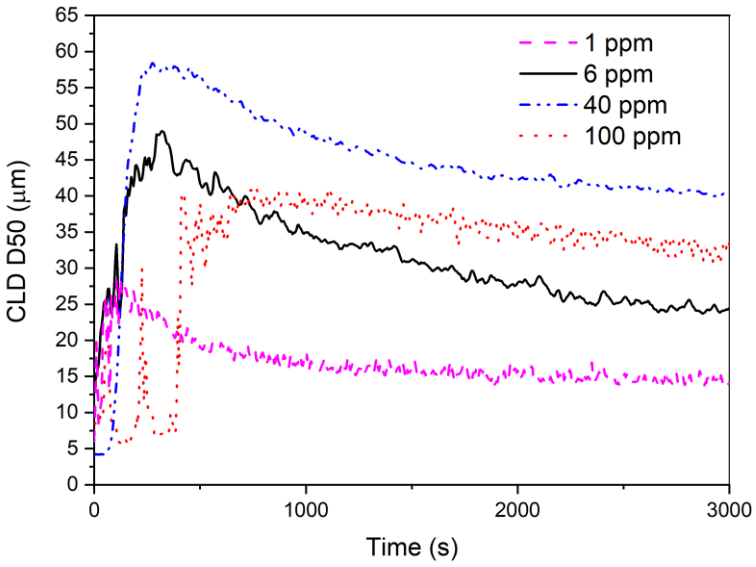

Figure 4.8 Median particle diameter of the chord length distribution (CLD) measured by the FBRM as a function of time for each polymer dose.

In order to confirm that floc size would be maintained over the course of the acoustic experiments, further measurements FBRM measurements were taken using the

chosen floc concentration (40 ppm) with calcite particles flocculated at a concentration of 40 g l^{-1} over 2 hours. As acoustic measurements were taken 30 minutes after the flocculant was added and were typically completed in just over an hour this measurement time therefore spans that used to take acoustic measurements. Additionally, as acoustic measurements involved emptying periods during which the stirring rate was reduced, the constant stirring rate used in this study represents a worst-case scenario in terms of floc breakup would indicate the maximum possible deviations that might be observed in the particle size. As the mean particle number count and coefficient of variation (COV) are the model input parameters for the Hybrid model these were determined from FBRM results by converting chord length distributions to particle size distributions using the method proposed by Li and Wilkinson [131]. The model was implemented in Matlab 2019b using a function kindly provided by Dr Michael Johnson. Particles were assumed to be spherical and it was assumed that the particle size distribution would lie within the measurement bins of the FBRM. The results for the mean size and COV obtained from the FBRM as a function of measurement time are shown in Figure 4.9 below beyond 1800 seconds, after which acoustic measurements would nominally be taken. Although there is some variation in the mean size it remains relatively constant with time. Additionally, the values observed for both the mean size and COV are seen to agree with those determined using *ex situ* static light scattering (Table 4.1) indicating that values obtained for the other flocculated datasets may also be reliable.

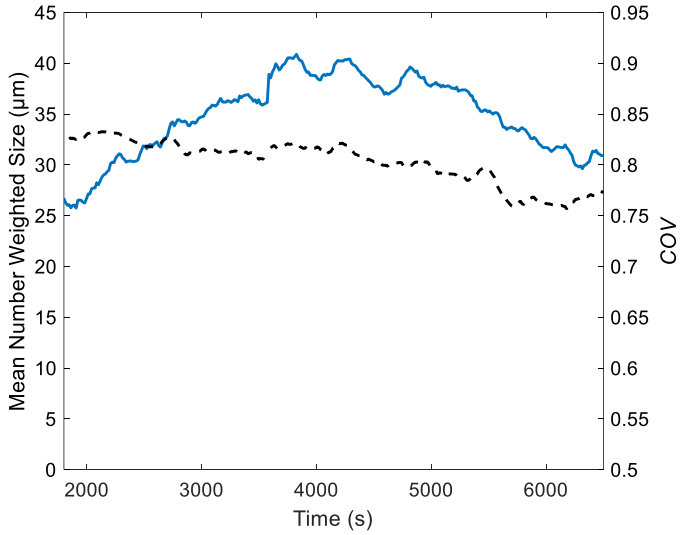

Figure 4.9 Mean size (——) and COV *(---)* as a function of time produced by conversion of FBRM chord length distributions to particle size distributions

4.2.6 Acoustic analysis methodology

The attenuation coefficient was found using the Extended *G-function* method (described in Section 2.3.4) and a heuristic expression [48], [159] used to find the backscattering constant. These values were then used with the experimental voltage profiles to find the transducer constant, k_t, for the system and recalculate the backscatter constant, k_s. This was performed using 1, 2 and 5 MHz probes from Sonatest Ltd., UK, additionally pulsed at ~+/- 15 % of their central frequency. Honite 16 was used as it generally gave decibel profiles that were both above the noise floor and the linear *G-function* distance profiles predicted by single scattering theory (Section 3.3, Figure 3.7 (h)) and so was therefore thought to be the particle system that was least affected by noise and erroneous values in the obtained k_t profiles. The same methodology described in Section 3.2.2 was employed to take the measurements using the Sonatest transducers with an alternate probe bracket (due to the greater diameter of the Sonatest probes). The profiles for 2.5 and 5 g l^{-1} were used to calculate the transducer constant, k_t, are shown in Appendix B (Figure B.1).

dG/dr fits for each sediment system studied here were taken in Matlab 2019b by searching for the maximum gradient for a line fit of ~0.05 m practical length. Raw data outside the noise floor was discarded when calculating these fits. The same distance over which *dG/dr* was calculated was also used to calculate k_s as it was thought that, as the algorithm searches for the maximum gradient, it would therefore identify a region for which the effects of the noise floor and near-field region were least significant. k_s values for the lowest two concentrations for each data set were averaged to calculate the form function.

The experimentally determined attenuation coefficient and backscatter constants for the cohesive sediments studied in this chapter were then converted to their dimensionless equivalents, the scattering cross-section, χ, and the form function, f, and normalised by the specific gravity and square root of specific gravity respectively to allow for comparison to predictions from modelling and to normalise results from both primary particles and flocs to facilitate direct comparisons between each sediment system. The densities for each case were estimated using the mean particle number size (Section 4.2.3, Table 4.1) and fractal dimension measured using static light scattering (Section 4.2.3, Figure 4.5) in combination with Equation 2.54. The

COV and number mean size were used to produce log-normal model fits to the PSDs shown in Section 4.2.3. The COV was taken into account during modelling using Equation 2.13 using 1,000,000 logarithmically space size classes between 0.1 μm and 1 cm in order to capture the full range of the particle size distributions measured with suitable accuracy.

The Hybrid model [47] was implemented in Matlab using code provided by Thorne *et al.* [47] with modifications made to implement the fractal dimensions relationship to the primary particle size in Equation 2.2. The Hybrid model was chosen as a comparison to the Irregular Solid Scattering model that was also implemented as it incorporates the floc density and compressional wave speed that could be expected to influence the scattering and attenuation parameters of the flocculated particles in suspension and has been shown to allow for more accurate modelling previously [31], [47]. The compressional wave speeds used in the model were 5450 m s^{-1} for calcite taken as an estimate from data collected by Verwer *et al.* [256], 4800 m s^{-1} for Magnesium Hydroxide taken from Duffy *et al.* [257] and 1400 m s^{-1} for BPS taken from Marshall and Lineback [258] for data from sediment cored from Lake Michigan as an estimate for typical sediment sound speed in lentic environments. The particulate densities used were 2710, 2340 and 2650 kg m^{-3} for calcite, magnesium hydroxide and BPS respectively as shown in Table 4.1. Primary particle sizes used to estimate floc density were taken from the particulate Mastersizer measurements and an estimate of 0.8 μm used for BPS was used as this was the location of a small tertiary peak in the Mastersizer data (Figure 4.4, Section 4.2.3).

Concentration inversion was performed using the same method as presented in Section 3.2.3 except that the dual frequency profiles were produced using frequency pairings across different probes with all possible combinations therein explored resulting in 27 frequency combinations for each material studied. Frequency combinations across the different probes were used as it was thought that this would produce attenuation coefficient ratio further than unity and hence give a more accurate inversion [15]. A table of the attenuation coefficient ratios determined from experimental data is presented at the end of Section 4.3.1.2.

4.3 Results and discussion

4.3.1 Raw data and determination of acoustic constants

In this section raw data and *G-function* profiles are presented and analysed with respect to their attenuation, given by the slope of the signal, the overall backscattering strength, and the effect on the signal as it approaches the noise floor. Following this the plots used to determine the attenuation coefficient, given by the slope of *dG/dr* versus concentration, and k_s obtained using the method given by Bux *et al.* [17] are discussed in relation to their change upon flocculation from primary particulates and with both insonification frequency and sediment type.

4.3.1.1 Decibel and G-function profiles

Figure 4.10 shows the raw decibel and *G-function* data for particulate calcite at the central frequency of each probe used in this study. The profiles seen here are typical for moderately attenuating species with the expected linear relationship between *G-function* and distance, indicative of the level of attenuation, seen until the signal reaches the noise floor of the probe [189] at which point the decibel profile flattens and the *G-function* profile follows a logarithmic increase with distance. Additionally, the typical increase in attenuation with increasing frequency is also observed, as shown in Figure 4.11, that would be predicted by Equation 2.59 that has also been observed by previous authors for irregularly shaped sediments [33], [48], [143], [174], [175].

Figure 4.12 shows the decibel and *G-function* profiles for flocculated calcite. The observed attenuation for the flocculated calcite is seen here to be similar to that seen in the particulate case and for 1 and 2.25 MHz is seen to decrease slightly as shown in Figure 4.13. Although a size increase typically leads to a larger scattering cross-section and therefore greater attenuation, as the calcite flocs will also become increasingly porous with size, the attenuation may also decrease as the acoustic contrast (indicated by the sound speed ratio $\zeta(a)$, Equation 2.55) will decrease with increasing size and porosity [47], [166]. This small decrease in attenuation (Figure 4.11 and Figure 4.13, also evidenced in Table 4.3) might be attributed to the decrease in bulk concentration due to a small degree of particulate build-up on pipework within the tank (it should be noted that this has been taken account of by

using the concentration determined from sampling for further calculations). This build up is not thought to be significantly altering the concentration over the course of the measurements, however, as there is only very minimal scatter seen for the time-averaged decibel profiles. Additionally, an increase in the overall scattering strength, indicated by the peak values close to the transducer, is seen in the 5 MHz data and for higher (>2.3 g l^{-1}) concentrations in the 2.25 MHz data when comparing the flocculated and particulate cases. Furthermore, the attenuation is also seen to decrease slightly upon flocculation with no signals reaching the noise floor until the upper concentration measurements at 5 MHz (as opposed to at 1 MHz in the particulate case, also evidenced more clearly in Table 4.3). Such an increase may again be attributed to the larger size and the tendency of scattering strength, linked through the form function (*f*, Equation 2.58), to increase with particle size.

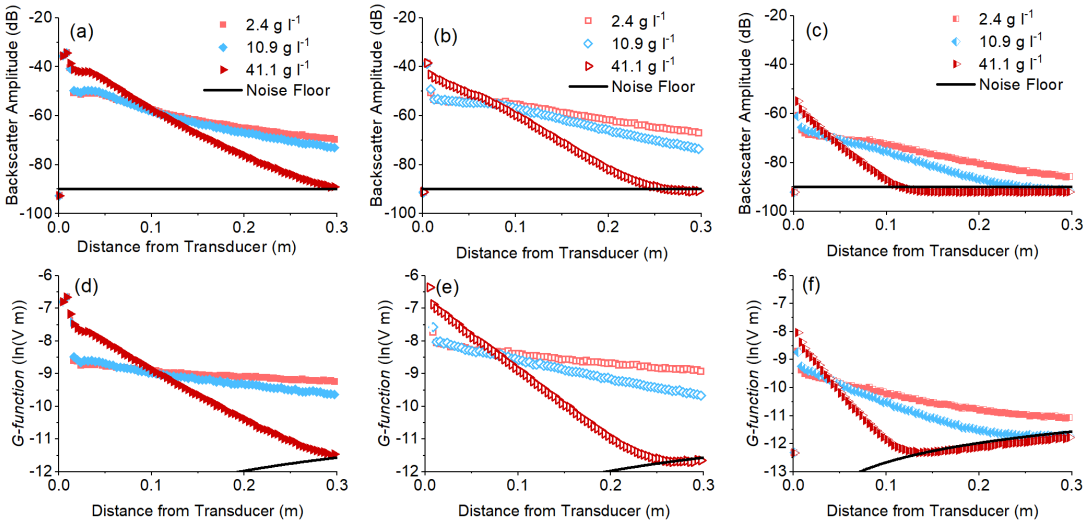

Figure 4.10 a) – c) Decibel profiles and d) – f) *G-function* profiles for particulate calcite at 1, 2.25 and 5 MHz both including the near-field correction factor

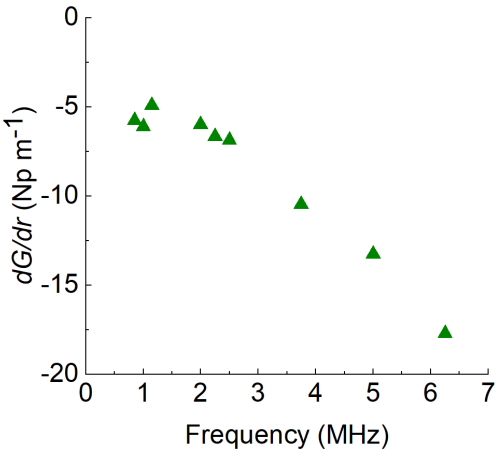

Figure 4.11 Attenuation plotted as a function of frequency for particulate calcite for a weighed concentration of 10 g l^{-1}

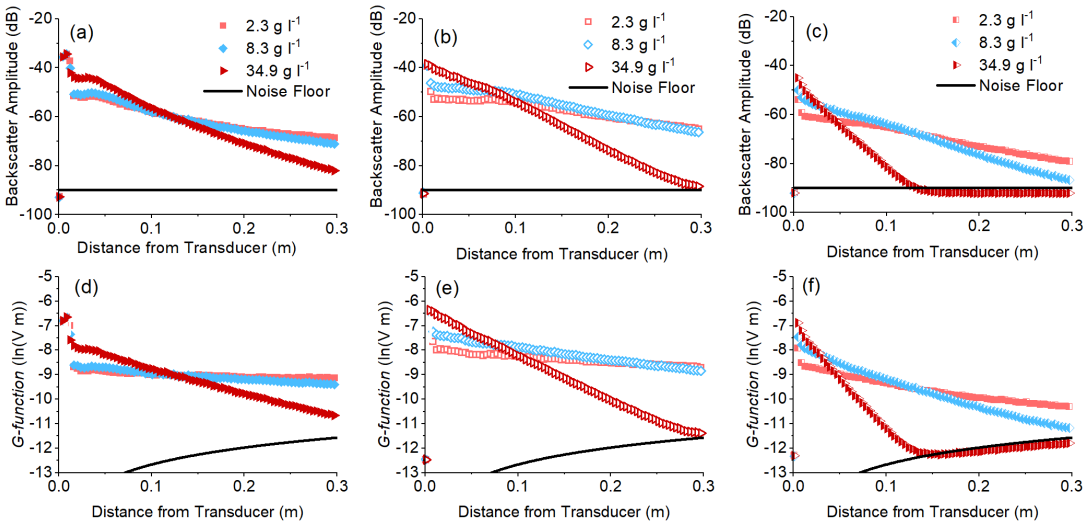

Figure 4.12 a) – c) Decibel profiles and d) – f) *G-function* profiles for flocculated calcite at 1, 2.25 and 5 MHz both including the near-field correction factor

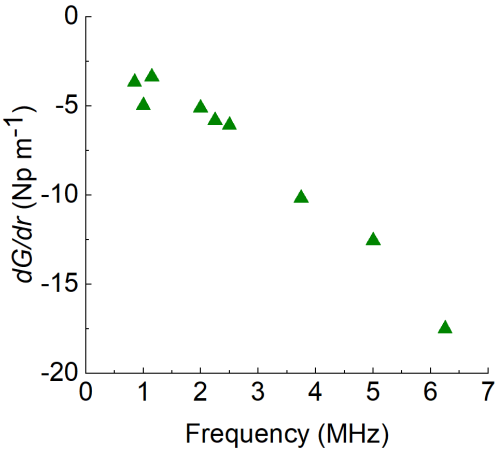

Figure 4.13 Attenuation plotted as a function of frequency for flocculated calcite for a weighed concentration of 10 g l^{-1}

In contrast to the results seen for the particulate calcite (Figure 4.10), the particulate magnesium hydroxide data, shown in Figure 4.14, indicates a high degree of attenuation and the expected linear relationship between the *G-function* and distance is limited to a small window close to the probe for the highest concentrations. The high degree of curvature in the *G-function* profiles, despite the signal being above the instrument noise floor, is indicative of multiple scattering effects, resulting from the large amount of attenuation, that cause the effective noise floor of the system to become elevated as has been observed in recent publications [187], [188], [235] and in results presented in the previous chapter (see Section 3.3.1, Figure 3.7).

Figure 4.16 shows the decibel and *G-function* profiles for magnesium hydroxide after flocculation. In both the particulate and flocculated case the expected increase in

attenuation with frequency is not seen, where a slightly decreasing attenuation is actually observed with increasing frequency for particulate magnesium hydroxide (Figure 4.15) and a decrease followed by an increase in attenuation with increasing frequency for flocculated magnesium hydroxide (Figure 4.17). These results contrast with expected relationship between frequency and attenuation that suggests that attenuation increases with frequency and is discussed further in Section 4.3.1.2. No significant change in the peak scattering strength, even very close to the transducer, was seen between the particulate and flocculated case. However, this change may be obscured by the much greater attenuation in the particulate case.

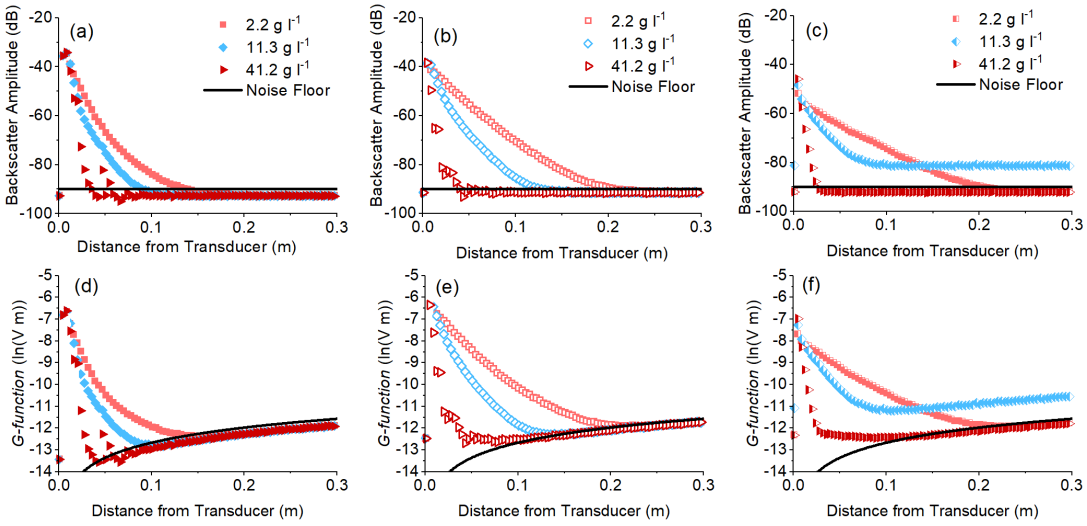

Figure 4.14 a) – c) Decibel profiles and d) – f) *G-function* profiles for particulate magnesium hydroxide at 1, 2.25 and 5 MHz both including the near-field correction factor

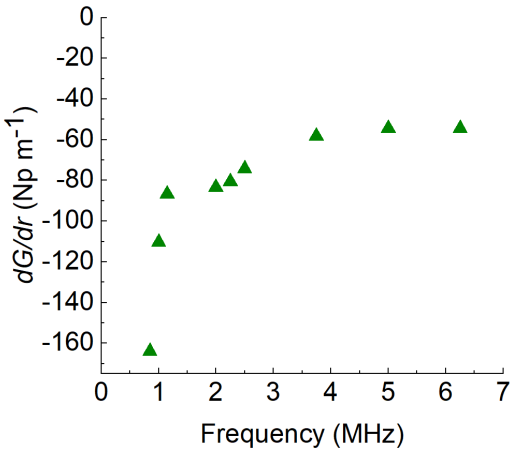

Figure 4.15 Attenuation plotted as a function of frequency for particulate magnesium hydroxide for a weighed concentration of 10 g l^{-1}

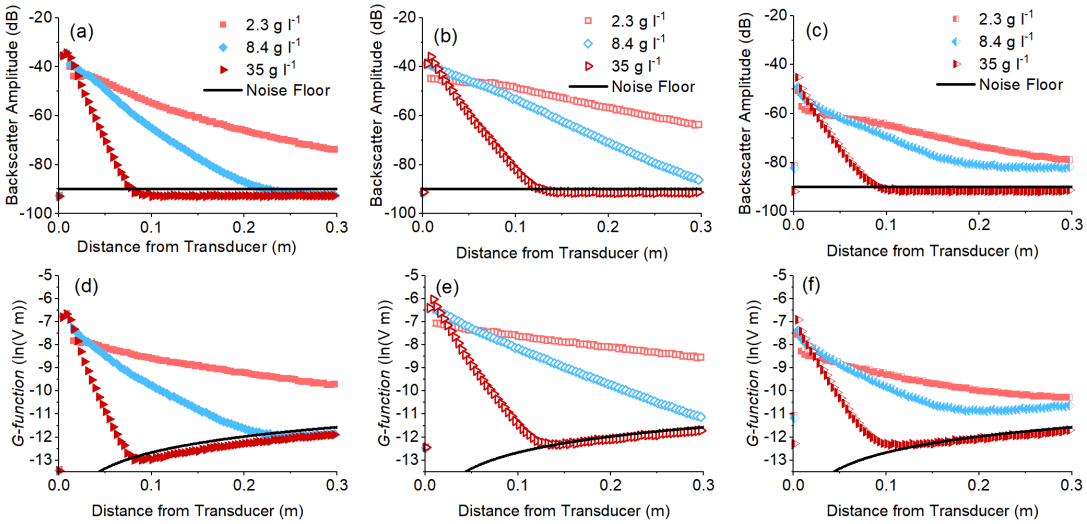

Figure 4.16 a) – c) Decibel profiles and d) – f) *G-function* profiles for flocculated magnesium hydroxide at 1, 2.25 and 5 MHz both including the near-field correction factor

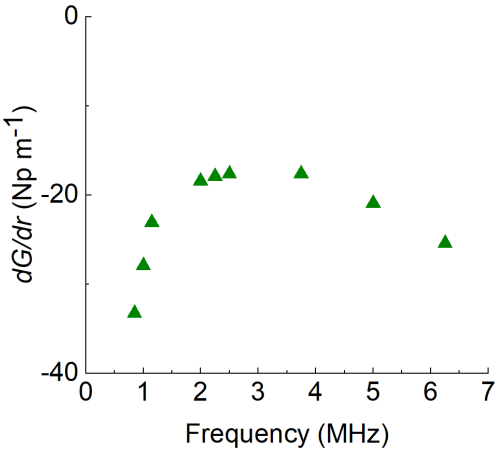

Figure 4.17 Attenuation plotted as a function of frequency for flocculated magnesium hydroxide for a weighed concentration of 10 g l^{-1}

Finally, the BPS data shown in Figure 4.18 seems to indicate attenuation values similar to those seen for the flocculated calcite (Figure 4.12) albeit with a greater degree of curvature likely caused by the aforementioned multiple scattering effects enhancing the effective noise floor of the system [235] and thus causing deviation from the expected linearity between the *G-function* and distance. Otherwise, however, the expected trend of increasing attenuation with increasing frequency is clearly seen for the BPS in Figure 4.19 and indicates that sediments that have been allowed to aggregate through natural flocculation processes such as algal growth may follow similar trends to simulant systems. Such data may allow for better estimation of the acoustic parameters necessary for concentration measurement in long term waste repositories where organic matter has been allowed to produce similar particle structures [50].

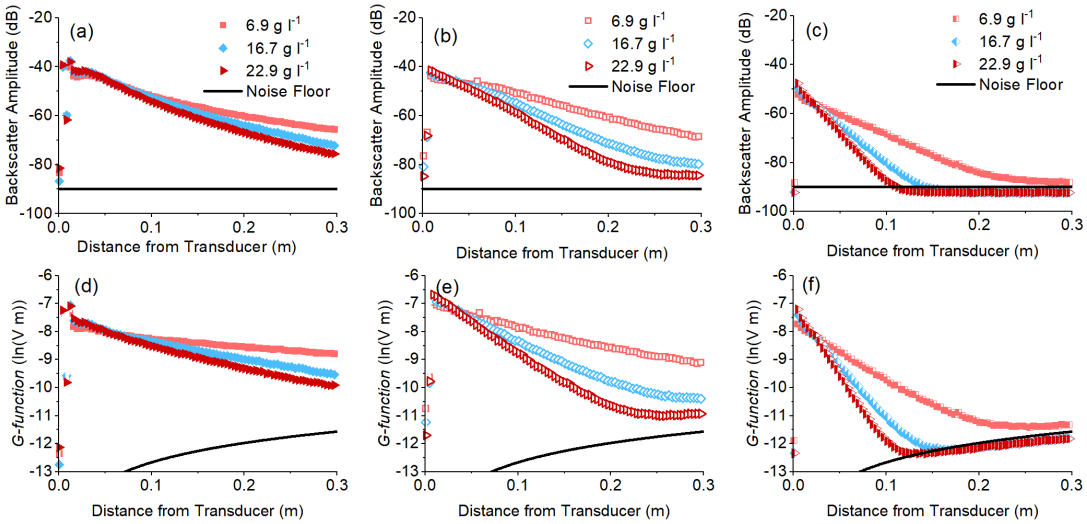

Figure 4.18 a) – c) Decibel profiles and d) – f) *G-function* profiles for BPS at 1, 2.25 and 5 MHz both including the near-field correction factor

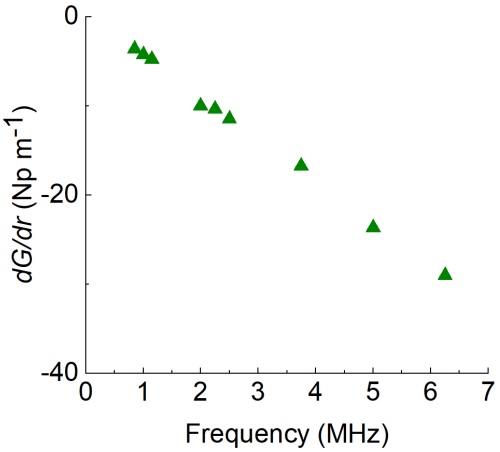

Figure 4.19 Attenuation plotted as a function of frequency for BPS hydroxide for a weighed concentration of 10 g l^{-1}

Overall, the expected increase of attenuation with frequency [15], [17], [33], [160], [185], [259] are readily observed in the calcite and BPS data indicating the potential of ABS to qualitatively characterise the concentration and flocculation state of sediments of varying mineralogical and organic composition. Furthermore the significant differences seen between the three sediments used in this study indicate that ABS may also possibly be used to characterise changes in the aggregate micro-structure of a system provided changes in concentration and size can be accounted for by supporting information from another *in situ* measurement device such as FBRM [260] or PVM [110], [134] technology though this would require extensive further study to conclude with certainty.

4.3.1.2 Determination of the Attenuation Coefficient (ζ)

Figure 4.20 shows the values obtained from the *G-function* profiles presented in the previous section as part of the method previously developed by Rice *et al.* [15] (See Section 2.3.4) that has also been utilised successfully by recent authors [17]. Good linear fits are seen for all the *dG/dr* fits in Figure 4.20 and an increase in the attenuation coefficient, *ζ,* with frequency, indicated by an increasingly negative gradient on the plots, is clearly seen in Figure 4.20 and Figure 4.21. This result is also expected so long as the particles remain within the Rayleigh regime (*ka << 1)* but above *ka* values at which viscous attenuation effects begin to dominate the acoustic signal.

As is the case for the particulate calcite, the flocculated calcite results presented in Figure 4.22 exhibit an increase in the attenuation with frequency. Such results indicate the importance of a widely varied frequency if the dual frequency method is to be employed so that an ideal probe/frequency range can be selected. More importantly perhaps, is the indication from these results that in some cases flocculation does not induce a significant change in the attenuation coefficient thus allowing the ABS to act as a robust device for concentration measurements even during aggregation processes. For both the particulate and flocculated cases, the change in attenuation with frequency is approximately linear but begins to plateau slightly at the highest frequency used. As the dual frequency method relies on a sufficient difference between the attenuation at two different frequencies, identification of such plateaus may allow for quick determination of the frequency limits for application of the dual frequency method.

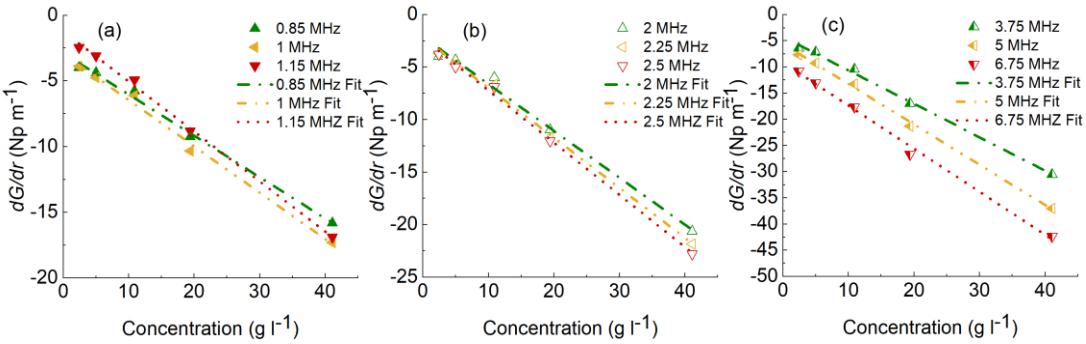

Figure 4.20 *dG/dr* vs concentration plots for particulate calcite to allow for determination of attenuation coefficient at a) 1, b) 2.25 and c) 5 MHz

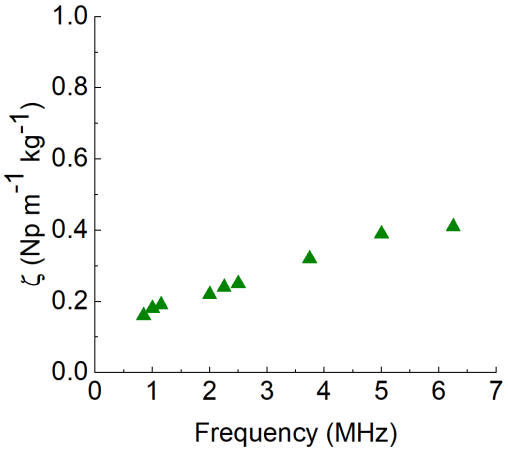

Figure 4.21 Attenuation coefficient vs frequency plot for particulate calcite

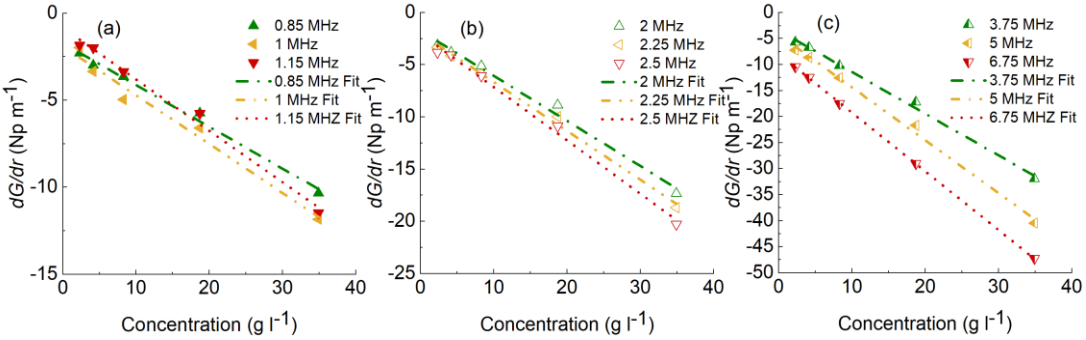

Figure 4.22 *dG/dr* vs concentration plots for flocculated calcite to allow for determination of attenuation coefficient at a) 1, b) 2.25 and c) 5 MHz

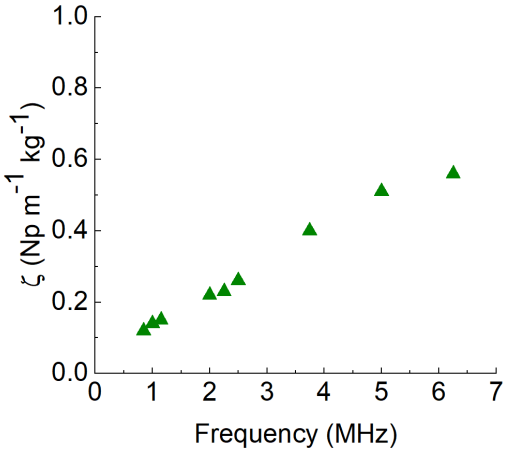

Figure 4.23 Attenuation coefficient vs frequency plot for flocculated calcite

Figure 4.24 and Figure 4.26 show the attenuation data for particulate and flocculate magnesium hydroxide respectively. Most notably the attenuation for the particulate magnesium hydroxide systems is typically almost an order of magnitude greater than those seen for the calcite with a significant reduction in attenuation when flocculated (although still more attenuating when compared to the flocculated calcite). The exact cause of this excess attenuation is unknown however it may be related to the

nanocrystalline aggregate structure of the primary particulates [134], [251] that may also be interacting with the acoustic wave. Duhkin and Goetz [151] hypothesised that, for gels made by either very small nanoparticles or polymer, structural attenuation will become significant and needs to be accounted for, and suggested such a result had been observed by Hayashi *et al.* [261] and may also be the case here.

In both cases a decrease is seen in attenuation with increasing frequency for the 1 MHz probe before becoming insensitive at higher frequencies. Such a result contrasts with scattering attenuation theory that predicts an increase in attenuation with frequency [33]. It has also been postulated by Portune [262] that inter-particle thermo-elastic absorption becomes the dominant absorptive acoustic mechanism for dense polycrystalline ceramics at low frequencies and may therefore be causing the increase in attenuation with decreasing frequency that is not predicted by scattering theory [33]. A similar result has been observed to a small degree for calcite suspensions previously studied by Inam and Frances [263] and was attributed to a decreasing signal-to-noise ratio at lower frequencies that is also observed in the decibel data collected here for magnesium hydroxide (shown in Figure 4.14). An increase in attenuation with decreasing frequency has also been observed by Bux [264] for aggregated latex where it was suggested that enhanced inter-particle interactions in the networked structure at longer wavelengths may be the reason for deviation from the expected increase in attenuation with increasing frequency.

In the data presented here it would seem that the decrease in attenuation with frequency becomes less pronounced upon flocculation. The absence of this effect at larger particle sizes may therefore indicate that inter-particle viscous effects, known to decrease with increasing particle size as the average inter-particle distance increases [143], are the cause of this phenomenon. Indeed, overlap of the viscous layer surrounding neighbouring particles has been attributed by previous authors [185], [265] to cause a peak value in attenuation per wavelength as thermal or viscous layer overlap causes reduced energy dissipation (i.e. attenuation) and has been proposed by Fugate and Friedrichs [35] to be significant even for flocculated particles. Such results are not promising for concentration inversion, therefore, due to the inversion method's reliance on the measured particle system lying within the Rayleigh regime with no significant multiple scattering effects. *dG/dr* values for particulate magnesium

hydroxide at high concentrations are also generally seen to fit poorly with the linear fit used to find ζ; likely caused by enhancement of the noise floor due to the excessive attenuation in the system (approximately an order of magnitude greater than the calcite when comparing the particulate cases). Such an effect is predicted by Dukhin and Goetz [185], however, as they propose that the peak attenuation is shifted to higher frequencies at high concentrations. For a selected frequency, therefore, as the concentration is increased the attenuation will increase until the peak value moves past the selected frequency subsequently causing a decrease in attenuation (see Figure 1 in Dukhin and Goetz [185]) and may possibly be the case here though this is generally indicated to occur only at much higher solids content than used in this study.

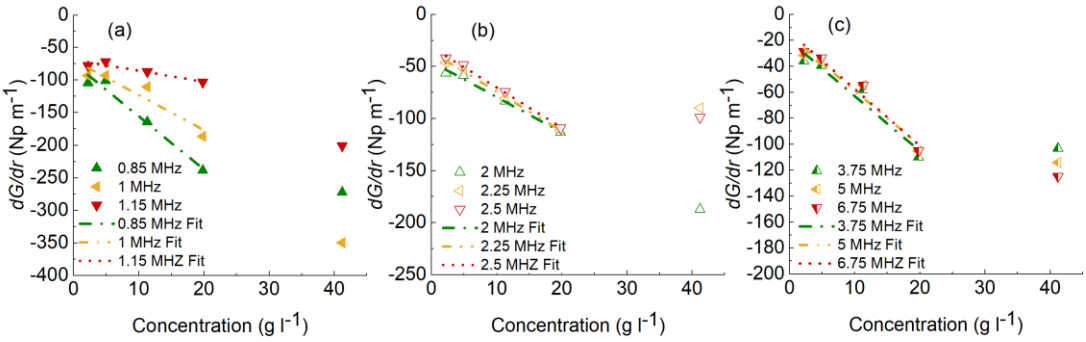

Figure 4.24 *dG/dr* vs concentration plots for particulate magnesium hydroxide to allow for determination of attenuation coefficient at a) 1, b) 2.25 and c) 5 MHz

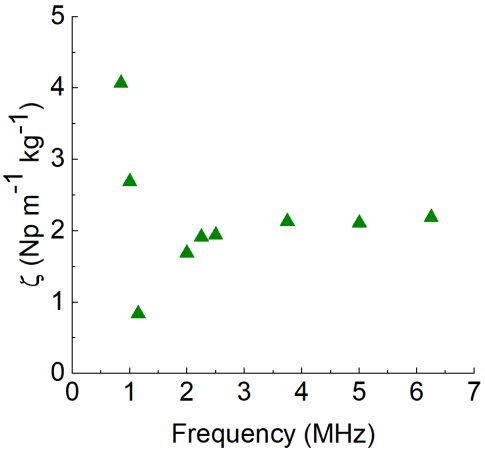

Figure 4.25 Attenuation coefficient vs frequency plot for particulate magnesium hydroxide

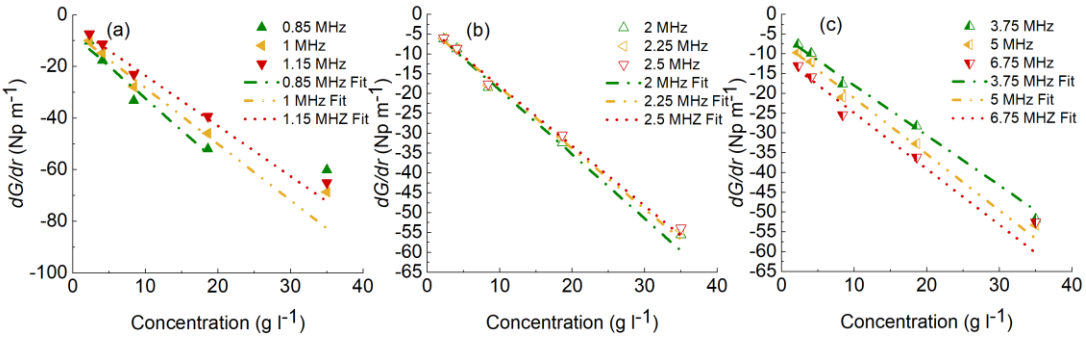

Figure 4.26 *dG/dr* vs concentration plots for flocculated magnesium hydroxide to allow for determination of attenuation coefficient at a) 1, b) 2.25 and c) 5 MHz

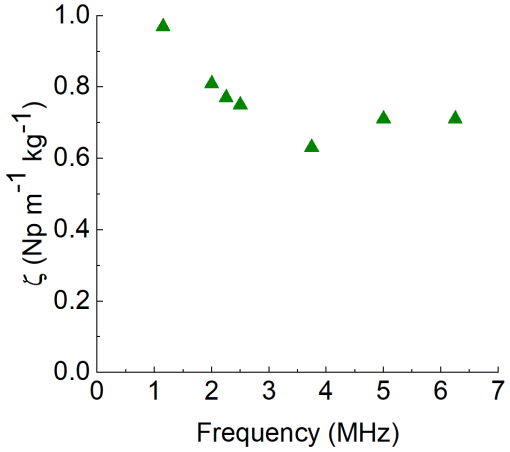

Figure 4.27 Attenuation coefficient vs frequency plot for flocculated magnesium hydroxide

Attenuation plots for the BPS are shown in Figure 4.28 and demonstrate a good linear fit with observed attenuation values slightly greater than those seen for flocculated calcite; this may be the result of the presence of silty sediment in the BPS that will have a high density and hence acoustic contrast [255]. Qualitatively, *dG/dr* values seen for the BPS are small enough that a reliable correlation between attenuation and concentration can be drawn. This therefore highlights the ability of ABS to draw similar relationships for wastes at Sellafield that might resemble the naturally occurring flocs studied here. Additionally, the attenuation exhibits a clear frequency dependence over all frequencies used for this study and is likely related to the much wider size distribution observed for this sediment (see Section 4.2.3) meaning that a significant portion of the particles always lie within the Rayleigh regime where the attenuation will be sensitive to the frequency [15], [33]. It is for this reason that accurate representation of the size distribution needs to be incorporated or accounted for in acoustic modelling and such effects are discussed in the proceeding section (Section 4.3.2). *dG/dr*, attenuation coefficient values with corresponding R^2 values and the attenuation coefficient ratios used for the dual frequency analysis in 4.3.3 are shown in Table 4.3, Table 4.4 and below. Overall, all particle datasets presented here

show a good linear fit up to 20 g l^{-1} indicating that, even if precise concentration profiles cannot be produced, the qualitative relationship between *dG/dr* and concentration could be used to give an estimate for the *in situ* concentration up to moderate concentrations that would still be of great use for optimising settling and transport processes at Sellafield Ltd, and in other industrial applications with similar requirements for remote measurement.

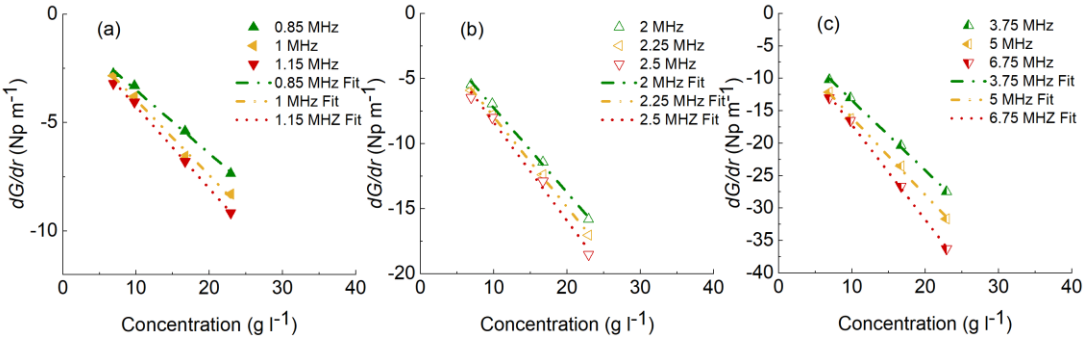

Figure 4.28 *dG/dr* vs concentration plots for BPS to allow for determination of attenuation coefficient at a) 1, b) 2.25 and c) 5 MHz

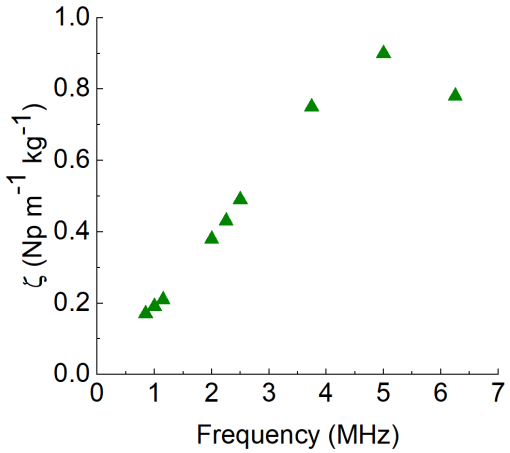

Figure 4.29 Attenuation coefficient vs frequency plot for particulate calcite

Table 4.3 *dG/dr* values with corresponding R^2 determined from fits of graphs from Section 4.3.1 for calcium carbonate and magnesium hydroxide particulates and flocs and BPS flocs

		Calcite Particulates		Calcite Flocs		Magnesium Hydroxide Particulates		Magnesium Hydroxide Flocs		BPS	
		dG/dr	R^2	*dG/dr*	R^2	*dG/dr*	R^2	*dG/dr*	R^2	*dG/dr*	R^2
0.85 MHz	Conc 1	-4.0	0.88	-2.3	0.70	-104.5	0.99	-10.3	0.99	-3.1	0.95
	Conc 2	-4.4	0.94	-3.0	0.86	-101.2	0.99	-17.7	0.997	-3.6	0.87
	Conc 3	-5.8	0.94	-3.7	0.88	-164.1	0.95	-33.3	0.99	-6.0	0.97
	Conc 4	-9.3	0.98	-5.7	0.95	-238.6	0.90	-51.9	0.99	-8.6	0.99
	Conc 5	-15.8	1.00	-10.3	0.99	-272.2	0.93	-60.1	0.94	-	-
1 MHz	Conc 1	-3.9	0.88	-2.0	0.68	-92.8	0.999	-10.0	0.99	-4.7	0.91
	Conc 2	-4.8	0.90	-3.4	0.85	-92.6	0.999	-14.8	0.99	-4.2	0.86
	Conc 3	-6.1	0.95	-5.0	0.93	-110.4	0.98	-27.9	0.996	-7.7	0.98
	Conc 4	-10.3	0.99	-6.6	0.96	-186.3	0.93	-45.9	0.998	-10.4	0.99
	Conc 5	-17.3	0.997	-11.8	0.99	-349.9	0.93	-68.6	0.97	-	-
1.15 MHz	Conc 1	-2.5	0.83	-1.8	0.60	-77.6	0.99	-7.4	0.98	-4.5	0.93
	Conc 2	-3.1	0.82	-2.0	0.56	-71.6	0.99	-11.3	0.99	-4.8	0.91
	Conc 3	-4.9	0.95	-3.4	0.86	-86.8	0.98	-23.1	0.997	-8.7	0.98
	Conc 4	-8.8	0.98	-5.8	0.97	-103.5	0.87	-39.4	0.998	-10.9	0.99
	Conc 5	-16.9	1.00	-11.5	0.99	-200.6	0.60	-65.1	0.99	-	-
2 MHz	Conc 1	-4.0	0.90	-3.2	0.87	-56.3	0.99	-6.2	0.96	-8.6	0.96
	Conc 2	-4.3	0.87	-3.8	0.88	-58.4	0.997	-8.7	0.98	-10.0	0.94
	Conc 3	-6.0	0.96	-5.1	0.96	-83.5	0.99	-18.4	0.997	-15.5	0.99
	Conc 4	-11.0	0.99	-8.9	0.99	-113.2	0.99	-32.4	0.999	-20.5	1.00
	Conc 5	-20.7	0.997	-17.3	0.997	-187.3	0.62	-55.6	0.999	-	-
2.25 MHz	Conc 1	-3.7	0.89	-3.3	0.85	-46.1	0.99	-6.1	0.96	-8.9	0.93
	Conc 2	-4.7	0.89	-4.2	0.84	-51.8	0.996	-8.7	0.98	-10.3	0.98
	Conc 3	-6.7	0.95	-5.8	0.96	-80.7	0.99	-17.9	0.995	-16.4	0.99
	Conc 4	-11.7	0.99	-10.0	0.99	-111.2	0.995	-31.0	0.998	-22.4	1.00
	Conc 5	-21.8	0.998	-18.7	0.997	-89.7	0.26	-54.4	0.998	-	-
2.5 MHz	Conc 1	-3.8	0.88	-3.8	0.91	-42.0	0.99	-6.0	0.95	-9.4	0.97
	Conc 2	-5.0	0.89	-4.1	0.92	-48.5	0.99	-8.6	0.96	-11.4	0.98
	Conc 3	-6.9	0.97	-6.1	0.97	-74.2	0.995	-17.6	0.99	-17.8	0.99
	Conc 4	-12.0	0.99	-10.9	0.99	-109.0	0.997	-30.5	0.996	-25.1	1.00
	Conc 5	-22.8	0.998	-20.3	0.998	-99.0	0.32	-53.8	0.998	-	-
3.75 MHz	Conc 1	-6.4	0.89	-5.7	0.96	-36.0	0.99	-7.6	0.97	-15.3	0.99
	Conc 2	-7.1	0.94	-6.7	0.97	-39.5	0.99	-9.9	0.99	-16.7	0.99
	Conc 3	-10.5	0.97	-10.2	0.990	-58.2	0.997	-17.6	0.996	-28.3	1.00
	Conc 4	-17.0	0.996	-17.2	0.996	-110.1	0.999	-28.2	0.998	-38.4	1.00
	Conc 5	-30.5	0.998	-32.0	0.999	-103.3	0.93	-51.8	0.998	-	-
5 MHz	Conc 1	-7.7	0.92	-7.2	0.97	-31.5	0.99	-9.7	0.97	-19.5	0.98
	Conc 2	-9.3	0.96	-8.6	0.98	-36.3	0.99	-12.0	0.98	-23.6	0.99
	Conc 3	-13.3	0.98	-12.6	0.99	-54.6	0.996	-20.9	0.99	-37.2	1.00
	Conc 4	-21.3	0.99	-21.7	0.997	-105.4	0.999	-32.7	0.996	-47.9	1.00
	Conc 5	-37.0	0.997	-40.4	0.999	-114.1	0.95	-53.3	0.99	-	-
6.75 MHz	Conc 1	-10.8	0.97	-10.5	0.98	-28.6	0.99	-13.0	0.99	-25.4	1.00
	Conc 2	-13.0	0.99	-12.5	0.98	-33.7	0.99	-15.8	0.99	-29.0	1.00
	Conc 3	-17.7	0.995	-17.5	0.99	-54.5	0.99	-25.4	0.998	-43.4	1.00
	Conc 4	-26.7	0.998	-29.1	0.996	-104.9	0.998	-36.1	0.998	-49.0	0.99
	Conc 5	-42.3	0.996	-47.3	0.996	-124.9	0.96	-52.5	0.98	-	-

Table 4.4 Attenuation coefficient values with corresponding correlation coefficient for the fit

	Calcite Particulates		Calcite Flocs		Magnesium Hydroxide Particulates		Magnesium Hydroxide Particulates		BPS	
	ξ	R^2	ξ	R^2	ξ	R^2	ξ	R^2	ξ	R^2
0.85 MHz	0.16	0.99	0.12	0.99	4.07	0.97	4.07	0.97	4.07	0.99
1 MHz	0.18	0.99	0.14	0.98	2.69	0.89	1.69	0.99	2.69	0.95
1.15 MHz	0.19	1.00	0.15	0.99	0.84	0.90	2.13	0.95	0.84	0.98
2 MHz	0.22	0.99	0.22	0.99	1.69	0.99	2.69	0.89	1.69	1.00
2.25 MHz	0.24	1.00	0.23	0.99	1.91	0.99	1.91	0.99	1.91	0.99
2.5 MHz	0.25	1.00	0.26	0.99	1.94	1.00	2.11	0.95	1.94	0.99
3.75 MHz	0.32	1.00	0.40	1.00	2.13	0.95	0.84	0.90	2.13	0.99
5 MHz	0.39	1.00	0.51	1.00	2.11	0.95	1.94	1.00	2.11	1.00
6.75 MHz	0.41	1.00	0.56	1.00	2.19	0.97	2.19	0.97	2.19	0.97

Table 4.5 Attenuation coefficient ratio values for each frequency pairing used for dual frequency concentration inversion

Frequency 1	Frequency 2	Calcite Particulates	Calcite Flocs	Magnesium Hydroxide Particulates	Magnesium Hydroxide Flocs	Barnon Pond Sludge
		ξ_1/ξ_2				
0.85 MHz	2 MHz	0.70	0.56	0.42	0.65	0.46
0.85 MHz	2.25 MHz	0.66	0.51	0.47	0.62	0.40
0.85 MHz	2.5 MHz	0.63	0.47	0.48	0.61	0.35
0.85 MHz	3.75 MHz	0.49	0.30	0.52	0.51	0.23
0.85 MHz	5 MHz	0.41	0.24	0.52	0.57	0.19
0.85 MHz	6.25 MHz	0.38	0.21	0.54	0.57	0.22
1 MHz	2 MHz	0.79	0.65	0.63	0.74	0.51
1 MHz	2.25 MHz	0.74	0.60	0.71	0.70	0.45
1 MHz	2.5 MHz	0.71	0.55	0.72	0.69	0.40
1 MHz	3.75 MHz	0.55	0.35	0.79	0.58	0.26
1 MHz	5 MHz	0.46	0.28	0.78	0.65	0.22
1 MHz	6.25 MHz	0.43	0.25	0.81	0.65	0.25
1.15 MHz	2 MHz	0.85	0.69	0.50	0.83	0.56
1.15 MHz	2.25 MHz	0.80	0.63	0.44	0.79	0.50
1.15 MHz	2.5 MHz	0.77	0.58	0.43	0.77	0.44
1.15 MHz	3.75 MHz	0.60	0.37	0.39	0.65	0.29
1.15 MHz	5 MHz	0.49	0.29	0.40	0.73	0.24
1.15 MHz	6.25 MHz	0.46	0.26	0.38	0.73	0.28
2 MHz	3.75 MHz	0.70	0.54	0.79	0.78	0.51
2 MHz	5 MHz	0.58	0.43	0.80	0.88	0.42
2 MHz	6.25 MHz	0.54	0.38	0.77	0.87	0.49
2.25 MHz	3.75 MHz	0.75	0.58	0.90	0.83	0.57
2.25 MHz	5 MHz	0.62	0.46	0.91	0.93	0.47
2.25 MHz	6.25 MHz	0.58	0.41	0.87	0.92	0.55
2.5 MHz	3.75 MHz	0.78	0.64	0.91	0.84	0.65
2.5 MHz	5 MHz	0.65	0.50	0.92	0.94	0.54
2.5 MHz	6.25 MHz	0.60	0.45	0.89	0.94	0.63

4.3.1.3 Determination of the sediment backscatter constant, k_s

Figure 4.30 shows the profiles of the backscatter constant, k_s, for the particulate calcite. Average values for k_s were taken for the lowest two concentrations and over a suitable range for which k_s was constant as detailed in the methodology, Section 4.2.5. To calculate k_s, k_t was determined for the transducers using data collected in the same experimental setup using Honite-16 at 2.5 and 5 g l^{-1} (profiles that were used for the calculation are shown in Appendix Figure B.1). The values of k_s are seen here (and in all other sediment sets) to be generally linear with distance at low concentrations but to exponentially increase with distance when the concentration (and hence attenuation) is high. The increase with distance can also be seen to correspond to data that is close to the noise floor (Section 4.3.1.1) and occurs at an earlier distance point when attenuation, indicated by the *dG/dr* values (Sections 4.3.1.2, Table 4.3) is higher. An increase or decrease in the backscatter constant with concentration has been observed in previous publications, however, for both non-cohesive [15] and cohesive [166]. In the case of cohesive sediments, the increase in the backscatter constant with concentration may be attributed to increasing aggregation effects causing an increase in size and hence *ks.* Aggregation at higher concentrations is not thought to be occurring here for the flocculated sediment as the covalent bridges formed during bridging flocculation do not typically reform significantly upon breaking [94]. For non-cohesive sediments, it has otherwise been attributed to the propagation of errors in estimating the attenuation coefficient and hence in the calculation of k_s [15].

For the particulate calcite (Figure 4.30) no significant change in the backscatter constant can be seen across all frequencies studied although a small increase at the highest frequencies is present. Comparing the particulate data (Figure 4.30) to the floc data (Figure 4.31) it can be seen that the flocculated calcite produces higher values of k_s in general while also exhibiting the increase with frequency predicted by Equation 2.58 that is the expected frequency response within the Rayleigh regime [120], [166]. An increase in the backscatter constant on flocculation is indicative that a better signal to noise ratio may be seen in the data compared to that of calcite as their attenuation values were fairly similar and thus Equation 2.5 predicts a larger value for the backscattered voltage signal and hence a higher signal-to-noise ratio. As the observed frequency relationship also indicates that the scattering is likely Rayleigh

then it may also be possible to apply acoustic particle sizing methods that rely on this Rayleigh relationship [266].

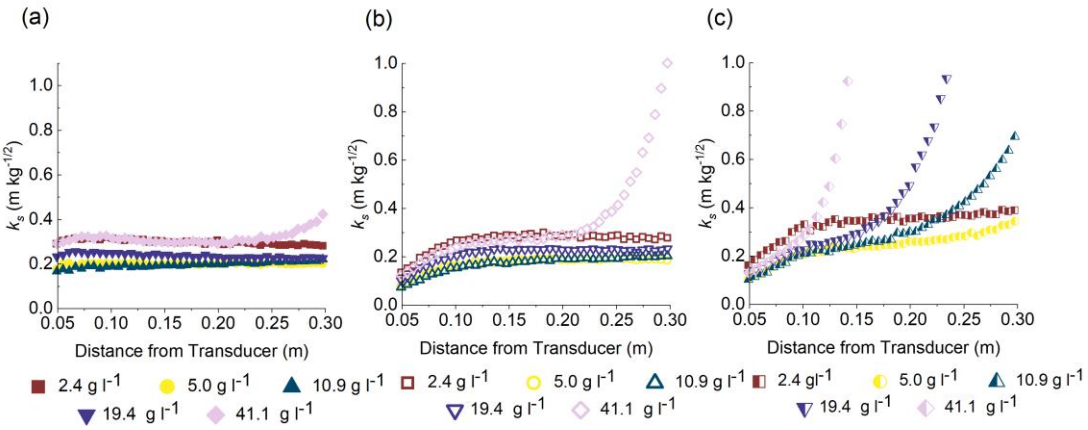

Figure 4.30 a) – c) k_s profiles for particulate calcite at 1, 2.25 and 5 MHz

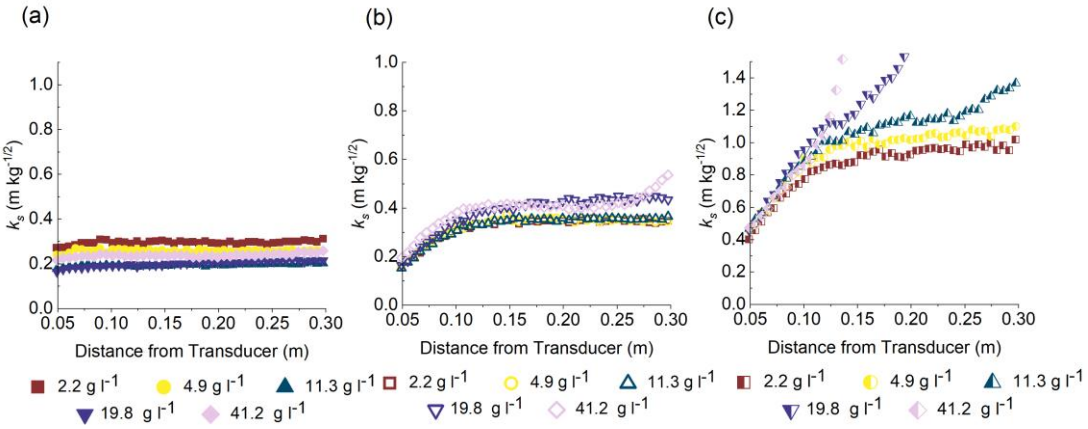

Figure 4.31 a) – c) k_s profiles for flocculated calcite at 1, 2.25 and 5 MHz

The k_s data for particulate and flocculate magnesium hydroxide are shown in Figure 4.32 and Figure 4.33 respectively. Due to the aforementioned increase in the noise floor, caused by multiple scattering effects, the profiles exhibit non-linearity even for some of the low values of concentration. The non-linearity of k_s with distance is seen for the particulate results most strongly and is therefore attributed here to a poor signal-to-noise ratio as a result of the small particle size (and hence overall backscatter strength) and high levels of attenuation. Despite these effects, similar overall trends to the calcite results are seen; upon flocculation the backscatter constant is seen to increase and also increases with increasing frequency.

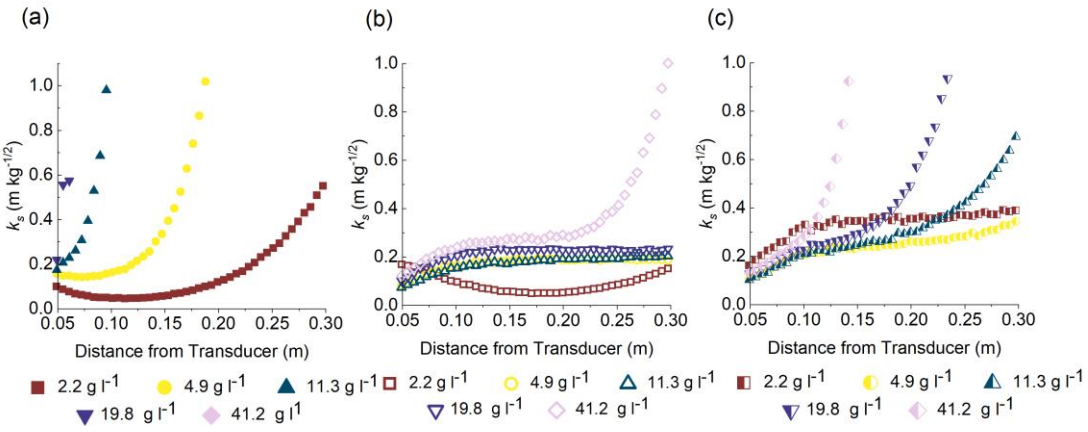

Figure 4.32 a) – c) k_s profiles for particulate magnesium hydroxide at 1, 2.25 and 5 MHz

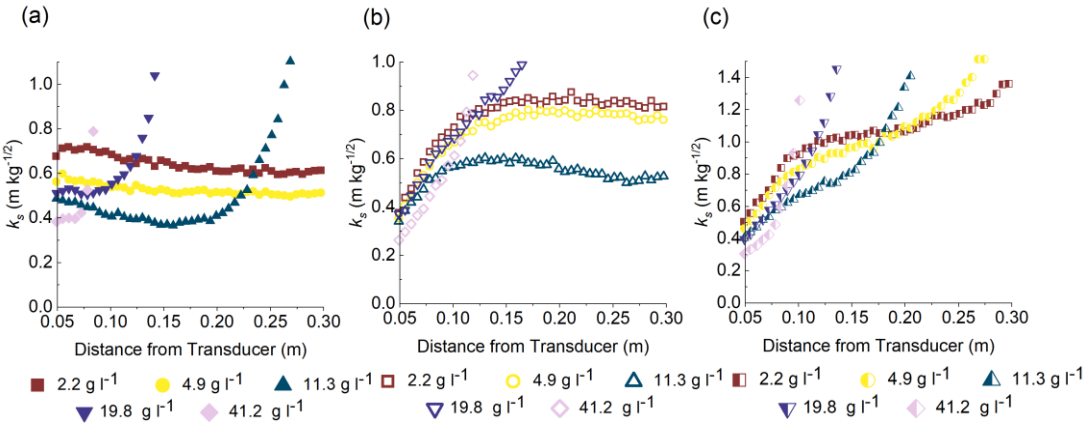

Figure 4.33 a) – c) k_s profiles for flocculated magnesium hydroxide at 1, 2.25 and 5 MHz

The k_s profiles for BPS are shown in Figure 4.34 and, similar to the flocculated magnesium hydroxide results, non-linearity for signals approaching the noise floor can be observed with an increase in the backscatter constant seen with increasing frequency. In particular, concentration data from the 5 MHz probe may be questionable as assessment of k_s profiles indicates no constant region for any concentrations of BPS investigated here. For all particle data sets presented here the monotonic relationship of k_s with distance is seen here at up to 5 g l^{-1} with deviations seen for the most highly attenuating suspensions likely caused by errors in the estimation of the attenuation coefficient propagating through into the calculation of k_s as has been found by Rice *et al.* [15].

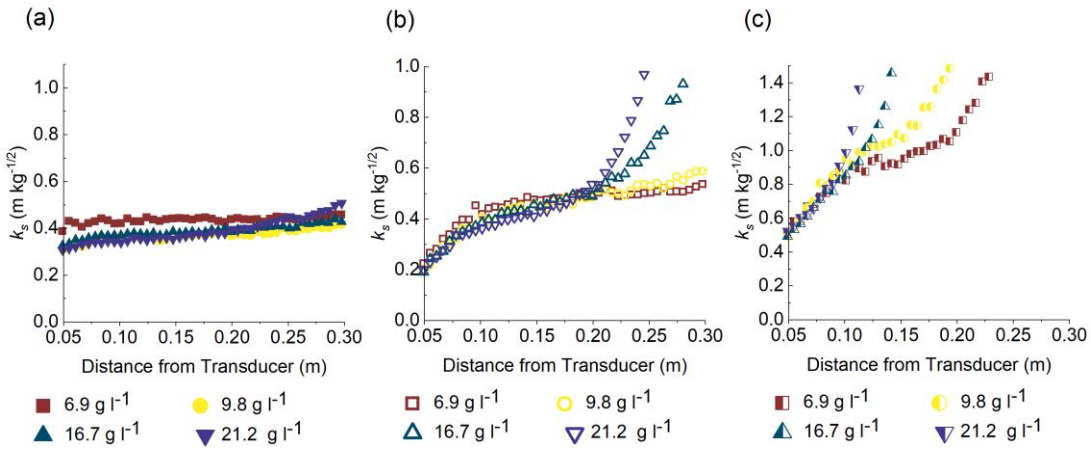

Figure 4.34 a) – c) k_s profiles for BPS at 1, 2.25 and 5 MHz

4.3.2 Comparison of experimentally determined acoustic constants to model values

In order to investigate the change in attenuation and backscatter strength more fully the sediment backscatter constant, k_s, and attenuation coefficient, ζ, were converted to their dimensionless equivalents, the form function, f (Equation 2.9), and the scattering cross-section, χ (Equation 2.12) and density normalised as per the method of Bux *et al.* [17]. The density of the flocs was estimated using the data shown in Table 4.1 calculated using Equation 2.2. Results are then compared to the Solid Scattering model [48] and Hybrid Model [47] using the measured coefficient of variation from the Mastersizer PSDs. Following this, investigation into the variation of modelling results with the fractal dimension and coefficient of variation in the floc PSD is undertaken. The specific gravity normalised Solid Scattering model [48] (calculated by dividing the result of Section 2.3.2, Equation 2.25 by the specific gravity calculated from Equation 2.2) (blue solid line) was also compared to the specific gravity normalised experimental data and Hybrid model [47] (Section 2.3.10, Equation 2.59). Specific gravity normalisation has been shown previously to allow for comparison between datasets comprising varying densities [17], [224] and therefore allows for direct comparison between the flocculated and particulate datasets presented here.

4.3.2.1 Scattering Cross-Section Data

Results for the calcite floc (blue) and particulate (red) experiments are shown in Figure 4.35 as a function of frequency expressed in terms of the acoustic wavenumber,

k, and the particle radius, *a*. The Hybrid and Solid Scattering models were both plotted for the particulate system to provide a visualisation for the difference between the modelled aggregate and floc at the same frequencies.

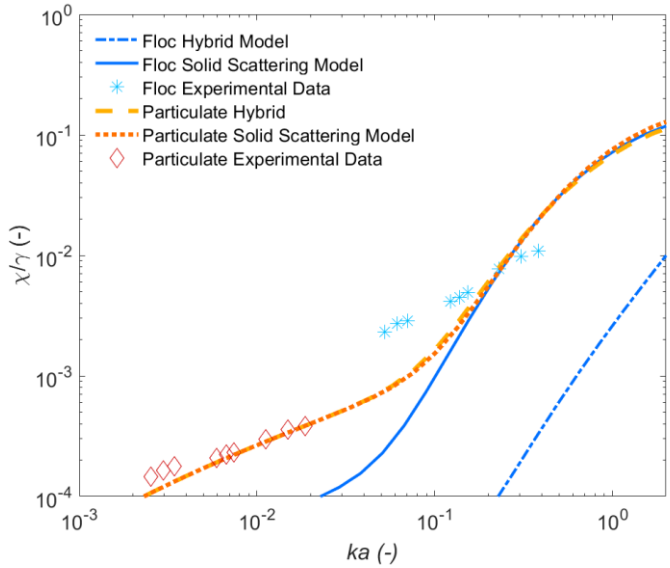

Figure 4.35 Specific gravity normalised scattering cross section for calcite flocs (γ = 1.24) and particulates (γ = 2.71) as a function of frequency expressed in terms of *ka*.

For the particulate case, the specific gravity normalised scattering cross section was seen to be in good agreement with model results and tended toward a plateau at ~10^{-4} and displayed the expected trend with frequency typical of the viscous scattering regime that is the dominant form of attenuation as particle size is decreased [17], [183]. For the flocculated results a decreased sensitivity to frequency is seen compared to both the Hybrid and Solid Scattering model that may be attributed to a wider size distribution *in situ* than was measured. As similar COV results were observed by both the *in situ* FBRM and *ex situ* SLS, however, this may be unlikely although deviations between ABS and light based measurements have been observed previously [10], [120], [121] and possibly be the result of the measurement limitations of the FBRM. As data at the highest frequencies for the flocculated calcite is seen to agree fairly well with the Solid Scattering model the deviation at low frequencies may simply be due to a poor model fit for the low *ka* region, as acoustic data used to fit the heuristic model on which the Hybrid model is based was limited to *ka* > 0.2 [48]. Furthermore, the values for the model parameters (ε_1, ε_2 and ε_3, Equations 2.58 and 2.59) used in this study were the same as those used Thorne *et al.* [47] who stated that these values may depend on floc structure and their variability is still to be determined. It was additionally stated by Thorne *et al.* [47] that well controlled laboratory studies have

not been performed for flocs at $0.01 < ka < 0.5$ and so deviations from initial modelling is to be expected. Interestingly, the floc values that agree best with the model also coincide with the same region for which the attenuation values were most sensitive to frequency (indicated by the *dG/dr* values, see Figure 4.20).

For the flocculated case, the experimental data in Figure 4.35 was seen to be highly underpredicted by the Hybrid model, however, due to the low floc density (1238 kg m^{-3}) and hence acoustic contrast predicted by Equations 2.2 and 2.55 with increasing floc size that is governed by the fractal dimension. Equation 2.2 was used to calculate the density of the floc for the mean number size that was then used in Equation 2.55 to find the acoustic contrast. The acoustic contrast value was then used to calculate the irregular fluid form function and scattering cross-section through Equations 2.56-2.59 and the resultant value normalised by the specific gravity of the floc.

In order to more accurately fit the Hybrid model to the flocculated data, the effect of varying fractal dimension, and hence the specific gravity of the flocs, was investigated and the results are shown in Figure 4.36. From the fits shown a fractal dimension of ~2.8 – 2.95, corresponding to a specific gravity of ~1.9 – 2.5, appears to fit the experimental data more accurately than the Hybrid model, although significant deviation still exists between experimental and modelled datasets.

A more accurate fit by the Solid Scattering model is not entirely unexpected, as it has been proposed more recently by Vincent and MacDonald [120] that the acoustic signal is dominated by scattering from the smaller (~5–25 μm) more tightly bound aggregates that make up the macro structure of the floc. In their study they found, using light scattering and ABS data, that these aggregates (termed “flocculi”) were best modelled using the density of the unflocculated sediment due to their small size and likely higher fractal dimension and are therefore accurately represented in these results by the Solid Scattering model that only uses the unflocculated sediment density as a model input. Although the volume of large (~100 μm) flocs was shown to be high for the flocculated calcite used in this study (Section 4.2.3, Figure 4.2 (a)) their corresponding number count is low with a number mean diameter of ~30 μm. Although aggregates of this size would still have a relatively low density predicted

using Equation 2.55, it is possible that during the initial stages of flocculation the fractal dimension may be higher as the bridging flocculation mechanism, that produces high density flocs [71], would be dominant as polymer on the particle surface will not typically have time to reconform onto the particle surface before forming a bridging contact. It should be noted that the experimental results presented here are also normalised with respect to the specific gravity and thus inherently take the floc density into account. The Hybrid model, however, also accounts for the change in sound speed in the floc with changing porosity/density through Equation 2.55. It cannot be stated with certainty here whether the smaller flocs are denser and thus are better reflected by the Solid Scattering model or whether the Hybrid model is inaccurate in determining the effect of porosity on the speed of sound in the floc. The former statement is likely the true case however as similar results has been obtained by Vincent and MacDonald in the past [120].

With regards to the light scattering measurements used to determine the fractal dimension, as the scattering strength of large particles will be much greater than that of small particles, it is not unfeasible that the fractal dimension of the larger particles will dominate the measurement result and mask this higher fractal dimension. Furthermore, as fractal dimension fits are taken over a number of q values (that represent the length scale of the scattered wave vector) if this fractal dimension is only present for a small size range of particles it may be hard to deduce using the linear fit method applied here. Even with an adjustment to the fractal dimension, the experimental floc data have a notably reduced sensitivity to frequency in Figure 4.36 than is predicted by either model and may indicate either that the size distribution used in calculations is not accurate as discussed or that the heuristic fits used are not accurate for the size distributions at low ka.

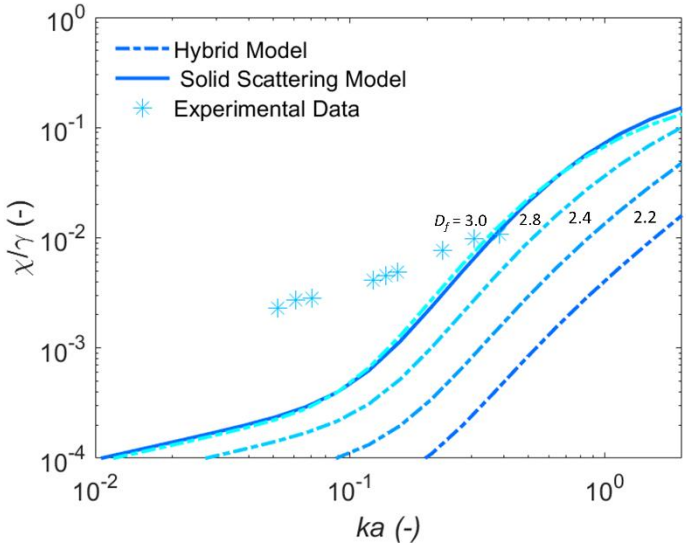

Figure 4.36 Specific gravity normalised scattering cross section for flocculated calcite as a function of frequency expressed in terms of *ka* with the effect of a variation in fractal dimension (D_f) shown for the Hybrid model.

Model results for the BPS data are shown in Figure 4.37 using the COV determined from the PSD (Section 4.2.3, Table 4.1) [267]–[269]. A fairly good fit to the experimental data by the density normalised solid scattering model is seen although a slightly higher sensitivity than would be predicted is seen as well as larger scattering cross-section values in general. Although the volume distributions for BPS (Section 4.2.3, Figure 4.4) exhibit a large degree of multi-modality the number distribution produced only a narrow peak at ~0.8 μm with low polydispersity indicated by the low COV value (Table 4.1). The bi-modality of the distribution is not thought to explain the deviation between the Solid Scatter model and experimental results seen here, however, as a bi-modal distribution has been shown by Moate and Thorne [266] to give lower scattering cross-section values than those predicted using a log-normal distribution if the COV and mean size are held constant.

An increase in both absolute values and frequency sensitivity of the model could also be achieved by a decrease in the COV, however, indicating that perhaps only a narrow distribution of particles around the mean number value are dominating the acoustic signal that may be likely if some size fractions of the BPS are comprised of low density, organic material that would not scatter or attenuate significantly. Despite a good fit to the Solid Scattering Model, the Hybrid model is still seen to underestimate the flocculated experimental values significantly due to the low density (1525 kg m^{-3}) predicted from the floc size and fractal dimension that was arrived at in Section 4.2.3.

The underestimation of the density normalised scattering cross-section by the Hybrid model was also observed in the flocculated calcite results (Figure 4.35) although this effect is less evident in the case of BPS because, although the fractal dimension value (D_f = *2.12)* is lower the much smaller number mean diameter results in a relatively high floc density (ρ_{floc} = 1525 kg m^{-3}). The relative accuracy of the Solid Scattering model compared to the Hybrid model shown in the results here further supports the hypothesis of Vincent and MacDonald [120] that the acoustic scattering response is due to the dense particulate clusters that are the building blocks of the overall floc structure.

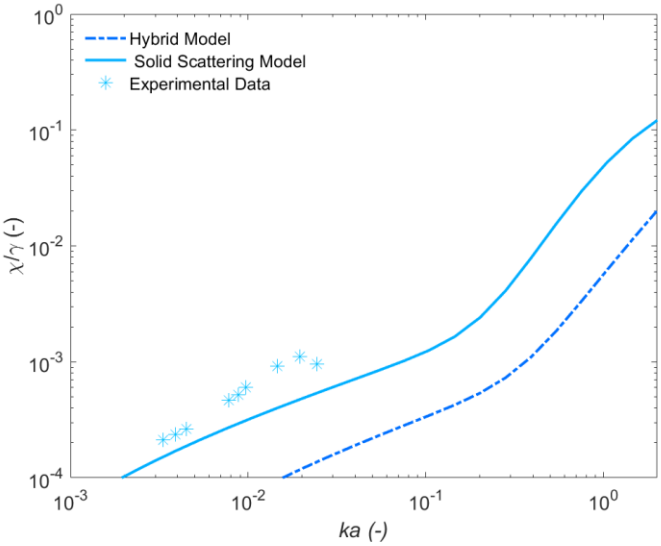

Figure 4.37 Specific gravity normalised scattering cross section for BPS as a function of frequency expressed in terms of ka.

The effect of varying the coefficient of variation, COV, was investigated for the BPS data to determine if the use of a narrower size distribution would provide a better model fit for the Irregular Solid Scatter model (Section 4.2.3, Figure 4.4), and the results are shown in Figure 4.38. From the model lines it can be seen that with a decreasing COV the gradient of the model line (on a log scale) increases, as do the values in the modelled range. Even at the lowest COV value investigated the experimental results were still seen to lie above the predicted results at higher frequencies. The largest difference was only around 30 %, however, and may perhaps be a good fit when considering possible compounding errors in the model input PSD and acoustic parameters (primary particle size, floc size, fractal dimension, density, and sediment compressional wave speed). To fully investigate the robustness of the

model to the estimated parameters for BPS (density, size and compressional wave speed) the effect of varying their values is investigated in Figure 4.39 and Figure 4.40.

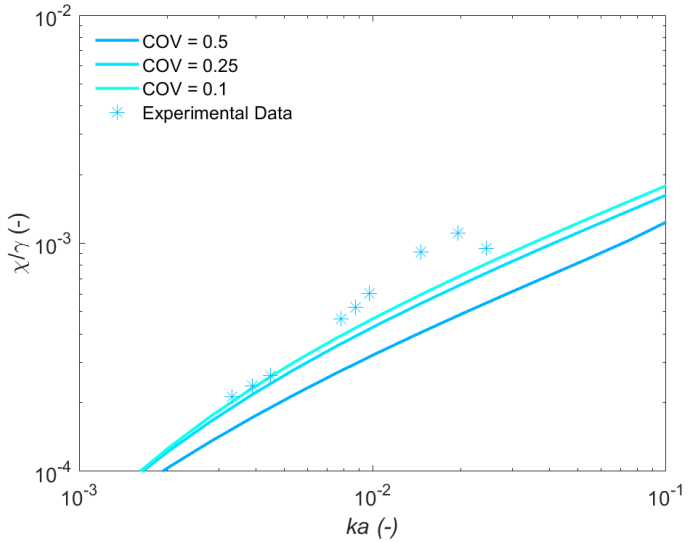

Figure 4.38 Specific gravity normalised scattering cross section for BPS as a function of frequency expressed in terms of *ka* with the effect changing the coefficient of variation (COV) for the flocculated PSD shown for the solid scattering model.

With regards to the estimated primary particle characteristics for BPS (density, size and compressional wave speed), changing the primary particle size would have no effect on the model fits for the flocculated particle systems as the floc density term, used to convert measured attenuation constant values to scattering cross section values through Equation 2.12, is eliminated by density normalisation while the Irregular Solid Scattering model does not use the floc density as a model input. The effect of varying the compressional wave speed in the sediment (c_s) is shown in Figure 4.39 below for the Irregular Solid Scatterer model. The scattering cross-section is seen to increase in the cases where the input compressional wave speed is both doubled and halved due to the increase in acoustic contrast that is a function of the square of the difference in the compressibility of the scatterer and the bulk medium (see Equations 2.25 and 2.27). Thus, as the compressibility of the sediment (given by $\kappa = 1/\rho c^2$) approaches the compressibility of water the scattering cross-section will approach a minimum across all frequencies. While the difference between the model lines below ka = 0.04 is minimal above this value there is fairly significant deviation with the maximum difference observed in both cases to occur at ka = ~0.25 with a difference of 16% seen for the case where the compressional wave speed was halved and 50% in the case where the compressional wave speed was doubled from the

original model input value that indicates some degree of robustness of the model with respect to the input compressional wave speed.

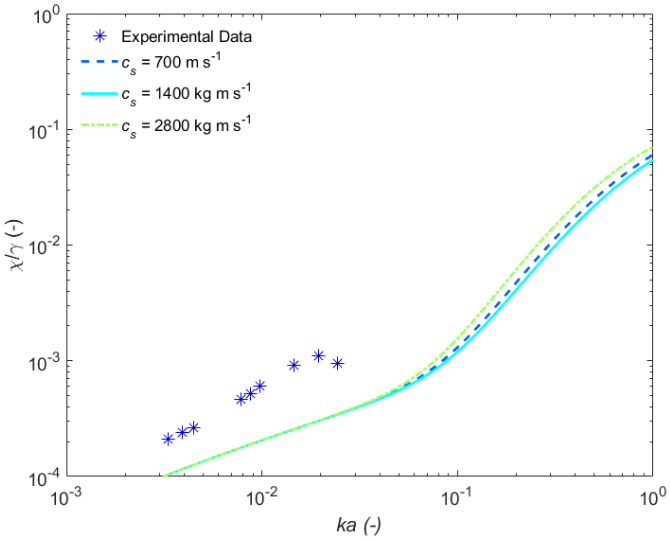

Figure 4.39 Specific gravity normalised scattering cross section for BPS as a function of frequency expressed in terms of *ka* with the effect changing the compressional wave speed shown for the solid scattering model.

Finally, the effect of varying the primary particle density is shown in Figure 4.40 below. When doubling the primary particle density an increase in the scattering cross section is observed below *ka* = 0.1, while a decreased scattering cross-section is observed above this value. The increase in the scattering cross section with increasing density below *ka* = 0.1 can be attributed to both the increase in acoustic contrast of the sediment as well as the increase in the viscous cross-section (determined from Urick's model, Equations 2.28-2.30). The decrease in scattering cross section with increasing density observed at higher *ka* values (~*ka* = 0.2) is a result of the viscous attenuation term (that is strongly affected by particle density, Equations 2.28-2.30) becoming increasingly insignificant compared to the scattering cross section coupled with the normalisation with respect to the specific gravity. When halving the primary particle density used for modelling, a significant decrease of nearly an order of magnitude can be seen as the density difference between the fluid and the sediment is reduced by approximately a factor of five that subsequently causes a significant decrease in the scattering cross-section as the compressional wave speed in the particle decreases via Equation 2.55. This is further compounded by a decrease in the viscous cross section at low *ka* values. As *ka* increases the difference becomes smaller, though still significant, as viscous attenuation becomes less significant.

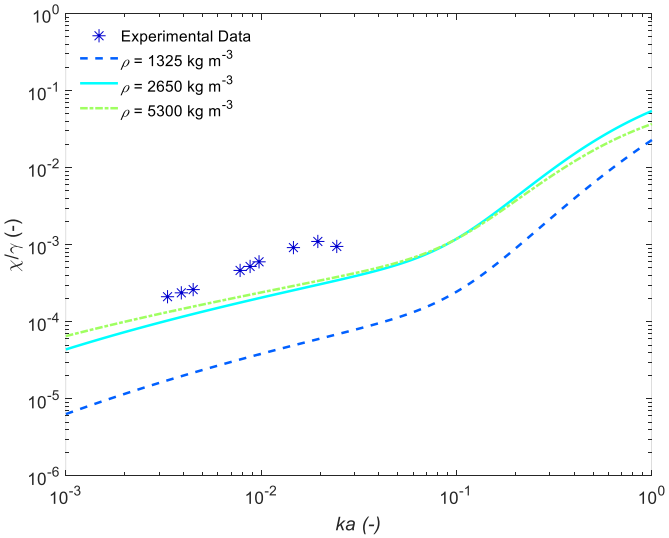

Figure 4.40 Specific gravity normalised acoustic cross section for BPS as a function of frequency expressed in terms of *ka* with the effect of changing the primary particle density shown for the solid scattering model.

Results shown also highlight the importance of determining the primary particle size distribution, as this has been demonstrated to strongly affect the acoustic response across all modelled *ka* values. While an underestimation of the density induces large error in the modelled scattering cross-section, a relatively small change is seen if this value is overestimated, though the corresponding error grows larger at the upper and lower *ka* limits shown here. Interestingly, the compressional wave speed has a comparatively small effect at low *ka* but becomes more significant at high *ka*. For an induced error in the input compressional wave speed (+100% and -50%) the resultant error in the estimated specific gravity normalised cross-section is relatively small at $ka < 0.4$. This indicates some degree of robustness of the model with respect to the input compressional wave speed at low *ka* and that even significant errors in the estimated compressional wave speed used for BPS (1400 m s^{-1}, [258]) would not cause significant model deviation from experimental results. While some degree of error likely exists in the input density to the model (as natural sediments will contain a wide variety of materials with differing densities quoted), densities from literature indicates a narrow range of around 2600 – 2700 kg m^{-3} [253] and are therefore not thought to be the cause for the model deviation observed for the BPS data shown in Figure 4.37.

In terms of experimental particle characterisation techniques, particle size and COV measurements taken in the Mastersizer 2000 are likely the most significant sources of

error, due the shear that is inherent in the agitation system used to suspend the particles in the measurement cell that is necessary to perform the measurement. Excessive shear may be causing particle breakup that would lead to a decrease in the measured particle size and an increase in the COV as the particle size distribution width is increased. To illustrate the importance of accurate size and COV estimations, it was therefore decided to attempt to fit the Hybrid model to experimental datasets by varying the input floc size and COV for experimental and model results. As the results for the Hybrid model shown in Figure 4.36 demonstrated that an adjustment in the fractal dimension increased the absolute values towards those predicted by the solid scattering model without affecting the frequency dependence (i.e. the gradient) of the model on a log-log scale, the fractal dimension was also adjusted to fit the Hybrid model to experimental data. Variation of both of the fractal dimension and COV would therefore allow for adjustment of the absolute values through the fractal dimension and the frequency dependence through the COV value, to allow fitting of experimental data to the Hybrid model.

As the largest source of error in the measurements was the floc size, due to possible aggregation during transport and breakdown due the shear conditions in the Mastersizer dispersion unit, the floc size was varied between 7 –150 μm and ideal fits produced for each size that are shown in Figure 4.41. A fractal dimension of 2.9 was found to fit the data well for all sizes except 7.2 μm for which the fractal dimension had to be increased to 2.95 to produce an acceptable fit. The modelled fractal dimension values indicated modelled floc densities between 2010 – 2600 kg m^{-3}, in agreement with previous authors [35], [120] who found that the decreased floc density does not significantly reduce the attenuation compared to a solid particle of the same size.

The results shown in Figure 4.41 indicate that, if the floc PSD is unknown, then multiple values of floc size can provide a good model fit by varying the COV used for the PSD in the Hybrid model. This result critically highlights then the need to independently measure particle size accurately, and in so doing flags a limitation of the acoustic backscatter models. Model results are also in agreement with the findings of Guerrero and Frederico [1] that the same value of attenuation may correspond to either a small particle size with a high COV or a larger, well-sorted sediment.

Guerrero and Frederico [1] and Guerrero *et al*. [270] have attempted to resolve this problem by taking either the ratio of the attenuation coefficient (Section 2.3.1, Equation 2.12) to the square of the particle backscattering coefficient (Section 2.3.1, Equation 2.9) (ABR) or ratio of the square of the backscatter coefficients at different frequencies (BBR). The ABR and BBR are then compared to model plots (produced using the Solid Scattering model from Thorne and Meral [48]) to predict an estimated range for the attenuation coefficient. Although this method is only able to predict a viable range for the value of the attenuation coefficient if the PSD of the sediment is unknown, the ranges produced are not unduly large and indicate that this method is still of interest for future studies.

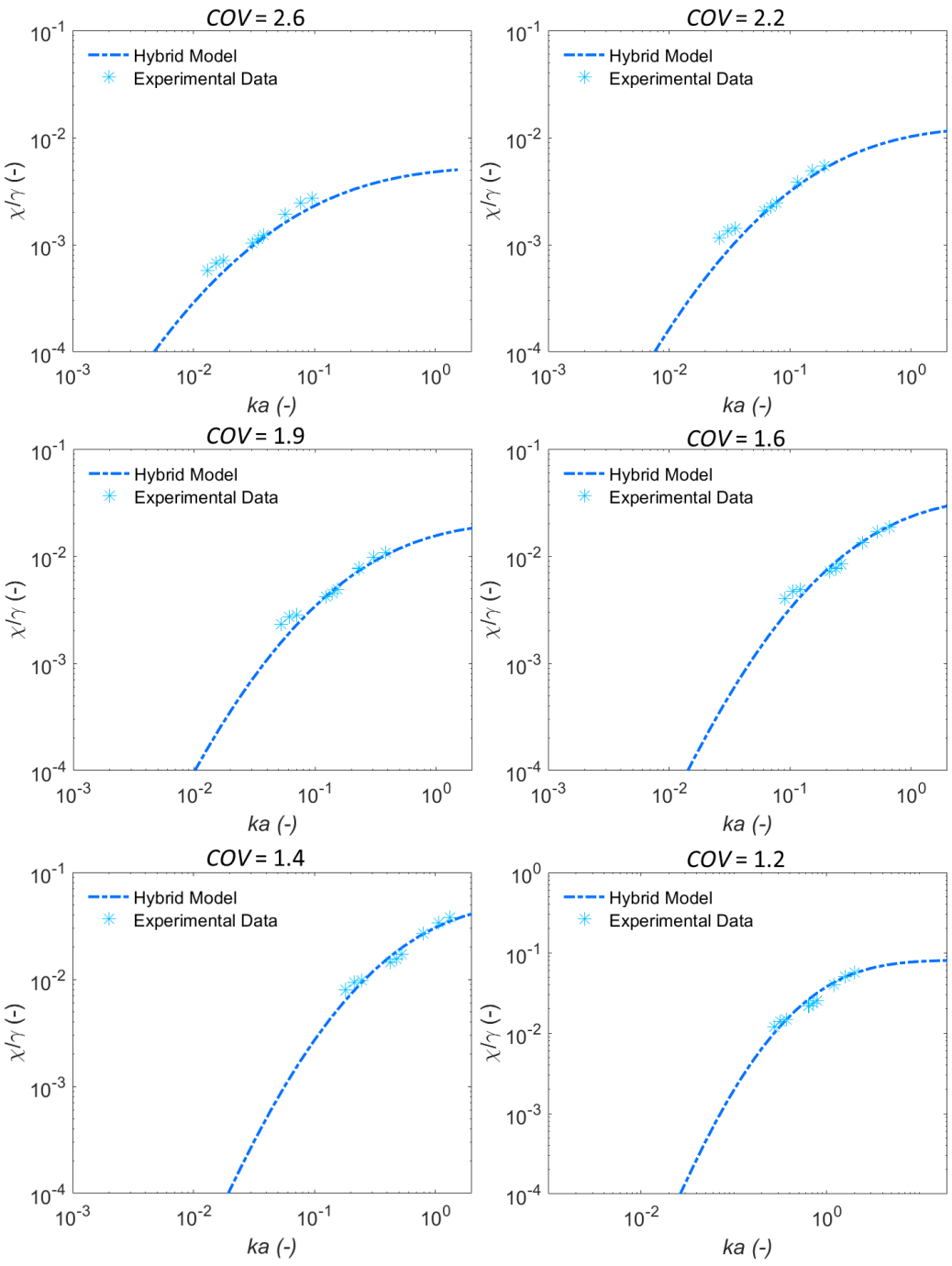

Figure 4.41 Showing experimental data for calcite flocs using the Hybrid model at number mean sizes of a) 7.2, b) 14.5 and c) 28.9, d) 50, e) 100 and f) 150 µm with corresponding floc densities of 2531, 2281, 2195, 2131, 2055 and 2013 kg m^{-3} respectively.

The use of the backscattering constant values (expressed in terms of the form function, Section 2.3.10, Equation 2.58)) in combination with the attenuation (expressed in terms of the scattering cross-section) is therefore investigated in the following section to determine if doing so will allow for correct identification of the floc size and COV by producing an ideal fit to both datasets. The same conditions used to produce the model fits in Figure 4.41 were used to model the form function for flocculated calcite

(shown in Section 4.3.2.1, Figure 4.46) to see if the average particle size and COV that is "seen" by the acoustics can be grounded by attempting to fit both the scattering cross section and form function (assuming a log-normal distribution for the flocs and the assumptions inherent in the Hybrid model [47]) (Section 2.3.10).

The scattering cross-section data for the magnesium hydroxide is shown in Figure 4.42. In the particulate case a significantly higher attenuation than would be predicted by either model is seen. From the raw profiles (Figure 4.14) evidence of multiple scattering is seen that may be contributing to the deviation of these results from model values due to excess attenuation or experimental error due low signal-to-noise ratio evidence by the decibel profiles in Figure 4.14. Irregularities in the particle surface, shown previously to enhance attenuation for irregularly shaped quartz [48], may be enhancing the attenuation. Indeed, the hexagonal platelet structure of the magnesium hydroxide particulates, coupled with their aggregated particle structure may be causing an enhancement in acoustic attenuation due its comparatively larger surface area. Additional structural attenuation may also be the cause of the departure between modelled and experimental results for the magnesium hydroxide particulates and has been observed previously in 0.5 – 2 μm suspensions of alumina across a similar *ka* range by Dukhin and Goetz [151]. Structural attenuation was said to become applicable in the case of gels formed by either nanoparticle or by polymers. If aggregation of the magnesium hydroxide is occurring in solution, then the formation of particle structures which contain solid concentrations significant enough to cause such losses may account for the excess attenuation observed here [271].

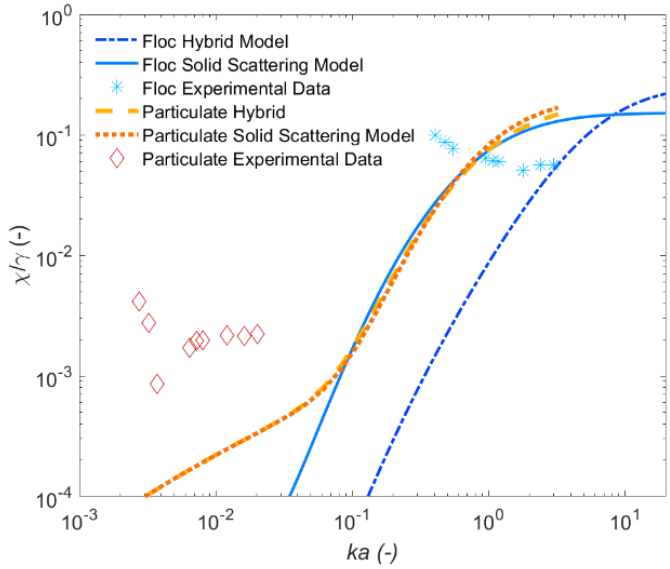

Figure 4.42 Specific gravity normalised scattering cross section for magnesium hydroxide flocs and particulates as a function of frequency expressed in terms of *ka*.

4.3.2.2 Form Function Data

The form function data for each particle system, normalised by the square root of the specific gravity, along with model predictions are shown across page. As seen earlier, (Figure 4.30, Section 4.3.1.3) the particle backscatter constant, k_s, and hence the form function (Figure 4.43) was not seen to change significantly with frequency for calcite particulates leading to a plateau in the experimental form function data at low *ka* in Figure 4.43. An increase in the form function with frequency was seen for magnesium hydroxide (Figure 4.44) particulates above *ka* = 0.0065 with a similar frequency relationship (on a log-log scale) predicted by both the Hybrid and Solid Scattering models. Below *ka* = 0.0065, a decrease in the form function with increasing frequency is seen for particulate magnesium hydroxide that is not predicted by modelling. Observing the raw decibel and *G-function* profiles for the particulate magnesium hydroxide for the lowest frequency band probe (Figure 4.14 (a) and (d)) there is a distinct non-linearity in the decay of the signal with distance that may be evidence of multiple scattering causing an increase in the system noise that could be the cause of the artificial enhancement to the backscattering coefficient and form function.

The values observed for the particulate data sets correspond best with the model data for the highest frequencies however order of magnitude differences are still observed between model and experimental datasets at all *ka* values. The experimental

deviations from the modelled data are attributed here to the aforementioned (Section 4.3.2.1) lack of datasets in the low *ka* region used to fit the model [47], [48] that has been observed by previous authors [17] and emphasises the need to extend heuristic modelling attempts to account for the decreasing change in scattering cross-section and form function with frequency at low *ka* observed in the experimental datasets shown here. The physical cause of this plateau is unknown but may correspond to multiple scattering effects increasing the noise in the system, thus artificially enhancing the backscatter coefficient, k_s, and hence the form function, *f*. Alternatively it may be the case that COV is underreported during particle size measurements that would otherwise cause a plateau in the form function at high and low *ka* values.

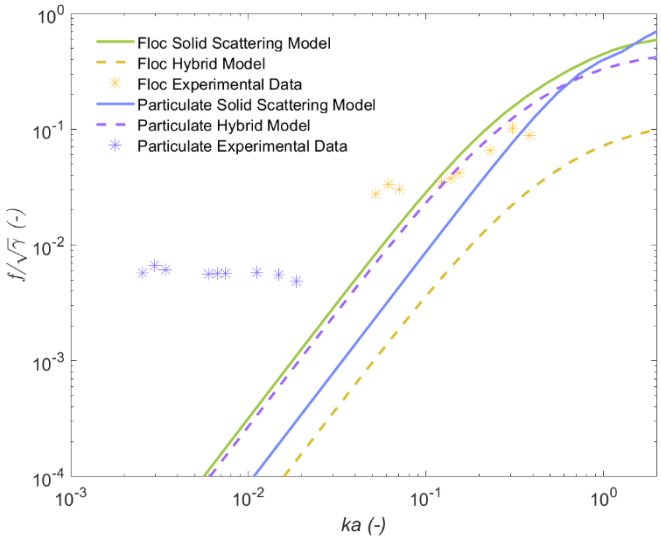

Figure 4.43 Form function for calcite flocs and particulates, normalised by $\sqrt{\gamma}$, as a function of frequency expressed in terms of ka.

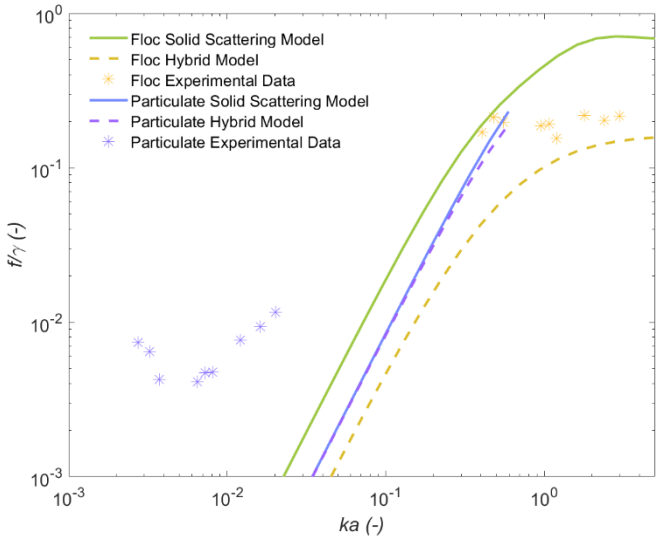

Figure 4.44 Form function for magnesium hydroxide flocs and particulates, normalised by $\sqrt{\gamma}$, as a function of frequency expressed in terms of *ka*.

Observing the data for the largest two floc systems studied, the majority of the floc data for magnesium hydroxide (Figure 4.44) and calcite (Figure 4.43) lie between the Solid Scattering and Hybrid models. The calcite floc data at low frequencies is greater than the Solid Scattering model and exhibits a reduced sensitivity to frequency than predicted. This decreased frequency sensitivity was also seen in the scattering cross-section results for flocculated calcite (Section 4.3.2.1, Figure 4.35) and may similarly indicate that, in modelling terms, a greater COV seems to be observed by the ABS results compared to the light scattering and FBRM results, when using the same mean number particle size that is demonstrated in Figure 4.46 (c). The flocculated particle results from both magnesium hydroxide and calcite also support the scattering cross-section results for the same datasets in the previous section in that some degree of reduced scattering and attenuation is seen for the floc compared to a solid particle of the same size, in agreement with a number of previous authors [31], [47], [166], [268], [269].

The BPS data (Figure 4.45) was seen to obtain similar errors to those observed for the particulate calcite (Figure 4.43) when compared to the model results. A plateau in the form function at a value ~10^{-2} is observed that is also consistent for the particulate calcite data. Hence these datasets in the low *ka* (< 0.03) region should be incorporated into future heuristic model fits. Revaluating these fits would then allow for prediction of acoustic parameters for flocs across a wide size range without the need to significantly adjust the measurement frequency that may be limited for an ABS

system due to spatial resolution requirements, excessive attenuation at high frequencies and cost or accessibility related system limitations.

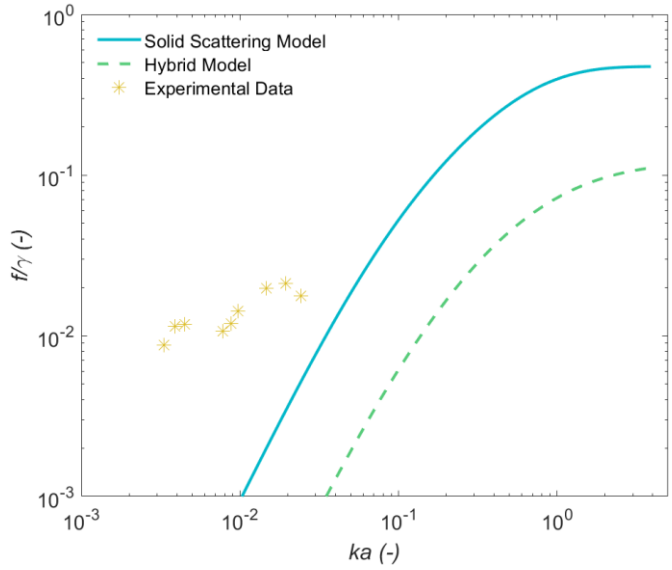

Figure 4.45 Form function for BPS flocs, normalised by $\sqrt{\gamma}$, as a function of frequency expressed in terms of *ka*.

In order to compare to optimised fits of the scattering cross-section produced for the flocculated calcite data (Section 4.3.2.1, Figure 4.41), modelling variables (mean particle size, fractal dimension and COV) were replicated and the same fits produced for the form function data shown in Figure 4.46. While empirical fits to existing form function and scattering cross-section data have been produced to take account of changing COV by Thorne and Meral [48] these are limited to values of *ka* above 0.1 and, while useful when accurate particle size data is limited such as when sieving sediments, are otherwise less rigorous than calculating the ensemble form function and scattering cross-section values directly.

Similar to the scattering cross-section results, the same model fit for the Solid Scattering and Hybrid model can be replicated using either a smaller mean size with a larger COV or a large mean size with a smaller COV that presents an obstacle when attempting to identify both the particle size and size distribution width. With regards to eliminating potential fits, it is not thought that the larger mean size fits (Figure 4.46 (d) – (f)) to the ABS data are reasonable as they significantly differ from the size measured using light scattering, Table 4.1 (that was similarly observed in FBRM results, Figure 4.9). Nonetheless, it is clear that nearly identical fits to

scattering cross section (Figure 4.41) can be obtained using different combinations of floc size and COV similar to the observation by Guerrero and Federico [1] that the same can be said for the attenuation coefficient. Results here also show that the same conclusion can be drawn for the form function as well that precludes the ability to obtain a full particle size distribution through the model comparisons used here.

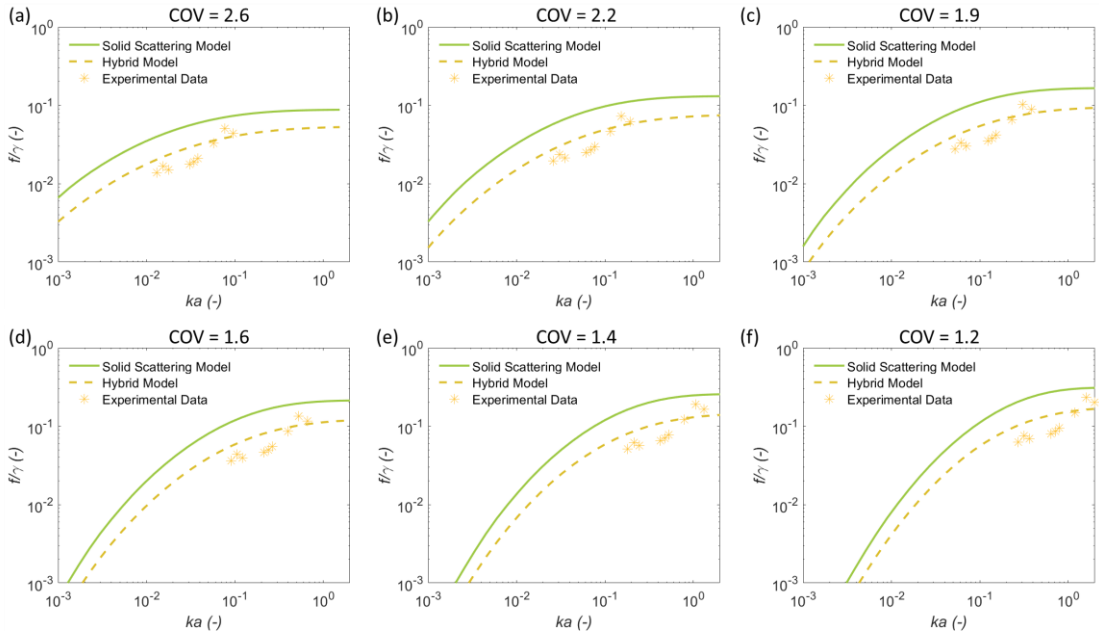

Figure 4.46 Showing experimental data for calcite flocs using the Hybrid model at number mean sizes of a) 7.2, b) 14.5 and c) 28.9, d) 50, e) 100 and f) 150 µm and a fractal dimension of 2.9 with corresponding floc densities of 2531, 2281, 2195, 2131, 2055 and 2013 kg m^{-3} respectively.

Considering now the fractal dimension and resulting particle density required to produce the fits using the Hybrid model [47] (Figure 4.46) to the flocculated calcite data, a fractal dimension value of D_f = 2.9, indicating high particle density, was found to produce good fits for the Hybrid model for flocculated calcite (Figure 4.41). The higher fractal dimension used to produce the fits would indicate that the floc scattering and attenuation properties are not as significantly reduced as would be predicted by the Hybrid model when using the fractal dimension values measured using static light scattering (D_f = 2.35, Table 4.1). The high density that is therefore "seen" by the acoustics may indicate that the fractal dimension measured using static light scattering may not be adequately capturing the structure of the flocs produced during the initial stages of flocculation where much denser flocs may be formed due to low polymer coverage.

Alternatively, it may be the case that as the experimental data for the flocculated particle systems studied was found to lie closer to the solid scattering model (i.e. a fractal dimension of D_f = 3.0), the theory of Vincent and MacDonald [120], that the acoustic signal is dominated by the tightly bound aggregates that make up the macrostructure of the floc (based on data collected by MacDonald *et al.* [166]), is considered to be more valid than the Hybrid model theory presented by Thorne *et al.* [47] (based on the same dataset) for the data presented here. As floc sizes studied here are typically smaller than those studied by MacDonald *et al.* [166], due to the slightly higher shear environment, it is also likely that a significant portion of the flocs have been broken such that a large number of the smaller, denser "flocculi" are dominating the acoustic signal and may be the underlying cause of this result. As the flocs are broken down by shear the flocculi that were previously held in close proximity within the floc will be further apart. The corresponding increase in inter-particle distance will reduce the degree of viscous layer overlap and therefore lead to an increase in the observed attenuation. As the effect of viscous layer overlap on the attenuation and scattering cross-section is not incorporated into the Hybrid model, it may instead be captured here when adjusting the fractal dimension to fit the experimental data to the model. In terms of future work, viscous layer overlap effects coupled with a thorough understanding of the changes in interparticle spacing within a given floc system during both flocculation and shear must be included in the model to model the acoustic scattering cross-section of flocculated particle systems more accurately.

Experimental data was also seen to lie below the solid scattering model in some cases, however, and may be a result of overlap between the viscous layers surrounding these particles that would lead to a reduction in the measured attenuation [237] compared to the value predicted using the solid scattering model. As the inter-particle spacing within the floc will increase with particle size this may also explain the results found by MacDonald *et al.* [166] where flocs scattered less than solid scatterers for smaller sizes but tended toward the solid values for larger flocs; beyond a critical floc size the inter-particle spacing will exceed the viscous layer depth around the particles thus reducing the dampening of the attenuation from inter-particle scattering and causing it to tend to the higher solid scattering model values.

4.3.2.3 Comparison of scattering cross section and form function across all measured datasets

In order to determine if production of new heuristic fits to the data collected in Chapters 3 and 4 might be viable, all cross section and form function results are shown below in Figure 4.47. The Betteridge *et al.* [159] model is used to show comparison of the data collected in Section 4.3 to the glass data analysed in Section 3.3 and to give a general representation of the heuristic fits often employed [47], [48], [159] to represent the form function, *f*, and scattering cross-section, χ. For completion, a similar chart showing the irregular model fit for glass particles is shown in Appendix B (Figure B.2). A general decrease of the scattering cross-section with decreasing frequency in experimental values at low *ka* is fairly well represented by the model although deviation is seen in the experimental data due to the unusually large attenuation observed for the magnesium hydroxide particulates. Continuing to higher *ka* values, however, experimental data from the flocculated calcite system continues to change with frequency with same slope on a log-scale as at low *ka* while the slope predicted using solid scattering theory (Figure 4.35) is much higher while significantly underpredicting the measured scattering cross-section. This is attributed here to the inclusion of a size distribution in experimental data that has been demonstrated in Section 4.3.2 to cause a smoothing effect on the model and may therefore indicate that the size distributions used are not sufficiently accurate.

To confirm the consistency of the data collected, results are also compared to those collected by Bux *et al.* [17] whose results are shown in Figure 4.48. From the data of Bux [264] it can be seen that the results from the barytes, titania and PMMA dispersion correspond well with the particulate data obtained here with some deviations between experimental results that are likely the result of differences in the particle size distributions and compressional waves speeds across the sediments. The decreased attenuation observed for the MMA emulsion is likely the result of both their droplet structure that would encourage fluid scattering characteristics and so its fit to the solid scattering model is expected to be inaccurate even if the viscous effects are included. Overall, therefore, it would appear that so long as the particle size distribution and viscous effects are incorporated into heuristic predictions, relatively accurate values for the scattering cross-section can be determined for the particulate sediment systems studied here.

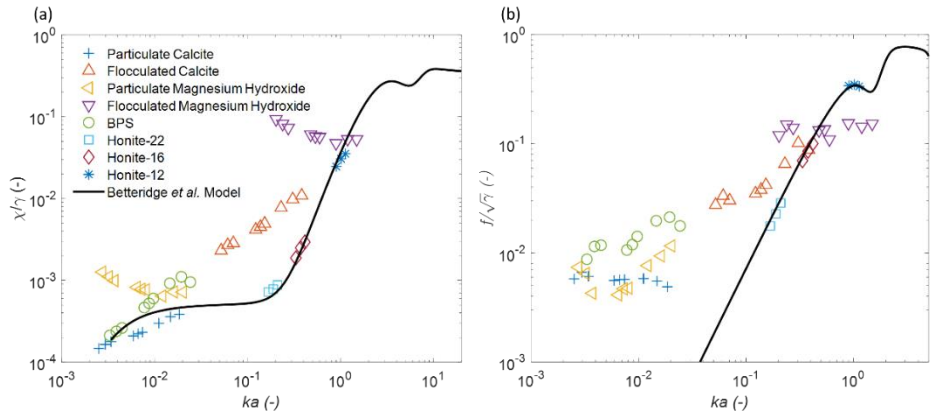

Figure 4.47 a) χ and b) f normalised by the specific gravity and square root of specific gravity respectively presented with model results from Betteridge *et al.* [159] including viscous effects calculated using Urick's [143] model for glass beads insonified at 2 MHz

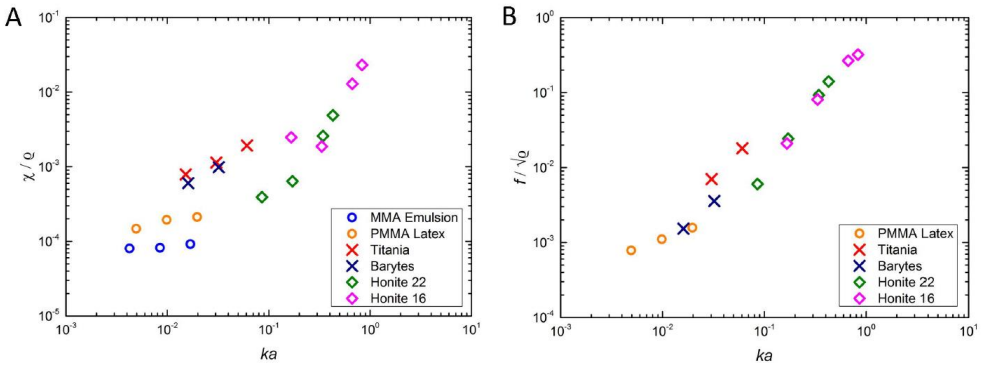

Figure 4.48 Measurements from Bux [264] (also utilised by Bux *et al.* [17]) for a) χ and b) f normalised by the specific gravity and square root of specific gravity respectively

Experimental results for the form function, f, indicate a similarly decreased sensitivity to frequency as was observed for χ that is the result of inclusion of a size distribution in the experiments causing a smoothing effect. Nearly all datasets reach roughly the same value as might be predicted at high ka but plateau at a value between 10^{-2} and 10^{-3} at low ka rather than decreasing asymptotically as might be predicted. The lower limit of ~10^{-3} was seen by Bux [264] for the PMMA particles that may possibly be a result of differing acoustic wave speeds, their relatively low acoustic contrast and thermal attenuation effects on the calculated form function. The consistent model deviation in the experimental form function data collected at low ka therefore indicates that adjustment of the heuristic fits for f in the low ka range should be the subject of future work to allow for more accurate prediction of the form function as this plateau has now been observed across multiple datasets by multiple authors. Results for both the scattering cross-section and form function also clearly demonstrate the ability of specific gravity normalisation to allow direct comparison of experimental results from particle sets of different densities while still retaining

non-dimensionality in the measured acoustic constants. Some deviation between results may still be expected, however, due to differences in the particle size distributions and acoustic wave speed in the sediment.

4.3.3 Concentration inversion data

For dual frequency data shown in this section, the lowest frequency available for the lower frequency probe was used in order to achieve a greater difference in the attenuation coefficient ratio and hence improve accuracy in the produced profile [15]. For the higher frequency probe, the central frequency was used as, although the highest frequency would provide a greater difference in attenuation coefficients, it was found that the large amount of attenuation at the highest frequencies caused errors to be induced in the resulting dual frequency profile. These inaccuracies are discussed in more detail for each individual sediment in this section.

Single and dual frequency inversion results and plots of gravimetric concentration versus the concentration determined using ABS for particulate calcite are shown in Figure 4.49-Figure 4.52. An accurate (within 20% of the nominal value) single frequency inversion is obtained up until ~10 g l^{-1} for the 1 MHz probe above which higher concentrations and frequencies increase the attenuation (See Section 4.3.1.2, Table 4.3) such that it is great enough to induce multiple scattering and an increase in the noise floor. The increase in the noise floor then invalidates the inversion, causing it to deviate to either zero or infinity due to the errors induced by the attenuation coefficient that has been described by previous authors [15], [33], [189] and in results shown in Section 3.3.3. The concentration profiles obtained using the dual frequency method [14], [15], [161] were seen to improve results compared to the single frequency inversion in the near-field close to the transducer and indicate a sufficiently large difference between the attenuation coefficients at the measured frequencies to obtain a stable inversion [15]. This near-field improvement is likely a result of the inclusion of data from the higher frequency probes in the calculation for which the near-field results are more accurate. Aside from these near-field effects, however, the results from the lowest frequency probe set gave the most accurate results at high concentrations that may be linked to the multiple scattering effects caused by high attenuation (discussed above in Section 4.3.1) that would become more pronounced with increasing frequency.

Consulting the table of *dG/dr* values (Section 4.3.1.2, Table 4.3) it can be seen that instabilities consistently begin to occur above a *dG/dr* value of ~-10 Np m^{-1} that may provide an indicator of the limit for this concentration inversion method. As this result is similarly observed for the dual frequency results it is thought that this is not a result of mathematical error propagation through the profile but a real limit to the concentration inversion model's assumption of negligible multiple scattering [33], even when grounding the value of the attenuation coefficient by taking measurements at multiple concentrations [15], [17]. Similar results were also seen for the Honite 12 system in Chapter 3, but such a result may perhaps not apply in system with a significantly higher sediment backscattering constant, k_s, in which the multiple scattered signals will not increase the system noise above a level such that the signal-to-noise ratio is low enough to cause significant deviation from the single scattering model. Overall, however, an improvement in comparison to the data presented in Section 3.3.3 is seen that is caused by the extended frequency range available with the new set of probes allowing a greater range of frequencies thus allowing for values of the attenuation coefficient ratio further from unity to be measured.

Largely similar results to the particulate case are seen for the flocculated calcite inversion results shown in Figure 4.53- Figure 4.56 however the inversion is seen to be accurate up to ~35 g l^{-1} for the single and dual frequency inversion using the 1 MHz probe for the single frequency inversion (Figure 4.54) and for certain frequency pairings between the 1 MHz and 2.25 MHz probes and 2.25 MHz and 5 MHz probes for the dual frequency inversion (Figure 4.56 (a) and (b)). This success for flocculated results is attributed to the lower attenuation values seen in the flocculated case (Section 4.3.1.2, Table 4.3). Indeed, a similar *dG/dr* limit of ~-10 Np m^{-1} is seen as was also observed for the particulate case. Again, the dual frequency method is seen to successfully resolve inversion issues in the near-field region but is limited as, when using data from a signal that is not well predicted by the single frequency inversion, the resulting profile will be highly erroneous. If such a process is to be automated for an instrument, therefore, careful analysis of suitable signals using this *dG/dr* limit of -10 Np m^{-1} should be included in the processing algorithm during calibration so

that such inaccuracies are not propagated through when calculating calibration constants and constraints algorithmically [225].

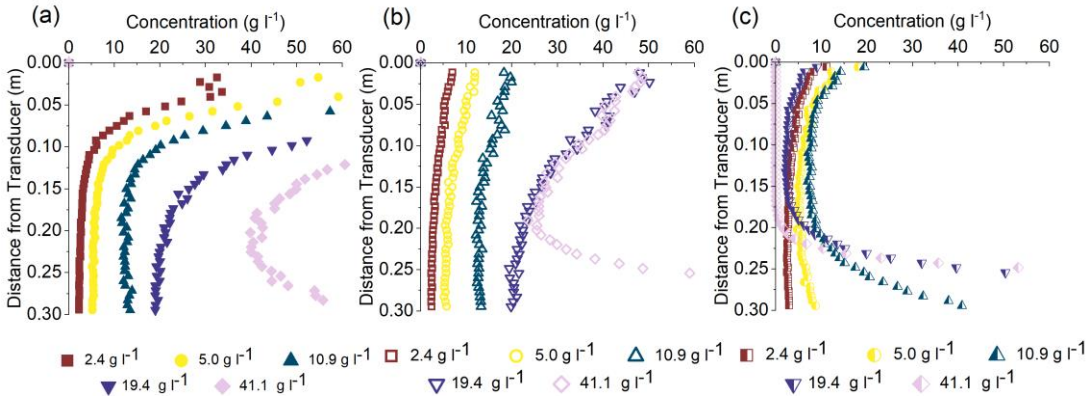

Figure 4.49 Single frequency inversion profiles for particulate calcite at a) 1, b) 2.25 and c) 5 MHz

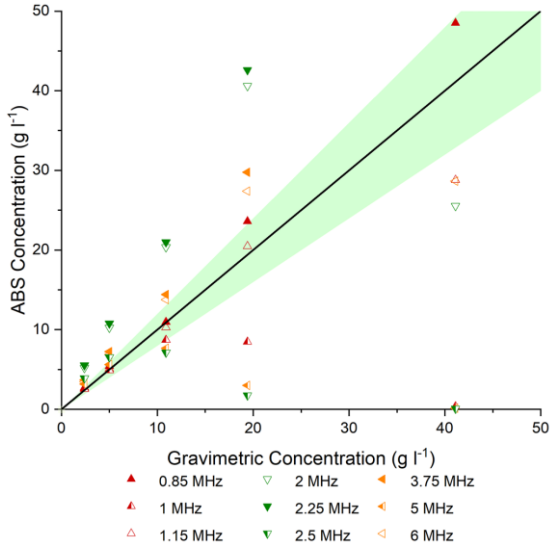

Figure 4.50 Concentration as measured by ABS vs gravimetric concentration for single frequency inversion profiles for particulate calcite with the shaded area representing a 20% error margin

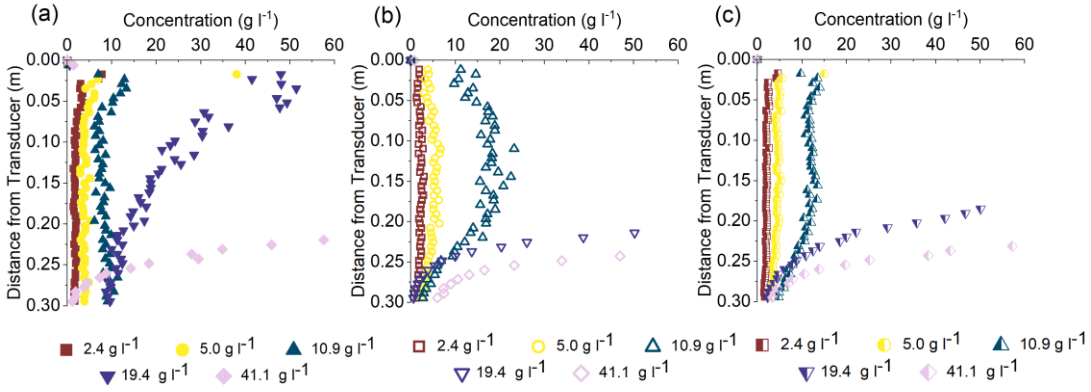

Figure 4.51 Dual Frequency inversion profiles for particulate calcite for frequency pairings of a) 0.85 and 2.25 MHz, b) 2 MHz and 5 MHz and c) 0.85 and 5 MHz

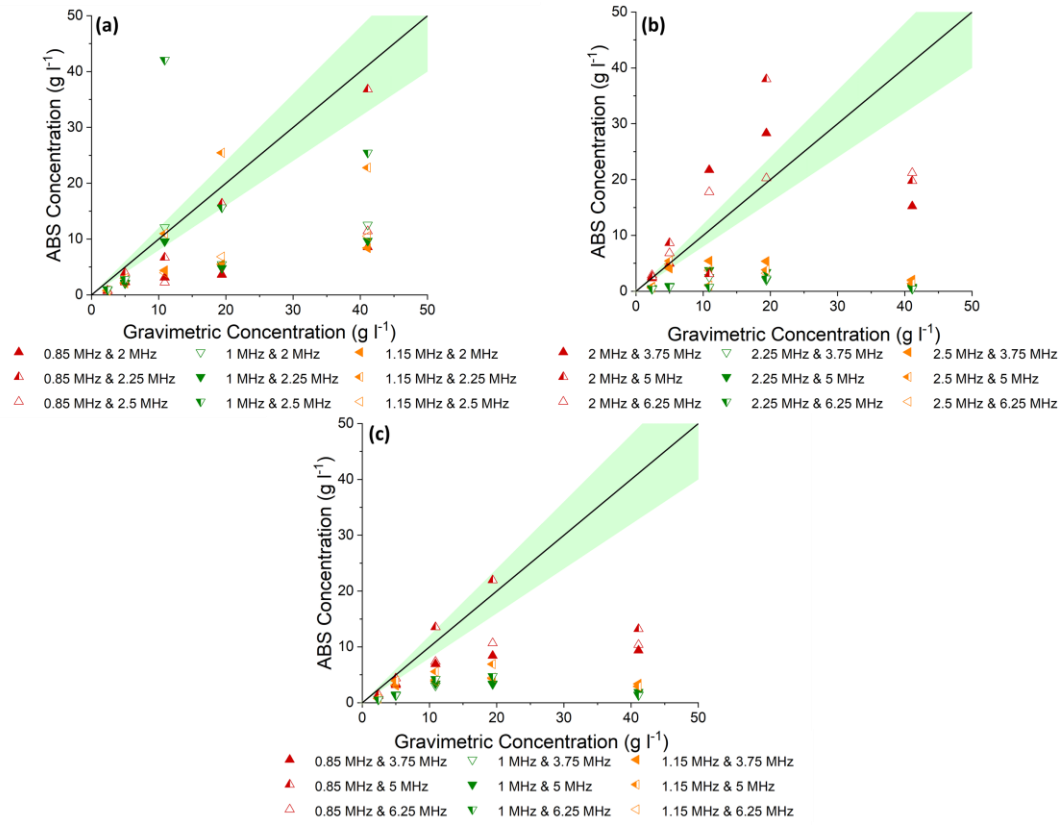

Figure 4.52 Concentration as measured by ABS vs gravimetric concentration for dual frequency inversion profiles for particulate calcite for a) 1 and 2.25 MHz, b) 2.25 and 5 MHz and c) 1 and 5 MHz central frequency probe pairings with the shaded area representing a 20% error margin

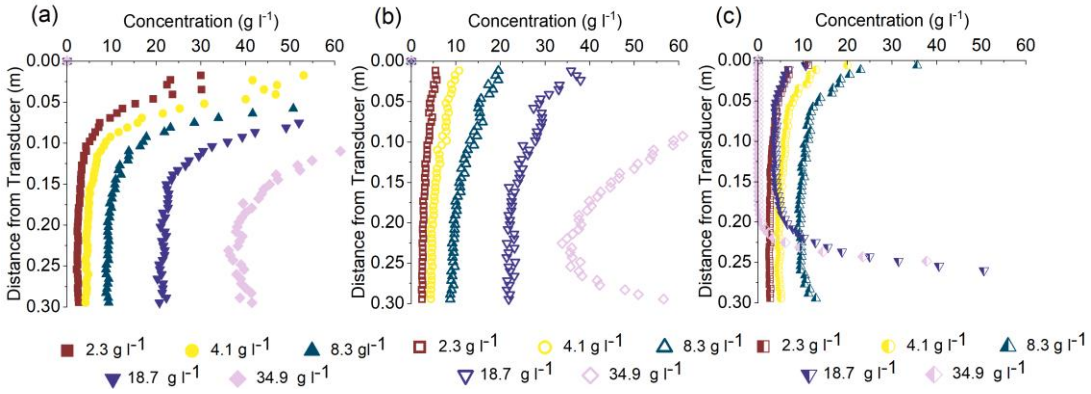

Figure 4.53 Single Frequency inversion profiles for flocculated calcite at a) 1, b) 2.25 and c) 5 MHz

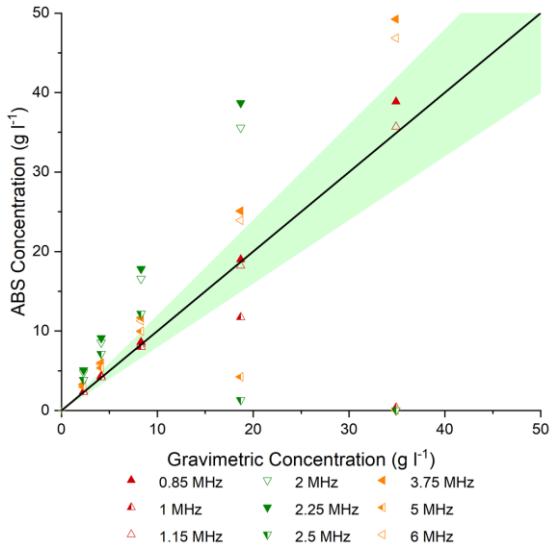

Figure 4.54 Concentration as measured by ABS vs gravimetric concentration for single frequency inversion profiles for flocculated calcite with the shaded area representing a 20% error margin

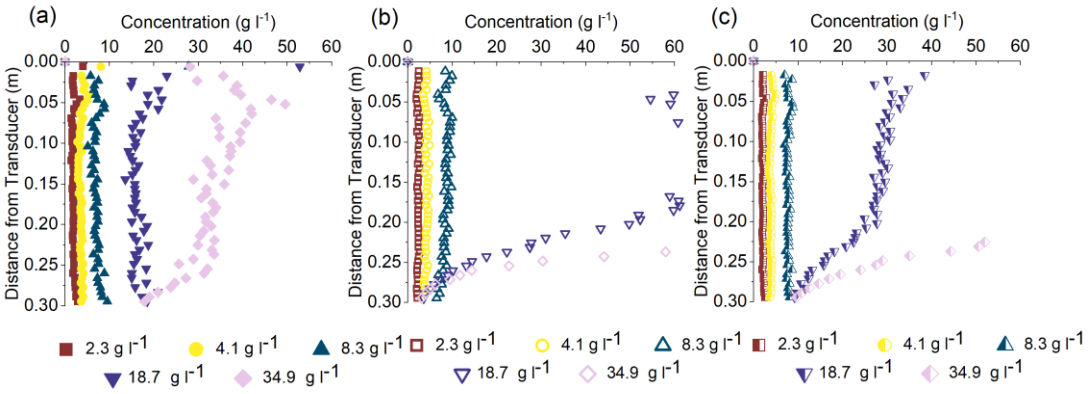

Figure 4.55 Dual Frequency inversion profiles for flocculated calcite for frequency pairings of a) 0.85 and 2.25 MHz, b) 2 MHz and 5 MHz and c) 0.85 and 5 MHz

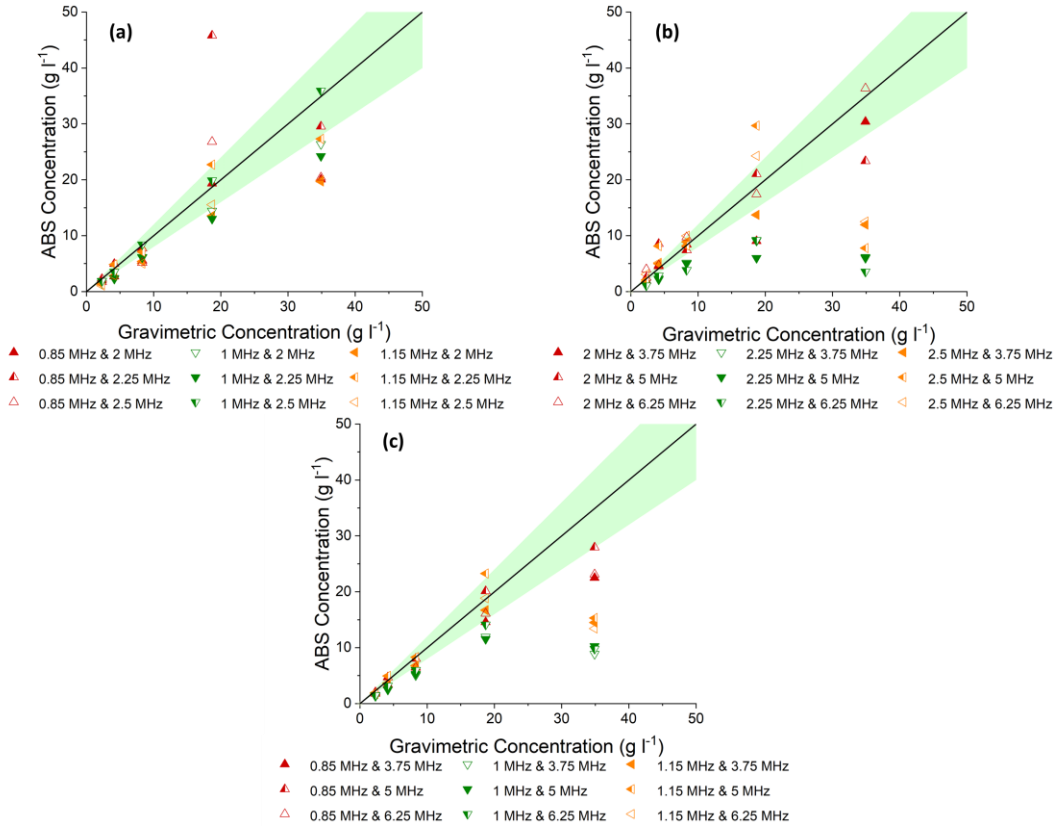

Figure 4.56 Concentration as measured by ABS vs gravimetric concentration for dual frequency inversion profiles for flocculated calcite for a) 1 and 2.25 MHz, b) 2.25 and 5 MHz and c) 1 and 5 MHz central frequency probe pairings with the shaded area representing a 20% error margin

Due to the excessive attenuation and resultant multiple scattering for both magnesium hydroxide particulates and flocs, evident from the raw decibel profiles (Section 4.3.1.1, Figure 4.14 and Figure 4.16), the concentration profile data (Figure 4.57-Figure 4.64) is limited to accurate profiles for only 2 – 5 g l^{-1} for the single frequency inversion (Figure 4.58 and Figure 4.62). Although the *dG/dr* limit of -10 Np m^{-1} (Section 4.3.1.2, Table 4.3) for a valid concentration inversion, which was seen for the particulate and flocculated calcite data (Figure 4.49 and Figure 4.53), is also seen for the flocculated magnesium hydroxide data the same is not true for the particulate magnesium hydroxide data (Figure 4.57) for which *dG/dr* values were significantly larger than the -10 Np m^{-1} limit. While some frequency pairings appear to obtain somewhat accurate results in the particulate case (Figure 4.60), when consulting the decibel profiles (Figure 4.14) it can be seen that much of these data lie at the noise floor and are likely just approaching toward zero and so the dual frequency concentration inversion data for magnesium hydroxide particulates is considered invalid. The dual frequency inversion for both the particulate and flocculated case (Figure 4.60 and Figure 4.64) is unable to resolve the profiles more accurately than

the single frequency inversion in the near field for both the particulate and flocculated case (Figure 4.59 and Figure 4.63). The instabilities in the dual frequency inversion are likely a result of incorporation of data above the previously established *dG/dr* limit of -10 Np m^{-1}. Incorporation of invalid inversions (for which *dG/dr* is greater than -10 Np m^{-1}) results in highly erroneous inversions, however, as seen in Figure 4.63 (a). The use of this *dG/dr* limit may possibly be used to exclude "bad data" and can therefore be a useful tool for limiting the number of calculations if the dual frequency process were to be automated to enhance data mining. Contrasting dual frequency results may then be more easily identified as being an erroneous measurement rather than actual concentration variation in the system.

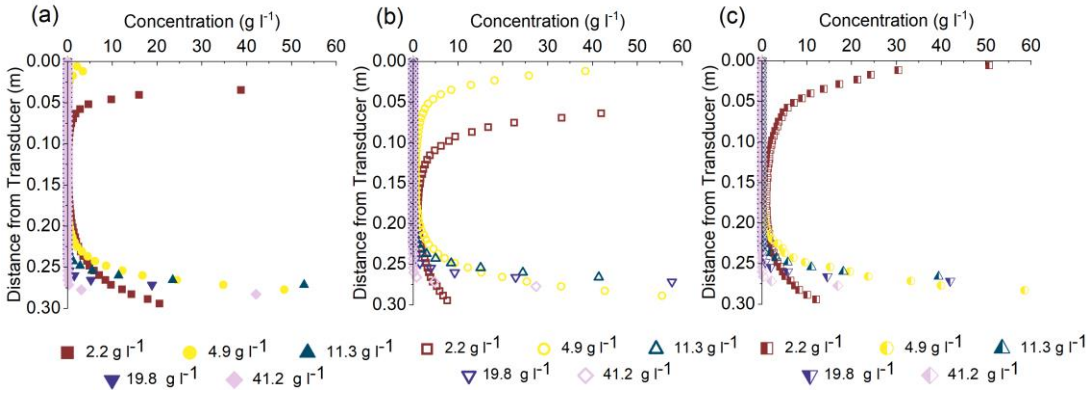

Figure 4.57 Single Frequency inversion profiles for particulate magnesium hydroxide at a) 1, b) 2.25 and c) 5 MHz

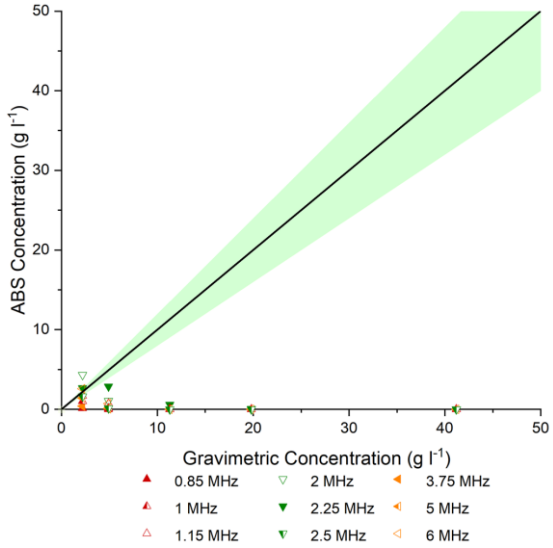

Figure 4.58 Concentration as measured by ABS vs gravimetric concentration for single frequency inversion profiles for particulate magnesium hydroxide with the shaded area representing a 20% error margin

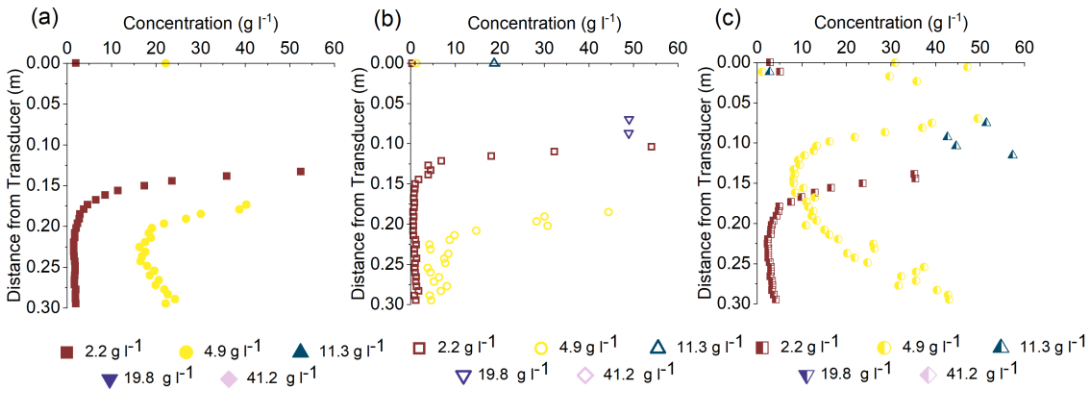

Figure 4.59 Dual Frequency inversion profiles for particulate magnesium hydroxide for frequency pairings of a) 0.85 and 2.25 MHz, b) 2 MHz and 5 MHz and c) 0.85 and 5 MHz

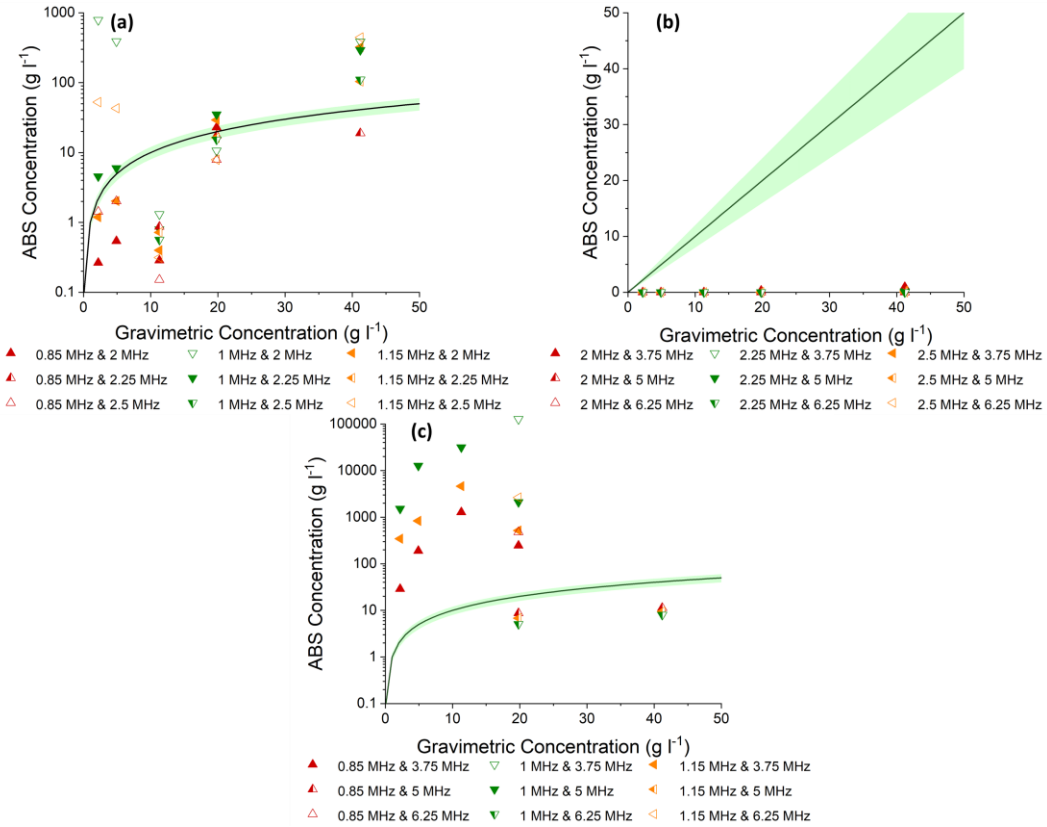

Figure 4.60 Concentration as measured by ABS vs gravimetric concentration for dual frequency inversion profiles for particulate magnesium hydroxide for a) 1 and 2.25 MHz, b) 2.25 and 5 MHz and c) 1 and 5 MHz central frequency probe pairings with the shaded area representing a 20% error margin

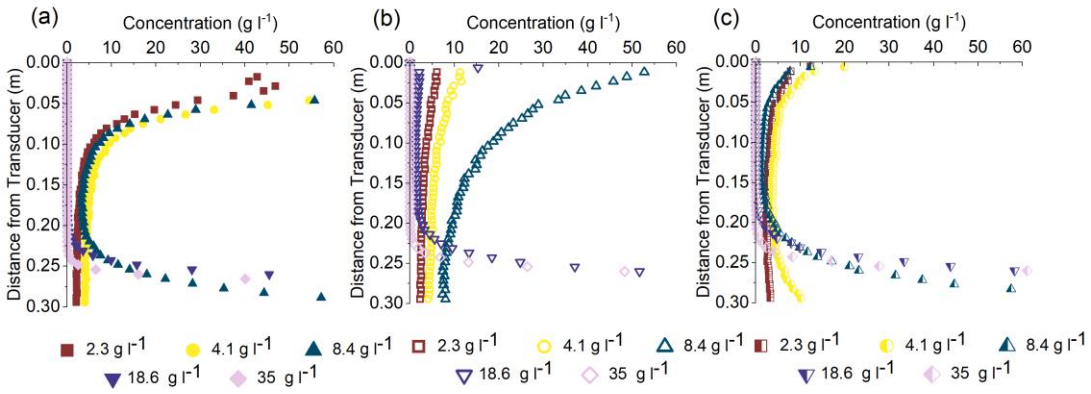

Figure 4.61 Single Frequency inversion profiles for flocculated magnesium hydroxide at a) 1, b) 2.25 and c) 5 MHz

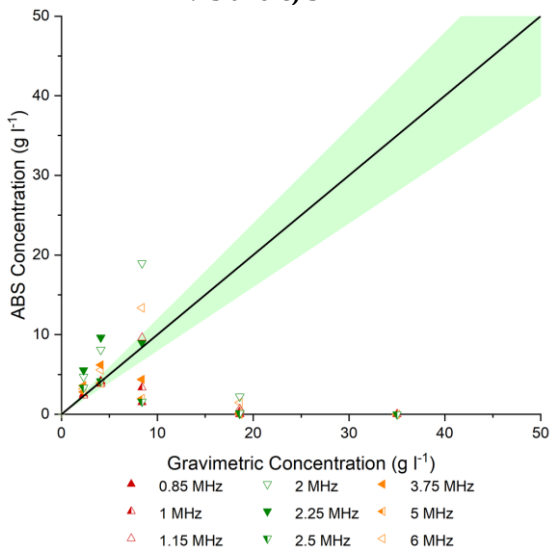

Figure 4.62 Concentration as measured by ABS vs gravimetric concentration for single frequency inversion profiles for flocculated magnesium hydroxide with the shaded area representing a 20% error margin

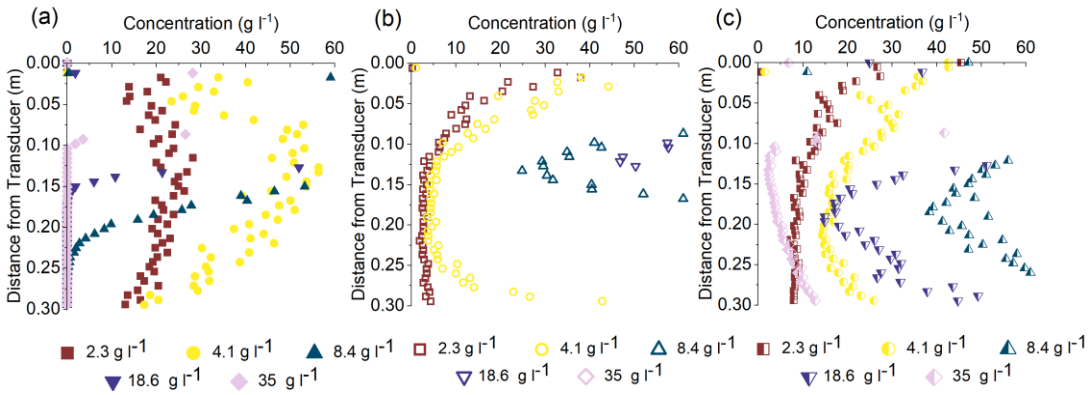

Figure 4.63 Dual Frequency inversion profiles for flocculated magnesium hydroxide for frequency pairings of a) 0.85 and 2 MHz, b) 2 MHz and 3.75 MHz and c) 0.85 and 3.75 MHz

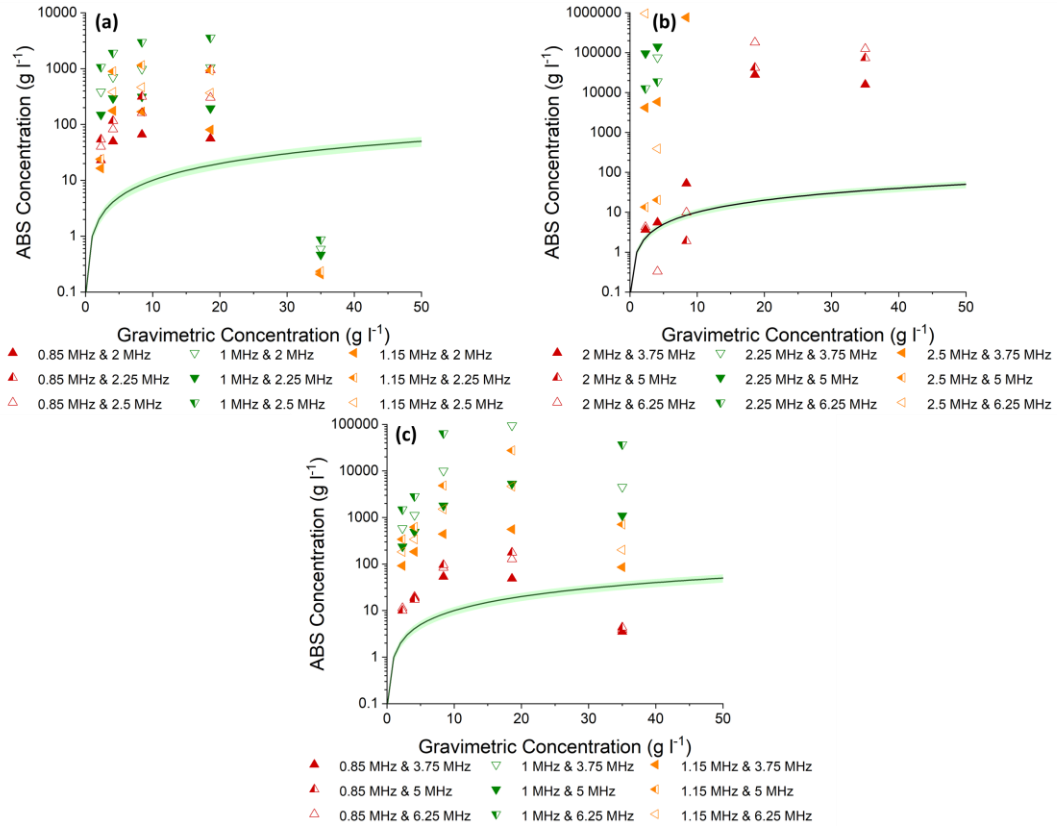

Figure 4.64 Concentration as measured by ABS vs gravimetric concentration for dual frequency inversion profiles for flocculated magnesium hydroxide for a) 1 and 2.25 MHz, b) 2.25 and 5 MHz and c) 1 and 5 MHz central frequency probe pairings. with the shaded area representing a 20% error margin

The BPS inversion data, shown in Figure 4.65-Figure 4.68 below, obtained similar results to the flocculated calcite data where the lowest frequency probe generally produced the most accurate results that might be expected due to the two systems sharing similar scattering and attenuation parameters. For the two highest frequency probes, however, the dual frequency inversion appears to become erroneous at intermediate distances from the probe and results appeared less accurate than those seen for flocculated calcite (Figure 4.56 versus Figure 4.68). These results were also seen to have an enhanced noise floor compared to the flocculated calcite (Figure 4.18 (b)), however, and is likely the cause of the errors seen for the dual frequency method for these probes.

Enhancement of the noise floor has been attributed previously by Haught et al. [272] to the increase in background noise caused by higher sediment concentration when performing experiments at high and low flow in the Fraser River at Mission, British Columbia and that the change in noise floor was also dependent on the probe frequency used. For their lowest frequency probe, 300 kHz, the noise floor increased

by 89-116% for large flows (and thus higher sediment concentrations) where sediment concentration was increased from 16 to 263 mg l^{-1}. While the concentrations studied here are orders of magnitude higher than those studied by Haught et al. it is likely that a similar relationship is applicable here. By taking passive acoustic measurements, where the transducer is set to only receive incoming signals, this change in noise floor may be better quantified in future work and mitigated against when either determining effective measurement limits or directly correcting profiles to remove the effect of the noise floor when performing calibration measurements by applying the methods suggested by Haught et al. [272]. It should also be noted that the signal-to-noise ratio may also depend on the turbulent kinetic energy [188] (here dependent on the stirring rate in the tank) and it was suggested by Merckelbach [273] that sediment particles may regroup due to small scale eddies thus changing the resulting backscatter strength. For the systems studied here, however, as the stirring rate is constant (thus the turbulent kinetic energy is also constant) and the flattening of the profiles is observed at a particular distance and not a enhancement of the backscatter across the entire length of the profile, it is thought that the noise floor enhancement observed by Haught et al. [272] is the cause of the flattening of the profiles seen in the results shown here.

The cause of the observed difference in the noise floor between BPS and the other sediments studied is still in question, however, as the concentrations studied for each sediment are similar. The most obvious difference separating BPS is the very wide particle size distribution seen for the sediment (Section 4.2.3, Figure 4.4). Current theory suggests that the signal-to-noise ratio will increase with the standard deviation for a non-uniform size distribution of particles [266]. Despite this, it has been found by Salehi and Strom [188] that, for signal-to-noise ratios below 30, this relationship was not absolute for kaolinite suspensions of similar mean size and standard deviation and that individual calibration across sediment sizes and size distributions should be performed to produce accurate inversion results. Although no independent verification of the noise floor was determined by Salehi and Strom [188], intuitively the conclusion may be drawn that, similar to increases in concentration, an increase in particle size distribution and resulting increase in attenuation [266] may also increase the noise floor in a given system and where attenuation begins to reduce the

signal close to the noise floor the effect may be readily observed. This result cannot be verified with certainty and remains an area to be explored in future work.

Directly comparing k_s values (Appendix B, Table B.2) it can be seen that BPS exhibits a higher backscattering constant, indicating that the signal to noise ratio may be improved compared to calcite. The *dG/dr* values (Table 4.3), however, are almost twice that of calcite for comparable concentrations (e.g. concentration 4 that corresponds to ~20 g l^{-1} for both datasets) and indicate a similar limit of -10 Np m^{-1} as was observed for all previous datasets (excluding magnesium hydroxide particulates for which inversion results are questionable). This increased attenuation may also possibly be related to the large PSD width observed for BPS (Figure 4.4), however, as a larger size range has been generally shown to increase attenuation [266]. A limiting total attenuation, above which attenuation cannot be measured, has been found by Kalashnikov and Challis [274] to exist at 6 Np. For a backscatter system this would correspond to a path length of 0.6 m for a system with an attenuation value of 10 Np m^{-1} (i.e. a range of 0.3 m for the experimental setup shown here owing to the fact that the received signal must also travel back to the transducer before it is detected) thus the limiting attenuation value observed here is not unexpected and corresponds well with the literature value.

For future work, correct identification of the noise floor by examination of far-field signals (that could not be measured in all cases here due to tank size limitations) or by using passive acoustic measurements should therefore be performed for each profile as it can even be seen to change with concentration such as for the magnesium hydroxide results (Figure 4.14 and Figure 4.16) and strongly affects results obtained from the concentration inversion. Overall, it can be seen across all the results presented here that, so long as attenuation is not excessive (*dG/dr* < -10 Np m^{-1}) and raw decibel signals are not adversely affected by the system noise then an accurate concentration inversion is possible with improvements in the accuracy in the near-field generally seen when applying the dual frequency method. For completion, errors in the inverted concentration profiles are plotted as a function of the measured attenuation for the both the single and dual frequency methods in Appendix B, Figure B.3 and Figure B.4 and as 3-D MATLAB figures available at https://github.com/alastair-tonge/Novel-characterisation-of-complex-dispersions-usi

ng-acoustic-backscatter-systems-Supplementary-Data. The average error in the inverted concentration profiles over a distance of 0.1 to 0.2 m from the probe are also shown in table format in Appendix B, Table B.3-Table B.6 for both the single and dual frequency inversion.

In terms of the application of the ABS to measure flocculated particles in processes at Sellafield Ltd. it would be recommended to use probes of around 1 MHz as typically signals from this frequency showed the lowest levels of attenuation and therefore attained the most accurate concentration inversions and sediment concentration were high enough to produce backscatter profiles with sufficient signal-to-noise ratios.

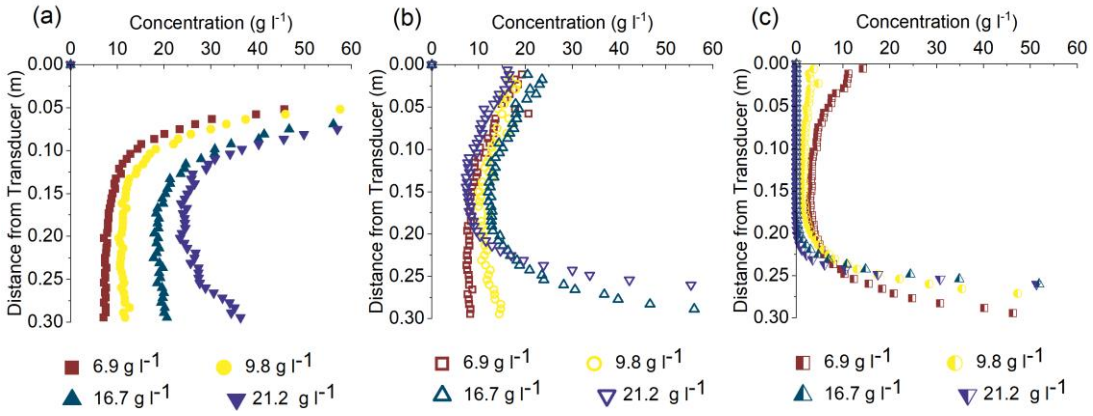

Figure 4.65 Single Frequency inversion profiles for BPS at a) 1, b) 2.25 and c) 5 MHz

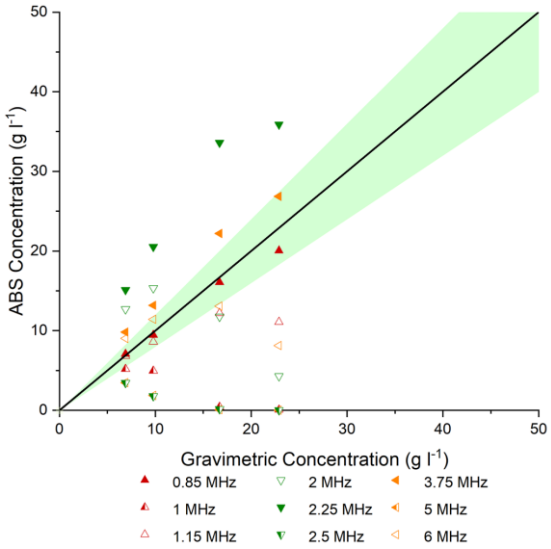

Figure 4.66 Concentration as measured by ABS vs gravimetric concentration for single frequency inversion profiles for BPS with the shaded area representing a 20% error margin

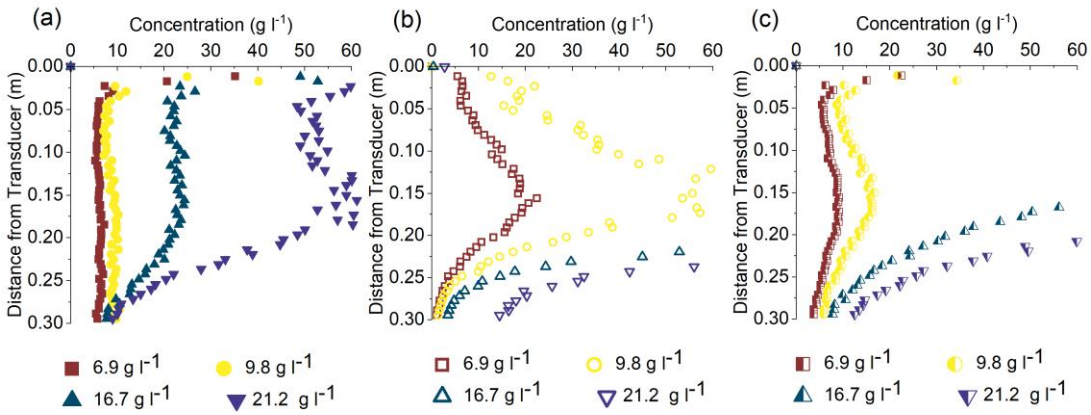

Figure 4.67 Dual Frequency inversion profiles for BPS for frequency pairings of a) 0.85 and 2.25 MHz, b) 2 MHz and 5 MHz and c) 0.85 and 5 MHz

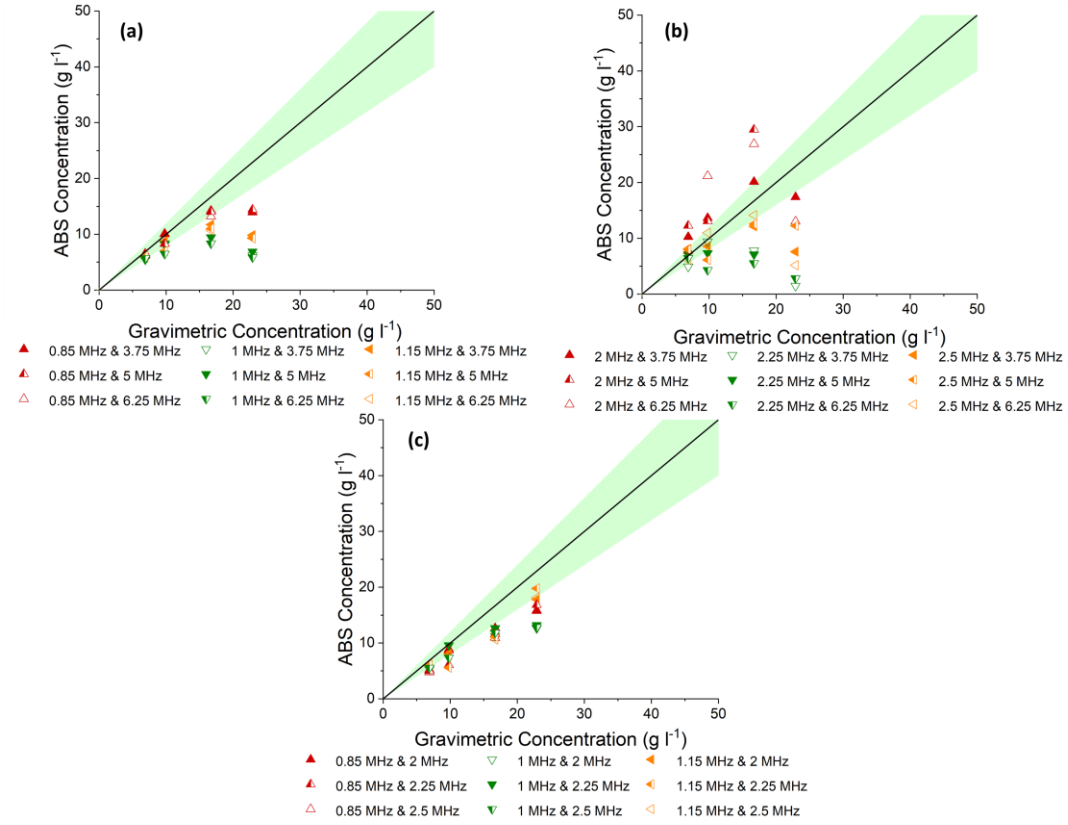

Figure 4.68 Concentration as measured by ABS vs gravimetric concentration for dual frequency inversion profiles for BPS for a) 1 and 2.25 MHz, b) 2.25 and 5 MHz and c) 1 and 5 MHz central frequency probe pairings with the shaded area representing a 20% error margin

4.4 Conclusions

Backscattering and attenuation constants for three flocculated systems and two primary particle sets have been studied as a function of frequency, concentration, particle size distribution and fractal dimension determined using multiple transducers pulsed across varying frequency ranges using the method of Bux *et al.* [17]. Results for the scattering cross-section, χ, and the form function, f, were compared to modelled

values calculated using the Hybrid model from Thorne *et al.* [47] and the Irregular Solid Scattering model from Thorne and Meral [48]. An important floc structural parameter, the fractal dimension, as well as the particle size distribution were determined using static light scattering to provide model inputs for the flocculated particle systems studied. Model results were probed by varying the fractal dimension and standard deviation in the modelled particle size distribution and compared to experimental data. Raw decibel profiles were converted to concentration profiles using both the single [33] and dual frequency [161] methods to investigate the applicability of *in situ* ABS to measure concentration changes and their sensitivity to flocculation state and particle size.

Experimental comparison to model results was found to indicate generally that the scattering and attenuation values correspond most closely to those modelled using the specific gravity normalised [17] Solid Scattering model from Thorne and Meral [48]. Results were in agreement with the findings of Vincent and MacDonald [120] that indicated that acoustic scattering may be dominated by the tightly bound aggregates of primary particles that make up the macrostructure of the floc. It is also proposed here, however, that viscous layer overlap may be the predominant cause of the reduction in attenuation seen for larger flocs studied by Thorne *et al.* [47] and therefore provides a unique insight as to how the initially contrasting theories derived from the same dataset may be united in future modelling efforts.

Results presented here also indicate that in the low *ka* regime, although scattering cross section values generally fit with model predictions for the particulate sediment systems, there is significantly larger attenuation observed in the magnesium hydroxide results that is attributed here to either structural losses [151] or high irregularity in shape caused by to the nanocomposition of the primary particles [134]. The scattering cross-section for the flocculated systems (excluding magnesium hydroxide results) were found to deviate from the model results and lay on a straight line (on a log-scale) as opposed to following the plateau and sharp increase predicted by the model.

The form function in the low *ka* region showed a consistent deviation from the model with relatively low variability in the data for the flocculated particle systems and

therefore highlights the potential to accurately revaluate the heuristic fits in the low *ka* region using data presented here and by other authors [17]. Similar but more scattered deviation from the modelled form function was also observed for the particulate systems studied. Such fits would allow for prediction of the acoustic properties of particles in mineral and engineering waste slurries that commonly contain particle size fractions down to 0.1 μm. If these properties can be reliably predicted this will subsequently allow for the concentration or size inversion techniques that have been explored here to be applied to optimise sediment settling and transport processes by taking *in situ* ABS measurements.

Although an exact conclusion cannot be drawn here but remains a subject of interest for future modelling studies, the potential to fit acoustic data to the Hybrid model by altering the fractal dimension and standard deviation of the log-normal size distribution when data is available over a number of frequencies is demonstrated. Fit results to the flocculated calcite data indicated that multiple mean sizes in combination with changes in the particle size distribution COV could provide nearly identical fits to the model data. Although realistic bounds for the mean size and COV must therefore be determined through additional measurement techniques such as light scattering the results presented clearly demonstrate the additional data analysis available by taking measurements at several frequencies using multiple probes pulsed at a number of frequencies across a modest bandwidth (~6 MHz here). The ability of ABS to accurately determine particle size distributions remains of interest for future work as small, concentrated particles are commonly encountered in mineral and slurry processing the ability of the ABS to characterise the sediment size distribution would allow for greater understanding dewatering and networking in settling dispersion and settled bed structures [24], [26] especially in cases where ABS may be applied at the lower detection limit of other devices such as FBRM or light scattering.

Despite deviations from model values, concentration inversions were found to be adequate for both single and dual frequency methods so long as the raw data were clear of the noise floor with an improvement in the accuracy of the profiles seen in the near field when using the dual frequency method. Across all sediment systems studied the dual frequency method provided an improvement in accuracy over the single frequency method (when compared the accuracy of the most accurate of the

two corresponding single frequency inversions) for 168 of the concentration profiles produced out of a total of 675 dual frequency inversion profiles (approx. 25 %, derived from data shown in Appendix B, Table B.3-Table B.6). Of these 168 profiles 61 profiles were accurate to within 20% of the known concentration value. It is clear that, while the dual frequency method will not always provide an increase in accuracy compared to both single frequency profiles, it still provides an opportunity for accuracy improvement in some cases and allows for a large amount of additional data to be generated that may prove useful for data mining and machine learning/ optimisation techniques.

Multiple scattering effects that were typically enhanced at high concentrations and frequencies were seen to cause a practical increase in the noise floor for the most highly attenuating dispersions studied. Overall, these results demonstrate the ability of ABS to characterise flocculated dispersions *in situ* in terms of their acoustic constants (such as the attenuation coefficient, estimated from *dG/dr* vs concentration plots Figure 4.20-Figure 4.28) however phenomena such as viscous layer overlap and system noise mean that it is not absolutely certain these are the fundamental acoustic constants as their values may be somewhat affected by these phenomena. So long as these phenomena can be neglected accurate acoustic constants can be produced but otherwise, they must be accounted for in future modelling efforts. Figure 4.49-Figure 4.68 indicate the ability of ABS to produce accurate concentration profiles even up to ~35 g l^{-1} for some of the systems studied so long as *dG/dr* does not exceed ~-10 Np m^{-1} and raw decibel data is not too close to the system noise floor (see also Appendix B, Figure B.3 and Figure B.4) a value that corresponds well with the 6 Np limit predicted by Kalashnikov and Challis [274] when considering the 0.6 m signal path in experiments performed here. Such measurements have not been performed previously and represent a new advancement in the development of ABS as an *in situ* concentration profiling device for cohesive sediments. The ability to measure higher concentration increases the relevance of ABS for application in engineering environments, where cohesive sediments are often encountered at intermediate concentrations during settling and transport processes.

Chapter 5 Use of *in situ* acoustic backscatter systems to characterise separation of flocculated calcite in a laboratory scale thickener

5.1 Introduction

To aid in the transportation, dewatering and storage of radioactive UK legacy waste sludges at Sellafield Ltd., the application of an Acoustic Backscatter System (ABS) was investigated in this study, as a method for monitoring suspended solids concentration and consolidation of cohesive and aggregated sludges (that form the basis of many wastes at Sellafield) that could bring significant improvements to waste management efficiency and model predictions of these systems in operational environments. However, while there is high potential applicability of ABS technology in the nuclear waste sector, currently there is very little data available on the application of ABS to fine cohesive and aggregated sludges, particularly at high solids concentrations, which form the basis of many wastes encountered at Sellafield. This lack of system data greatly limits the current utilization of acoustics in real industrial applications.

This study therefore attempts to infer changes in the settled bed density of a laboratory scale thickener as a function of bed height and underflow flow rate through simultaneous ABS measurements both horizontally through the bed and vertically downward through the settling zone. The solids residence time and underflow concentrations are modelled based on bed height measurements taken with the ABS and a modified mass balance from Bürger, Diehl and Nopens [275]. Underflow concentration values from the model are then compared to those from underflow sampling at 15-minute intervals for a flocculated calcite sediment system. Horizontal attenuation measurements at multiple heights were also performed in a second experiment and each potential operational scenario of the thickener (start-up, steady-state operation with a stable bed, and bed depletion) investigated.

5.2 Materials and method

Omyacarb 2 calcite (d_{50} approximately 2 μm) was chosen as a simulant material for spent nuclear fuel (SNF) in this study as it has been used previously for ABS studies in both the same laboratory scale thickener [189] and in large scale settling trials [38]. Its polymer flocculation and settling dynamics have also been studied extensively [127], [240], [244] [94] and are of great interest for mining and waste processing operations involving limestone or marble. ABS measurements were performed in a laboratory scale thickener at the University of Melbourne, to assess the application of the ABS as a real-time monitoring device for high concentration (~30 %v/v) solid-liquid separation systems, similar to those that might be encountered during nuclear waste dewatering processes. Figure 5.1 shows a schematic of the laboratory scale thickener used and the placement of the ABS probes. The heat exchangers shown were not active for the experiments performed, but the pipe length for the entry heat exchanger was retained to provide a total flocculation length of 6 m. The settling zone was a Perspex column ~1 m high and 0.3 m diameter, shown in Figure 5.2 (a) and (b), with a fitted metal cone for underflow discharge accompanied by two scraper rakes (1 x 1 cm), shown in Figure 5.2 (c) that rotated radially from a central mixing rod. An aqueous calcite feed, diluted in-line with mains tap water from a 50 %w/w slurry, at a nominal ~4 %w/w concentration was pumped at 105 L hr^{-1} in-line with a 2000 ppm aqueous, high molecular weight, anionic polymer solution (AN934SH, SNF (Australia) Pty Ltd.) to produce 200 g (polymer) t^{-1} (solid) in the mixed inlet feed. A mean pipe velocity of 0.389 m s^{-1} was achieved along the 6 m of pipe length before entering the feedwell of the thickener (Figure 5.2 (d)) allowing for flocculation under moderate turbulent conditions to occur, in order to create a highly flocculated suspension, typical of mineral wastes.

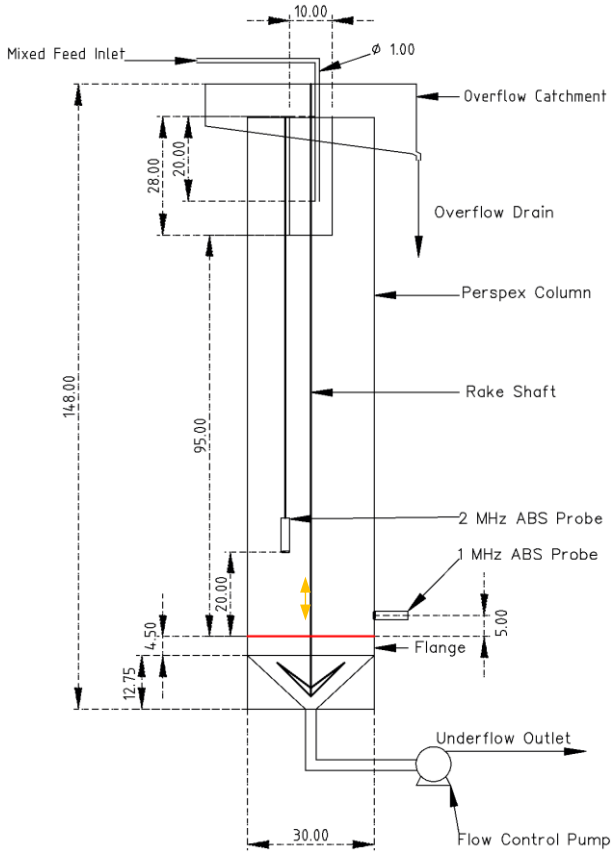

Figure 5.1a) Laboratory-scale thickener column diagram (all measurements are given in millimetres).

Figure 5.2 a) Overall view of the setup used for the laboratory-scale thickener experiments b) the observed flocs during operation c) The rake and funnel section and d) the feedwell.

By careful operation of the pump at the tank outlet, pseudo-continuous operation of the thickener was achieved after the consolidated sediment bed had been allowed to

build-up to an equilibrium height of ~0.175 m. Once the desired bed height was reached the underflow rate was gradually increased and set to achieve steady-state (constant bed height) operation of the tank. The volume of feed allowed for ~5 hours of continuous operation.

A second experiment under otherwise the same conditions was performed except that the bed was initially allowed to build up to 0.3 m before setting the underflow to slightly higher than the inlet solids slurry rate (12.7 L hr^{-1} as opposed to 10 L hr^{-1}) in order to decrease the bed height. In this way, ABS attenuation relationships with concentration during thickener emptying scenarios can also be investigated so that acoustic measurements taken here cover all possible states of thickener operation (bed build up, steady state operation and bed depletion). Furthermore, this was performed in order to see if there was observed minimum height at which on ABS attenuation measurements and sample outlet concentrations would subsequently decrease. Finally, in order to determine the ability of the ABS to build up a concentration profile for the bed attenuation measurements were taken using two 1 MHz probes mounted on the tank outer face facing horizontally at 5 and 15 cm above the base of the thickener column. Attenuation measurements from each probe are then compared to determine if a qualitative relationship can be drawn between increased bed depth/ concentration and horizontal acoustic attenuation.

Acoustic measurements were taken using a commercial Aquascat1000 (Aquatec Group Ltd., UK) with 1 and 2 MHz transducers, where the 1 MHz probe was positioned on a bracket on the outer tank face facing horizontally through the settled bed at 5 cm above the base of the column and the 2 MHz probe facing vertically downward submerged 20 cm above the column base initially (See Figure 5.1). [189] The 2 MHz probe was also periodically moved upward, as the consolidated bed built up initially over time, to ensure that the first 0.1 m of the 0.3 m measurement zone was in the settling zone directly above the bed. The vertical probe allowed for tracking of the sediment bed height via the interface reflection of the acoustic signal as well as indicating any changes in the particle size or concentration in the settling zone above the bed throughout the trial. The horizontal probe allowed for continuous qualitative measurement of changes in settled bed density from bed height and underflow rate changes, via attenuation of the backscattered acoustic signal, as demonstrated in

previous work by Hunter *et al.* [189]. Here, however, measurements were taken through the tank wall to investigate the ability of ABS to take measurements non-intrusively.

The size of the flocculated aggregates at the column inlet were estimated using online measurements from a Focussed Beam Reflectance Measurement (FBRM) probe (Lasentec/ Mettler-Toledo Ltd., UK), taken in a once-through flow system (total flocculation length of 5.34 m and a pipe internal diameter of 7.7 mm) designed to mimic the shear conditions and nominal sediment and polymer concentration used for the thickener experiments (~4 %w/w calcite and 195 g t^{-1} (solid) with a flocculation length of 6 m and a hydraulic pipe diameter of 10 mm). The pressure drop and hence the energy dissipation rate was calculated using the Blasius friction factor, from which the shear rate could then be found as per the method used by Heath *et al.* [94]. The initial flow rate of the slurry in the pipe reactor was therefore calculated such that the product of the shear rate and residence time in the pipe reactor and the thickener feedwell were of similar values (dimensionless values of 5616 for the thickener versus 5900 for the pipe reactor) while still keeping the flow rate high enough to suspend the flocs in the pipe and get sufficient counts from the FBRM to obtain a statistically accurate particle size measurement.

5.3 Transitive volume balance

In order to model the solids residence time and outlet concentration from the thickener as a function of measured bed height a volume balance was performed between the outlet and the top of the settled bed detailed below. Within the thickening zone the increase of mass per unit time in an arbitrary interval between two heights (h_1, h_2) is given by Bürger, Diehl and Nopens [275] as

$$\frac{d}{dt}\int_{h1}^{h2} AC(z,t)dh = A(\phi_{h1} - \phi_{h2}) + \int_{h1}^{h2} Q_f(t)C_f(t)\delta(h)dh \qquad \textbf{5.1}$$

Where the first term represents the mass accumulation with time (t) given by the cross-sectional area, A, and the integral of concentration with respect to height over the interval width. The second term represents the sediment mass flux in and out ($\phi_{z1} - \phi_{z2}$) due to the downward velocity caused by both the underflow and

hindered settling/ compression of the bed. The third term represents the contribution of the feed to the mass accumulation in the interval given by the feed flow rate (Q_f), concentration (M_f), defined as the solids volume fraction multiplied by the solid density, and the Dirac delta distribution (δ). The sediment flux term (ϕ) is given by [275]

$$\phi\left(M, \frac{\partial M}{\partial h}, h, t\right) = v_{hs}(M)M + \frac{Q_u(t)M}{A} - \left(\, d_{comp}(M) + d_{disp}(h)\,\right)\frac{\partial M}{\partial h} \qquad \textbf{5.2}$$

where d_{comp} is the reduction to the hindered settling velocity (v_{hs}) due to the effective solids stress of the network that occurs when the bed concentration exceeds the gel point, and the bed forms a cohesive network while, d_{disp} represents dispersion effects. Both terms are expressed in a form analogous to Fick's law diffusion, in terms of a concentration gradient $\partial M/\partial h$. If the balance is performed at the surface of the bed the sediment flux-in term (ϕ_{h1}) would be 0 as there is no bed above this point to cause a flux and only the contribution from the feed would cause mass accumulation. Setting $\phi_{h1} = 0$ and dividing Equation 5.1 by A and M we obtain

$$\frac{d}{dt}\int_{h1}^{h2} dh = \left(-\frac{\phi_{h2}}{M(t)}\right) + \int_{h1}^{h2} \frac{Q_f(t)M_f(t)}{M(t)A}\,\delta(h)dh \qquad \textbf{5.3}$$

By performing the integration and substituting Equation 5.2 into Equation 5.3 the change in height of the top layer of the bed ($h2$) from a reference point ($h1$) (defined here as dh_{bed}) at each time step (dt) can be defined:

$$\frac{dh_{bed}}{dt} = -\frac{Q_u(t)M}{A} - \left[v_{hs}(M) - \left(\, d_{comp}(M) + d_{disp}(h)\,\right)\frac{\partial M}{\partial h}\right] + \int_{h1}^{h2} \frac{Q_f(t)M_f(t)}{M(t)A}\,\delta(h)dh\,\frac{dh_{bed}}{dt} \qquad \textbf{5.4}$$

$$\int_{h1}^{h2} \delta(h)dh = 1 \qquad \textbf{5.5}$$

As the effective solids stress of the network is not known the hindered settling, compression and dispersion terms were collected into a single parameter ($dh_{compression}$) such that

$$dh_{compression} = -\left[v_{hs}(M) - \left(\, d_{comp}(M) + d_{disp}(h)\,\right)\frac{\partial M}{\partial h}\right] \qquad \textbf{5.6}$$

dh_{bed} was measured in this experiment by the vertically facing 2 MHz ABS probe and the feed and underflow were know at all time steps. Therefore, using MATLAB,

a transitive volume balance model between the top of the bed and the top of the underflow cone was set up such that the thickness of each newly settled layer (*dh)* is given by

$$dz = \frac{\left(\frac{M_f * Q_{feed}}{M_h}\right)}{A} \quad \textbf{5.7}$$

where M_f is the feed concentration (in w/v), Q is the flowrate, M_h is the settled layer concentration and A is the cross-sectional area of the tank. The value of M_h was adjusted so that the output concentration from the model (shown below) approximately matched the values determined from sampling. The change in height due to compression of the bed at each time step (i) can be given in terms of the model parameters

$$dh(i)_{compression} = dh(i)_{bed} + \frac{dt * Q(i)_u}{A} - dh \quad \textbf{5.8}$$

where $dh(i)_{bed}$ is the change in height of the bed at each time step as measured by the ABS and dt is the value of the time step. As a new layer j_n lands at each time step the position of the layer j_n is given by

$$h(j_n, i) = h(i)_{bed} \quad \textbf{5.9}$$

where $h(i)_{bed}$ is the height of the bed at each time step. The new position of the already settled layers ($j_1 \ldots j_{n-1}$) at each time step is then given by

$$\mathrm{h}\,(\,j1 \ldots jn-1, i\,) = h\,(\,j1 \ldots jn-1, i-1\,) - \frac{Q(i)_u dt}{A} + dh(i)_{compression} \quad \textbf{5.10}$$

And the residence time corresponding to each layer at each time step can be calculated as follows.

$$t_{res}(\,j1 \ldots jn-1, i\,) = t(i) - t(\,j1 \ldots jn-1, i\,) \quad \textbf{5.11}$$

Completing the volume balance at the outlet, as the total downward velocity of the layers is known from $\frac{dt*Q(i)_u}{A_{tank}} - dh(i)_{compression}$ the predicted mass flow and concentration at the outlet is given by

$$M_{out} = \left(\frac{dt * Q(i)_u}{A_{tank}} - dh(i)_{compression}\right) AM_h \quad \textbf{5.12}$$

and by dividing by $Q(i)_u$ the concentration (w/v) at the outlet can then be found

$$M_{out} = \left(\frac{dt}{A_{tank}} - \frac{dh(i)_{compression}}{Q_u}\right) AM_h \quad \textbf{5.13}$$

5.4 Results and discussion

5.4.1 Determination of floc size using FBRM

Figure 5.3 shows FBRM data for the conditions used in the pipe flow reactor that most closely mimicked those at the thickener feed outlet. Although the particle size is seen to decrease slightly with time the change is not significant and is likely due to small fluctuations in flocculant and slurry feed rate and concentration. The mean value for the square-weighted chord length, demonstrated previously by other authors to be a good measure of flocculated particle size calculated from a chord length distribution [191], [276], was 512.7 μm. Although the particle size observed here is large compared to those seen by other authors it should be noted that the flocculant dose was much higher (200 g of flocculant per tonne of solids compared to 20 g t^{-1} used by Heath *et al.* [94]) and from visual inspection of the flocs in the tank (Figure 5.2 (c)) this value seems reasonable.

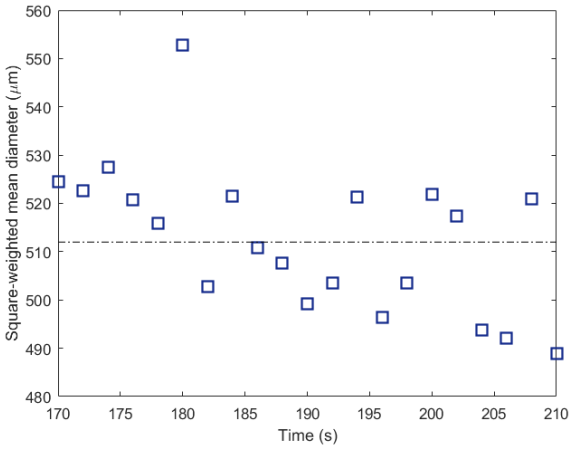

Figure 5.3 FBRM square-weighted chord length data obtained from flow reactor for shear conditions corresponding to laboratory scale thickener feed shear history. Dot-dash line shows mean value.

5.4.2 Laboratory scale thickener results

Figure 5.4 (a) and (b) show time averaged decibel signals at different times over the course of the trial for the 1 and 2 MHz probes with signals averaged over 15- and 1-minute intervals respectively. At all times shown, the profiles appear qualitatively similar. For the horizontal 1 MHz data, at very small distances (<0.03 m) the signal is complicated by ringing interference from the Perspex wall and is ignored in analysis. After this point, the signal decays in an approximately linear fashion with distance,

until reaching the noise floor of the instrument. The gradient of the decibel profiles between 0.03 and 0.085 m from the probe was used to approximate the bed attenuation (in dB/m) through the settled bed. The backscatter profiles for the vertically mounted 2 MHz profiles (Figure 5.4 (b)) were used in a similar fashion to monitor the acoustic response of the particles close to the inlet of the settling tank with attenuation values determined over a range of 0.04-0.08 m in front of the probe face. Here, the signal peak at very small distances (<0.02 m) is due to ringing interference from the probe itself, whereas after this point, the signal decays in a more logarithmic fashion, due to the much lower concentration in the dispersion zone above the bed.

The logarithmic decay of the decibel signal with distance is seen because, at low particle concentrations, additional signal components from scattering are significant compared to the attenuation signal components causing the relationship to appear logarithmic. Mathematically, this can be seen from Equation 2.5, the equation governing the form of the acoustic signal in volts, and Equation 2.33 the natural logarithm of Equation 2.5. Although plotting in decibels involves instead taking the logarithm with base 10 multiplied by a factor of 20 the shape of the plots would remain the same as on a natural log scale. At high particle concentrations however, due to the general increase of the attenuation signal with particle concentration [46], [160], [189] these scattering components are not seen to have as significant an effect on the signal-distance relationship and the signal appears more linear with distance. This change in the signal-distance relationship with concentration has also been observed by Hunter *et al.* for spherical glass particle dispersions up to 50 g l^{-1} [160]. The attenuation values shown in Figure 5.4 (b) are seen to remain relatively constant throughout the course of the experiment, indicating the inlet particle concentration and aggregate sizes did not change significantly. Here, the signal peak at very small distances (<0.02 m) is due to ringing interference from the probe itself, whereas after this point, the signal decays in a more logarithmic fashion, due to the much lower concentration in the dispersion zone above the bed.

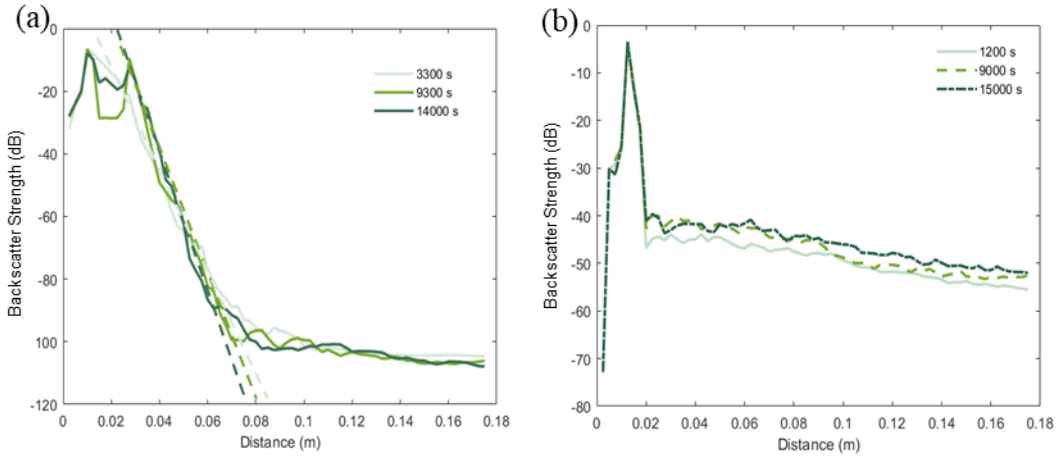

Figure 5.4 a) Backscatter strength in decibels vs distance for a) horizontally mounted 1 MHz probe (averaged over 15 minutes, dashed lines indicate attenuation fits) and b) vertically mounted 2 MHz probe (averaged over 1 minute)

Figure 5.5 (a) shows the bed height as determined from the bed reflection using the vertically mounted 2 MHz ABS probe and the visually determined height at the edge of the tank. The secondary y-axis shows the underflow rate at all stages during the experiment. The initial value for the underflow rate corresponded to one third of the concentrated slurry feed rate to allow a bed to form in the thickener. As the observed bed height approached 15 cm at around 4920 s the underflow rate was increased gradually and set to maintain the thickener at steady state operation, such that the bed height would remain constant. The final value set for the underflow rate was ~20 % higher than the slurry feed rate to account for lower solids concentration in the underflow.

The initial period after turning the underflow pump up to its final value maintained a relatively constant bed height. Good agreement was seen between the height determined from the bed reflection using the ABS and the visually determined height early on in the experiment however sediment was seen to pile in the centre of the tank as the bed built up causing a larger reading for the height of the bed to be measured with the ABS for most of the experiment. However, the bed height seen by the ABS gradually decreased while the visual height measurement increased from ~13000 s onward. It was assumed this change was caused by “ratholing” of the bed. “Ratholing” or “coring” is where the centre of the bed collapses due to the excessive underflow creating a channel through which thinner sludge can be pulled from above [243]. Due to the potential change in slope of the bed formed over time, it was not possible to eliminate the error reliably, although for most of the time, the offset between the two

measurement techniques was relatively constant (suggesting minimal changes to the slumping angle) before ratholing occurs toward the end of the experiment.

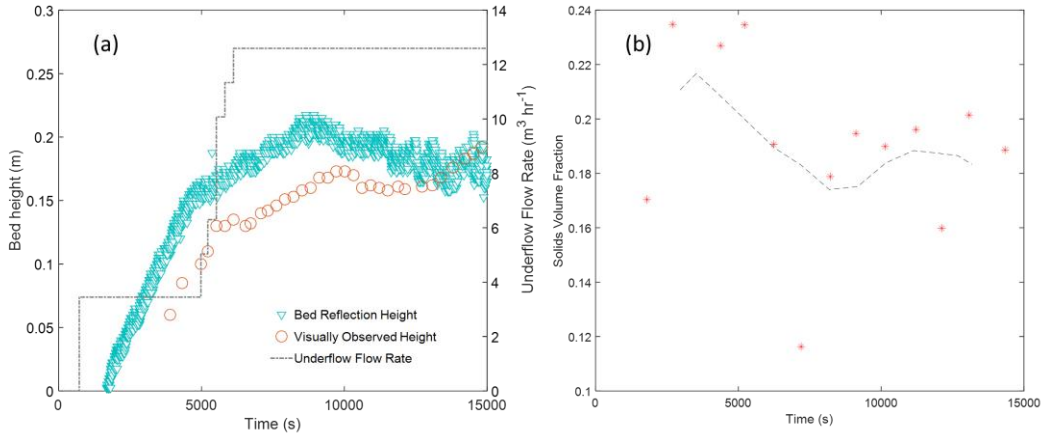

Figure 5.5 a) bed height as measured with the ABS backscatter and visual measurements with underflow flow rate vs time and b) underflow sample data vs time (dotted line indicates 5-point moving average)

Figure 5.5 (b) shows underflow sample data over the course of the experiment. At the beginning of the run, when the bed was still building up, the initial underflow sample had a volume fraction of only 0.17 that increases up to 0.23 when the bed height was increased from ~0.05 to 0.1 m. This indicates an increase in sediment concentration with bed height; an effect that has been widely reported and is due to both the increased residence time within the bed and the larger compressive forces exerted on the bed [23]–[25].

Figure 5.6 shows a colour map of solids residence time vs bed height during the experiment calculated using the algorithm described in Equations 5.6-5.11. The solids residence time of the underflow reaches a maximum at ~9000 s when the bed height is at a maximum as would be expected. To confirm that the residence times estimated were reasonable, using a bed height of 0.175 m and an estimated bed concentration of 508 g l^{-1} from the underflow concentrations, the residence time in the bed from the mass balance was calculated to be 3757 s; in good agreement with the value of ~3250 s at steady state found using the volume-balance model (Equations 5.1-5.11). It does, however, indicate the need to carefully select C_Z for this model so that the calculated residence times are realistic.

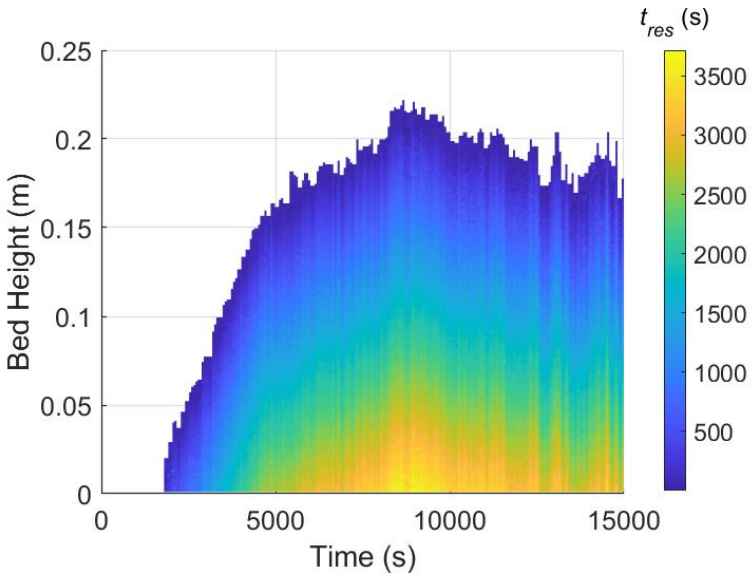

Figure 5.6 Solids residence time as a function of bed height measured using the ABS for all times where the bed level was above the height of the underflow cone calculated from the volume-balance model (Equations 5.4-5.11, for C_z 400 g l^{-1}).

Realistically, the value of C_Z should also be selected as a known initially settled layer concentration, typically assumed by other authors to be the gel point of the suspension [23]. Here the value of C_Z was selected such that the modelled output concentration (shown in Figure 5.7) would match the sample concentrations. In order to determine the validity of these results the mass balance at the outlet was performed (Equations 5.12 and 5.13) to calculate the predicted outlet concentration at each time step and the results compared to sample data in Figure 5.7. The velocity of the particles due to sedimentation and compression ($dh(i)_{compression}$) was found to be negative (downward) for nearly all times steps throughout the experiment as would be expected if particles do not move upward in the bed. Some positive values were seen as the bed initially built up likely due to bed slope causing an overestimation of the increase in bed height with time, causing a corresponding overestimation of $dh(i)_{compression}$ (Equation 5.8). This overestimation is then carried through to the model concentration calculation leading to significantly underestimated concentrations at time steps before ~2000 s.

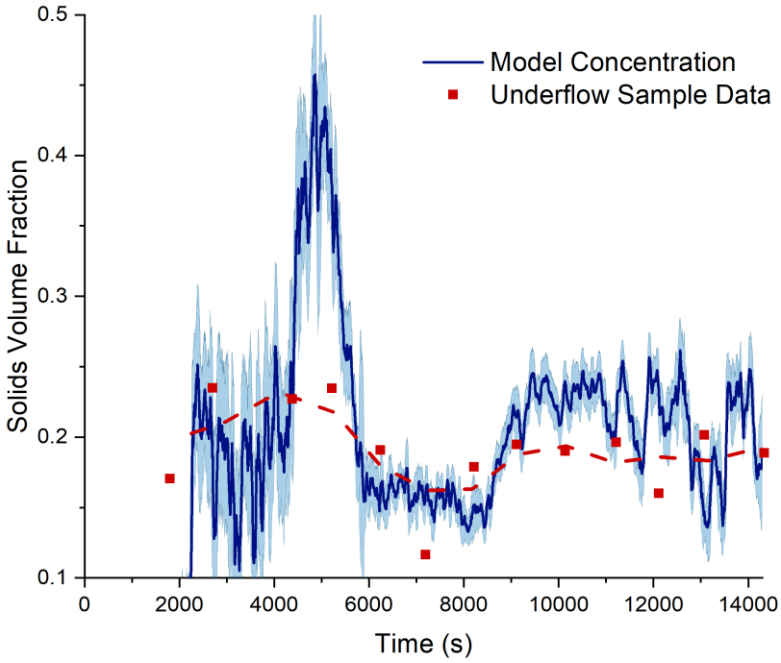

Figure 5.7 Sample data (dashed line indicates 3-point moving average) and mass/volume balance model data (10-minute moving average, shaded area represents +/- 1 standard deviation over same moving average period) for laboratory scale thickener outlet concentration as a function of time

Overall, Figure 5.7 shows fairly good agreement between the mass balance predictions for the outlet concentration and the sample data. Although there is significant variation in the model data due to changes in bed slope and bed disturbances, caused by sudden changes in the underflow rate and sampling, values predicted by the model follow a similar trend to sample data. In particular, a disturbance due to the increased underflow at ~5200 s can be seen as the bed moved down at a higher rate than would be predicted likely due to temporary rheological changes in the bed from the increased flow rate. While a definite conclusion cannot be drawn without direct sampling of the sediment within the thickener results shown here may indicate the potential of ABS to be used to measure bed height and allow for modelling of the thickener outlet concentration.

An increase in the value given for M_h increased the predicted outlet concentration value for the model (Equation 5.13); an effect that is more significant at early time steps when the underflow rate was low as the value of $dh_{compression}/Q_u$ was larger and so M_{out} was more sensitive to M_h. The solids flux through the column during steady-state operation, determined by mass balance based on slurry feed samples, was found to be 0.094 t hr^{-1} m^{-2}. Figure 5.8 (a) shows attenuation through the settling zone for the vertically facing 2 MHz probe averaged over 4 – 8 cm in front of the probe

face with a moving average window of 60 seconds. Although there are fluctuations seen in the attenuation value, caused by having to move the probe periodically up as the height of the bed increased, it is relatively constant with time for the period of steady state operation (~9000 – 12000 s). Were particle size or concentration to increase it is likely there would be an increase in the backscattered signal at short distances and the signal would attenuate more rapidly with increasing distance from the probe [33], [189]. If changes in particle size and concentration could be measured in tandem in a similar system to confirm this conclusion, such as by using FBRM measurements and feedwell sample data, qualitative information about changes to conditions in the feedwell, such as flocculant dosage or particle concentration, could be correlated to acoustic backscatter data and thus used to optimise the flocculation process applied to the feed in an industrial application.

Figure 5.8 (b) shows the horizontal attenuation through the settled bed obtained using the 1 MHz probe at a height of 0.05 m above the column base. Attenuation values were determined over a range from 0.03 to 0.085 m (as indicated in Figure 5.1) to minimise the effect of noise on the probe signal that may result when the backscattered pressure is too low to cause a linear piezoelectric response due to material resistances when converting the acoustic echo to a voltage [189], [277]. Attenuation values seen by the 1 MHz probe in the bed were greater than an order of magnitude larger than those seen with the 2 MHz probe in the settling zone. Given a feedwell diameter of 0.1 m, a feedwell concentration of 60 g l^{-1} and a tank diameter of 0.3 m the concentration in the tank, diluted due to the increase in cross-sectional area, was found to be 6.7 g $l^{-`1}$ compared to the ~525 g l^{-1} bed concentration from sampling. Thus, the observed difference in attenuation can be attributed to the much greater sediment concentration within the bed.

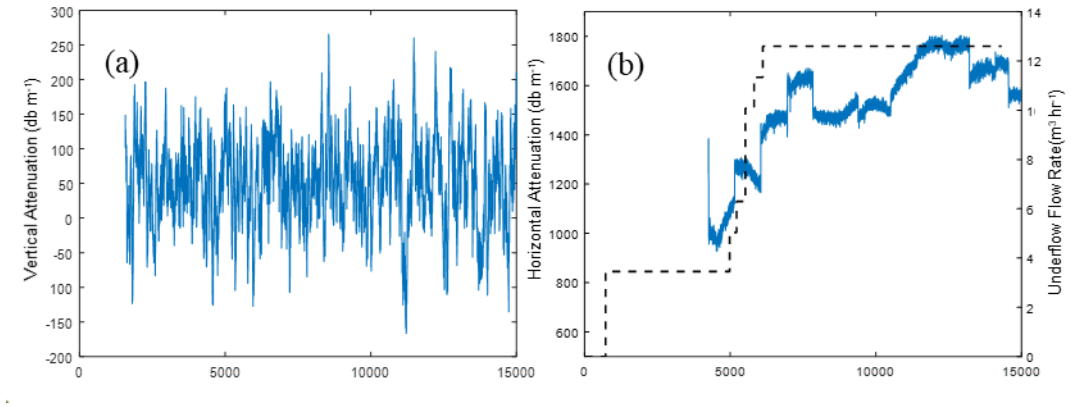

Figure 5.8 ABS signal attenuation a) through the settling zone for the 2 MHz probe vs time and b) through the settled bed for the 1 MHz probe with underflow flow rate on the secondary y-axis

The rapid changes in attenuation at 15-minute intervals are due to sample collection at the underflow, causing a sudden disturbance in the bed and the section therefore seen by the probe. Both increases and decreases in attenuation are seen due to this disturbance, however, as heterogeneity in the bed structure can cause a bed layer of significantly higher or lower particle concentration to suddenly replace the layer measured by the probe, these rapid changes, while difficult to account for completely, actually highlight the sensitivity of the measurement.

It is also noted that increases in attenuation should translate directly to greater bed density, although, while the correlation is linear within a certain region, it is not known whether the high densities of the consolidated bed are outside of this range [160], [189]. Despite these disturbances, there is an apparent clear overall trend observed between the horizontal attenuation and the underflow rate (again shown on the right-hand axis) which is correlated to the overall bed height changes (Figure 5.5). Here, the average attenuation (accounting for sampling disturbances) increases until the bed height is equilibrated, and then remains relatively constant with time. As the bed height increases, the compressive forces and residence time of the layer measured by the probe increase (see, Figure 5.6 (a) at a height of 0.05 m from the column base). The increased bed volume above the measurement zone increases the dewatering of the suspension and therefore leads to an increase in the acoustic attenuation at that height. This result indicates the ability of the ABS to both qualitatively track changes in bed densification through the thickener, while giving insight into the effects of sampling and raking on sediment bed structure. Nevertheless, it does also appear,

when looking at the underflow sample data, that the attenuation results do not correlate directly.

While it is evident the overall bed concentration decreases after the underflow rate is turned up, this effect is not seen by the ABS attenuation results. This discrepancy is likely because the residence time in the upper section of the bed becomes higher over time (as can be seen in Figure 5.6 (a) at a height of 0.05 m from the column base) and so the sediment has had a greater amount of dewatering time at the measurement height of the acoustic probes. Thus, while the concentration at the outlet may decrease temporarily, the concentration in other parts of the bed is higher as the height has increased leading to a greater residence time. This is demonstrated in Figure 5.9 where the horizontal attenuation and modelled solids residence time is plotted as a function of time. A clear correlation can be seen between the measured attenuation and the modelled residence time. As an increase in residence time will increase dewatering, and subsequently particle concentration, this implies that the horizontal attenuation measured during the experiments provides the ability to track changes in bed concentration within the thickener.

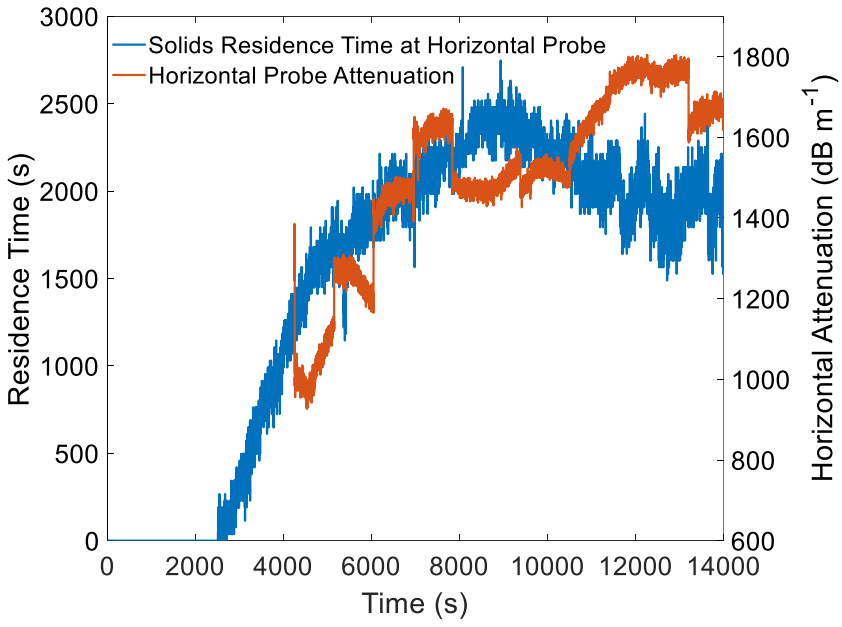

Figure 5.9 Modelled solids residence time at height of horizontal probe (0.05 m, left axis) and horizontal attenuation measured by ABS (right axis) through the settled bed.

For ABS measurements performed by Hunter et al. [189] in the same experimental setup, taken vertically through the bed, the signal was only able to penetrate 70 mm into the bed and the attenuation was found to be depth dependent and so attenuation

measurements could only be compared for the same bed depth. The influence of bed depth on the acoustic attenuation seen by Hunter et al. [189] can be eliminated, however, by taking horizontal measurements through the bed at multiple bed heights operating on a similar principle to the Acoustiscan scanning device [278] albeit on a larger scale. The distance through the bed that the acoustic signal must travel then will be the same for each measurement allowing the effect of bed height and depth on acoustic attenuation, and hence sediment concentration, to be isolated. If multiple probes were placed along the vertical axis facing horizontally into the settled bed, it would be possible to directly infer a density profile through the settled bed, and therefore assess and optimise thickener performance in real-time where sampling would be hazardous, costly or in processes where rapid response times are needed due to unpredictable feed characteristics.

In order to investigate if a significant attenuation difference could be observed at different bed heights measurements were taken in the same system using slightly different operating conditions (detailed in Section 5.2). Summarily, the bed height was allowed to reach a greater height (0.3 m, as measured from the top of the flange indicated in Figure 5.1 (a)) before the underflow was turned on to investigate the effect on ABS and sample measurements during a simulation of thickener emptying scenarios so that ABS measurements during all phases of thickener operation would be obtained. ABS attenuation from two horizontally mounted probes, in conjunction with visually observed heights are shown in Figure 5.10 (a) and sample data obtained from the underflow in Figure 5.10 (b) for all times beginning when the underflow was switched on. For completeness, residence time modelling for the second experiment was also performed (Appendix C, Figure C.2) so that residence time results from each experiment can be compared directly as a reference for attenuation results. As the underflow rates were identical for the times shown for the second experiment the bed height provides a good general representation of residence time, however, and is used for reference in the discussion here for simplicity.

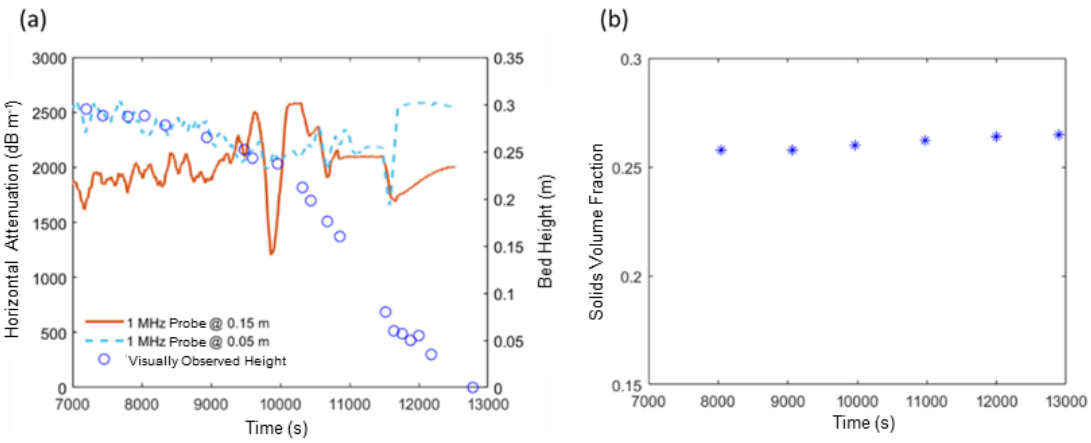

Figure 5.10 a) ABS attenuation and bed height measurements and b) underflow sample data for all experiment times beginning when the underflow pump was switched on

The ABS attenuation data shown in Figure 5.10 (a) clearly demonstrates an increased attenuation at increased bed depth (i.e. at a lower height on the thickener) as might be expected. As the attenuation due to water is negligible in comparison to the overall attenuation (approximately 0.23 dB m^{-1} using the equation from Ainslie and McColm [170]) the change in attenuation with particle concentration should otherwise be approximately linear and would indicate a ~20 % increase in solids fraction over a depth of 10 cm. This values seems reasonable given the sample data from the previous experiment, shown in Figure 5.5 (b), shows a rise in sample volume fraction from ~0.17 to 0.23 for a change in bed height of around 10 cm (occurring between 2500 and 5000 seconds, bed height data shown is in Figure 5.5 (a)). Additionally, higher attenuation values for the second experiment are seen by the probe at 0.05 m height compared to those typically seen in the previous experiment (Figure 5.8 (b)) and are supported by the higher sample solids volume fraction that was obtained from the underflow (data shown in Figure 5.10 (b)). This cannot be directly confirmed without direct solids samples from within the thickener but does indicate at least a qualitative capability of the acoustic apparatus to determine the change in solids concentration with height through the bed.

Although attenuation values for the previous experiment were higher for the probe at 0.05 m height toward the end of the first experiment this is thought to be caused by the aforementioned ratholing effects causing sediment to build up around the sides of the tank and subsequently densify leading to higher attenuation values as the tank is emptied. Some degree of variation may therefore be expected in the attenuation values

toward the end of the experiment as a concentrated clump of sediment may simply remain in front of the probe, enhancing the observed attenuation or suddenly fall away and cause a rapid reduction. These effects were also likely the cause of the fixed attenuation value observed for the probe at 0.05 m as the bed was not seen to fall away from in front of the probe until the last height measurement. Attenuation values before this point were seen to decrease as expected with the overall bed height for the probe at 0.05 m. For the probe at 0.15 m more noise in the data is seen past ~10000 seconds and can matched to the point at which the signal was able to penetrate through and see a reflection from the central impeller shaft (Appendix C, Figure C.1(b) accompanied by a small increase in attenuation. Although this increase in attenuation may not be expected as the settling zone will be at a lower particle concentration than the bed the floc concentration would still be high. A temporary reduction was seen indicated by the valley at ~10000 seconds before returning to similar values seen prior. The exact cause is unknown but may be related to the high concentration and lack of inter-particle contacts in the settling zone that may enhance attenuation [150].

Indeed, the lack of reflection from the central rake shaft prior to this point, despite similar decibel levels in the intervening distance, may indicate that the acoustic signal was experiencing significant multiple scattering within the bed compared to the settling zone. In either case this effect is only seen for 1000 seconds and may simply be due to concentrated sediment falling away from the walls and causing a temporary increase in concentration localised in front of the probe. If multiple probes were placed along the vertical axis facing horizontally into the settled bed (or at an angle to allow for interpolation between heights) and samples from within the thickener were taken to confirm changes in acoustic signals, results obtained here indicate that it may be possible to directly infer a density profile through the settled bed, and therefore assess and optimise thickener performance in real-time where sampling would be hazardous, costly or in processes where rapid response times are needed due to unpredictable feed characteristics.

5.5 Conclusions

To assess the application for continuous, high concentration (~30 %v/v) thickened wastes, an ABS was utilised to characterise a pseudo-steady state laboratory thickener

over 5 hours, using flocculated calcite as a representative test material. Measurements were taken both horizontally through a consolidated bed using a 1 MHz transducer and through the vertical axis with a 2 MHz transducer to measure sediment concentration above the settled bed and track bed height via the interface reflection. Characterisation of flocculated aggregate diameters was initially determined to be ~510 μm, using an inline Focussed Beam Reflectance Measurement (FBRM) device, while the submerged 2 MHz probe indicated little changes to the dispersion concentration or size over time.

It has been shown that *in-situ* ABS measurements can be used to track a laboratory thickener bed height, simultaneously to changes in the bed density at a certain level, through measurement of the attenuation of acoustic signal with distance. Changes in settled bed density, due to increasing bed height and changes in the underflow flow rate, were qualitatively measured via differences to the acoustic signal attenuation over time. An initial increase in attenuation with bed height was observed as the bed densified due to local compression. Once an equilibrium bed height was reached, the acoustic attenuation remained fairly constant with time, although the bulk underflow density was reduced with the increase in underflow rate. The solids residence time in the bed, determined from a transitive volume-balance model, was found to be ~3250 s for pseudo-steady state operation at a maintained bed height of ~0.175 m agreeing well with the value determined from the mass balance (3757 s). Output concentrations using the model were similar to the values determined through sampling and indicate the potential ability to model output thickener concentration using continuous bed height measurements taken using a single vertically facing ABS probe.

A second experiment in which ABS measurements taken at multiple heights simultaneously from the exterior of the tank horizontally through the bed indicated that an increase in ABS attenuation was seen at greater bed depths and decreased as the bed height was reduced. Higher attenuation values at the same depth as the prior experiment were seen and were corroborated with sample data collected at the thickener outlet that showed a higher output concentration supporting the ability of ABS attenuation measurements to qualitatively determine *in situ* concentration values during thickener operation non-invasively. By using horizontally mounted ABS

probes at various heights to measure concentration through the bed, while tracking bed height and the signal attenuation in the settling zone and the surface of the bed using a vertically mounted probe, it would be possible to optimise thickening and other dewatering processes in real-time. Such data could be used in acoustic, [15], [33] CFD [11, 26] and settling models [23], [24] enable comparison of model data to *in-situ* process data and aid in the dewatering and transport of legacy nuclear wastes. Results of the study therefore highlight the potential the ABS as a remote process monitoring tool for both relatively dilute suspensions and concentrated thickened mineral sludges, with potential applications across waste processing sites at Sellafield Ltd.

Chapter 6 Conclusions and future research outlook

This report detailed the limitations of characterisation of cohesive and non-cohesive dispersions using acoustic backscatter systems *in situ*. The ability to determine acoustic parameters for both cohesive and non-cohesive sediments over a range of concentrations and frequencies was demonstrated as well as a novel method for determining the near-field correction factor that corrects ABS measurements taken close to the probe. Novelty is further derived from the application of the high spatio-temporal resolution signal generator and broadband probes that allowed for variation of the frequency range during measurement without the need for additional probes. By taking measurements at multiple frequencies a large volume of data could be easily collected and allowed for identification of the ideal frequency range that might be used in different deployment scenarios. As the target application of the ABS system is to characterise the legacy wasteforms present at Sellafield Ltd. that may vary significantly in size, then variation of the frequency may be necessary to obtain reliable measurements of concentration during *in situ* measurement.

Experimental values found for the form function and scattering cross-section of the glass particles were found to agree well with predictions from the Betteridge *et al*. model [159] when accounting for viscous attenuation using Urick's [143] model. The experimental values of the scattering cross-section determined for the cohesive sediments studied in Chapter 4 were found to agree fairly well with irregular Solid Scattering model [48] when experimental and model results were normalised to the specific gravity of the floc and solid particulates respectively as per the extended *G-function* method [15], [17]. Typically, lower attenuation values than those predicted by the Solid Scattering model were observed for the flocculated sediments, however, and is attributed here to a reduction in attenuation due to viscous layer overlap in flocculated particles as the Hybrid model was found to significantly underpredict experimental data. The application of models that encompass these effects [139], [183], [237], [279] is therefore of interest for future work.

A method to measure the standard deviation and density of a flocculated particle distribution by fitting the Hybrid model to experimental results has been evaluated that has been shown to produce realistic results so long as the average particle size can be determined independently and ABS measurements at multiple frequencies are available. The application of this technique to ABS measurements has not been explored previously and provides a method to extract additional particle size data in concentrated environments and at small particle sizes where light-based measurement methods have been shown to fail. Future work should therefore focus on accurately measuring the size distribution of flocs *in situ* so that ABS PSD results obtained using the fitting technique can be corroborated with greater certainty. As previous authors have shown a clear discrepancy between both acoustic and different light-based instruments when measuring flocculated dispersions [10], [16], [120], [242] a variety of instruments should be used coupled with a thorough understanding of the size and flocculation/ aggregation kinetics of the primary particle dispersion so that flocculated particle distributions can be reliably reproduced and measured. Exact knowledge of flocculated particle size distributions would then allow experimental results for χ and f to be deconvoluted from the experimental size distribution to allow a general heuristic model to be fit over the data to which a size distribution could be applied to predict acoustic parameters for any given size distribution.

With regards to the current accuracy of the heuristic fits for f, significant but consistent deviations in experimental results from model predictions of the form function at low ka were observed for the cohesive sediments studied here and represent data that will allow heuristic fits to be extended to low particle sizes and frequencies. Fit results obtained using the data may then be used to predict sediment acoustic parameters accurately and allow for concentration and size inversion of *in situ* ABS measurements where particle size or concentration is unknown. If a range of frequencies are employed with accurate heuristic fits then particle size may be measured acoustically using the theories given by previous authors [182], [266] and the size distribution determined using the novel frequency fitting technique described in Chapter 4. The corroboration of attenuation and scattering values measured using ABS and the techniques applied here with those taken using acoustic spectroscopy would therefore be invaluable as they would allow for the extensive modelling procedures afforded by using such a setup to be applied to ABS devices in industrial

process applications. Quantification of a process sample's acoustic characteristics using spectroscopy could then be reliably applied to established ABS sonar equations to allow for *in situ* characterisation of both cohesive and non-cohesive sediments.

The target application of the ABS was to produce concentration profiles *in situ* for flocculated dispersions that has been demonstrated to be accurate in Section 4.3.3 up to ~2.5 – 35 g l^{-1} depending on the particle system and frequency used and is typically limited by the attenuation of the dispersion for the single frequency method [33] (see also Appendix B, Figure B.3 and Figure B.4). These results generally demonstrated the *dG/dr* limit of ~-10 Np m^{-1} for an accurate inversion (within 20% of the nominal value) that was also seen for the glass particle sediment results shown in Section 3.3.3. The attenuation limit of ~-10 Np m^{-1} for an accurate concentration inversion corresponds well with the 6 Np limit found by Kalashnikov and Challis [274] when considering the total path length for the acoustic signal in all experiments was 0.6 m.

Results using the dual frequency method [15], that represents a potential area for both data mining and statistical methods [225], were generally shown to increase the accuracy of concentration profiling in the near-field of the transducer (Section 4.3.3). Similar limits for the dual frequency inversion was seen on the attenuation as with the single frequency method although direct comparison to the measured attenuation values is complicated somewhat by the use of two voltage profiles (see Appendix B, Figure B.4). Across all sediment systems studied the dual frequency method provided an improvement in accuracy over the single frequency method (when compared the accuracy of the most accurate of the two corresponding single frequency inversions) for 168 of the concentration profiles produced out of a total of 675 dual frequency inversion profiles (approx. 25 %, derived from data shown in Appendix B, Table B.3-Table B.6). Of these 168 profiles 61 profiles were accurate to within 20% of the known concentration value.

A qualitative relationship was able to be drawn between concentration and attenuation up to 40 g l^{-1} for all but the most highly attenuating suspension (particulate magnesium hydroxide) studied in the calibration tank even where direct concentration inversion of the voltage profile was not possible. The use of the single and dual frequency inversion methods demonstrated here have not been applied previously to

cohesive sediments at concentrations where attenuation becomes significant (> 5 g l^{-1}) and strongly indicate the ability of ABS to characterise flocculated dispersion concentration using the established sonar equations in moderately concentrated dispersions that might be encountered during legacy waste reprocessing at Sellafield Ltd. In cases where attenuation is high enough to inhibit direct inversion of the profiles the qualitative method can be applied; however, the effect of multiple scattering in combination with instrument noise limits at high concentrations was seen to limit even the qualitative relationship drawn between concentration and attenuation. Future work should therefore focus on either expanding the qualitative correlations to higher particle concentrations so that heuristic calibration curves could be produced or extending the ABS sonar equations to account for the multiple scattering effects at high concentration. Incorporation of transmission acoustics theory would prove by useful and novel in this regard as transmission acoustics models have been shown to accurately model highly concentrated dispersions and the subsequent inter-particle thermal and viscous overlap effects [216], [279] but have not yet been applied to ABS measurements for which these effects may still be significant and thus should be accounted for so that changes in attenuation with concentration can be correctly accounted for.

Results shown in Chapter 5 indicated the ability of the ABS to provide bed height measurements via the interface reflection of the acoustic signal and to non-invasively measure *in situ* changes in thickener operation via the linear relationship between concentration and attenuation. An increase in thickener output concentration in the second thickener experiment, determined through sampling, was directly correlated with an increased attenuation measured at the same height through the column in each experiment with identical underflow rates. Acoustic attenuation measured at multiple heights horizontally through the bed during thickener operation additionally indicated increased attenuation at greater bed depths and horizontal attenuation in both cases increased as bed height was increased. Using bed height measurements taken both visually and using the ABS residence time maps as a function of bed height were produced so that attenuation at a fixed height could be correlated to the modelled residence time. Output concentrations modelled as a by-product were also found to correlate well with sample data, although significant noise existed due to natural variation in the bed height that were not captured by the 1-D measurements of the bed

height taken using the ABS. This noise in bed height measurements could be eliminated by taking planar measurements and rotating about the central axis to map the bed surface and possibly allow for 3-D modelling of the bed concentration that could be further corroborated with numerical [27], [280] models that incorporate the bed yield stress horizontal attenuation measurements. Results such as these may further understanding of solids settling dynamics and improve thickening operations at Sellafield Ltd. Residence time results were found to correlate well with attenuation measurements in both experiments although some disturbances in the attenuation was seen due to both build-up of the sediment around the edges of the tank during bed depletion and when ABS measurements are transitioning from the bed to the settling zone. Overall, results are promising for *in situ* characterisation of the concentration and settling fronts in the types of naturally flocculated dispersions that may be encountered at Sellafield and in other industries that involve aggregated particle processes.

The key findings and novel techniques derived as a result of the work in this thesis are summarised below.

- **The single and dual frequency concentration inversion methods were found to typically be accurate so long as the attenuation is not greater than ~-10 Np m^{-1} and system noise is not adversely affecting the backscattered signal. Beyond ~-10 Np m^{-1} excessive noise and model deviations causes erroneous profiles to be produced however a qualitative correlation between attenuation and concentration can be drawn up to higher limit that was seen to vary between sediments.**

- **A novel method is derived to determine the near field correction factor by fitting near field data to extrapolated *dG/dr* fits taken as part of the *G-function* method [15]. The proposed method only requires that measurements be taken in a homogeneous dispersion at concentrations where attenuation is significant enough to reliably fit the *dG/dr* slopes to experimental data. It therefore represents a powerful tool to correct for damage to the face of the probes, manufacturer error and fouling on the probe surface.**

- **The measured scattering cross-section and form function compared well to modelling for the glass particles studied; however, significant variation in the scattering cross-section was seen in the long wavelength regime for the particulate and flocculated sediments studied in Chapter 4 that is attributed here to structural attenuation effects that are not modelled. A consistent plateau in the form function in the long wavelength regime is also seen that is not represented by current heuristic fits and therefore represents potential data that may be used to revaluate these fits for low particle sizes and insonification frequencies.**

- **The experimental values for the flocculated particle scattering cross-section and form function were most closely represented by the specific gravity normalised Solid Scattering model [48]. The experimental floc data was typically overestimated by the Solid Scattering model, however, indicating that flocs do scatter and attenuate less than solid particles of the same size. As this reduction was significantly overpredicted by the Hybrid model [47] when using the measured values for the floc fractal dimension it is proposed here that the reduction in attenuation on flocculation is due to viscous layer overlap causing multiple scattering within the floc.**

- **A novel method to determine flocculated particle size distribution and specific acoustic impedance by fitting the Hybrid model to experimental data is provided so long as the mean flocculated particle size can be determined independently of acoustic measurements and ABS measurements at multiple frequencies are available.**

- **Non-invasive attenuation measurement using ABS were demonstrated to be able to characterise concentration changes in a settled bed by taking measurements through the outer wall of a laboratory scale thickener. Attenuation was seen to increase at greater bed depths and with increasing bed height. A simple numerical method for mapping the residence time in a settled bed during transitive operation is proposed that requires only bed height measurements and an assumed initially settled layer density from which the thickener output concentration can also be estimated.**

Appendix A

A.1 Semi-Empirical Backscatter Power Scale Factor Modelling

To convert between a measured echo value from a transducer (typically given in RMS voltage) and the output of a single particle scattering model (typically in Pascals with an associated incident wave pressure) a reference is required as this backscattered amplitude is an absolute value. Experimentally, Weser *et al*. [46] have proposed a simple experimental method to measure the transfer function of the whole system using a well-defined plane reflector of reflection coefficient E in order to provide a reference measurement and normalise the received echo-voltage as follows. To convert between a measured echo value from a transducer (typically given in RMS voltage) and the output of a single particle scattering model (typically in pascals) with an associated incident wave pressure) a reference is required as this backscattered amplitude is an absolute value. Experimentally, Weser *et al*. [46] have proposed a simple experimental method to measure the transfer function of the whole system using a well-defined plane reflector of reflection coefficient *E* in order to provide a reference measurement and normalise the received echo-voltage as follows

$$\Omega_{echo}(f,t) = \frac{\Omega_{meas}(f,t)}{\Omega_{ref}(f,t)}.E \qquad \textbf{A.1}$$

Where $\Omega_{meas}(f,t)$ is the measured backscatter signal, $\Omega_{ref}(f,t)$ is the captured reflection signal and $\Omega_{echo}(f,t)$ is the normalised echo signal which can then be input as Ω_{Σ} into Equation 2.5. An alternative method, utilised in this study, is to take the transducer receiver sensitivity (R) and voltage transfer function (T_v) defined by Thorne *et al.* as [33].

$$V_{rms} = R.T_v.P_{rms} \qquad \textbf{A.2}$$

Where P_{rms} is the backscattered pressure of the acoustic wave in the suspension. Equation A.2 can be combined with the following equation from Weser *et al.* [46] can be combined with the following equation from Weser *et al.* [46] can be combined with the following equation from Weser *et al.* [46]

$$\Omega_{\Sigma} = \frac{P_{rms}}{\widehat{P_0}} \qquad \textbf{A.3}$$

Where $\widehat{P_0}$ is the incident acoustic wave pressure to produce.

$$\frac{P_{RMS}}{\widehat{P_0}} = \frac{V_{RMS}}{\widehat{P_0}.R.T_v} = \Omega_\Sigma \qquad \textbf{A.4}$$

By modelling Ω_Σ using equation 2.50 and a single particle scattering model such as the Faran model [194] to estimate the single particle scattering power, Ω_p, the $P_0.R.T_v$ term can be estimated for each frequency and probe by fitting the experimental data to the model as all these terms should be constant for fixed system settings [33].

In general terms, the packing factor (W) in the Weser *et al.* model can be defined from the "excluded volume" (v_e, the volume around a particle that the centre of another particle cannot occupy), the average number of observed scatterers ($\bar{N}$), its variance (σ_N) and the volume concentration of scatterers ($\bar{n}$) by [192] as shown in Equation A.5 below.

$$W = [(1 - v_e.\bar{n}.\left(1 + \frac{\sigma_N^2}{\bar{N}^2}\right)] \qquad \textbf{A.5}$$

A broadening of the particle size distribution would therefore both increase the particle number variance and the excluded volume leading to a decrease in the packing factor and the backscattered amplitude.

A.2 Additional results

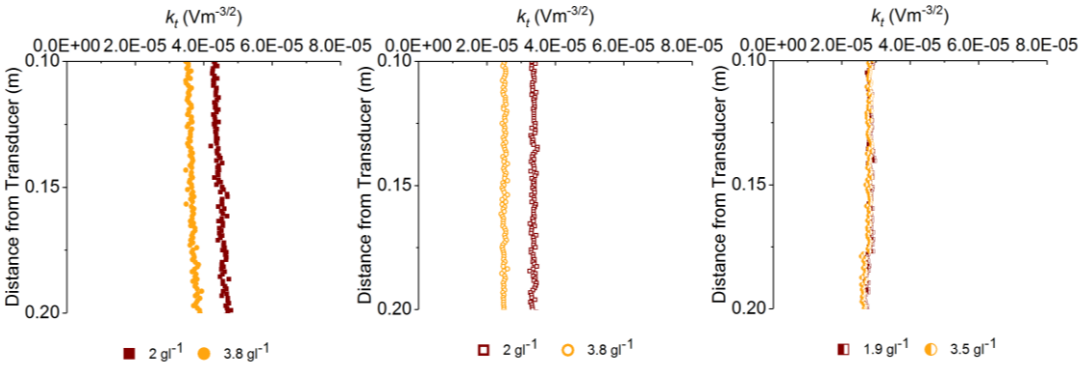

Figure A.1 k_t calculated using the Extended *G-function* method as a function of distance from the transducer for a) Honite 22, b) Honite 16 and c) Honite 12 at 2.25 MHz

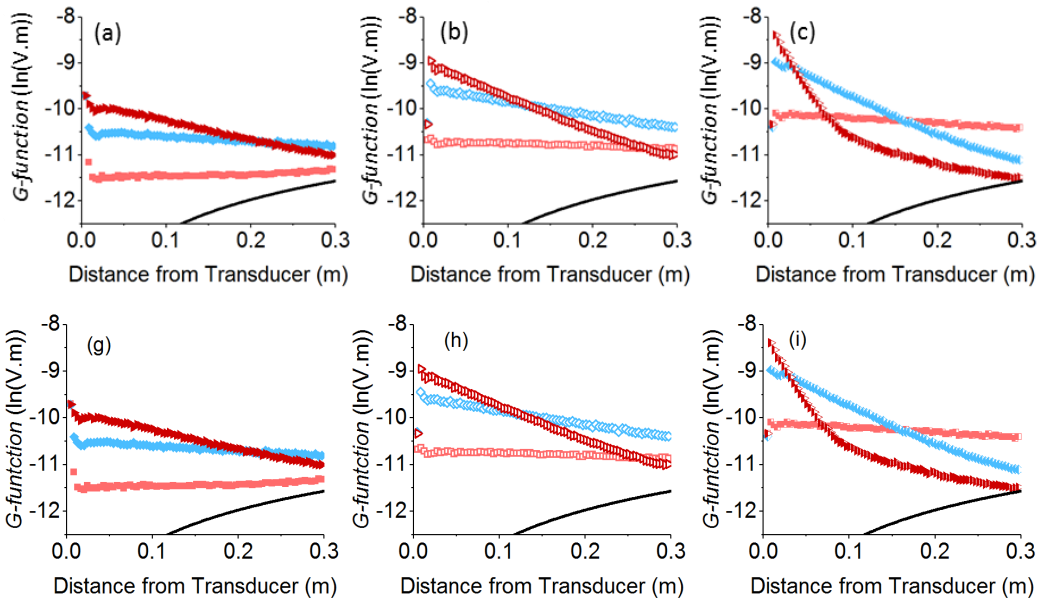

Figure A.2 Showing *G-function* profiles adjusted using NFCF from Downing *et al.* for a) Honite 22, b) Honite 16 and c) Honite 12 at 2.25 MHz

Table A.1 Showing experimentally determined values of the attenuation coefficient, ξ ,values and corresponding R^2 values obtained from *dG/dr/dM* fits for three sizes of glass particles (Honite 22, Honite 16 and Honite 12)

		Honite 22		Honite 16		Honite 12	
		ξ	R^2	ξ	R^2	ξ	R^2
Probe 1	2 MHz	0.025	0.99	0.034	0.97	0.18	0.999
	2.25 MHz	0.028	0.99	0.044	0.98	0.23	0.999
	2.5 MHz	0.031	0.99	0.055	0.98	0.25	0.992
Probe 2	2 MHz	0.027	0.97	0.034	0.98	0.17	0.997
	2.25 MHz	0.029	0.99	0.045	0.98	0.21	0.997
	2.5 MHz	0.033	0.99	0.056	0.97	0.25	0.996
Probe 3	2 MHz	0.027	0.98	0.033	0.98	0.17	0.997
	2.25 MHz	0.028	0.99	0.044	0.98	0.20	0.995
	2.5 MHz	0.033	0.99	0.055	0.97	0.24	0.993
Probe 4	2 MHz	0.028	0.99	0.035	0.97	0.17	0.998
	2.25 MHz	0.029	0.99	0.046	0.99	0.22	0.999
	2.5 MHz	0.033	0.99	0.056	0.97	0.25	0.996
Probe 5	2 MHz	0.026	0.97	0.035	0.98	0.18	0.997
	2.25 MHz	0.030	0.99	0.043	0.97	0.22	0.998
	2.5 MHz	0.033	0.99	0.057	0.98	0.25	0.993
Probe 6	2 MHz	0.027	0.99	0.034	0.98	0.18	1.000
	2.25 MHz	0.030	1.00	0.045	0.98	0.21	0.999
	2.5 MHz	0.034	0.99	0.056	0.97	0.25	0.995
Probe 7	2 MHz	0.030	0.98	0.051	0.00	0.18	0.998
	2.25 MHz	0.031	0.98	0.073	0.01	0.23	0.999
	2.5 MHz	0.035	0.96	0.064	0.00	0.26	0.994
Probe 8	2 MHz	0.029	0.65	0.034	0.97	0.17	0.998
	2.25 MHz	0.032	0.78	0.044	0.96	0.21	0.999
	2.5 MHz	0.034	0.75	0.055	0.96	0.25	0.998

Table A.2 Showing *dG/dr* values and corresponding R^2 values obtained for three sizes of glass particles (Honite 22, Honite 16 and Honite 12)

		Probe 1																							
		2 MHz								2.25 MHz								2.5 MHz							
		Conc 1	Conc 2	Conc 3	Conc 4	Conc 5	Conc 6	Conc 7	Conc 8	Conc 1	Conc 2	Conc 3	Conc 4	Conc 5	Conc 6	Conc 7	Conc 8	Conc 1	Conc 2	Conc 3	Conc 4	Conc 5	Conc 6	Conc 7	Conc 8
Honite 22	dG/dr	-0.07	-0.42	-0.66	-1.70	-2.14	-4.03	-5.00	-6.48	-0.29	-0.53	-1.10	-1.51	-2.45	-4.61	-5.46	-7.45	-0.03	-0.94	-0.96	-1.76	-2.81	-5.08	-6.19	-8.06
	R^2	0.00	0.01	0.08	0.53	0.72	0.93	0.94	0.95	0.00	0.02	0.41	0.53	0.75	0.95	0.95	0.98	0.00	0.02	0.29	0.70	0.79	0.92	0.95	0.98
Honite 16	dG/dr	-0.81	-1.20	-1.50	-2.60	-4.48	-6.19	-7.46	-9.14	-1.12	-0.91	-1.80	-3.30	-5.40	-7.69	-9.23	-11.85	-1.20	-1.40	-2.22	-3.97	-6.87	-9.65	-11.38	-14.81
	R^2	0.18	0.54	0.62	0.74	0.90	0.93	0.97	0.97	0.24	0.22	0.59	0.76	0.95	0.96	0.97	0.99	0.29	0.51	0.66	0.85	0.96	0.97	0.98	0.99
Honite 12	dG/dr	-1.30	-2.03	-4.93	-7.33	-14.84	-20.69	-16.39	-20.66	-1.35	-2.50	-5.92	-9.13	-18.68	-24.30	-18.99	-20.00	-1.81	-2.79	-7.38	-11.29	-20.57	-25.12	-19.32	-21.98
	R^2	0.32	0.62	0.96	0.96	0.98	0.99	0.99	0.99	0.39	0.76	0.94	0.97	0.99	0.99	0.98	0.96	0.56	0.80	0.96	0.99	0.99	0.99	0.97	0.99
		Probe 2																							
		2 MHz								2.25 MHz								2.5 MHz							
		Conc 1	Conc 2	Conc 3	Conc 4	Conc 5	Conc 6	Conc 7	Conc 8	Conc 1	Conc 2	Conc 3	Conc 4	Conc 5	Conc 6	Conc 7	Conc 8	Conc 1	Conc 2	Conc 3	Conc 4	Conc 5	Conc 6	Conc 7	Conc 8
Honite 22	dG/dr	0.36	0.31	-1.21	-1.48	-2.58	-3.95	-5.26	-6.52	0.07	-0.35	-1.02	-1.48	-3.10	-4.38	-5.56	-7.29	0.11	-0.41	-1.03	-1.62	-3.57	-5.20	-6.25	-8.38
	R^2	0.01	0.01	0.09	0.42	0.82	0.91	0.93	0.96	0.00	0.01	0.39	0.44	0.75	0.90	0.94	0.96	0.00	0.01	0.24	0.61	0.85	0.94	0.97	0.97
Honite 16	dG/dr	-0.90	-1.05	-1.41	-2.70	-4.14	-5.88	-7.16	-9.22	-0.87	-0.91	-1.99	-3.25	-5.47	-7.62	-9.42	-12.00	-1.03	-1.16	-2.41	-4.18	-6.86	-9.85	-11.66	-14.64
	R^2	0.24	0.22	0.50	0.72	0.87	0.95	0.96	0.99	0.16	0.22	0.63	0.81	0.95	0.97	0.98	0.98	0.21	0.32	0.72	0.88	0.97	0.98	0.99	0.99
Honite 12	dG/dr	-1.09	-2.02	-5.13	-7.16	-14.41	-21.69	-17.32	-17.00	-1.47	-2.43	-6.09	-8.82	-17.22	-25.51	-20.17	-21.87	-1.45	-3.00	-6.99	-10.45	-20.27	-28.02	-20.93	-25.11
	R^2	0.23	0.63	0.93	0.95	0.98	0.99	0.99	0.97	0.50	0.72	0.95	0.97	0.99	0.995	0.99	0.99	0.46	0.81	0.97	0.98	0.99	0.99	0.99	0.99
		Probe 3																							
		2 MHz								2.25 MHz								2.5 MHz							
		Conc 1	Conc 2	Conc 3	Conc 4	Conc 5	Conc 6	Conc 7	Conc 8	Conc 1	Conc 2	Conc 3	Conc 4	Conc 5	Conc 6	Conc 7	Conc 8	Conc 1	Conc 2	Conc 3	Conc 4	Conc 5	Conc 6	Conc 7	Conc 8
Honite 22	dG/dr	-0.20	0.16	-0.81	-1.31	-2.75	-4.02	-5.19	-6.59	-0.14	-0.13	-0.80	-1.48	-2.93	-4.48	-5.34	-7.15	0.19	-0.01	-0.76	-1.64	-3.38	-4.91	-6.08	-8.00
	R^2	0.00	0.00	0.15	0.49	0.84	0.90	0.94	0.97	0.00	0.00	0.18	0.55	0.83	0.91	0.95	0.96	0.00	0.00	0.13	0.56	0.79	0.94	0.94	0.97
Honite 16	dG/dr	-0.86	-1.08	-1.63	-2.55	-4.30	-6.16	-7.10	-9.13	-1.03	-0.98	-1.76	-3.04	-5.41	-7.71	-9.12	-11.73	-1.17	-1.24	-2.30	-4.02	-7.06	-9.71	-11.65	-14.51
	R^2	0.17	0.35	0.55	0.85	0.92	0.97	0.97	0.98	0.29	0.26	0.53	0.76	0.94	0.97	0.97	0.98	0.45	0.47	0.69	0.87	0.95	0.98	0.98	0.99
Honite 12	dG/dr	-1.15	-2.04	-4.91	-6.99	-13.89	-21.44	-16.33	-14.66	-1.31	-2.47	-5.98	-8.74	-16.75	-24.81	-17.24	-20.64	-1.58	-2.91	-6.95	-10.83	-19.90	-25.31	-17.33	-22.04
	R^2	0.37	0.65	0.93	0.97	0.99	0.99	0.98	0.97	0.42	0.68	0.95	0.98	0.98	0.99	0.98	0.98	0.48	0.75	0.97	0.99	0.99	0.99	0.98	0.99
		Probe 4																							
		2 MHz								2.25 MHz								2.5 MHz							
		Conc 1	Conc 2	Conc 3	Conc 4	Conc 5	Conc 6	Conc 7	Conc 8	Conc 1	Conc 2	Conc 3	Conc 4	Conc 5	Conc 6	Conc 7	Conc 8	Conc 1	Conc 2	Conc 3	Conc 4	Conc 5	Conc 6	Conc 7	Conc 8
Honite 22	dG/dr	-0.08	0.22	-0.45	-1.34	-2.75	-4.13	-4.82	-6.81	-0.05	-0.12	-0.80	-1.44	-2.92	-4.36	-5.66	-7.26	0.22	0.05	-0.81	-1.78	-3.41	-5.12	-6.03	-8.24
	R^2	0.00	0.00	0.03	0.53	0.87	0.91	0.91	0.96	0.00	0.00	0.11	0.38	0.88	0.89	0.95	0.95	0.00	0.00	0.15	0.55	0.84	0.92	0.95	0.98
Honite 16	dG/dr	-0.87	-0.73	-1.58	-1.55	-3.98	-5.93	-7.21	-8.99	-0.92	-1.08	-1.88	-2.35	-5.12	-7.58	-9.49	-11.93	-0.96	-1.09	-2.46	-3.25	-6.64	-9.82	-11.58	-14.36
	R^2	0.19	0.22	0.63	0.40	0.89	0.93	0.97	0.97	0.21	0.37	0.57	0.64	0.93	0.97	0.98	0.99	0.23	0.39	0.69	0.80	0.97	0.98	0.99	0.99
Honite 12	dG/dr	-1.11	-1.96	-4.81	-6.76	-13.98	-20.82	-20.03	-20.48	-1.30	-2.34	-5.89	-8.68	-18.08	-24.94	-24.02	-22.21	-1.41	-2.87	-6.95	-10.52	-20.39	-27.18	-24.12	-27.07
	R^2	0.23	0.63	0.91	0.96	0.98	0.99	0.99	0.98	0.41	0.64	0.95	0.98	0.99	0.99	0.99	0.98	0.34	0.81	0.96	0.99	0.99	0.99	0.98	0.99
		Probe 5																							
		2 MHz								2.25 MHz								2.5 MHz							
		Conc 1	Conc 2	Conc 3	Conc 4	Conc 5	Conc 6	Conc 7	Conc 8	Conc 1	Conc 2	Conc 3	Conc 4	Conc 5	Conc 6	Conc 7	Conc 8	Conc 1	Conc 2	Conc 3	Conc 4	Conc 5	Conc 6	Conc 7	Conc 8
Honite 22	dG/dr	-0.03	-0.28	-0.79	-1.27	-3.60	-3.91	-4.96	-6.75	-0.26	-0.29	-1.07	-1.57	-3.21	-4.54	-5.87	-7.63	-0.54	-0.32	-1.01	-1.80	-3.41	-5.41	-6.30	-8.54
	R^2	0.00	0.00	0.13	0.49	0.52	0.86	0.94	0.96	0.00	0.01	0.38	0.51	0.83	0.93	0.94	0.96	0.04	0.01	0.20	0.66	0.85	0.95	0.95	0.97
Honite 16	dG/dr	-0.92	-1.12	-1.52	-2.51	-4.36	-6.28	-7.51	-9.25	-1.16	-1.06	-2.08	-3.40	-5.65	-7.64	-9.33	-11.77	-1.22	-1.33	-2.42	-4.12	-7.10	-9.80	-11.81	-15.10
	R^2	0.13	0.36	0.49	0.69	0.88	0.95	0.97	0.98	0.24	0.27	0.55	0.80	0.94	0.98	0.99	0.99	0.34	0.45	0.74	0.88	0.98	0.99	0.99	0.99
Honite 12	dG/dr	-1.10	-1.95	-5.09	-7.45	-14.73	-21.87	-15.73	-16.94	-1.10	-2.31	-5.71	-8.78	-17.80	-25.13	-17.08	-20.61	-1.49	-3.03	-7.29	-11.11	-20.58	-25.19	-17.98	-22.79
	R^2	0.34	0.65	0.95	0.96	0.99	0.99	0.98	0.96	0.38	0.59	0.93	0.97	0.99	0.99	0.98	0.98	0.44	0.79	0.96	0.98	0.99	0.99	0.98	0.98
		Probe 6																							
		2 MHz								2.25 MHz								2.5 MHz							
		Conc 1	Conc 2	Conc 3	Conc 4	Conc 5	Conc 6	Conc 7	Conc 8	Conc 1	Conc 2	Conc 3	Conc 4	Conc 5	Conc 6	Conc 7	Conc 8	Conc 1	Conc 2	Conc 3	Conc 4	Conc 5	Conc 6	Conc 7	Conc 8
Honite 22	dG/dr	0.03	-0.09	-0.58	-1.18	-2.96	-4.08	-4.88	-6.59	-0.44	-0.23	-0.79	-1.49	-3.12	-4.52	-5.59	-7.65	0.07	0.00	-0.77	-1.63	-3.36	-5.14	-6.17	-8.40
	R^2	0.00	0.00	0.04	0.31	0.53	0.91	0.92	0.96	0.02	0.00	0.17	0.43	0.88	0.90	0.93	0.97	0.00	0.00	0.12	0.62	0.81	0.95	0.95	0.97
Honite 16	dG/dr	-1.07	-0.95	-1.66	-2.78	-4.17	-5.96	-7.43	-9.30	-0.72	-1.08	-1.94	-3.07	-5.54	-7.75	-9.44	-11.97	-0.91	-1.40	-2.33	-4.00	-7.09	-9.78	-11.44	-14.86
	R^2	0.29	0.31	0.46	0.65	0.91	0.95	0.97	0.99	0.13	0.24	0.72	0.85	0.94	0.96	0.97	0.98	0.18	0.33	0.67	0.90	0.97	0.97	0.98	0.99
Honite 12	dG/dr	-1.28	-1.91	-4.76	-7.23	-14.63	-20.82	-18.88	-21.03	-1.52	-2.44	-6.00	-8.66	-17.70	-23.89	-21.59	-23.00	-1.49	-2.84	-7.09	-10.79	-20.54	-25.70	-23.50	-25.13
	R^2	0.30	0.63	0.92	0.98	0.99	0.99	0.99	0.98	0.50	0.76	0.94	0.97	0.99	0.99	0.99	0.98	0.47	0.84	0.95	0.98	0.99	0.99	0.99	0.98
		Probe 7																							
		2 MHz								2.25 MHz								2.5 MHz							
		Conc 1	Conc 2	Conc 3	Conc 4	Conc 5	Conc 6	Conc 7	Conc 8	Conc 1	Conc 2	Conc 3	Conc 4	Conc 5	Conc 6	Conc 7	Conc 8	Conc 1	Conc 2	Conc 3	Conc 4	Conc 5	Conc 6	Conc 7	Conc 8
Honite 22	dG/dr	0.78	0.69	-0.16	-1.20	-2.39	-3.94	-4.87	-6.71	0.55	0.69	-0.26	-1.16	-2.75	-4.42	-5.26	-7.14	0.98	0.76	-1.05	-1.30	-3.43	-4.90	-6.20	-8.05
	R^2	0.10	0.08	0.00	0.40	0.70	0.89	0.92	0.94	0.02	0.08	0.01	0.29	0.75	0.90	0.92	0.97	0.17	0.12	0.01	0.32	0.84	0.94	0.94	0.97
Honite 16	dG/dr	-1.00	-0.89	-8.68	29.32	-39.13	-5.99	-7.20	-9.22	-1.03	-1.21	24.95	-10.06	46.68	-7.72	-8.93	-11.55	-0.91	-1.17	-24.12	29.51	57.37	-9.64	-11.18	-14.60
	R^2	0.31	0.15	1.00	1.00	1.00	0.91	0.97	0.99	0.26	0.37	1.00	1.00	1.00	0.95	0.97	0.98	0.19	0.43	1.00	1.00	1.00	0.96	0.98	0.99
Honite 12	dG/dr	-1.04	-1.97	-4.88	-6.95	-14.56	-20.16	-16.24	-20.54	-1.33	-2.34	-6.09	-9.20	-18.74	-23.70	-20.53	-23.36	-1.44	-2.97	-7.27	-11.37	-21.42	-25.71	-19.86	-23.13
	R^2	0.25	0.65	0.94	0.96	0.99	0.99	0.98	0.97	0.32	0.70	0.93	0.98	0.99	0.99	0.98	0.98	0.53	0.79	0.97	0.98	0.99	0.99	0.95	0.99
		Probe 8																							
		2 MHz								2.25 MHz								2.5 MHz							
		Conc 1	Conc 2	Conc 3	Conc 4	Conc 5	Conc 6	Conc 7	Conc 8	Conc 1	Conc 2	Conc 3	Conc 4	Conc 5	Conc 6	Conc 7	Conc 8	Conc 1	Conc 2	Conc 3	Conc 4	Conc 5	Conc 6	Conc 7	Conc 8
Honite 22	dG/dr	0.93	0.55	-0.41	-1.22	3.49	-3.93	-4.84	-6.51	0.57	0.37	-0.41	-1.14	2.07	-4.32	-5.45	-7.36	0.65	0.27	-0.46	-1.30	2.48	-4.88	-5.95	-7.77
	R^2	0.10	0.03	0.01	0.20	0.57	0.90	0.95	0.95	0.05	0.00	0.01	0.33	0.48	0.86	0.93	0.96	0.04	0.00	0.03	0.50	0.27	0.89	0.95	0.97
Honite 16	dG/dr	-0.71	-0.78	-1.59	-2.37	-4.33	-6.10	-7.16	-9.13	-0.78	-0.99	-1.69	-3.30	-5.62	-7.69	-9.18	-11.44	-0.82	-1.37	-2.27	-4.11	-6.90	-9.74	-11.67	-14.51
	R^2	0.07	0.15	0.56	0.78	0.90	0.95	0.97	0.98	0.13	0.32	0.59	0.82	0.94	0.97	0.99	0.98	0.23	0.43	0.73	0.88	0.97	0.98	0.99	0.99
Honite 12	dG/dr	-1.20	-1.84	-4.81	-6.95	-13.96	-21.46	-20.57	-18.29	-1.47	-2.27	-5.67	-8.51	-17.12	-24.55	-24.18	-22.01	-1.56	-2.85	-6.85	-10.37	-20.62	-26.46	-24.47	-28.51
	R^2	0.38	0.55	0.93	0.95	0.99	0.99	0.99	0.98	0.60	0.71	0.94	0.97	0.99	0.99	0.99	0.98	0.57	0.79	0.96	0.98	0.99	0.99	0.99	0.98

Table A.3 Showing k_s values and corresponding standard deviation values obtained for three sizes of glass particles (Honite 22, Honite 16 and Honite 12)

		Probe 1																							
		2 MHz								2.25 MHz								2.5 MHz							
		Conc 1	Conc 2	Conc 3	Conc 4	Conc 5	Conc 6	Conc 7	Conc 8	Conc 1	Conc 2	Conc 3	Conc 4	Conc 5	Conc 6	Conc 7	Conc 8	Conc 1	Conc 2	Conc 3	Conc 4	Conc 5	Conc 6	Conc 7	Conc 8
Honite 22	k_s	0.157	0.128	0.125	0.122	0.056	0.126	0.123	0.125	0.156	0.129	0.125	0.122	0.116	0.127	0.124	0.129	0.163	0.122	0.120	0.120	0.116	0.122	0.120	0.126
	σ	0.003	0.002	0.002	0.002	0.001	0.001	0.002	0.002	0.003	0.003	0.002	0.002	0.001	0.002	0.002	0.002	0.004	0.007	0.002	0.002	0.001	0.003	0.003	0.003
Honite 16	k_s	0.442	0.316	0.246	0.141	0.227	0.339	0.306	0.320	0.419	0.339	0.424	0.390	0.243	0.405	0.415	0.421	0.391	0.367	0.289	0.391	0.230	0.319	0.363	0.369
	σ	0.006	0.004	0.003	0.003	0.005	0.008	0.006	0.005	0.010	0.005	0.005	0.004	0.006	0.009	0.008	0.005	0.012	0.007	0.006	0.005	0.008	0.012	0.009	0.006
Honite 12	k_s	0.946	1.050	0.917	1.100	1.070	1.290	1.870	4.900	0.953	1.040	1.050	1.110	1.070	1.310	2.180	5.110	0.985	1.010	1.090	1.160	1.110	1.330	2.390	5.910
	σ	0.018	0.017	0.013	0.019	0.019	0.058	0.400	2.170	0.016	0.016	0.016	0.023	0.019	0.093	0.605	3.530	0.016	0.018	0.021	0.026	0.013	0.153	1.800	1.880
		Probe 2																							
		2 MHz								2.25 MHz								2.5 MHz							
		Conc 1	Conc 2	Conc 3	Conc 4	Conc 5	Conc 6	Conc 7	Conc 8	Conc 1	Conc 2	Conc 3	Conc 4	Conc 5	Conc 6	Conc 7	Conc 8	Conc 1	Conc 2	Conc 3	Conc 4	Conc 5	Conc 6	Conc 7	Conc 8
Honite 22	k_s	0.160	0.125	0.125	0.120	0.118	0.127	0.126	0.130	0.160	0.125	0.123	0.123	0.124	0.128	0.126	0.131	0.160	0.125	0.122	0.124	0.120	0.129	0.128	0.132
	σ	0.003	0.002	0.003	0.002	0.001	0.002	0.002	0.002	0.003	0.003	0.002	0.002	0.003	0.002	0.002	0.003	0.004	0.003	0.003	0.003	0.003	0.003	0.002	0.004
Honite 16	k_s	0.426	0.332	0.899	0.139	0.300	0.745	0.590	0.704	0.425	0.333	0.422	0.348	0.350	0.379	0.353	0.397	0.434	0.324	0.468	0.396	0.403	0.372	0.369	0.378
	σ	0.006	0.006	0.006	0.008	0.005	0.007	0.008	0.005	0.008	0.006	0.009	0.010	0.007	0.009	0.011	0.008	0.011	0.008	0.012	0.014	0.009	0.015	0.014	0.007
Honite 12	k_s	0.995	1.000	1.060	1.130	1.090	1.300	2.250	4.510	0.982	1.020	1.060	1.120	1.060	1.330	2.350	6.030	0.972	1.030	1.020	1.090	1.020	1.170	2.270	4.390
	σ	0.015	0.016	0.019	0.022	0.017	0.048	0.346	1.200	0.014	0.017	0.019	0.018	0.015	0.075	0.582	1.200	0.015	0.019	0.016	0.023	0.015	0.101	0.667	1.940
		Probe 3																							
		2 MHz								**2.25 MHz**								**2.5 MHz**							
		Conc 1	Conc 2	Conc 3	Conc 4	Conc 5	Conc 6	Conc 7	Conc 8	Conc 1	Conc 2	Conc 3	Conc 4	Conc 5	Conc 6	Conc 7	Conc 8	Conc 1	Conc 2	Conc 3	Conc 4	Conc 5	Conc 6	Conc 7	Conc 8
Honite 22	k_s	0.158	0.127	0.121	0.117	0.106	0.125	0.125	0.129	0.157	0.128	0.121	0.110	0.027	0.125	0.125	0.122	0.194	0.165	0.162	0.160	0.072	0.164	0.160	0.158
	σ	0.004	0.002	0.002	0.002	0.001	0.002	0.002	0.002	0.003	0.002	0.002	0.002	0.002	0.002	0.002	0.003	0.004	0.003	0.003	0.003	0.003	0.002	0.003	0.004
Honite 16	k_s	0.473	0.285	0.032	0.018	0.016	0.156	0.108	0.253	0.418	0.340	0.384	0.332	0.325	0.340	0.321	0.357	0.546	0.394	0.298	0.171	0.266	0.399	0.371	0.410
	σ	0.006	0.005	0.005	0.006	0.005	0.006	0.006	0.005	0.007	0.007	0.006	0.010	0.006	0.008	0.009	0.007	0.008	0.007	0.008	0.013	0.010	0.011	0.013	0.006
Honite 12	k_s	0.944	1.050	1.090	1.140	1.150	1.300	1.930	4.720	0.936	1.060	0.998	1.070	1.080	1.300	2.180	4.690	0.996	1.100	0.927	1.120	1.040	1.460	2.900	7.310
	σ	0.014	0.016	0.017	0.017	0.013	0.049	0.394	2.310	0.016	0.019	0.019	0.017	0.021	0.085	0.854	1.600	0.016	0.018	0.017	0.022	0.014	0.149	0.968	3.670
		Probe 4																							
		2 MHz								**2.25 MHz**								**2.5 MHz**							
		Conc 1	Conc 2	Conc 3	Conc 4	Conc 5	Conc 6	Conc 7	Conc 8	Conc 1	Conc 2	Conc 3	Conc 4	Conc 5	Conc 6	Conc 7	Conc 8	Conc 1	Conc 2	Conc 3	Conc 4	Conc 5	Conc 6	Conc 7	Conc 8
Honite 22	k_s	0.192	0.168	0.166	0.159	0.151	0.166	0.162	0.167	0.200	0.159	0.157	0.157	0.150	0.157	0.155	0.161	0.197	0.162	0.164	0.155	0.154	0.164	0.163	0.166
	σ	0.003	0.002	0.002	0.001	0.001	0.002	0.002	0.002	0.003	0.002	0.003	0.002	0.002	0.002	0.002	0.003	0.005	0.003	0.003	0.003	0.003	0.003	0.003	0.003
Honite 16	k_s	0.519	0.421	0.521	0.469	0.291	0.475	0.498	0.533	0.482	0.458	0.355	0.470	0.278	0.386	0.438	0.471	0.532	0.408	1.120	0.167	0.361	0.899	0.730	0.911
	σ	0.007	0.004	0.013	0.002	0.005	0.015	0.010	0.011	0.008	0.005	0.020	0.003	0.007	0.018	0.016	0.012	0.010	0.006	0.026	0.003	0.009	0.027	0.019	0.015
Honite 12	k_s	1.000	1.090	1.070	1.130	1.050	1.450	2.990	7.720	1.040	1.050	1.110	1.200	1.110	1.520	3.420	8.880	1.050	1.040	1.080	1.140	1.080	1.470	2.860	7.380
	σ	0.016	0.014	0.018	0.017	0.015	0.056	0.292	1.580	0.014	0.019	0.017	0.017	0.015	0.085	0.380	1.220	0.019	0.015	0.018	0.020	0.013	0.113	0.574	1.660
		Probe 5																							
		2 MHz								**2.25 MHz**								**2.5 MHz**							
		Conc 1	Conc 2	Conc 3	Conc 4	Conc 5	Conc 6	Conc 7	Conc 8	Conc 1	Conc 2	Conc 3	Conc 4	Conc 5	Conc 6	Conc 7	Conc 8	Conc 1	Conc 2	Conc 3	Conc 4	Conc 5	Conc 6	Conc 7	Conc 8
Honite 22	k_s	0.198	0.162	0.162	0.160	0.160	0.166	0.163	0.168	0.198	0.161	0.159	0.161	0.153	0.164	0.163	0.169	0.196	0.163	0.160	0.155	0.144	0.165	0.163	0.169
	σ	0.002	0.002	0.002	0.001	0.004	0.002	0.002	0.002	0.003	0.002	0.002	0.002	0.002	0.002	0.003	0.003	0.004	0.003	0.002	0.003	0.003	0.003	0.003	0.003
Honite 16	k_s	0.527	0.414	0.515	0.430	0.411	0.435	0.422	0.494	0.539	0.402	0.569	0.475	0.472	0.447	0.442	0.475	0.581	0.359	0.034	0.019	0.018	0.183	0.133	0.316
	σ	0.008	0.005	0.007	0.007	0.008	0.009	0.007	0.006	0.010	0.006	0.011	0.010	0.011	0.008	0.008	0.007	0.011	0.007	0.011	0.012	0.014	0.013	0.012	0.008
Honite 12	k_s	1.040	1.050	1.080	1.150	1.050	1.500	3.110	8.720	1.020	1.070	1.050	1.110	1.030	1.400	2.970	7.180	0.997	1.100	1.110	1.140	1.120	1.460	2.780	7.390
	σ	0.013	0.014	0.016	0.020	0.017	0.042	0.400	3.940	0.012	0.019	0.018	0.019	0.016	0.083	0.734	1.590	0.015	0.022	0.021	0.028	0.017	0.150	1.350	3.660
		Probe 6																							
		2 MHz								**2.25 MHz**								**2.5 MHz**							
		Conc 1	Conc 2	Conc 3	Conc 4	Conc 5	Conc 6	Conc 7	Conc 8	Conc 1	Conc 2	Conc 3	Conc 4	Conc 5	Conc 6	Conc 7	Conc 8	Conc 1	Conc 2	Conc 3	Conc 4	Conc 5	Conc 6	Conc 7	Conc 8
Honite 22	k_s	0.193	0.166	0.161	0.145	0.032	0.164	0.165	0.162	0.235	0.206	0.204	0.202	0.091	0.207	0.201	0.201	0.232	0.209	0.212	0.205	0.193	0.213	0.208	0.217
	σ	0.003	0.002	0.002	0.002	0.003	0.002	0.002	0.002	0.003	0.003	0.002	0.002	0.002	0.002	0.002	0.002	0.004	0.003	0.003	0.003	0.003	0.002	0.003	0.003
Honite 16	k_s	0.520	0.421	0.472	0.398	0.386	0.401	0.384	0.453	0.655	0.479	0.359	0.200	0.304	0.448	0.430	0.501	0.627	0.507	0.618	0.543	0.330	0.507	0.565	0.644
	σ	0.007	0.004	0.009	0.010	0.008	0.007	0.008	0.005	0.008	0.007	0.009	0.008	0.012	0.011	0.010	0.007	0.010	0.009	0.013	0.012	0.016	0.014	0.012	0.008
Honite 12	k_s	0.990	1.110	1.030	1.100	1.070	1.450	2.930	7.540	0.990	1.080	0.873	1.060	0.954	1.620	3.950	11.100	0.997	1.080	1.040	1.060	0.989	1.590	4.210	11.200
	σ	0.017	0.014	0.015	0.015	0.015	0.052	0.314	0.990	0.016	0.018	0.017	0.018	0.016	0.095	0.482	1.930	0.015	0.015	0.021	0.024	0.013	0.134	0.612	1.760
		Probe 7																							
		2 MHz								**2.25 MHz**								**2.5 MHz**							
		Conc 1	Conc 2	Conc 3	Conc 4	Conc 5	Conc 6	Conc 7	Conc 8	Conc 1	Conc 2	Conc 3	Conc 4	Conc 5	Conc 6	Conc 7	Conc 8	Conc 1	Conc 2	Conc 3	Conc 4	Conc 5	Conc 6	Conc 7	Conc 8
Honite 22	k_s	0.244	0.198	0.197	0.198	0.187	0.198	0.195	0.206	0.239	0.202	0.206	0.196	0.193	0.207	0.206	0.212	0.240	0.201	0.205	0.204	0.203	0.212	0.207	0.215
	σ	0.003	0.003	0.002	0.002	0.002	0.002	0.002	0.002	0.005	0.004	0.003	0.003	0.002	0.002	0.003	0.003	0.006	0.005	0.009	0.004	0.003	0.003	0.003	0.004
Honite 16	k_s	0.584	0.550	0.420	0.543	0.313	0.449	0.501	0.581	0.644	0.490	1.320	0.191	0.408	1.010	0.820	1.110	0.635	0.499	0.607	0.495	0.459	0.485	0.478	0.587
	σ	0.007	0.005	0.001	0.002	0.001	0.004	0.002	0.003	0.009	0.006	0.001	0.002	0.002	0.005	0.002	0.005	0.010	0.006	0.002	0.002	0.002	0.006	0.003	0.004
Honite 12	k_s	1.030	1.050	1.060	1.120	1.050	1.720	4.730	14.100	1.050	1.020	1.040	1.070	1.010	1.620	3.880	11.100	1.030	1.040	1.020	1.080	0.984	1.710	4.720	13.400
	σ	0.015	0.016	0.017	0.017	0.015	0.065	0.337	1.790	0.018	0.016	0.024	0.021	0.026	0.103	0.510	2.120	0.012	0.017	0.020	0.032	0.022	0.139	1.460	2.220
		Probe 8																							
		2 MHz								**2.25 MHz**								**2.5 MHz**							
		Conc 1	Conc 2	Conc 3	Conc 4	Conc 5	Conc 6	Conc 7	Conc 8	Conc 1	Conc 2	Conc 3	Conc 4	Conc 5	Conc 6	Conc 7	Conc 8	Conc 1	Conc 2	Conc 3	Conc 4	Conc 5	Conc 6	Conc 7	Conc 8
Honite 22	k_s	0.239	0.202	0.201	0.204	0.194	0.209	0.207	0.215	0.237	0.204	0.202	0.196	0.181	0.208	0.206	0.216	0.233	0.208	0.204	0.184	0.042	0.209	0.210	0.217
	σ	0.004	0.003	0.002	0.002	0.001	0.002	0.002	0.002	0.004	0.004	0.003	0.002	0.001	0.003	0.002	0.003	0.005	0.004	0.003	0.003	0.002	0.003	0.003	0.004
Honite 16	k_s	0.651	0.484	0.672	0.547	0.529	0.502	0.508	0.580	0.690	0.445	0.044	0.025	0.025	0.210	0.160	0.393	0.625	0.509	0.556	0.456	0.437	0.457	0.439	0.548
	σ	0.007	0.005	0.006	0.005	0.007	0.007	0.006	0.004	0.008	0.005	0.007	0.009	0.010	0.009	0.006	0.006	0.008	0.008	0.009	0.011	0.012	0.012	0.010	0.008
Honite 12	k_s	1.020	1.060	0.999	1.050	0.963	1.560	3.790	11.500	0.993	1.080	1.040	1.100	1.040	1.580	3.420	11.600	0.984	1.090	0.980	1.030	0.981	1.560	3.650	11.000
	σ	0.014	0.018	0.015	0.019	0.014	0.048	0.244	1.050	0.012	0.016	0.016	0.017	0.018	0.088	0.386	1.180	0.013	0.019	0.017	0.017	0.014	0.119	0.519	1.570

A.3 Error in Calculated Concentration using the Dual Frequency Method

As defined by Rice *et al.* [15], when applying the dual frequency method Equation 2.48 (Section 2.3.6) can be written as follows, where the expression for the calculated particle concentration, *M,* is given as

$$M = AB \tag{A.6}$$

where

$$A = J_1^{\left(1-\frac{\xi_1}{\xi_2}\right)^{-1}} \tag{A.7}$$

and

$$B = J_2^{\left(1-\frac{\xi_2}{\xi_1}\right)^{-1}} \tag{A.8}$$

In which $\frac{\xi_1}{\xi_2}$ is the ratio of the attenuation coefficient at each frequency. Defining the overall error in the measured concentration, δM, divided by the expected value in terms of A and B we obtain Equation A.9.

$$\frac{\delta M}{M} = \sqrt{\left(\frac{\delta A}{A}\right)^2 + \left(\frac{\delta B}{B}\right)^2} \tag{A.9}$$

In the expressions given by Rice *et al.* [15] the ∂A term is given by the following Equations in terms of the product of partial differentials involving Φ_1 (containing the scattering constant, range and water attenuation term, Equation A.12), J_1 (containing the sediment concentration and attenuation term, Equation A.13) and K_1 (the product of the scattering constant, k_s, and the transducer constant, k_t).

$$\delta A = \delta K_1 \left| \frac{\partial({\Phi_1}^2)}{\partial K_1} \frac{\partial J_1}{\partial({\Phi_1}^2)} \frac{\partial A}{\partial J_1} \right| \tag{A.10}$$

Using the following identities:

$$V^2(r) = \Phi^2(r) J(r) \tag{A.11}$$

$$\Phi^2(r) = \left(\frac{k_s k_t}{\psi r}\right) e^{-4r\alpha_w} \tag{A.12}$$

$$J(r) = M e^{-4\int_0^r \xi(r')M(r')dr'} = \frac{V^2(r)}{\Phi^2(r)} \tag{A.13}$$

The partial differentials can then be expressed in terms of ${\Phi_1}^2$ shown below

$$\frac{\partial J_1}{\partial(\Phi^2)} = -\frac{J_1}{{\Phi_1}^2} \quad \textbf{A.14}$$

$$\frac{\partial({\Phi_1}^2)}{\partial K_1} = \frac{2}{K_1}{\Phi_1}^2 \quad \textbf{A.15}$$

And

$$\frac{\partial A}{\partial J_1} = \frac{A}{J_1}\left(1 - \frac{\xi_1}{\xi_2}\right)^{-1} \quad \textbf{A.16}$$

Substituting Equations A.14-A.16 into equation A.10and simplifying we obtain the following expression for the absolute error in A as a function of the attenuation coefficient at each frequency, ξ_1 and ξ_2, and the relative error in the combined scattering term, K_1.

$$\delta A = -2A\left(1 - \frac{\xi_1}{\xi_2}\right)^{-1}\left|\frac{\delta K_1}{K_1}\right| \quad \textbf{A.17}$$

A similar expression for B is obtained using the same procedure replacing J_1, Φ_1 and K_1 with J_2, Φ_2 and K_2 to obtain

$$\delta B = -2B\left(1 - \frac{\xi_2}{\xi_1}\right)^{-1}\left|\frac{\delta K_2}{K_2}\right| \quad \textbf{A.18}$$

Substituting these expressions into equation A.9 the relative error in M due to the combined error from both signals can be expressed in terms of the relative error in K_1 and K_2

$$\frac{\delta M}{M} = \sqrt{\left(-2\left(1 - \frac{\xi_1}{\xi_2}\right)^{-1}\left|\frac{\delta K_1}{K_1}\right|\right)^2 + \left(-2\left(1 - \frac{\xi_2}{\xi_1}\right)^{-1}\left|\frac{\delta K_2}{K_2}\right|\right)^2} \quad \textbf{A.19}$$

Appendix B

Table B.1 attenuation coefficient values with corresponding correlation coefficient for the fit

	Calcite Particulates		Calcite Flocs		Magnesium Hydroxide Particulates		Magnesium Hydroxide Flocs		BPS	
	ξ	R^2	ξ	R^2	ξ	R^2	ξ	R^2	ξ	R^2
0.85 MHz	0.157148	0.994534	0.120134	0.991495	4.066885	0.973254	1.241241	0.965039	0.173068	0.989576
1 MHz	0.176412	0.993557	0.140263	0.978211	2.693927	0.891996	1.089977	0.982239	0.194352	0.945322
1.15 MHz	0.190246	0.997516	0.147843	0.991091	0.840447	0.898822	0.974462	0.98438	0.214057	0.978007
2 MHz	0.223251	0.991609	0.215824	0.989189	1.689694	0.987973	0.808621	0.988631	0.379634	0.995964
2.25 MHz	0.238202	0.996815	0.233622	0.994675	1.908751	0.994782	0.765839	0.987277	0.427478	0.992712
2.5 MHz	0.248476	0.996461	0.2555	0.994118	1.939085	0.996464	0.752364	0.986878	0.49095	0.992929
3.75 MHz	0.31935	0.99699	0.401003	0.995607	2.128128	0.949455	0.632252	0.984577	0.750872	0.987134
5 MHz	0.385039	0.997799	0.507684	0.995505	2.10907	0.95487	0.709657	0.983082	0.902271	0.998374
6.75 MHz	0.41085	0.995185	0.564049	0.999937	2.188128	0.965762	0.70667	0.969653	0.777514	0.97382

Table B.2 k_s values and corresponding standard deviation over the range of values averaged to produce the value

		Calcite Particulates		Calcite Flocs		Magnesium Hydroxide Particulates		Magnesium Hydroxide Flocs		BPS	
		k_s	σ	k_s	σ	k_s	σ	k_s	σ	k_s	σ
0.85 MHz	Conc 1	0.27	0.009	0.240	0.004	0.250	0.033	0.570	0.019	0.330	0.008
	Conc 2	0.17	0.006	0.210	0.004	0.280	0.019	0.440	0.023	0.250	0.007
	Conc 3	0.15	0.005	0.150	0.003	0.290	0.065	0.340	0.038	0.260	0.010
	Conc 4	0.20	0.005	0.140	0.004	0.580	0.230	0.380	0.016	0.240	0.004
	Conc 5	0.24	0.007	0.170	0.005	13.000	4.800	0.510	0.300	-	-
1 MHz	Conc 1	0.31	0.016	0.300	0.006	0.240	0.023	0.700	0.023	0.420	0.014
	Conc 2	0.20	0.011	0.250	0.009	0.230	0.012	0.560	0.018	0.340	0.017
	Conc 3	0.18	0.011	0.190	0.006	0.130	0.009	0.470	0.022	0.350	0.014
	Conc 4	0.25	0.012	0.180	0.007	0.092	0.028	0.520	0.013	0.330	0.012
	Conc 5	0.30	0.017	0.230	0.007	0.670	0.260	0.470	0.130	-	-
1.15 MHz	Conc 1	0.28	0.008	0.280	0.007	0.170	0.017	0.640	0.046	0.410	0.017
	Conc 2	0.18	0.009	0.230	0.015	0.140	0.008	0.540	0.042	0.370	0.008
	Conc 3	0.15	0.017	0.180	0.010	0.054	0.005	0.490	0.019	0.340	0.020
	Conc 4	0.21	0.022	0.180	0.013	0.015	0.003	0.530	0.042	0.330	0.021
	Conc 5	0.28	0.016	0.220	0.013	0.013	0.007	0.490	0.098	-	-
2 MHz	Conc 1	0.26	0.015	0.300	0.005	0.170	0.006	0.590	0.070	0.360	0.034
	Conc 2	0.16	0.009	0.280	0.013	0.130	0.002	0.530	0.067	0.340	0.027
	Conc 3	0.13	0.017	0.260	0.015	0.061	0.002	0.450	0.054	0.300	0.036
	Conc 4	0.19	0.016	0.350	0.005	0.020	0.001	0.450	0.091	0.270	0.037
	Conc 5	0.23	0.015	0.320	0.023	0.015	0.006	0.370	0.092	-	-
2.25 MHz	Conc 1	0.26	0.017	0.300	0.025	0.190	0.005	0.690	0.063	0.430	0.028
	Conc 2	0.17	0.010	0.330	0.014	0.150	0.004	0.460	0.099	0.360	0.039
	Conc 3	0.15	0.015	0.310	0.020	0.084	0.001	0.420	0.077	0.320	0.048
	Conc 4	0.22	0.008	0.360	0.022	0.031	0.001	0.460	0.100	0.330	0.034
	Conc 5	0.23	0.019	0.360	0.029	0.070	0.034	0.350	0.084	-	-
2.5 MHz	Conc 1	0.26	0.012	0.360	0.010	0.190	0.006	0.480	0.110	0.450	0.039
	Conc 2	0.17	0.010	0.340	0.026	0.160	0.007	0.450	0.100	0.480	0.029
	Conc 3	0.18	0.004	0.380	0.014	0.095	0.003	0.410	0.081	0.390	0.052
	Conc 4	0.20	0.012	0.400	0.028	0.040	0.002	0.440	0.100	0.330	0.059
	Conc 5	0.23	0.015	0.440	0.012	0.100	0.049	0.350	0.089	-	-
3.75 MHz	Conc 1	0.27	0.029	0.520	0.047	0.340	0.010	0.680	0.078	0.600	0.073
	Conc 2	0.17	0.014	0.570	0.048	0.220	0.016	0.620	0.071	0.700	0.067
	Conc 3	0.15	0.018	0.570	0.065	0.180	0.018	0.450	0.071	0.580	0.091
	Conc 4	0.20	0.014	0.620	0.079	0.120	0.006	0.430	0.080	0.580	0.085
	Conc 5	0.20	0.021	0.630	0.061	0.095	0.035	0.290	0.045	-	-
5 MHz	Conc 1	0.21	0.044	0.740	0.077	0.390	0.017	0.630	0.130	0.690	0.110
	Conc 2	0.21	0.016	0.950	0.031	0.290	0.020	0.580	0.120	0.710	0.110
	Conc 3	0.13	0.029	0.900	0.079	0.250	0.026	0.490	0.080	0.660	0.098
	Conc 4	0.16	0.032	1.100	0.068	0.190	0.012	0.500	0.100	0.680	0.110
	Conc 5	0.17	0.036	0.640	0.110	0.160	0.050	0.390	0.100	-	-
6.75 MHz	Conc 1	0.22	0.039	0.710	0.120	0.520	0.018	0.690	0.110	0.610	0.044
	Conc 2	0.15	0.028	0.750	0.120	0.310	0.027	0.600	0.099	0.560	0.047
	Conc 3	0.15	0.028	0.750	0.120	0.320	0.033	0.480	0.057	0.400	0.014
	Conc 4	0.17	0.026	0.710	0.110	0.270	0.018	0.460	0.078	0.370	0.040
	Conc 5	0.17	0.032	0.600	0.100	0.250	0.078	0.360	0.110	0.000	0.000

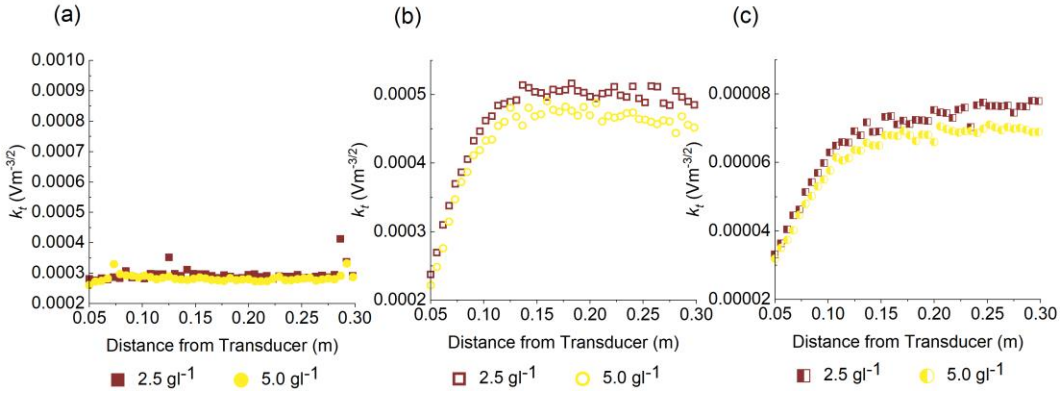

Figure B.1 k_t calibration profiles for a) 1 MHz, b) 2.25 MHz and c) 5 MHz Sonatest probes produced using data for Honite 16 operating at their central frequency

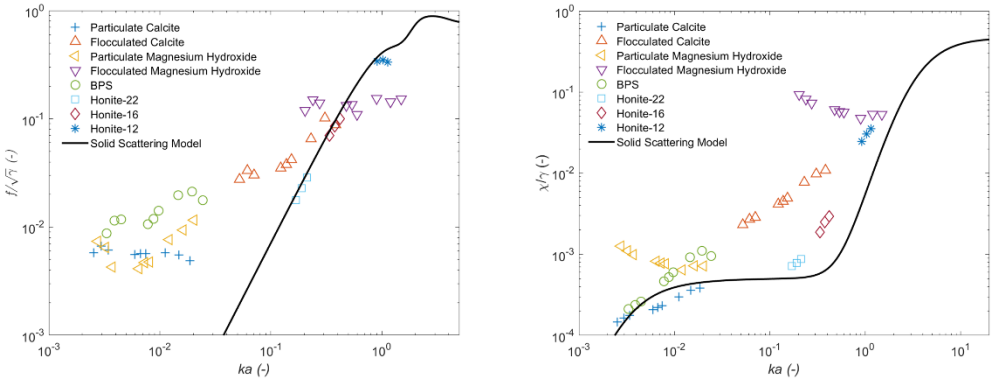

Figure B.2 All scattering cross-section and form function data compared to irregular solid scattering model [48] modelled for glass particles insonified at 2 MHz

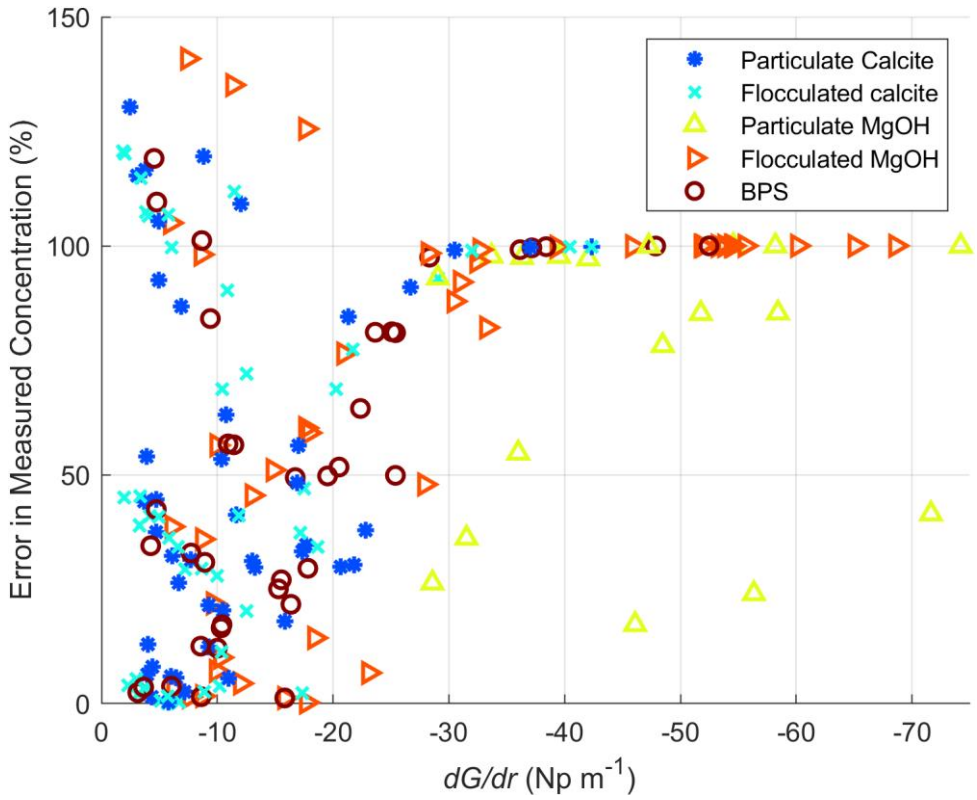

Figure B.3 Error in measured concentration using single frequency inversion (averaged between 0.1 and 0.2 m from the probe) as a function of measured attenuation for all sediment systems and frequencies. 3-D MATLAB plots inlcuding sampled concentration values plotted on a third axis avilable at https://github.com/alastair-tonge/Novel-characterisation-of-complex-dispersions-using-acoustic-backscatter-systems-Supplementary-Data

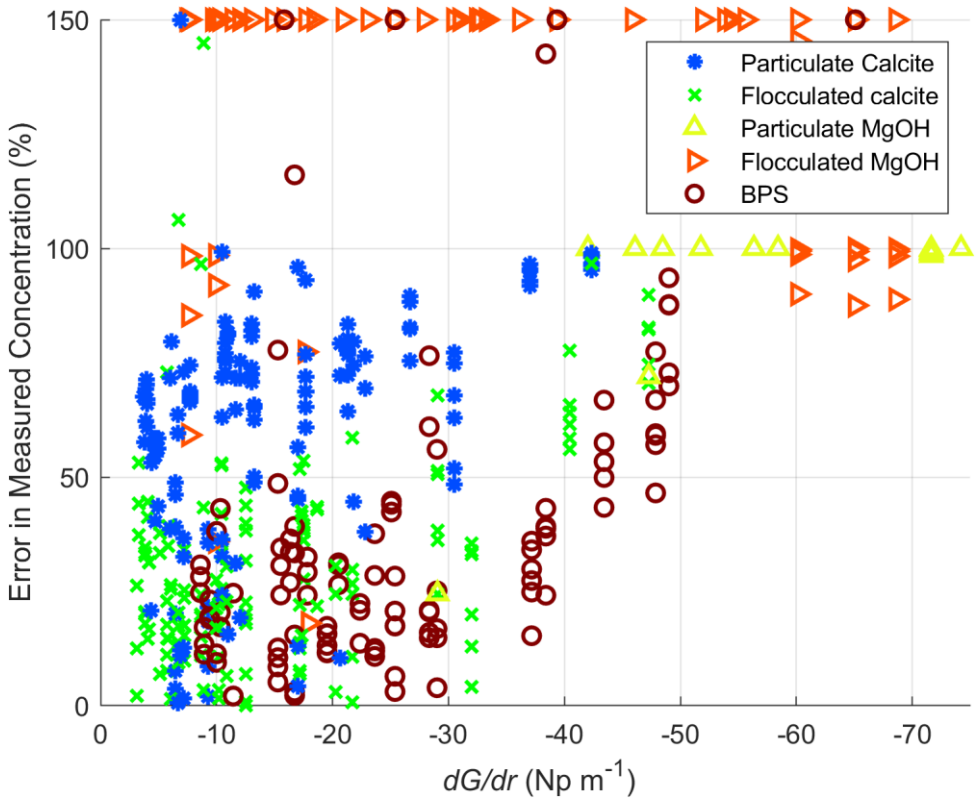

Figure B.4 Error in measured concentration using dual frequency inversion (averaged between 0.1 and 0.2 m from the probe) as a function of largest (most negative) measured attenuation of the two frequencies used for all sediment systems and frequency pairings. Error values above 150% have been set to 150% to facilitate visibility of all data. 3-D MATLAB plots inlcuding sampled concentration values plotted on a third axis avilable at https://github.com/alastair-tonge/Novel-characterisation-of-complex-dispersions-using-acoustic-backscatter-systems-Supplementary-Data

Table B.3 Percentage error compared to gravimetrically weighed concentration for single frequency inversion of cohesive sediments averaged over 0.1 to 0.2 m from the probe

	Frequency	Nominal Concentration				
		2.4	5	10.9	19.4	41.1
Calcite Particulates	0.85 MHz	13	8	0.4	22	18
	1 Mhz	54	45	32	53	33
	1.15 Mhz	130	115	93	120	48
	2 MHz	6	1	6	5	30
	2.25 MHz	44	37	26	41	30
	2.5 MHz	117	105	87	109	38
	3.75 MHz	6	3	20	56	99
	5 MHz	31	12	30	85	100
	6.25 MHz	63	31	35	91	100
	Frequency	Nominal Concentration				
		2.3	4.14	8.3	18.7	34.9
Calcite Flocs	0.85 MHz	4	5	3	2	11
	1 Mhz	45	45	41	34	41
	1.15 Mhz	121	120	115	107	112
	2 MHz	2	3	1	3	2
	2.25 MHz	39	41	36	28	34
	2.5 MHz	107	107	100	90	69
	3.75 MHz	0.1	0.3	4	37	99
	5 MHz	29	29	20	77	100
	6.25 MHz	69	72	47	93	100
	Frequency	Nominal Concentration				
		2.2	4.9	11.3	19.8	41.2
Magnesium Hydroxide Particulates	0.85 MHz	95	100	100	100	100
	1 Mhz	82	99	100	100	100
	1.15 Mhz	21	41	95	100	100
	2 MHz	24	85	100	100	100
	2.25 MHz	17	85	100	100	100
	2.5 MHz	97	78	100	100	100
	3.75 MHz	55	98	100	100	100
	5 MHz	36	97	100	100	100
	6.25 MHz	26	98	100	100	100
	Frequency	Nominal Concentration				
		2.3	4.1	8.4	18.6	35
Magnesium Hydroxide Flocs	0.85 MHz	10	0	82	100	100
	1 Mhz	56	51	48	100	100
	1.15 Mhz	141	135	7	100	100
	2 MHz	3	2	14	97	100
	2.25 MHz	39	36	59	92	100
	2.5 MHz	105	98	126	88	100
	3.75 MHz	1	7	60	98	100
	5 MHz	22	4	76	99	100
	6.25 MHz	45	1	81	99	100
	Frequency	Nominal Concentration				
		6.9	9.8	16.7	22.9	-
BPS	0.85 MHz	2	4	4	13	-
	1 Mhz	42	34	33	17	-
	1.15 Mhz	119	110	101	57	-
	2 MHz	2	12	27	52	-
	2.25 MHz	31	17	22	64	-
	2.5 MHz	84	57	30	81	-
	3.75 MHz	25	49	98	100	-
	5 MHz	50	81	100	100	-
	6.25 MHz	50	82	99	100	-

Table B.4 Percentage error compared to gravimetrically weighed concentration for dual frequency inversion of cohesive sediments averaged over 0.1 to 0.2 m from the probe for 1 and 2.25 MHz central frequency probes

	Frequency Pairing	Nominal Concentration				
		2.4	5	10.9	19.4	41.1
Calcite Particulates	0.85 & 2 MHz	67	53	72	82	79
	0.85 & 2.25 MHz	66	56	60	72	80
	0.85 & 2.5 MHz	61	56	12	75	76
	1 & 2 MHz	71	55	80	81	72
	1 & 2.25 MHz	69	58	64	65	74
	1 & 2.5 MHz	62	59	11	72	69
	1.15 & 2 MHz	70	21	39	16	10
	1.15 & 2.25 MHz	68	40	1	31	45
	1.15 & 2.5 MHz	58	44	150	19	38
	Frequency Pairing	Nominal Concentration				
		2.3	4.14	8.3	18.7	34.9
Calcite Flocs	0.85 & 2 MHz	13	33	33	3	43
	0.85 & 2.25 MHz	37	31	35	28	44
	0.85 & 2.5 MHz	20	41	26	30	31
	1 & 2 MHz	26	35	38	43	42
	1 & 2.25 MHz	53	31	39	17	43
	1 & 2.5 MHz	33	45	26	23	24
	1.15 & 2 MHz	2	20	7	145	15
	1.15 & 2.25 MHz	44	17	15	21	22
	1.15 & 2.5 MHz	18	15	1	6	3
	Frequency Pairing	Nominal Concentration				
		2.2	4.9	11.3	19.8	41.2
Magnesium Hydroxide Particulates	0.85 & 2 MHz	88	89	97	16	1.17E+04
	0.85 & 2.25 MHz	46	59	96	48	683
	0.85 & 2.5 MHz	108	22	93	78	608
	1 & 2 MHz	35	59	99	60	6.71E+04
	1 & 2.25 MHz	2294	777	97	60	978
	1 & 2.5 MHz	3.58E+04	7.85E+03	88	46	837
	1.15 & 2 MHz	98	98	92	12	54
	1.15 & 2.25 MHz	99	99	94	18	152
	1.15 & 2.5 MHz	99	99	95	22	168
	Frequency Pairing	Nominal Concentration				
		2.3	4.1	8.4	18.6	35
Magnesium Hydroxide Flocs	0.85 & 2 MHz	895	1.12E+03	689	201	100
	0.85 & 2.25 MHz	613	4.18E+03	1.92E+03	332	99
	0.85 & 2.5 MHz	6.41E+03	7.09E+03	3.66E+03	950	99
	1 & 2 MHz	1.66E+03	1.91E+03	1.83E+03	1.53E+03	100
	1 & 2.25 MHz	9.33E+02	9.17E+03	5.43E+03	1.87E+03	99
	1 & 2.5 MHz	1.67E+04	1.71E+04	1.16E+04	5.55E+03	98
	1.15 & 2 MHz	2.25E+03	2.73E+03	3.64E+03	4.97E+03	100
	1.15 & 2.25 MHz	945	2.16E+04	1.36E+04	4.87E+03	99
	1.15 & 2.5 MHz	4.63E+04	4.69E+04	3.54E+04	1.92E+04	97
	Frequency Pairing	Nominal Concentration				
		6.9	9.8	16.7	22.9	-
BPS	0.85 & 2 MHz	25	9	24	31	-
	0.85 & 2.25 MHz	13	17	27	22	-
	0.85 & 2.5 MHz	19	2	24	42	-
	1 & 2 MHz	31	11	35	31	-
	1 & 2.25 MHz	17	20	36	21	-
	1 & 2.5 MHz	23	2	33	45	-
	1.15 & 2 MHz	28	38	31	26	-
	1.15 & 2.25 MHz	11	43	34	14	-
	1.15 & 2.5 MHz	19	25	29	44	-

Table B.5 Percentage error compared to gravimetrically weighed concentration for dual frequency inversion of cohesive sediments averaged over 0.1 to 0.2 m from the probe for 2.25 and 5 MHz central frequency probes

	Frequency Pairing	Nominal Concentration				
		2.4	5	10.9	19.4	41.1
Calcite Particulates	2 & 3.75 MHz	4	2	99	46	63
	2 & 5 MHz	66	18	50	72	95
	2 & 6.25 MHz	77	81	65	82	98
	2.25 & 3.75 MHz	20	37	63	4	48
	2.25 & 5 MHz	68	2	66	83	95
	2.25 & 6.25 MHz	79	82	77	90	98
	2.5 & 3.75 MHz	8	73	72	96	52
	2.5 & 5 MHz	74	9	91	80	97
	2.5 & 6.25 MHz	84	84	93	88	99
	Frequency Pairing	Nominal Concentration				
		2.3	4.14	8.3	18.7	34.9
Calcite Flocs	2 & 3.75 MHz	18	9	2	52	13
	2 & 5 MHz	24	20	7	27	66
	2 & 6.25 MHz	53	44	40	68	82
	2.25 & 3.75 MHz	73	13	17	7	4
	2.25 & 5 MHz	34	24	20	30	64
	2.25 & 6.25 MHz	26	48	38	51	83
	2.5 & 3.75 MHz	8	106	11	13	33
	2.5 & 5 MHz	10	97	1	59	78
	2.5 & 6.25 MHz	53	32	54	51	90
	Frequency Pairing	Nominal Concentration				
		2.2	4.9	11.3	19.8	41.2
Magnesium Hydroxide Particulates	2 & 3.75 MHz	100	100	100	98	98
	2 & 5 MHz	100	100	100	100	99
	2 & 6.25 MHz	100	100	100	100	100
	2.25 & 3.75 MHz	100	100	100	100	100
	2.25 & 5 MHz	100	100	100	100	100
	2.25 & 6.25 MHz	100	100	100	100	100
	2.5 & 3.75 MHz	100	100	100	100	100
	2.5 & 5 MHz	100	100	100	100	100
	2.5 & 6.25 MHz	100	100	100	100	100
	Frequency Pairing	Nominal Concentration				
		2.3	4.1	8.4	18.6	35
Magnesium Hydroxide Flocs	2 & 3.75 MHz	59	36	526	1.49E+05	4.48E+04
	2 & 5 MHz	1.82E+05	1.43E+05	9.12E+06	2.53E+14	2.96E+13
	2 & 6.25 MHz	4.21E+06	3.47E+06	4.70E+09	1.58E+18	7.60E+16
	2.25 & 3.75 MHz	85	92	18	9.77E+05	3.57E+05
	2.25 & 5 MHz	4.16E+07	9.49E+03	2.89E+08	1.40E+23	7.48E+21
	2.25 & 6.25 MHz	5.13E+09	1.85E+06	7.96E+12	7.57E+28	8.64E+26
	2.5 & 3.75 MHz	98	98	77	2.25E+05	2.10E+05
	2.5 & 5 MHz	485	397	1.64E+08	1.80E+26	1.02E+26
	2.5 & 6.25 MHz	5.59E+05	4.68E+05	7.74E+13	2.11E+33	1.33E+32
	Frequency Pairing	Nominal Concentration				
		6.9	9.8	16.7	22.9	-
BPS	2 & 3.75 MHz	49	39	21	24	-
	2 & 5 MHz	17	13	27	67	-
	2 & 6.25 MHz	3	25	58	88	-
	2.25 & 3.75 MHz	13	116	61	43	-
	2.25 & 5 MHz	12	12	15	77	-
	2.25 & 6.25 MHz	28	4	53	94	-
	2.5 & 3.75 MHz	78	33	77	143	-
	2.5 & 5 MHz	16	38	25	47	-
	2.5 & 6.25 MHz	6	56	67	88	-

Table B.6 Percentage error compared to gravimetrically weighed concentration for dual frequency inversion of cohesive sediments averaged over 0.1 to 0.2 m from the probe for 1 and 5 MHz central frequency probes

	Frequency Pairing	Nominal Concentration				
		2.4	5	10.9	19.4	41.1
Calcite Particulates	0.85 & 3.75 MHz	49	37	36	57	77
	0.85 & 5 MHz	67	39	63	78	92
	0.85 & 6.25 MHz	73	71	69	82	95
	1 & 3.75 MHz	46	33	33	45	75
	1 & 5 MHz	69	36	65	77	93
	1 & 6.25 MHz	75	74	72	83	96
	1.15 & 3.75 MHz	39	13	24	13	68
	1.15 & 5 MHz	68	22	49	64	93
	1.15 & 6.25 MHz	76	73	61	75	97
	Frequency Pairing	Nominal Concentration				
		2.3	4.14	8.3	18.7	34.9
Calcite Flocs	0.85 & 3.75 MHz	15	20	22	22	36
	0.85 & 5 MHz	18	15	19	11	58
	0.85 & 6.25 MHz	33	38	36	38	71
	1 & 3.75 MHz	23	17	22	14	34
	1 & 5 MHz	25	11	18	1	62
	1 & 6.25 MHz	42	40	39	36	75
	1.15 & 3.75 MHz	11	14	3	8	20
	1.15 & 5 MHz	15	19	0.04	24	56
	1.15 & 6.25 MHz	36	23	28	24	72
	Frequency Pairing	Nominal Concentration				
		2.2	4.9	11.3	19.8	41.2
Magnesium Hydroxide Particulates	0.85 & 3.75 MHz	1.21E+03	3.78E+03	1.13E+04	1.15E+03	1.23E+06
	0.85 & 5 MHz	1.56E+04	1.69E+04	4.10E+04	2.53E+03	1.86E+06
	0.85 & 6.25 MHz	6.90E+04	2.59E+05	2.81E+05	1.05E+04	8.33E+06
	1 & 3.75 MHz	2.16E+07	8.24E+07	6.74E+07	2.32E+03	2.27E+10
	1 & 5 MHz	3.40E+09	1.43E+09	8.35E+08	1.33E+04	4.12E+10
	1 & 6.25 MHz	1.44E+12	1.29E+13	7.23E+11	6.45E+05	1.36E+13
	1.15 & 3.75 MHz	100	100	100	56	72
	1.15 & 5 MHz	100	100	100	66	77
	1.15 & 6.25 MHz	100	100	100	74	81
	Frequency Pairing	Nominal Concentration				
		2.3	4.1	8.4	18.6	35
Magnesium Hydroxide Flocs	0.85 & 3.75 MHz	333	352	535	163	90
	0.85 & 5 MHz	3.89E+03	4.38E+03	5.17E+03	2.89E+03	145
	0.85 & 6.25 MHz	1.03E+04	1.19E+04	2.15E+04	2.86E+04	3.06E+03
	1 & 3.75 MHz	395	385	894	587	89
	1 & 5 MHz	7.84E+03	8.22E+03	1.79E+04	2.50E+04	476
	1 & 6.25 MHz	2.53E+04	2.75E+04	1.20E+05	5.12E+05	1.28E+04
	1.15 & 3.75 MHz	333	319	1.04E+03	847	88
	1.15 & 5 MHz	1.47E+04	1.51E+04	5.77E+04	1.48E+05	1.93E+03
	1.15 & 6.25 MHz	6.49E+04	6.96E+04	7.66E+05	8.42E+06	1.06E+05
	Frequency Pairing	Nominal Concentration				
		6.9	9.8	16.7	22.9	-
BPS	0.85 & 3.75 MHz	8	2	15	39	-
	0.85 & 5 MHz	13	11	30	57	-
	0.85 & 6.25 MHz	17	15	43	70	-
	1 & 3.75 MHz	11	3	21	39	-
	1 & 5 MHz	16	12	36	59	-
	1 & 6.25 MHz	21	17	50	73	-
	1.15 & 3.75 MHz	5	15	16	37	-
	1.15 & 5 MHz	12	29	34	60	-
	1.15 & 6.25 MHz	17	34	50	74	-

Appendix C

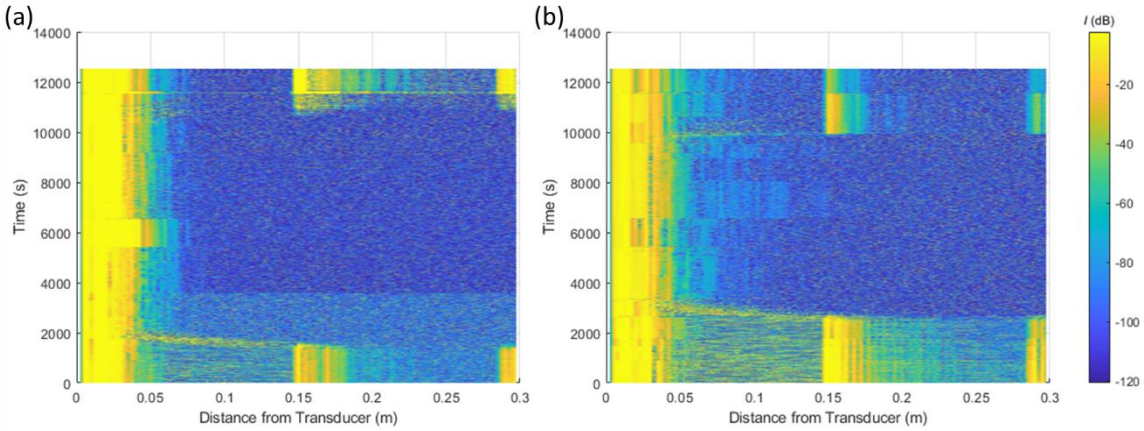

Figure C.1 Raw decibel data collected for second thickener experiment facing horizontally through the settled bed for the 1 MHz probe at a) 0.05 m and b) 0.15 m from the base of the thickener column

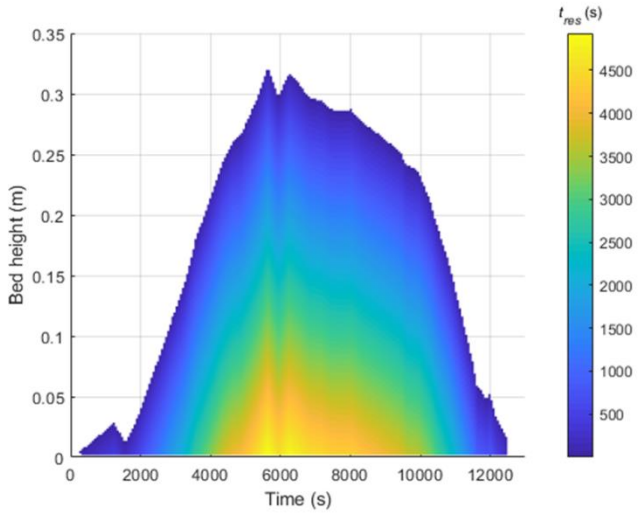

Figure C.2 Colour map of residence time as a function of experiment time and bed height for the second set of thickener experiments

References

[1] M. Guerrero and V. Di Federico, “Suspended sediment assessment by combining sound attenuation and backscatter measurements – analytical method and experimental validation,” *Adv. Water Resour.*, vol. 113, pp. 167–179, Mar. 2018.

[2] P. D. Thorne and P. J. Hardcastle, “Acoustic measurements of suspended sediments in turbulent currents and comparison with *in-situ* samples,” *J. Acoust. Soc. Am.*, vol. 101, no. 5, pp. 2603–2614, May 1997.

[3] P. D. Thorne, D. Hurther, R. D. Cooke, I. Caceres, P. A. Barraud, and A. Sánchez-Arcilla, “Developments in acoustics for studying wave-driven boundary layer flow and sediment dynamics over rippled sand-beds,” *Cont. Shelf Res.*, vol. 166, pp. 119–137, 2018.

[4] S. Naqshband, J. S. Ribberink, D. Hurther, P. A. Barraud, and S. J. M. H. Hulscher, “Experimental evidence for turbulent sediment flux constituting a large portion of the total sediment flux along migrating sand dunes,” *Geophys. Res. Lett.*, vol. 41, no. 24, pp. 8870–8878, Dec. 2014.

[5] M. S. Greenwood, J. L. Mai, and M. S. Good, “Attenuation measurements of ultrasound in a kaolin–water slurry: A linear dependence upon frequency,” *J. Acoust. Soc. Am.*, vol. 94, no. 2, pp. 908–916, Aug. 1993.

[6] J. Bux, N. Paul, T. N. Hunter, J. Peakall, J. M. Dodds, and S. Biggs, “In situ characterization of mixing and sedimentation dynamics in an impinging jet ballast tank via acoustic backscatter,” *AIChE J.*, vol. 63, no. 7, pp. 2618–2629, 2017.

[7] A. K. Rai and A. Kumar, “Continuous measurement of suspended sediment concentration: Technological advancement and future outlook,” *Measurement*, vol. 76, pp. 209–227, Dec. 2015.

[8] J. A. C. Bunt, P. Larcombe, and C. F. Jago, “Quantifying the response of optical backscatter devices and transmissometers to variations in suspended particulate matter,” *Cont. Shelf Res.*, 1999.

[9] J. Downing, “Twenty-five years with OBS sensors: The good, the bad, and the ugly,” *Cont. Shelf Res.*, vol. 26, no. 17–18, pp. 2299–2318, Nov. 2006.

[10] G. W. Graham, E. J. Davies, W. A. M. Nimmo-Smith, D. G. Bowers, and K. M. Braithwaite, “Interpreting LISST-100X measurements of particles with complex shape using digital in-line holography,” *J. Geophys. Res. Ocean.*, vol. 117, no. C5, pp. 1–20, 2012.

[11] R. E. Challis, M. J. W. Povey, M. L. Mather, and A. K. Holmes, “Ultrasound techniques for characterizing colloidal dispersions,” *Reports Prog. Phys.*, vol. 68, no. 7, pp. 1541–1637, 2005.

[12] H. I. Schlaberg, J. H. Baas, M. Wang, J. L. Best, R. A. Williams, and J. Peakall, “Electrical Resistance Tomography for Suspended Sediment Measurements in Open Channel Flows Using a Novel Sensor Design,” *Part. Part. Syst. Charact.*, vol. 23, no. 3-4, pp. 313–320, Oct. 2006.

[13] P. D. Thorne and D. Hurther, “An overview on the use of backscattered sound for measuring suspended particle size and concentration profiles in non-cohesive inorganic sediment transport studies,” *Cont. Shelf Res.*, vol. 73, pp. 97–118, Feb. 2014.

[14] D. Hurther, P. D. Thorne, M. Bricault, U. Lemmin, and J.-M. Barnoud, “A multi-frequency Acoustic Concentration and Velocity Profiler (ACVP) for boundary layer measurements of fine-scale flow and sediment transport processes,” *Coast. Eng.*, vol. 58, no. 7, pp. 594–605, Jul. 2011.

[15] H. P. Rice, M. Fairweather, T. N. Hunter, B. Mahmoud, S. Biggs, and J. Peakall, “Measuring particle concentration in multiphase pipe flow using acoustic backscatter: generalization of the dual-frequency inversion method.,” *J. Acoust. Soc. Am.*, vol. 136, no. 1, pp. 156–169, 2014.

[16] M. Guerrero, N. Rüther, S. Haun, and S. Baranya, “A combined use of acoustic and optical devices to investigate suspended sediment in rivers,” *Adv. Water Resour.*, vol. 102, pp. 1–12, 2017.

[17] J. Bux, J. Peakall, H. P. Rice, M. S. Manga, S. Biggs, and T. N. Hunter, “Measurement and density normalisation of acoustic attenuation and backscattering constants of arbitrary suspensions within the Rayleigh scattering regime,” *Appl. Acoust.*, vol. 146, pp. 9–22, 2019.

[18] J. J. Hastings, D. Rhodes, A. S. Fellerman, D. Mckendrick, and C. Dixon, “New approaches for sludge management in the nuclear industry,” *Powder Technol.*, vol. 174, no. 1–2, pp. 18–24, May 2007.

[19] C. R. Gregson, J. J. Hastings, H. E. Sims, H. M. Steele, and R. J. Taylor, “Characterisation of plutonium species in alkaline liquors sampled from a UK legacy nuclear fuel storage pond,” *Anal. Methods*, vol. 3, no. 9, pp. 1957–1968, 2011.

[20] S. F. Jackson, S. D. Monk, and Z. Riaz, “An investigation towards real time dose rate monitoring, and fuel rod detection in a First Generation Magnox Storage Pond (FGMSP),” *Appl. Radiat. Isot.*, vol. 94, pp. 254–259, Dec. 2014.

[21] V. Ajao, H. Bruning, H. Rijnaarts, and H. Temmink, “Natural flocculants from fresh and saline wastewater: Comparative properties and flocculation performances,” *Chem. Eng. J.*, vol. 349, pp. 622–632, Oct. 2018.

[22] UK Nuclear Decomissioning Authority, “UK Radioactive Waste Inventory - Low Level Waste,” *About Radioactive Waste*, 2016. [Online]. Available: https://ukinventory.nda.gov.uk/about-radioactive-waste/what-is-radioactivity/what-are-the-main-waste-categories/.

[23] S. P. Usher and P. J. Scales, “Steady state thickener modelling from the compressive yield stress and hindered settling function,” *Chem. Eng. J.*, vol. 111, no. 2–3, pp. 253–261, Aug. 2005.

[24] S. P. Usher, R. Spehar, and P. J. Scales, “Theoretical analysis of aggregate densification: Impact on thickener performance,” *Chem. Eng. J.*, vol. 151, no. 1–3, pp. 202–208, Aug. 2009.

[25] R. Spehar, A. Kiviti-Manor, P. Fawell, S. P. Usher, M. Rudman, and P. J. Scales, “Aggregate densification in the thickening of flocculated suspensions in an un-networked bed,” *Chem. Eng. Sci.*, vol. 122, pp. 585–595, Jan. 2015.

[26] P. Grassia, Y. Zhang, A. D. Martin, S. P. Usher, P. J. Scales, A. H. Crust, and R. Spehar, “Effects of aggregate densification upon thickening of Kynchian suspensions,” *Chem. Eng. Sci.*, vol. 111, pp. 56–72, May 2014.

[27] P. J. Scales, A. Kumar, B. B. G. van Deventer, A. D. Stickland, and S. P. Usher, “Compressional dewatering of flocculated mineral suspensions,” *Can. J. Chem. Eng.*, vol. 93, no. 3, pp. 549–552, Nov. 2014.

[28] A. R. Heath and P. T. L. Koh, “Combined Population Balance and CFD Modelling of Particle Aggregation by Polymeric Flocculant,” in *Third International Conference on CFD in the Minerals and Process Industries*, 2003, pp. 339–344.

[29] P. Garrido, R. Bürger, and F. Concha, “Settling velocities of particulate systems: 11. Comparison of the phenomenological sedimentation–consolidation model with published experimental results,” *Int. J. Miner. Process.*, vol. 60, no. 3–4, pp. 213–227, Dec. 2000.

[30] F. A. Benn, P. D. Fawell, J. Halewood, P. J. Austin, A. D. Costine, W. G. Jones, N. S. Francis, D. C. Druett, and D. Lester, “Sedimentation and consolidation

of different density aggregates formed by polymer-bridging flocculation," *Chem. Eng. Sci.*, vol. 184, no. 20, pp. 111–125, Jul. 2018.

[31] C. Sahin, R. Verney, A. Sheremet, and G. Voulgaris, "Acoustic backscatter by suspended cohesive sediments: Field observations, Seine Estuary, France," *Cont. Shelf Res.*, vol. 134, pp. 39–51, Feb. 2017.

[32] P. A. Vanrolleghem, B. D. Clercq, J. D. Clercq, M. Devisscher, D. J. Kinnear, and I. Nopens, "New measurement techniques for secondary settlers: A review," *Water Sci. Technol.*, vol. 53, no. 4–5, pp. 419–429, 2006.

[33] P. D. Thorne and D. M. Hanes, "A review of acoustic measurement of small-scale sediment processes," *Cont. Shelf Res.*, vol. 22, no. 4, pp. 603–632, Mar. 2002.

[34] K. L. Deines, "Backscatter estimation using Broadband acoustic Doppler current profilers," in *Proceedings of the IEEE Sixth Working Conference on Current Measurement (Cat. No.99CH36331)*, 1999, pp. 249–253.

[35] D. C. Fugate and C. T. Friedrichs, "Determining concentration and fall velocity of estuarine particle populations using ADV, OBS and LISST," *Cont. Shelf Res.*, vol. 22, no. 11–13, pp. 1867–1886, Jul. 2002.

[36] P. R. Smith, D. M. J. Cowell, B. Raiton, C. V. Ky, and S. Freear, "Ultrasound array transmitter architecture with high timing resolution using embedded phase-locked loops," *IEEE Trans. Ultrason. Ferroelectr. Freq. Control*, vol. 59, no. 1, pp. 40–49, 2012.

[37] D. M. J. Cowell, P. R. Smith, and S. Freear, "Phase-inversion-based selective harmonic elimination (PI-SHE) in multi-level switched-mode tone-and frequency-modulated excitation," *IEEE Trans. Ultrason. Ferroelectr. Freq. Control*, vol. 60, no. 6, pp. 1084–1097, 2013.

[38] T. N. Hunter, D. M. J. Cowell, T. Carpenter, S. Freear, J. Peakall, H. P. Rice, A. Tonge, M. Fairweather, and M. Barnes, "Large-scale trials of a real-time acoustic backscatter system for solids concentration measurement during nuclear waste cleanup," in *IEEE International Ultrasonics Symposium, IUS*, 2016.

[39] D. Eisma, *Suspended Matter in the Aquatic Environment*. Berlin: Springer-Verlag Berlin Heidelberg, 1993.

[40] S. N. Liss, I. G. Droppo, D. T. Flannigan, and G. G. Leppard, "Floc Architecture in Wastewater and Natural Riverine Systems," *Environ. Sci. Technol.*, vol. 30, no. 2, pp. 680–686, Jan. 1996.

[41] K. . Hildred, P. . Townson, G. . Hutson, and R. . Williams, “Characterisation of particulates in the BNFL Enhanced Actinide Removal Plant,” *Powder Technol.*, vol. 108, no. 2–3, pp. 164–172, Mar. 2000.

[42] S. Kumar, S. Bhattacharya, and N. R. Mandre, “Characterization and flocculation studies of fine coal tailings,” *J. South. African Inst. Min. Metall.*, vol. 114, no. 11, 2014.

[43] R. Holmstad, “Methods for Paper Structure Characterisation by Means of Image Analysis,” Norweigian University of Science and Technology, Trondheim, 2004.

[44] F. Xiao, K. M. Lam, X. Y. Li, R. S. Zhong, and X. H. Zhang, “PIV characterisation of flocculation dynamics and floc structure in water treatment,” *Colloids Surfaces A Physicochem. Eng. Asp.*, vol. 379, no. 1–3, pp. 27–35, Apr. 2011.

[45] W. Qasim and A. V. Mane, “Characterization and treatment of selected food industrial effluents by coagulation and adsorption techniques,” *Water Resour. Ind.*, vol. 4, pp. 1–12, Dec. 2013.

[46] R. Weser, S. Wöckel, B. Wessely, and U. Hempel, “Particle characterisation in highly concentrated dispersions using ultrasonic backscattering method,” *Ultrasonics*, vol. 53, no. 3, pp. 706–716, 2013.

[47] P. D. Thorne, I. T. MacDonald, and C. E. Vincent, “Modelling acoustic scattering by suspended flocculating sediments,” *Cont. Shelf Res.*, vol. 88, pp. 81–91, Oct. 2014.

[48] P. D. Thorne and R. Meral, “Formulations for the scattering properties of suspended sandy sediments for use in the application of acoustics to sediment transport processes,” *Cont. Shelf Res.*, vol. 28, no. 2, pp. 309–317, Feb. 2008.

[49] D. Carlisle and K. Adamson, “Fuel Pond Sludge –- Lessons Learned from Initial Desludging of Sellafield’s Pile Fuel Storage Pond,” in *WM2012 Conference*, 2012.

[50] T. Calvin, “Decommissioning Sellafield’s First Fuel Storage Pond,” *WM2011 Conf.*, 2011.

[51] J. Bratby, “Coagulation and Flocculation in Water and Wastewater Treatment,” *Water Intell. Online*, 2016.

[52] R. Divakaran and V. . Sivasankara Pillai, “Flocculation of kaolinite suspensions in water by chitosan,” *Water Res.*, vol. 35, no. 16, pp. 3904–3908, Nov. 2001.

[53] M. S. Nasser and A. E. James, “The effect of polyacrylamide charge density and molecular weight on the flocculation and sedimentation behaviour of kaolinite suspensions,” *Sep. Purif. Technol.*, vol. 52, no. 2, pp. 241–252, Dec. 2006.

[54] A. L. Ahmad, S. Ismail, and S. Bhatia, “Optimization of coagulation-flocculation process for palm oil mill effluent using response surface methodology,” *Environ. Sci. Technol.*, vol. 39, no. 8, pp. 2828–2834, 2005.

[55] F. Renault, B. Sancey, J. Charles, N. Morin-Crini, P.-M. Badot, P. Winterton, and G. Crini, “Chitosan flocculation of cardboard-mill secondary biological wastewater,” *Chem. Eng. J.*, vol. 155, no. 3, pp. 775–783, Dec. 2009.

[56] A. A. Tatsi, A. I. Zouboulis, K. A. Matis, and P. Samaras, “Coagulation–flocculation pretreatment of sanitary landfill leachates,” *Chemosphere*, vol. 53, no. 7, pp. 737–744, Nov. 2003.

[57] S. S. Wong, T. T. Teng, A. L. Ahmad, A. Zuhairi, and G. Najafpour, “Treatment of pulp and paper mill wastewater by polyacrylamide (PAM) in polymer induced flocculation,” *J. Hazard. Mater.*, vol. 135, no. 1–3, pp. 378–388, Jul. 2006.

[58] Q. Y. Yue, B. Y. Gao, Y. Wang, H. Zhang, X. Sun, S. G. Wang, and R. R. Gu, “Synthesis of polyamine flocculants and their potential use in treating dye wastewater,” *J. Hazard. Mater.*, vol. 152, no. 1, pp. 221–227, Mar. 2008.

[59] J. Zhong, X. Sun, and C. Wang, “Treatment of oily wastewater produced from refinery processes using flocculation and ceramic membrane filtration,” *Sep. Purif. Technol.*, vol. 32, no. 1–3, pp. 93–98, Jul. 2003.

[60] H. WANG, X. MIN, L. CHAI, and Y. SHU, “Biological preparation and application of poly-ferric sulfate flocculant,” *Trans. Nonferrous Met. Soc. China*, vol. 21, no. 11, pp. 2542–2547, Nov. 2011.

[61] B. Derjaguin and L. Landau, “Theory of the stability of strongly charged lyophobic sols and of the adhesion of strongly charged particles in solutions of electrolytes,” *Prog. Surf. Sci.*, vol. 43, no. 1–4, pp. 30–59, May 1993.

[62] M. Liu, J. Lu, L. Wei, K. Wang, and J. Zhao, “Magnesium hydroxide coagulation performance and floc properties in treating high pH reactive orange wastewater.,” *Water Sci. Technol.*, vol. 71, no. 9, pp. 1310–1316, 2015.

[63] M. A. A. Razali, Z. Ahmad, M. S. B. Ahmad, and A. Ariffin, “Treatment of pulp and paper mill wastewater with various molecular weight of polyDADMAC induced flocculation,” *Chem. Eng. J.*, vol. 166, no. 2, pp. 529–535, Jan. 2011.

[64] O. J. Rojas, M. Ernstsson, R. D. Neuman, and P. M. Claesson, “Effect of Polyelectrolyte Charge Density on the Adsorption and Desorption Behavior on Mica,” *Langmuir*, vol. 18, no. 5, pp. 1604–1612, Mar. 2002.

[65] R. P. Singh, G. P. Karmakar, S. K. Rath, N. C. Karmakar, S. R. Pandey, T. Tripathy, J. Panda, K. Kanan, S. K. Jain, and N. T. Lan, “Biodegradable drag reducing agents and flocculants based on polysaccharides: Materials and applications,” *Polym. Eng. Sci.*, vol. 40, no. 1, pp. 46–60, Jan. 2000.

[66] B. Dobias and H. Stechemesser, Coagulation and Flocculation, Second Edition. 2005.

[67] C. S. Lee, J. Robinson, and M. F. Chong, “A review on application of flocculants in wastewater treatment,” *Process Safety and Environmental Protection*, vol. 92, no. 6. 2014.

[68] O. Petric, Nedjeljka, Martinac, Vanja, Labor, Miroslav, Jurin, “Effect of 818A and 827N flocculants on seawater magnesia process,” *Metals of alloy technology*, vol. 33, no. 6, Inštitut za kovinske materiale in tehnologije, pp. 473–478, 1999.

[69] L. Wågberg and I. Åsell, “The action of cationic polymers in the fixation of dissolved and colloidal substances Part 2,” *Colloids Surfaces A Physicochem. Eng. Asp.*, vol. 104, no. 2–3, pp. 169–184, Nov. 1995.

[70] E. G. M. Pelssers, M. A. C. Stuart, and G. J. Fleer, “Kinetic aspects of polymer bridging: Equilibrium flocculation and nonequilibrium flocculation,” *Colloids and Surfaces*, vol. 38, pp. 15–25, 1989.

[71] Y. Zhou and G. V Franks, “Flocculation Mechanism Induced by Cationic Polymers Investigated by Light Scattering,” *Langmuir*, vol. 22, no. 16, pp. 6775–6786, Aug. 2006.

[72] M. F. Chong, “Advances in Water Treatment and Pollution Prevention,” in *Direct Flocculation Process for Wastewater Treatment BT*, S. K. Sharma and R. Sanghi, Eds. Dordrecht: Springer Netherlands, 2012, pp. 201–230.

[73] T. Suopajärvi, H. Liimatainen, O. Hormi, and J. Niinimäki, “Coagulation–flocculation treatment of municipal wastewater based on anionized nanocelluloses,” *Chem. Eng. J.*, vol. 231, pp. 59–67, Sep. 2013.

[74] K. E. Lee, N. Morad, T. T. Teng, and B. T. Poh, “Development, characterization and the application of hybrid materials in coagulation/flocculation of wastewater: A review,” *Chem. Eng. J.*, vol. 203, pp. 370–386, Sep. 2012.

[75] M. T. Radoiu, D. I. Martin, I. Calinescu, and H. Iovu, “Preparation of polyelectrolytes for wastewater treatment,” *J. Hazard. Mater.*, vol. 106, no. 1, pp. 27–37, Jan. 2004.

[76] O. S. Amuda, I. A. Amoo, and O. O. Ajayi, “Performance optimization of coagulant/flocculant in the treatment of wastewater from a beverage industry.,” *J. Hazard. Mater.*, vol. 129, no. 1–3, pp. 69–72, Feb. 2006.

[77] A. Ginos, T. Manios, and D. Mantzavinos, “Treatment of olive mill effluents by coagulation–flocculation–hydrogen peroxide oxidation and effect on phytotoxicity,” *J. Hazard. Mater.*, vol. 133, no. 1–3, pp. 135–142, May 2006.

[78] R. Sarika, N. Kalogerakis, and D. Mantzavinos, “Treatment of olive mill effluents: Part II. Complete removal of solids by direct flocculation with poly-electrolytes,” *Environ. Int.*, vol. 31, no. 2, pp. 297–304, Feb. 2005.

[79] J. M. Ebeling, K. L. Rishel, and P. L. Sibrell, “Screening and evaluation of polymers as flocculation aids for the treatment of aquacultural effluents,” *Aquac. Eng.*, vol. 33, no. 4, pp. 235–249, Oct. 2005.

[80] E. Sabah and Z. E. Erkan, “Interaction mechanism of flocculants with coal waste slurry,” *Fuel*, vol. 85, no. 3, pp. 350–359, Feb. 2006.

[81] Q. Kang, B. Gao, Q. Yue, W. Zhou, and D. Shen, “Residual color profiles of reactive dyes mixture during a chemical flocculation process,” *Colloids Surfaces A Physicochem. Eng. Asp.*, vol. 299, no. 1–3, pp. 45–53, May 2007.

[82] B. Bolto and J. Gregory, “Organic polyelectrolytes in water treatment,” *Water Research*. 2007.

[83] F. Renault, B. Sancey, P.-M. Badot, and G. Crini, “Chitosan for coagulation/flocculation processes – An eco-friendly approach,” *Eur. Polym. J.*, vol. 45, no. 5, pp. 1337–1348, May 2009.

[84] K. E. Lee, N. Morad, T. T. Teng, and B. T. Poh, “Development, characterization and the application of hybrid materials in coagulation/flocculation of wastewater: A review,” *Chem. Eng. J.*, vol. 203, pp. 370–386, Sep. 2012.

[85] J. Kleimann, C. Gehin-Delval, H. Auweter, and M. Borkovec, “Super-Stoichiometric Charge Neutralization in Particle−Polyelectrolyte Systems,” *Langmuir*, vol. 21, no. 8, pp. 3688–3698, Apr. 2005.

[86] J. A. Caskey and R. J. Primus, “The effect of anionic polyacrylamide molecular conformation and configuration on flocculation effectiveness,” *Environ. Prog.*, vol. 5, no. 2, pp. 98–103, May 1986.

[87] S. Biggs, M. Habgood, G. J. Jameson, and Y. De Yan, “Aggregate structures formed via a bridging flocculation mechanism,” *Chem. Eng. J.*, vol. 80, no. 1–3, pp. 13–22, 2000.

[88] A. Blanco, C. Negro, and J. Tijero, “Flocculation monitoring: focused beam reflectance measurement as a measurement tool,” *Can. J.*, vol. 80, no. 4, pp. 1–7, 2002.

[89] F. Sher, A. Malik, and H. Liu, “Industrial polymer effluent treatment by chemical coagulation and flocculation,” *J. Environ. Chem. Eng.*, vol. 1, no. 4, pp. 684–689, Dec. 2013.

[90] B. R. Sharma, N. C. Dhuldhoya, and U. C. Merchant, *Flocculants—an Ecofriendly Approach*, vol. 14, no. 2. 2006.

[91] L. Eriksson, B. Alm, and P. Stenius, “Formation and structure of polystyrene latex aggregates obtained by flocculation with cationic polyelectrolytes: 1. Adsorption and optimum flocculation concentrations,” *Colloids Surfaces A Physicochem. Eng. Asp.*, vol. 70, no. 1, pp. 47–60, Jan. 1993.

[92] H. Ohshima, “The Derjaguin–Landau–Verwey–Overbeek (DLVO) Theory of Colloid Stability,” *Electrical Phenomena at Interfaces and Biointerfaces*. pp. 27–34, 09-Mar-2012.

[93] D. C. Sobeck and M. J. Higgins, “Examination of three theories for mechanisms of cation-induced bioflocculation,” *Water Res.*, vol. 36, no. 3, pp. 527–538, Feb. 2002.

[94] A. R. Heath, P. A. Bahri, P. D. Fawell, and J. B. Farrow, “Polymer flocculation of calcite: Experimental results from turbulent pipe flow,” *AIChE J.*, vol. 52, no. 4, pp. 1284–1293, 2006.

[95] R. A. Williams, *Colloid and surface engineering : applications in the process industries*. Oxford [England]; Boston: Butterworth-Heinemann, 1992.

[96] G. B. J. Boer, de, G. F. M. Hoedemakers, and D. Thoenes, “Coagulation in turbulent flow. Part I,” *Chem. Eng. Res. Des.*, vol. 67, no. 3, pp. 301–307, 1989.

[97] P. Y. Burban, W. Lick, and J. Lick, “The flocculation of fine-grained sediments in estuarine waters,” *J. Geophys. Res.*, vol. 94, no. C6, pp. 8323–8330, 1989.

[98] R. Ham and R. Christman, “Agglomerate Size Changes in Coagulation.,” *J. Sanit. Eng. Div.*, vol. 95, no. 3, pp. 481–502, 1969.

[99] M. Elimelech, J. Gregory, X. Jia, and R. A. Williams, Particle deposition and aggregation: measurement, modelling and simulation. 1998.

[100] J. Gregory, “Polymer adsorption and flocculation in sheared suspensions,” *Colloids and Surfaces*, 1988.

[101] D. G. Thomas, “Turbulent disruption of flocs in small particle size suspensions,” *AIChE J.*, vol. 10, no. 4, pp. 517–523, Jul. 1964.

[102] D. Boer, de, G. B. J., Hoedemakers, G. F. M., Thoenes, “Coagulation in turbulent flow. Part II.,” *Chem. Eng. Res. Des.*, vol. 67, pp. 308–315, 1989.

[103] A. Blanco, C. Negro, E. Fuente, and J. Tijero, “Effect of shearing forces and flocculant overdose on filler flocculation mechanisms and floc properties,” *Ind. Eng. Chem. Res.*, vol. 44, no. 24, pp. 9105–9112, 2005.

[104] M. G. Rasteiro, F. A. P. Garcia, P. Ferreira, A. Blanco, C. Negro, and E. Antunes, “Evaluation of flocs resistance and reflocculation capacity using the LDS technique,” *Powder Technol.*, vol. 183, no. 2, pp. 231–238, Apr. 2008.

[105] M. Hartmann, “Light scattering by small particles. Von H. C. VANDE HULST. New York: Dover Publications, Inc. 1981. Paperback, 470 S., 103 Abb. und 46 Tab.,” *Acta Polym.*, vol. 35, no. 4, p. 338, Apr. 1984.

[106] T. . Sutherland, P. . Lane, C. . Amos, and J. Downing, “The calibration of optical backscatter sensors for suspended sediment of varying darkness levels,” *Mar. Geol.*, vol. 162, no. 2–4, pp. 587–597, Jan. 2000.

[107] J. Sullivan, M. Twardowski, J. R. V Zaneveld, and C. Moore, “Measuring optical backscattering in water,” *Light Scatt. Rev. 7*, pp. 189–224, Aug. 2013.

[108] R. W. Spinrad, J. R. V Zaneveld, and H. Pak, “Volume scattering function of suspended particulate matter at near-forward angles: a comparison of experimental and theoretical values,” *Appl. Opt.*, vol. 17, no. 7, pp. 1125–1130, 1978.

[109] J. P.-Y. Maa, J. Xu, and M. Victor, “Notes on the performance of an optical backscatter sensor for cohesive sediments,” *Mar. Geol.*, vol. 104, no. 1–4, pp. 215–218, Feb. 1992.

[110] D. Greaves, J. Boxall, J. Mulligan, A. Montesi, J. Creek, E. Dendy Sloan, and C. A. Koh, “Measuring the particle size of a known distribution using the focused beam reflectance measurement technique,” *Chem. Eng. Sci.*, vol. 63, no. 22, pp. 5410–5419, Nov. 2008.

[111] M. MacIver, “In Situ Mineral Sediment Characterization with Light Scattering and Image Analysis,” 2007.

[112] M. Li and D. Wilkinson, “Determination of non-spherical particle size distribution from chord length measurements. Part 1: Theoretical analysis,” *Chem. Eng. Sci.*, vol. 60, no. 12, pp. 3251–3265, Jun. 2005.

[113] K. Vay, W. Frieß, and S. Scheler, “Understanding reflection behavior as a key for interpreting complex signals in FBRM monitoring of microparticle preparation processes,” *Int. J. Pharm.*, vol. 437, no. 1–2, pp. 1–10, Nov. 2012.

[114] M. Li, D. Wilkinson, and K. Patchigolla, “Comparison of Particle Size Distributions Measured Using Different Techniques,” *Part. Sci. Technol.*, vol. 23, no. 3, pp. 265–284, Jul. 2005.

[115] R. G. Sparks and C. L. Dobbs, “The Use of Laser Backscatter Instrumentation for the on-line measurement of the particle size distribution of emulsions,” *Part. Part. Syst. Charact.*, vol. 10, no. 5, pp. 279–289, Nov. 1993.

[116] A. Tadayyon and S. Rohani, “Determination of Particle Size Distribution by Par-Tec® 100: Modeling and Experimental Results,” *Part. Part. Syst. Charact.*, vol. 15, no. 3, pp. 127–135, Jun. 1998.

[117] M. Li, D. Wilkinson, and K. Patchigolla, “Determination of non-spherical particle size distribution from chord length measurements. Part 2: Experimental validation,” *Chem. Eng. Sci.*, vol. 60, no. 18, pp. 4992–5003, Sep. 2005.

[118] M. C. Johnson, “Gas retention and release from nuclear legacy waste,” University of Leeds, 2018.

[119] O. S. Agimelen, A. Jawor-Baczynska, J. McGinty, J. Dziewierz, C. Tachtatzis, A. Cleary, I. Haley, C. Michie, I. Andonovic, J. Sefcik, and A. J. Mulholland, “Integration of in situ imaging and chord length distribution measurements for estimation of particle size and shape,” *Chem. Eng. Sci.*, vol. 144, pp. 87–100, Apr. 2016.

[120] C. E. Vincent and I. T. MacDonald, “A flocculi model for the acoustic scattering from flocs,” *Cont. Shelf Res.*, vol. 104, pp. 15–24, Aug. 2015.

[121] O. A. Mikkelsen, P. S. Hill, T. G. Milligan, and R. J. Chant, “In situ particle size distributions and volume concentrations from a LISST-100 laser particle sizer and a digital floc camera,” *Cont. Shelf Res.*, vol. 25, no. 16, pp. 1959–1978, Oct. 2005.

[122] P. S. Hill, J. P. Newgard, B. A. Law, and T. G. Milligan, “Flocculation on a muddy intertidal flat in Willapa Bay, Washington, Part II: Observations of suspended particle size in a secondary channel and adjacent flat,” *Cont. Shelf Res.*, vol. 60, pp. S145–S156, Jun. 2013.

[123] P. Meakin, “Fractal aggregates,” *Adv. Colloid Interface Sci.*, vol. 28, pp. 249–331, Jan. 1987.

[124] R. Jullien, “Aggregation phenomena and fractal aggregates,” *Contemp. Phys.*, vol. 28, no. 5, pp. 477–493, Sep. 1987.

[125] R. Amal, J. A. Raper, and T. D. Waite, “Fractal structure of hematite aggregates,” *J. Colloid Interface Sci.*, vol. 140, no. 1, pp. 158–168, Nov. 1990.

[126] A. F. Grabsch, P. D. Fawell, S. J. Adkins, and A. Beveridge, “The impact of achieving a higher aggregate density on polymer-bridging flocculation,” *Int. J. Miner. Process.*, vol. 124, pp. 83–94, Nov. 2013.

[127] A. R. Heath, P. A. Bahri, P. D. Fawell, and J. B. Farrow, “Polymer flocculation of calcite: Relating the aggregate size to the settling rate,” *AIChE J.*, vol. 52, no. 6, pp. 1987–1994, 2006.

[128] P. T. Spicer, W. Keller, and S. E. Pratsinis, “The Effect of Impeller Type on Floc Size and Structure during Shear-Induced Flocculation,” *J. Colloid Interface Sci.*, vol. 184, no. 1, pp. 112–122, Dec. 1996.

[129] O. A. Mikkelsen and M. Pejrup, “The use of a LISST-100 laser particle sizer for in-situ estimates of floc size, density and settling velocity,” *Geo-Marine Lett.*, vol. 20, no. 4, pp. 187–195, 2001.

[130] I. Sequoia Scientific, “Working limits of particle concentrations,” *Sequoia Scientific, Inc. Library*, 2018. [Online]. Available: https://www.sequoiasci.com/article/working-limits-particle-concentrations/. [Accessed: 23-Aug-2019].

[131] M. Li, D. Wilkinson, and K. Patchigolla, “Obtaining particle size distribution from chord length measurements,” *Part. Part. Syst. Charact.*, vol. 23, no. 2, pp. 170–74, 2006.

[132] Y. Kyoda, A. D. Costine, P. D. Fawell, J. Bellwood, and G. K. Das, “Using focused beam reflectance measurement (FBRM) to monitor aggregate structures formed in flocculated clay suspensions,” *Miner. Eng.*, vol. 138, pp. 148–160, Jul. 2019.

[133] S. of S. for T. and Industry, “Managing the Nuclear Legacy: A Strategy for Action,” London, 2002.

[134] M. Johnson, J. Peakall, M. Fairweather, S. Biggs, D. Harbottle, and T. N. Hunter, “Characterization of Multiple Hindered Settling Regimes in Aggregated Mineral Suspensions,” *Ind. Eng. Chem. Res.*, vol. 55, no. 37, pp. 9983–9993, 2016.

[135] J. A. Bamberger, H. K. Kytömaa, and M. S. Greenwood, “Slurry Ultrasonic Particle Size and Concentration Characterization BT - Science and Technology for Disposal of Radioactive Tank Wastes,” W. W. Schulz and N. J. Lombardo, Eds. Boston, MA: Springer US, 1998, pp. 485–495.

[136] A. Shukla, A. Prakash, and S. Rohani, “Particle size monitoring in dense suspension using ultrasound with an improved model accounting for low-angle scattering,” *AIChE J.*, vol. 56, no. 11, pp. 2825–2837, Nov. 2010.

[137] C. C. Sung, Y. J. Huang, J. S. Lai, and G. W. Hwang, “Ultrasonic measurement of suspended sediment concentrations: an experimental validation of the approach using kaolin suspensions and reservoir sediments under variable thermal conditions,” *Hydrol. Process.*, vol. 22, no. 16, pp. 3149–3154, Jul. 2008.

[138] J. Carlson and P.-E. Martinsson, “A simple scattering model for measuring particle mass fractions in multiphase flows,” *Ultrasonics*, vol. 39, no. 8, pp. 585–590, Jun. 2002.

[139] A. K. Hipp, G. Storti, and M. Morbidelli, “Acoustic characterization of concentrated suspensions and emulsions. 2. Experimental validation,” *Langmuir*, vol. 18, no. 2, pp. 405–412, Jan. 2002.

[140] M. Tourbin and C. Frances, “A survey of complementary methods for the characterization of dense colloidal silica,” *Part. Part. Syst. Charact.*, vol. 24, no. 6, pp. 411–423, Dec. 2007.

[141] V. Stolojanu and A. Prakash, “Characterization of slurry systems by ultrasonic techniques,” *Chem. Eng. J.*, vol. 84, no. 3, pp. 215–222, Dec. 2001.

[142] J. R. Pellam and J. K. Galt, “Ultrasonic propagation in liquids: I. Application of pulse technique to velocity and absorption measurements at 15 megacycles,” *J. Chem. Phys.*, vol. 14, no. 10, pp. 608–614, Oct. 1946.

[143] R. J. Urick, “The absorption of sound in suspensions of irregular particles,” *J. Acoust. Soc. Am.*, vol. 20, no. 3, pp. 283–289, 1948.

[144] P. S. Epstein and R. R. Carhart, “The Absorption of Sound in Suspensions and Emulsions. I. Water Fog in Air,” *J. Acoust. Soc. Am.*, vol. 25, no. 3, pp. 553–565, 1953.

[145] R. Hickling, “Analysis of Echoes from a Solid Elastic Sphere in Water,” *J. Acoust. Soc. Am.*, vol. 34, no. 10, pp. 1582–1592, Oct. 1962.

[146] J. R. Allegra and S. A. Hawley, “Attenuation of Sound in Suspensions and Emulsions: Theory and Experiments,” *J. Acoust. Soc. Am.*, vol. 51, no. 5B, pp. 1545–1564, 1972.

[147] A. E. Hay and G. Mercer, “On the theory of sound scattering and viscous absorption in aqueous suspensions at medium and short wavelengths,” *J. Acoust. Soc. Am.*, vol. 78, no. 5, pp. 1761–1771, 1985.

[148] J. Sheng and A. E. Hay, “An examination of the spherical scatterer approximation in aqueous suspensions of sand,” *J. Acoust. Soc. Am.*, vol. 83, no. 2, pp. 598–610, Feb. 1988.

[149] C. M. Atkinson and H. K. Kytömaa, “Acoustic wave speed and attenuation in suspensions,” *Int. J. Multiph. Flow*, vol. 18, no. 4, pp. 577–592, 1992.

[150] C. M. Atkinson and H. K. Kytömaa, “Acoustic properties of solid-liquid mixtures and the limits of ultrasound diagnostics—I: Experiments (data bank contribution),” *J. Fluids Eng.*, vol. 115, no. 4, pp. 665–675, Dec. 1993.

[151] A. S. Dukhin and P. J. Goetz, “New developments in acoustic and electroacoustic spectroscopy for characterizing concentrated dispersions,” *Colloids Surfaces A Physicochem. Eng. Asp.*, vol. 192, no. 1–3, pp. 267–306, Nov. 2001.

[152] P. D. Thorne, L. Hayhurst, and V. F. Humphrey, “Scattering by non-metallic spheres,” *Ultrasonics*, vol. 30, no. 1, pp. 15–20, Jan. 1992.

[153] P. D. Thorne, P. J. Hardcastle, and R. L. Soulsby, “Analysis of acoustic measurements of suspended sediments,” *J. Geophys. Res.*, vol. 98, no. C1, pp. 899–910, Jan. 1993.

[154] L. D. Hampton and C. M. McKinney, “Experimental Study of the Scattering of Acoustic Energy from Solid Metal Spheres in Water,” *J. Acoust. Soc. Am.*, vol. 33, no. 5, pp. 664–673, May 1961.

[155] S. A. Moore, J. Le Coz, D. Hurther, and A. Paquier, “Using multi-frequency acoustic attenuation to monitor grain size and concentration of suspended sediment in rivers,” *J. Acoust. Soc. Am.*, vol. 133, no. 4, pp. 1959–1970, Apr. 2013.

[156] A. E. Hay, “Sound scattering from a particle-laden, turbulent jet,” *J. Acoust. Soc. Am.*, vol. 90, no. 4, pp. 2055–2074, Oct. 1991.

[157] P. Fleckenstein, G. Storti, F. Deschwanden, P. Gruber, and M. Lattuada, “Modeling analysis of ultrasonic attenuation and angular scattering measurements of suspended particles,” *J. Acoust. Soc. Am.*, vol. 143, no. 2, pp. 1049–1063, 2018.

[158] E. D. Thosteson and D. M. Hanes, “A simplified method for determining sediment size and concentration from multiple frequency acoustic backscatter measurements,” *J. Acoust. Soc. Am.*, vol. 104, no. 2, pp. 820–830, Aug. 1998.

[159] K. F. E. Betteridge, P. D. Thorne, and R. D. Cooke, “Calibrating multi-frequency acoustic backscatter systems for studying near-bed suspended sediment transport processes,” *Cont. Shelf Res.*, vol. 28, no. 2, pp. 227–235, Feb. 2008.

[160] T. N. Hunter, L. Darlison, J. Peakall, and S. Biggs, “Using a multi-frequency acoustic backscatter system as an in situ high concentration dispersion monitor,” *Chem. Eng. Sci.*, vol. 80, no. 1, pp. 409–418, Oct. 2012.

[161] M. Bricault, “Rétrodiffusion acoustique par une suspension en milieu turbulent: application à la mesure de concentration pour l’étude de processus hydrosédimentaires.,” Grenoble Institut National Polytechnique, 2006.

[162] A. M. Crawford and A. E. Hay, “Determining suspended sand size and concentration from multifrequency acoustic backscatter,” *J. Acoust. Soc. Am.*, vol. 94, no. 6, pp. 3312–3324, Dec. 1993.

[163] A. Downing, P. D. Thorne, and C. E. Vincent, “Backscattering from a suspension in the near field of a piston transducer,” *J. Acoust. Soc. Am.*, vol. 97, no. 3, pp. 1614–1620, 1995.

[164] T. H. Lee and D. M. Hanes, “Direct inversion method to measure the concentration profile of suspended particles using backscattered sound,” *J. Geophys. Res.*, vol. 100, no. C2, pp. 2649–2657, 1995.

[165] P. D. Thorne, S. Sun, J. Zhang, I. Bjorno, and T. Mazoyer, “Measurements and analysis of acoustic backscattering by elastic cubes and irregular polyhedra,” *J. Acoust. Soc. Am.*, vol. 102, no. 5, pp. 2705–2713, Nov. 1997.

[166] I. T. MacDonald, C. E. Vincent, P. D. Thorne, and B. D. Moate, “Acoustic scattering from a suspension of flocculated sediments,” *J. Geophys. Res. Ocean.*, vol. 118, no. 5, pp. 2581–2594, May 2013.

[167] P. D. Thorne, D. Hurther, and B. D. Moate, “Acoustic inversions for measuring boundary layer suspended sediment processes,” *J. Acoust. Soc. Am.*, vol. 130, no. 3, pp. 1188–1200, Sep. 2011.

[168] G. P. Holdaway and P. D. Thorne, “Determination of a fast and stable algorithm to evaluate suspended sediment parameters from high resolution acoustic backscatter systems,” in *Seventh International Conference on Electronic Engineering*

in Oceanography, 1997. "Technology Transfer from Research to Industry.," 1997, pp. 86–92.

[169] D. M. Admiraal, M. H. García, and J. F. Rodríguez, "Entrainment response of bed sediment to time-varying flows," *Water Resour. Res.*, vol. 36, no. 1, pp. 335–348, Jan. 2000.

[170] M. A. Ainslie and J. G. McColm, "A simplified formula for viscous and chemical absorption in sea water," *J. Acoust. Soc. Am.*, vol. 103, no. 3, pp. 1671–1672, 1998.

[171] H. Gaunard, G., Uberall, "RST analysis of monostatic and bistatic acoustic echoes from an elastic sphere," *J. Acoust. Soc. Am.*, vol. 73, no. 1, pp. 1–12, 1983.

[172] V. C. Anderson, "Sound Scattering from a Fluid Sphere," *J. Acoust. Soc. Am.*, vol. 22, no. 4, pp. 426–431, 1950.

[173] V. J. Pinfield, D. M. Forrester, and F. Luppé, "Ultrasound Propagation in Concentrated Suspensions: Shear-mediated Contributions to Multiple Scattering," *Phys. Procedia*, vol. 70, pp. 213–216, 2015.

[174] P. D. Thorne and M. J. Buckingham, "Measurements of scattering by suspensions of irregularly shaped sand particles and comparison with a single parameter modified sphere model," *J. Acoust. Soc. Am.*, vol. 116, no. 5, pp. 2876–2889, Nov. 2004.

[175] A. S. Schaafsma and A. E. Hay, "Attenuation in suspensions of irregularly shaped sediment particles: A two-parameter equivalent spherical scatterer model," *J. Acoust. Soc. Am.*, vol. 102, no. 3, pp. 1485–1502, Sep. 1997.

[176] C. He and A. E. Hay, "Broadband measurements of the acoustic backscatter cross section of sand particles in suspension," *J. Acoust. Soc. Am.*, vol. 94, no. 4, pp. 2247–54, Oct. 1993.

[177] P. D. Thorne, G. P. Holdaway, and P. J. Hardcastle, "Constraining acoustic backscatter estimates of suspended sediment concentration profiles using the bed echo," *J. Acoust. Soc. Am.*, vol. 98, no. 4, pp. 2280–2288, Oct. 1995.

[178] G. H. Flammer, "Ultrasonic Measurement of Suspended Sediment," *Geol. Surv. Bull.*, 1962.

[179] R. H. J. Jansen, "The in-situ measurement of sediment transport by means of ultrasound scattering. A Delft Hydraulics Laboratory Report.," Delft, 1978.

[180] A. S. Schaafsma and W. J. G. J. Der Kinderen, “Ultrasonic instruments for the continuous measurement of suspended sand transport.,” in *Measuring techniques in hydraulic research. Proc. IAHR symposium, Delft, 1985*, 1986, pp. 125–136.

[181] P. M. Morse and K. U. Ingard, *Theoretical Acosutics*. Princeton, New Jersey: Princeton University Press, 1986.

[182] A. E. Hay and J. Sheng, “Vertical profiles of suspended sand concentration and size from multifrequency acoustic backscatter,” *J. Geophys. Res.*, vol. 97, no. C10, p. 15661, 1992.

[183] A. S. Dukhin and P. J. Goetz, “Acoustic and electroacoustic spectroscopy for characterizing concentrated dispersions and emulsions,” *Advances in Colloid and Interface Science*. 2001.

[184] W. O. Carpenter, J. P. Chambers, D. G. Wren, R. A. Kuhnle, and J. A. Diers, “Acoustic measurements of clay-size particles,” *J. Acoust. Soc. Am.*, vol. 126, no. 6, pp. EL190-195, 2009.

[185] A. S. Dukhin and P. J. Goetz, “Acoustic and electroacoustic spectroscopy for characterizing concentrated dispersions and emulsions,” *Adv. Colloid Interface Sci.*, vol. 92, no. 1–3, pp. 73–132, Sep. 2001.

[186] R. Meral, “Laboratory Evaluation of Acoustic Backscatter and LISST Methods for Measurements of Suspended Sediments,” *Sensors (Basel).*, vol. 8, no. 2, pp. 979–993, Feb. 2008.

[187] H. K. Ha, W.-Y. Hsu, J. P.-Y. Maa, Y. Y. Shao, and C. W. Holland, “Using ADV backscatter strength for measuring suspended cohesive sediment concentration,” *Cont. Shelf Res.*, vol. 29, no. 10, pp. 1310–1316, May 2009.

[188] M. Salehi and K. Strom, “Using velocimeter signal to noise ratio as a surrogate measure of suspended mud concentration,” *Cont. Shelf Res.*, vol. 31, no. 9, pp. 1020–1032, Jun. 2011.

[189] T. N. Hunter, S. P. Usher, S. Biggs, P. J. Scales, A. D. Stickland, and G. V. Franks, “Characterization of bed densification in a laboratory scale thickener, by novel application of an acoustic backscatter system,” *Procedia Eng.*, vol. 102, pp. 858–866, Jan. 2015.

[190] M. Kosonen, S. Kauvosaari, S. Gao, and B. Henriksson, “Performance optimization of paste thickening,” in *Proceedings of the 20th International Seminar on Paste and Thickened Tailings*, 2017, pp. 13–22.

[191] J. . Swift, K. Simic, R. R. . Johnston, P. . Fawell, and J. . Farrow, “A study of the polymer flocculation reaction in a linear pipe with a focused beam reflectance measurement probe,” *Int. J. Miner. Process.*, vol. 73, no. 2–4, pp. 103–118, Feb. 2004.

[192] L. Y. L. Mo and R. S. C. Cobbold, “A Stochastic Model of the Backscattered Doppler Ultrasound from Blood,” *IEEE Trans. Biomed. Eng.*, vol. BME-33, no. 1, pp. 20–27, 1986.

[193] J. K. Percus and G. J. Yevick, “Analysis of Classical Statistical Mechanics by Means of Collective Coordinates,” *Phys. Rev.*, vol. 110, no. 1, pp. 1–13, 1958.

[194] J. J. Faran, “Sound Scattering by Solid Cylinders and Spheres,” *J. Acoust. Soc. Am.*, vol. 23, no. 4, pp. 405–418, Jul. 1951.

[195] M. E. Anderson, “Faran model solution.” IEEE - Ultrasonics, Ferroelectrics and Frequency Constrol society, 1999.

[196] D. J. McClements, “Comparison of multiple scattering theories with experimental measurements in emulsions,” *J. Acoust. Soc. Am.*, vol. 91, no. 2, pp. 849–853, Feb. 1992.

[197] D. J. McClements, N. Herrmann, and Y. Hemar, “Influence of flocculation on the ultrasonic properties of emulsions: theory,” *J. Phys. D. Appl. Phys.*, vol. 31, no. 20, pp. 2950–2955, 1998.

[198] J. C. Austin and R. E. Challis, “The Effects of Flocculation on the Propagation of Ultrasound in Dilute Kaolin Slurries,” *J. Colloid Interface Sci.*, vol. 206, no. 1, pp. 146–157, Oct. 1998.

[199] A. H. Harker and J. A. G. Temple, “Velocity and attenuation of ultrasound in suspensions of particles in fluids,” *J. Phys. D. Appl. Phys.*, vol. 21, no. 11, pp. 1576–1588, 1988.

[200] K. J. Curran, P. S. Hill, T. G. Milligan, O. A. Mikkelsen, B. A. Law, X. Durrieu de Madron, and F. Bourrin, “Settling velocity, effective density, and mass composition of suspended sediment in a coastal bottom boundary layer, Gulf of Lions, France,” *Cont. Shelf Res.*, vol. 27, no. 10–11, pp. 1408–1421, Jun. 2007.

[201] A. J. Manning, J. V. Baugh, R. L. Soulsby, J. R. Spearman, and R. J. S. Whitehouse, “Cohesive Sediment Flocculation and the Application to Settling Flux Modelling,” in *Sediment Transport*, S. S. Ginsberg, Ed. Rijeka: IntechOpen, 2011, p. Ch. 5.

[202] A. B. Wood, “A Textbook of Sound. Third Edition. Bell, London, 1955. 610 pp. Illustrated. 42s.,” *J. R. Aeronaut. Soc.*, 1957.

[203] R. K. Johnson, “Sound scattering from a fluid sphere revisited,” *J. Acoust. Soc. Am.*, vol. 61, no. 2, pp. 375–377, Feb. 1977.

[204] E. L. Hamilton and R. T. Bachman, “Sound velocity and related properties of marine sediments,” *J. Acoust. Soc. Am.*, vol. 72, no. 6, pp. 1891–1904, Dec. 1982.

[205] M. J. Buckingham, “Theory of acoustic attenuation, dispersion, and pulse propagation in unconsolidated granular materials including marine sediments,” *J. Acoust. Soc. Am.*, vol. 102, no. 5, pp. 2579–2596, Nov. 1997.

[206] H. Medwin and C. S. Clay, “Chapter 7 - Sound Scattered by a Body,” in *Applications of Modern Acoustics*, H. Medwin and C. S. B. T.-F. of A. O. Clay, Eds. San Diego: Academic Press, 1998, pp. 234–286.

[207] D. M. Forrester and V. J. Pinfield, “The absorption of ultrasound in emulsions: computational modelling of thermal effects,” *Sci. Rep.*, vol. 8, no. 1, p. 12486, Aug. 2018.

[208] T. T. More, J. S. S. Yadav, S. Yan, R. D. Tyagi, and R. Y. Surampalli, “Extracellular polymeric substances of bacteria and their potential environmental applications,” *J. Environ. Manage.*, vol. 144, pp. 1–25, Nov. 2014.

[209] R. Weser, S. Wöckel, U. Hempel, B. Wessely, and J. Auge, “Particle characterization in highly concentrated suspensions by ultrasound scattering method,” *Sensors Actuators, A Phys.*, vol. 202, pp. 30–36, 2013.

[210] P. D. Thorne and S. C. Campbell, “Backscattering by a suspension of spheres,” *J. Acoust. Soc. Am.*, vol. 92, no. 2, pp. 978–986, Aug. 1992.

[211] J.-Y. Kim, S.-Y. Hong, B.-G. Cho, J.-H. Song, and H.-W. Kwon, “Development of acoustic target strength near-field equation for underwater vehicles,” *Proc. Inst. Mech. Eng. Part M J. Eng. Marit. Environ.*, p. 1475090218779292, Jun. 2018.

[212] X. Zhan, Y. Yang, J. Liang, D. Zou, J. Zhang, L. Feng, T. Shi, and X. Li, “In-line mixing states monitoring of suspensions using ultrasonic reflection technique,” *Ultrasonics*, vol. 65, pp. 43–50, Feb. 2016.

[213] Y. Ma, V. K. Varadan, and V. V Varadan, “Application of Twersky’s multiple scattering formalism to a dense suspension of elastic particles in water,” *J. Acoust. Soc. Am.*, vol. 75, no. 2, pp. 335–339, Feb. 1984.

[214] V. Twersky, “Acoustic bulk parameters in distributions of pair-correlated scatterers,” *J. Acoust. Soc. Am.*, vol. 64, no. 6, pp. 1710–1719, Dec. 1978.

[215] J. M. Furlan, V. Mundla, J. Kadambi, N. Hoyt, R. Visintainer, and G. Addie, "Development of A-scan ultrasound technique for measuring local particle concentration in slurry flows," *Powder Technol.*, vol. 215–216, pp. 174–184, Jan. 2012.

[216] A. K. Hipp, G. Storti, and M. Morbidelli, "Acoustic characterization of concentrated suspensions and emulsions. 1. Model analysis," *Langmuir*, vol. 18, no. 2, pp. 391–404, Jan. 2002.

[217] L. Schwartz and T. J. Plona, "Ultrasonic propagation in close-packed disordered suspensions," *J. Appl. Phys.*, vol. 55, no. 11, pp. 3971–3977, Jun. 1984.

[218] M. Kimura, "Velocity dispersion and attenuation in granular marine sediments: Comparison of measurements with predictions using acoustic models," *J. Acoust. Soc. Am.*, vol. 129, no. 6, pp. 3544–3561, Jun. 2011.

[219] M. Kimura, "Frame bulk modulus of porous granular marine sediments," *J. Acoust. Soc. Am.*, vol. 120, no. 2, pp. 699–710, Aug. 2006.

[220] A. K. Hipp, G. Storti, and M. Morbidelli, "On multiple-particle effects in the acoustic characterization of colloidal dispersions," *J. Phys. D. Appl. Phys.*, vol. 32, no. 5, pp. 568–576, 1999.

[221] A. S. Dukhin and P. J. Goetz, "Chapter 4. Acoustic theory for particulates," in *Ultrasound for Characterizing Colloids*, vol. 15, A. S. Dukhin and P. J. B. T.-S. in I. S. Goetz, Eds. Elsevier, 2002, pp. 101–152.

[222] X. Jia, "Codalike multiple scattering of elastic waves in dense granular media," *Phys. Rev. Lett.*, vol. 93, no. 15, 154303, Oct. 2004.

[223] J. H. Page, H. P. Schriemer, A. E. Bailey, and D. A. Weitz, "Experimental test of the diffusion approximation for multiply scattered sound," *Phys. Rev. E*, pp. 3106–3114, 1995.

[224] B. D. Moate and P. D. Thorne, "Interpreting acoustic backscatter from suspended sediments of different and mixed mineralogical composition," *Cont. Shelf Res.*, vol. 46, pp. 67–82, Sep. 2012.

[225] G. W. Wilson and A. E. Hay, "Acoustic backscatter inversion for suspended sediment concentration and size: A new approach using statistical inverse theory," *Cont. Shelf Res.*, vol. 106, pp. 130–139, Sep. 2015.

[226] J. W. Gartner, "Estimating suspended solids concentrations from backscatter intensity measured by acoustic Doppler current profiler in San Francisco Bay, California," *Mar. Geol.*, vol. 211, no. 3–4, pp. 169–187, Oct. 2004.

[227] H. K. Ha, J. P.-Y. Maa, K. Park, and Y. H. Kim, “Estimation of high-resolution sediment concentration profiles in bottom boundary layer using pulse-coherent acoustic Doppler current profilers,” *Mar. Geol.*, vol. 279, no. 1–4, pp. 199–209, Jan. 2011.

[228] C. Sahin, I. Safak, T.-J. Hsu, and A. Sheremet, “Observations of suspended sediment stratification from acoustic backscatter in muddy environments,” *Mar. Geol.*, vol. 336, pp. 24–32, Feb. 2013.

[229] J. F. Lynch, J. D. Irish, C. R. Sherwood, and Y. C. Agrawal, “Determining suspended sediment particle size information from acoustical and optical backscatter measurements,” *Cont. Shelf Res.*, vol. 14, no. 10, pp. 1139–1165, 1994.

[230] Guyson International Limited, “Blast Media Data Sheet - Guyson Honite.” p. 1, 2019.

[231] D. M. J. Cowell, S. Freear, J. Peakall, I. Smith, H. P. Rice, T. N. Hunter, D. Njobuenwu, M. Fairweather, M. Barnes, and G. Randall, “Development of a real-time acoustic backscatter system for solids concentration measurement during nuclear waste cleanup,” in *2015 IEEE International Ultrasonics Symposium (IUS)*, 2015, pp. 1–4.

[232] D. M. J. Cowell, T. Carpenter, S. Freear, J. Peakall, H. P. Rice, A. Tonge, M. Fairweather, T. N. Hunter, and M. Barnes, “Large-scale trials of a real-time acoustic backscatter system for solids concentration measurement during nuclear waste cleanup,” in *IEEE International Ultrasonics Symposium, IUS*, 2016, vol. 2016-Novem.

[233] S. Freear, D. M. J. Cowell, and R. P. Smith, “Ultrasound generation,” US20150348531A1, 2013.

[234] A. Tonge, J. Bux, D. Cowell, J. Peakall, S. Freear, and T. Hunter, “Concentration profiling using a novel acoustic backscatter system with single transducers pulsed at multiple frequencies,” in *IEEE International Ultrasonics Symposium, IUS*, 2017.

[235] O. Chmiel, I. Baselt, and A. Malcherek, “Applicability of acoustic concentration measurements in suspensions of artificial and natural sediments using an acoustic doppler velocimeter,” *Acoustics*, vol. 1, no. 1. pp. 59–77, 2018.

[236] A. Tourin, M. Fink, and A. Derode, “Multiple scattering of sound,” *Waves in Random Media*, vol. 10, no. 4, pp. R31–R60, Oct. 2000.

[237] V. J. Pinfield and D. M. Forrester, “Multiple scattering in random dispersions of spherical scatterers: Effects of shear-acoustic interactions,” *J. Acoust. Soc. Am.*, vol. 141, no. 1, pp. 649–660, Jan. 2017.

[238] K. F. E. Betteridge, P. D. Thorne, and P. S. Bell, “Assessment of acoustic coherent Doppler and cross-correlation techniques for measuring near-bed velocity and suspended sediment profiles in the marine environment,” *J. Atmos. Ocean. Technol.*, vol. 19, no. 3, pp. 367–380, 2002.

[239] J. Gregory and D. W. Nelson, “Monitoring of aggregates in flowing suspensions,” *Colloids and Surfaces*, vol. 18, no. 2–4, pp. 175–188, Jun. 1986.

[240] R. S. Nyström, J. B. Rosenholm, and K. Nurmi, “Flocculation of Semidilute Calcite Dispersions Induced by Anionic Sodium Polyacrylate-Cationic Starch Complexes,” *Langmuir*, vol. 19, no. 9, pp. 3981–3986, 2003.

[241] B. Gladman, S. P. Usher, and P. J. Scales, “Compressive rheology of aggregated particulate suspensions,” *Korea Aust. Rheol. J.*, vol. 18, no. 4, pp. 190–197, 2006.

[242] O. . Mikkelsen and M. Pejrup, “In situ particle size spectra and density of particle aggregates in a dredging plume,” *Mar. Geol.*, vol. 170, no. 3–4, pp. 443–459, Nov. 2000.

[243] A. E. Sparr and V. Grippi, “Gravity Thickeners for Activated Sludge,” *J. (Water Pollut. Control Fed.*, vol. 41, no. 11, pp. 1886–1904, 1969.

[244] A. R. Heath, P. A. Bahri, P. D. Fawell, and J. B. Farrow, “Polymer flocculation of calcite: Population balance model,” *AIChE J.*, vol. 52, no. 5, pp. 1641–1653, 2006.

[245] UK Nuclear Decomissioning Authority, “UK Radioactive Waste Inventory,” London, 2016.

[246] D. Gregory and K. Carlson, “Relationship of pH and Floc Formation Kinetics to Granular Media Filtration Performance,” *Environ. Sci. Technol.*, vol. 37, no. 7, pp. 1398–1403, Apr. 2003.

[247] L. Chen, D.-H. Chen, and C.-L. Wu, “Studying flocculation mechanism of chitosan with pyrene-fluorescence probe method,” *Chinese J. Chem.*, vol. 21, no. 9, pp. 1224–1228, Sep. 2003.

[248] F. Nindiyasari, A. Ziegler, E. Griesshaber, L. Fernández-Díaz, J. Huber, P. Walther, and W. W. Schmahl, “Effect of Hydrogel Matrices on Calcite Crystal Growth Morphology, Aggregate Formation, and Co-Orientation in Biomimetic

Experiments and Biomineralization Environments," *Cryst. Growth Des.*, vol. 15, no. 6, pp. 2667–2685, Jun. 2015.

[249] T. Li, F. Sui, F. Li, Y. Cai, and Z. Jin, "Effects of dry grinding on the structure and granularity of calcite and its polymorphic transformation into aragonite," *Powder Technol.*, vol. 254, pp. 338–343, Mar. 2014.

[250] G. Rong, G. Liu, D. Hou, and C.-B. Zhou, "Effect of particle shape on mechanical behaviors of rocks: a numerical study using clumped particle model," *ScientificWorldJournal.*, vol. 2013, p. 589215, Jul. 2013.

[251] H. XU and X. DENG, "Preparation and properties of superfine Mg(OH)2 flame retardant," *Trans. Nonferrous Met. Soc. China*, vol. 16, no. 2, pp. 488–492, Apr. 2006.

[252] H. Khatoon, P. Solanki, M. Narayan, L. Tewari, J. Rai, and C. Hina Khatoon, "Role of microbes in organic carbon decomposition and maintenance of soil ecosystem," *Int. J. Chem. Stud.*, vol. 5, no. 6, pp. 1648–1656, 2017.

[253] C. Yu, S. Kamboj Argonne, IL, C. [Argonne N. L. (ANL) Wang Argonne, IL, and J.-J. [Argonne N. L. (ANL) Cheng Argonne, IL, "Data Collection Handbook to Support Modeling Impacts of Radioactive Material in Soil and Building Structures," United States, 2015.

[254] P. Robin, C. Morel, F. Vial, B. Landrain, A. Toudic, Y. Li, and N. Akkal-Corfini, "Effect of Three Types of Exogenous Organic Carbon on Soil Organic Matter and Physical Properties of a Sandy Technosol," *Sustainability* , vol. 10, no. 4. 2018.

[255] J. Rühlmann, M. Körschens, and J. Graefe, "A new approach to calculate the particle density of soils considering properties of the soil organic matter and the mineral matrix," *Geoderma*, vol. 130, no. 3–4, pp. 272–283, Feb. 2006.

[256] K. Verwer, H. Braaksma, and J. Kenter, "Acoustic properties of carbonates: Effects of rock texture and implications for fluid substitution," *Geophysics*, vol. 73, Mar. 2008.

[257] T. S. Duffy, T. J. Ahrens, and M. A. Lange, "The shock wave equation of state of brucite Mg(OH)2," *J. Geophys. Res. Solid Earth*, vol. 96, no. B9, pp. 14319–14330, Aug. 1991.

[258] M. L. Silver and J. A. Lineback, "Velocity of Sound in Sediments Cored from Southern Lake Michigan," Urabana, IL, 1972.

[259] T. N. Hunter, J. Peakall, and S. Biggs, “An acoustic backscatter system for in situ concentration profiling of settling flocculated dispersions,” *Miner. Eng.*, vol. 27–28, pp. 20–27, Feb. 2012.

[260] A. Senaputra, F. Jones, P. D. Fawell, and P. G. Smith, “Focused beam reflectance measurement for monitoring the extent and efficiency of flocculation in mineral systems,” *AIChE J.*, vol. 60, no. 1, pp. 251–265, Jan. 2014.

[261] T. Hayashi, H. Ohya, S. Suzuki, and S. Endoh, “Errors in Size Distribution Measurement of Concentrated Alumina Slurry by Ultrasonic Attenuation Spectroscopy.,” *J. Soc. Powder Technol. Japan*, vol. 37, pp. 498–504, Jan. 2000.

[262] A. R. Portune, “Nondestructive ultrasonic characterization of armor grade silicon carbide,” 2011.

[263] M. A. Inam and C. Frances, “Effects of impurities on particle sizing by acoustic attenuation spectroscopy,” *Powder Technol.*, vol. 201, no. 1, pp. 21–26, Jul. 2010.

[264] J. Bux, “Novel characterisation of concentrated dispersions by in situ acoustic backscatter systems,” University of Leeds, 2016.

[265] A. S. Dukhin, V. N. Shilov, H. Ohshima, and P. J. Goetz, “Electroacoustic Phenomena in Concentrated Dispersions: New Theory and CVI Experiment,” *Langmuir*, vol. 15, no. 20, pp. 6692–6706, Sep. 1999.

[266] B. D. Moate and P. D. Thorne, “Measurements and inversion of acoustic scattering from suspensions having broad size distributions,” *J. Acoust. Soc. Am.*, vol. 126, no. 6, pp. 2905–2917, Dec. 2009.

[267] F. Hoyle, Managing Soil Organic Matter: A Practical Guide. 2013.

[268] M. Rouhnia, A. Keyvani, and K. Strom, “Do changes in the size of mud flocs affect the acoustic backscatter values recorded by a Vector ADV?,” *Cont. Shelf Res.*, vol. 84, pp. 84–92, Aug. 2014.

[269] H. Kyung Ha, J. Maa, and C. W. Holland, Acoustic density measurements of consolidating cohesive sediment beds by means of a non-intrusive “Micro-Chirp” acoustic system, vol. 30. 2010.

[270] M. Guerrero, R. N. Szupiany, and F. Latosinski, “Multi-frequency acoustics for suspended sediment studies: an application in the Parana River,” *J. Hydraul. Res.*, vol. 51, no. 6, pp. 696–707, Dec. 2013.

[271] M. Guerin and J. C. Seaman, “Characterizing clay mineral suspensions using acoustic and electroacoustic spectroscopy - A review,” *Clays Clay Miner.*, vol. 52, no. 2, pp. 145–157, 2004.

[272] D. Haught, J. G. Venditti, and S. A. Wright, “Calculation of in situ acoustic sediment attenuation using off-the-shelf horizontal ADCPs in low concentration settings,” *Water Resour. Res.*, vol. 53, no. 6, pp. 5017–5037, Jun. 2017.

[273] L. M. Merckelbach, “A model for high-frequency acoustic Doppler current profiler backscatter from suspended sediment in strong currents,” *Cont. Shelf Res.*, vol. 26, no. 11, pp. 1316–1335, 2006.

[274] A. N. Kalashnikov and R. E. Challis, “Errors and uncertainties in the measurement of ultrasonic wave attenuation and phase velocity,” *IEEE Trans. Ultrason. Ferroelectr. Freq. Control*, vol. 52, no. 10, pp. 1754–1768, 2005.

[275] R. Bürger, S. Diehl, and I. Nopens, “A consistent modelling methodology for secondary settling tanks in wastewater treatment,” *Water Res.*, vol. 45, no. 6, pp. 2247–2260, Mar. 2011.

[276] A. R. Heath, P. D. Fawell, P. A. Bahri, and J. D. Swift, “Estimating average particle size by focused beam reflectance measurement (FBRM),” *Part. Part. Syst. Charact.*, vol. 19, no. 2, pp. 84–95, 2002.

[277] M. Smerdon, A. and M. Simmons, S., “Testing the Limits of a Multi-Frequency Acoustic Sediment Profiling Instrument,” in *3rd International Conference & Exhibition on “Underwater Acoustic Measurements: Technologies & Results,”* 2009, pp. 532–538.

[278] P. V Nelson, M. J. W. Povey, and Y. Wang, “An ultrasound velocity and attenuation scanner for viewing the temporal evolution of a dispersed phase in fluids,” *Rev. Sci. Instrum.*, vol. 72, no. 11, pp. 4234–4241, Oct. 2001.

[279] R. E. Challis and V. J. Pinfield, “Ultrasonic wave propagation in concentrated slurries – The modelling problem,” *Ultrasonics*, vol. 54, no. 7, pp. 1737–1744, Sep. 2014.

[280] R. Bürger and A. Narváez, “Steady-state, control, and capacity calculations for flocculated suspensions in clarifier–thickeners,” *Int. J. Miner. Process.*, vol. 84, no. 1–4, pp. 274–298, Oct. 2007.